SMART DRUG DELIVERY SYSTEM FOR THE PREVENTION OF IMPLANT-ASSOCIATED INFECTIONS

Von der Fakultät für Lebenswissenschaften

der Technischen Universität Carolo-Wilhelmina zu Braunschweig

zur Erlangung des Grades eines

Doktors der Naturwissenschaften

(Dr. rer. nat.)

genehmigte

D i s s e r t a t i o n

von Yannick Bourgat
aus Grenoble

1. Referent: *Professor Dr. Henning Menzel*
2. Referent: *Professor Dr. Ingo Ott*
eingereicht am: 03.06.2021
mündliche Prüfung (Disputation) am: 10.09.2021

Druckjahr 2021

Veröffentlichungen der Dissertation

Teilergebnisse aus dieser Arbeit wurden mit Genehmigung der Fakultät für Lebenswissenschaften, vertreten durch den Mentor der Arbeit, in folgenden Beiträgen vorab veröffentlicht:

Publikationen

Bourgat, Y.; Tiersch, J. Koetz, H. Menzel, Enzyme degradable polymersomes from chitosan-g-[poly-L-lysine-b-ε-caprolactone] copolymer. Macromol. Biosci. (2020). DOI: 10.1002/mabi.202000259.

Bourgat, Y.; Mikolai, C.; Stiesch, M.; Klahn, P.; Menzel, H. Enzyme-Responsive Nanoparticles and Coatings Made from Alginate/Peptide Ciprofloxacin Conjugates as Drug Release System. Antibiotics (2021). DOI: 10.3390/antibiotics10060653.

Christ H. A., Bourgat Y., Menzel H., Optimization of critical parameters for carbodiimide mediated production of highly modified chitosan Carbohyd. Polym. (2021). DOI: 10.3390/polym13162702

Tagungsbeiträge / Posterbeiträge

Y. Bourgat: Synthesis of chitosan-g-[poly-L-lysine-b-poly-ε-caprolactone] copolymers. 16th EPF European Polymer Congress. (Poster) TU 018, July 2017

Y. Bourgat, B. Tiersch, J. Koetz: Enzyme degradable polymersomes from chitosan-g-[poly-L-lysine-b-poly-ε-caprolactone] copolymer. (Poster) 95, Jahrestagung Deutsche Gesellschaft für Biomaterialien, November 2017

Y. Bourgat, C. Mikolai, P. Klahn: Enzyme-responsive nanoparticles made from alginate/peptide ciprofloxacin, part 1. Jahrestagung Deutsche Gesellschaft für Biomaterialien. (Poster) 43, November 2018

Y. Bourgat, C. Mikolai, P. Klahn, Enzyme-responsive nanoparticles made from alginate/peptide ciprofloxacin Part 2. Macromolecular Colloquium Freiburg. (Poster) 5, February 2019

To my family and friends

Acknowledgements

To all the people who, in one way or another, have helped, supported and shared with me all the past years during which has been carried out this thesis.

To Prof. Henning Menzel for being my supervisor, for his support and guidance through all this time and for being directly responsible for this work. Thank you for your optimism and for making it a great memory.
To Henrik Christ for his time, excellent contributions and friendship.

To the Hannover Medical School and the Helmholtz Center for Infection Research for the collaboration.
To Frau Dr. Carina Mikolai, Herrn Dr. Andreas Winkel and Professor Dr. Meike Stiesch (Hannover Medical School) for evaluating the antimicrobial activity and for their support.

To Dr. Philipp Klahn for his time, support and for giving me the opportunity to work in his laboratory.

To Dr. Brigitte Tiersch (Institut für Kolloidchemie, University of Potsdam) for giving me the opportunity to work in her laboratory, and for her support during my stay at the University of Potsdam.

To the Braunschweig University of Technology for the “Hilpert Stipedium".

To all colleagues I have worked with over the past years (especially Elena and Maren), for all the good times we have had together in and outside the lab and for every wonderful day we’ve spent together.

To my good friends (Rocco, Uber, Kikito, Henrik) for always being there, listening and providing me a lot of joy.

To Heinz and Annette for their kindness, great support and encouragement.

To Mélanie for her love, patience and understanding (and for many other reasons that are not fitting in a single page).
To my family, Monika, Jean-Luc, Nils and Lena for being part of everything I do and because thanks to them I am who I am today.

To whom I dedicate this thesis especially Fabian Bourgat.

To all and everyone of you, thanks for everything.

Summary

Abbreviations

^{13}C-NMR	-	Carbon-13 nuclear magnetic resonance
^{19}F-NMR	-	Fluorine-19 nuclear magnetic resonance
^{1}H-NMR	-	Proton nuclear magnetic resonance
AcOH	-	Acetic acid
ADAMTS	-	A disintegrin and metalloprotease with thrombospondin motifs
Alg	-	Alginate
AM	-	Activated monomer
APD	-	Avalanche photo-diode Detector
Asp	-	Aspartic acid
ATP	-	Adenosine triphosphate
BCN-OH	-	(1R,8S,9S)-Bicyclo[6.1.0]non-4-yn-9-ylmethanol
Boc	-	Tert-Butoxycarbonyle
Boc-6-Ahx-OH	-	6-((tert-butoxycarbonyl)amino) hexanoic acid
CD_3OD	-	Deuterated methanol
CDCl3	-	Deuterated chloroform
CH_2Cl_2	-	Choroform
CIP	-	Ciprofloxacin
CMC	-	Critical micelle concentration
COSY	-	Correlated spectroscopy
CryoSEM	-	Cryo-scanning electron microscopy
CS	-	Chitosan
Cs	-	Chondroitin sulphate
CuAAC	-	Copper-catalyzed azide-alkyne Cycloaddition
D_2O	-	Deuterium oxide
DA	-	Degree of actelylation
DCl	-	Deuterium chloride
DCM	-	Dichloromethane
DDA	-	Degree of deacetylation
DDS	-	Drug-delivery-system
DIPEA	-	N,N-Diisopropylethylamine

DLS	-	Dynamic light scattering
DMF	-	Dimethylformamide
DMSO	-	Dimethylsulfoxid
DMTMM	-	4-(4,6-dimethoxy-1,3,5-triazin-2-yl)-4-methyl-morpholinium chloride
DNA	-	Deoxyribonucleic acid
DOX	-	Doxorubicin
DS	-	Degree of susbstitution
DVLO	-	Derjaguin, Verwey, Landau and Overbeek
ECM	-	Extracellular matrix
EDC	-	1-Ethyl-3-(3-Dimethylaminopropyl)carbodiimide
EDTA	-	Ethylenediaminetetraacetic acid
EPS	-	Extracellular polysaccharide substance
FT-IR	-	Fourier-transform infrared spectroscopy
GAG	-	Glycosaminoglycan
GlcN	-	Glucosamine
GlcNAc	-	N-acétylglucosamine
Gly-Phe-Ala-Leu	-	Glycine-Phenylalanine-alanine-Leucine
Gly-Phe-Leu-Gly	-	Glycine-Phenylalanine-Leucine-Glycine
GPC	-	Gas phase chromatography
GSH	-	Reduced glutathione
GSSG	-	Oxidized glutathione
H_2O	-	Water
HCl	-	Hydrochloric acid
HCTU	-	O-(1H-6-Chlorobenzotriazole-1-yl)-1,1,3,3-tetramethyluronium hexafluorophosphate
HMBC	-	Heteronuclear multiple bond correlation
HoBt	-	Hydroxybenzotriazol
HSQC	-	Heteronuclear single quantum coherence spectroscopy
IAI	-	Implant-associated infections
Lys	-	Lysine
Mal	-	Maleimide

MeOH	-	Methanol
MMP	-	Matrix metalloproteases
Mn	-	Number average molar mass
MS-ESI	-	Electrospray ionization mass spectrometry
Mw	-	Mass average molar mass
N_2	-	Nitrogen gas
Na_2SO_4	-	Sodium sulfate
NaCl	-	Sodium chloride
$NaHCO_3$	-	Sodium bicarbonate
NCA	-	N-Carboxyanhydride
NH-HMBC	-	Nitrogen-Heteronuclear multiple bond
NOESY	-	Nuclear Overhauser spectroscopy
NP	-	Nanoparticle
PBLA	-	Poly(β-benzyl L-aspartate)
PBS	-	Phosphate-buffered saline
PCL	-	Poly-ε-caprolactone
PDI	-	Polydispersity index
PEG	-	Polyethylene glycol
PEI	-	Polyethylenimine
PyAOP	-	(7-Azabenzotriazol-1-yloxy) tripyrrolidino phosphonium hexafluorophosphate
RA	-	Rotating analyzer
ROP	-	Ring opening polymerization
RT	-	Room temperature
S. aureus.	-	Staphylococcus aureus
SE	-	Spectroscopic ellipsometry
SEM	-	Scanning electron microscopy
$Sn(Oct)_2$	-	Tin(ii) 2-ethylhexanoate
TFA	-	Trifluoroacetic acid
THF	-	Tetrahydrofuran
Ti	-	Titanium
TMSCl	-	Trimethylsilyl chloride
UVVis	-	Ultraviolet-visible spectroscopy
PLL	-	Poly-L-lysine

Symbol directory

Dynamic light scattering

t, τ	-	Time
G (τ)	-	Time correlation
D	-	Diffusion coefficient
q	-	Scattering vector
k_B	-	Boltzmann constant
d(h)	-	Hydrodynamic diameter
η	-	Viscosity
I	-	Intensity
ζ	-	Zeta potential

Ellipsometry

Δ, δ	-	Phase difference
Ψ	-	Amplitude component
s	-	Perpendicular-polarized light
p	-	Parallel-polarized light
$R^{s, p}$	-	Reflection coefficients
E	-	Electric field
λ	-	Wavelength

Polymersomes

p	-	Packing parameter
V	-	Volume of the hydrophobic chain
a	-	Interfacial area per molecule
l	-	Length of the hydrophobic chain

1 Introduction

In the medical field, synthetic or natural biomaterials can be considered in any medical device or implant inserted into living tissue; dental implants and replacement heart values are examples. In recent years, biomaterials such as biopolymers, titanium alloys, stainless steel, ceramics, and composites have increased in prominence, especially for use in implants and musculoskeletal medicine[1]. Because of the ageing population which is in particular affected by degenerative diseases, the number of implantations performed has increased considerably[2]. Unfortunately, implantation of medical devices is a major source of nosocomial infections during the perioperative period[3]. Primary sources of contamination are the implant surface, surgical theater, surgical equipment, the surgeon and medical personnel, and patients[2][3]. Implant-associated infections are typically caused by microorganisms, including bacteria that grow in biofilms and cause chronic inflammation[4]. Besides high contamination sources, implanted foreign materials are highly suseptible to bacterial and fungal infection and implant-associated infection might occurs as long as they are in the body through the heamatogenous route. Because the mouth is a particularly suitable environment for the growth of microorganisms, this thesis focuses on dental implants and solving the challenge of preventing the formation of biofilm on the implant by providing solutions with infection-controlled release of antibacterial agents.

A biofilm is described as a collective of one or more types of microorganisms nonrandomly distributed in a glycocalyx coating that proliferate on a surface. Such a biofilm on the surface of an implant can cause severe medical complications. Biofilm formation involves six steps, beginning with the formation of a thin layer of proteins and glycoproteins, lodged by the saliva[5]. Primary adhesion involves the rapid adhesion of coaggregated planktonic bacteria on the protein layer (Figure 1-1, **Step 1**). The forces associated with bacterial adhesion include surface charge, Van der Waals forces, and hydrophobic interactions[6], collectively known as DVLO (Derjaguin, Verwey, Landau, and Overbeek) forces[7]. DVLO theory describes the interactions between cells and flat surfaces that involve a balance between the attractive Van der Waals interactions and repulsive forces. Furthermore, substratum roughness and properties such as ionic strength influence the attachment of bacteria. Primary adhesion is followed by cellular proliferation and intercellular adhesion (Figure 1-1, **Step 2**). Polysaccharides named extracellular polysaccharide substance (EPS) are excreted by the bacteria, resulting in an irreversible attachment. EPS is a well-organized and structured matrix released

by bacterial cells that accomplishes the following beneficial activities. First, EPS assists nutrient dissemination, which is necessary for cell growth. Second, the diverse composition of the charged polysaccharide facilitates the binding of external nutrient molecules, which leads to cells sustenance and growth[8].Third, cells encapsulated in the EPS matrix are well protected against external antagonistic agents such as antibiotics[9], disinfectants, and dynamic environments[10]. As part of the EPS matrix, intercellular signaling or quorum sensing enables the system to communicate through small diffusible signal molecules, and this significantly benefits bacteria in their effort to stave off competitors and rapidly adapt to changing environments[11]. The formation of biofilm creates satisfactory conditions for maturation and bacterial cell cluster formation (Figure 1-1, **Step 3**). Intercellular interactions that are mediated by adhesins and bacterial cell wall proteins contribute to clustering and subsequent microcolony formation[11]. Subsequently, three-dimensional growth and further biofilm maturation occur (Figure 1-1, **Step 4**). In **Step 5** (Figure 1-1), the biofilm reaches a critical mass and disperses planktonic bacteria, which are able to colonize other surfaces[12] (Figure 1-1, **Step 6**).

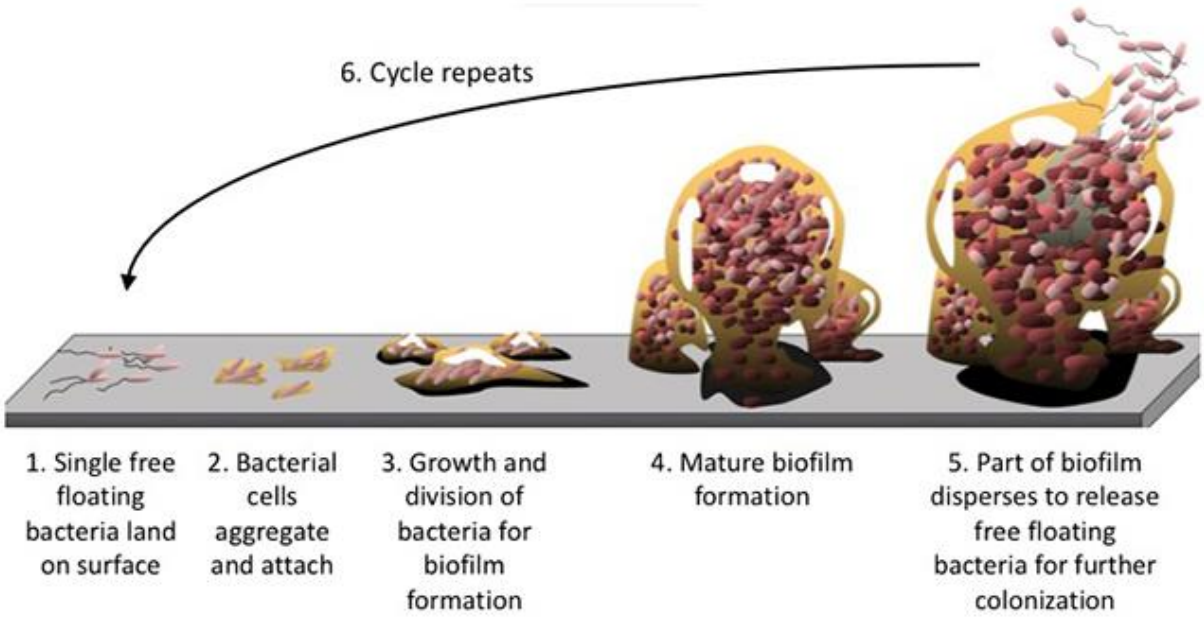

Figure 1-1 Schematic representation of biofilm development on a solid surface (Figure adapted from Monroe[13] under the creative commons license. Image credit: D. Davis).

Factors related to the failure of dental implants because of implant associated infections can be divided into four sources[14]:

- Implant: surface roughness, purity and sterility, oral exposure time.

- Patient (local and systemic factors): smoking, alcoholism, bone quality.
- Surgical technique/environment: perioperative bacterial contamination (e.g. saliva, instruments, gloves).
- Mechanical overloading: traumatic occlusion due to inadequate restorations.

To prevent implant-associated infections some basic nontechnological recommendations are proposed. Because it is known that contamination may occur through the inoculation with just a few microorganisms during implantation, adopting hygienic measures is the most efficient approach to prevent implant-asssociated infections. Therefore, meticulous antisepsis during surgery, strict adherence to basic hygienic rules such as effective hand disinfection, appropriate individual behavior in the operating room, and a clean air environment are essential for the prevention of implant-associated infections. Preventing rather than being forced to cure such infections is fundamental.

In addition to the aforementioned precautions, numerous strategies have been implemented in an effort to avoid implant-associated infections. Among them, some have focused on the development of various implant coating materials for use as the controllable means of delivering antibiotic in a sustained manner[15]. For instance, polymer coatings can locally release drugs, thereby reducing the toxicity and side effects associated with the use of high antibiotic doses[16].

More generally, antibacterial implant coatings can be divided into two categories: those with a repelling effect and those with a killing effect. Both types prevent the primary adhesion of living planktonic microbial cells on the implant. Repelling microbes is possible by using hydrogel coatings, which are mostly based on highly negatively charged polymers or incorporate ultrahydrophobic modifications. For instance, systems based on poly(2-alkyl-2-oxazoline), which is a hydrophilic polymer, strongly inhibit bacterial adhesion[17]. As a further example Tsibouklis et al. generated coatings from poly(methylpropenoxyfluoroalkylsiloxane)s and poly(perfluoroacrylate)s capable of inhibiting bacterial colonization on surfaces. The use of these polymers with low surface energy that can form smooth coatings is a potential means of inhibiting bacterial adhesion on surfaces[18].

Coatings in the killing effect category use antimicrobial materials to cause the death of bacteria. Such elimination of bacteria may be achieved through two different strategies: the release of an active ingredient or the use of antibacterial polymers that kill the bacteria upon contact. For example, it has been found that polycations exhibit

antibacterial effects against various bacteria[19]. The efficacy of such antibacterial polymers highly depends on incorporating hydrophobic moieties; effectiveness depends on the type, distribution, and amount of the hydrophobic component[20]. Both cationic and hydrophobic components enable the synthesis of a broad range of antimicrobial cationic polymers. Jingwei et al. designed and synthesized polymers with quaternary ammonium salts and various alkyl chain lengths. Eight of those polymers exhibited compelling antimicrobial activity, which could be further enhanced by increasing the hydrophobic chain length[21]. Another approach is the encapsulation or conjugation of bioactive substance, in order to have a sustained and controlled release. Khuller et al. have encapsulated an antibiotic, Streptomycin, in Poly-lactide-co-glycolide nanoparticles. They were able to increase the bioavailability of encapsulated streptomycin compared with intramuscular free and maintain steptomycin levels for four days in the plasma and for seven days in organs[22].

Roseeuw et al. developed a macromolecular transport system composed of dextran and mannose for targeting macrophages and conjugated norfloxacin as an antibiotic. Norfloxacin was linked to the polymer through various tetrapeptide linkers, such as Gly-Phe-Ala-Leu and Gly-Phe-Leu-Gly, which are cleaved by proteases such as cathepsin B[23]. Norfloxacin was linked to the C-terminal part of the peptide through a reaction with the piperazine moiety. The release was activated by pH variation and incubation with cathepsin B. On the other hand Tolle et al. described nanoparticles, which were generated through ionic gelation of negatively charged alginate and a positively charged enzyme-cleavable peptide[24]. The cleavage was triggered by a specific enzyme released during infections and induced the drug release.

Of these strategies, the latter one seems to be the most appropriate for the successful prevention of biofilm formation. By contrast, a coating with antimicrobial cationic polymers is efficient but only after making contact with the bacteria. Moreover, dead bacteria or proteins may overlay the coating, diminishing its efficacy. Therefore, even after absorption of surrounding proteins or dead bacteria, using nanocarriers to release drugs might be an effective approach to combat a pathogenic situation.

2 Aim

The long-term successful development of dental implants depends largely on the ability to keep them free of infections and therefore obviate any further surgical treatment. The aim of this research is to generate an encapsulation system to reduce drug usage, and prevent the growth of biofilms. The degradation of the material used in the system should take place as a direct consequence of a trigger, leading to the release of an antibiotic. The antibiotic should only be released during an infection or inflammation as a reaction by pathogenic bacteria contamination. Therefore, the focus of the dissertation was the production and characterization of suitable nanocarriers and their immobilization as a drug delivery system on implant surfaces such as titanium. Furthermore, degradation and release of model active ingredient shall be investigated.

3 Drug delivery systems

Synthesizing and bringing new drugs to market is usually a long and expensive process. As a consequence, conventional drugs that are deficiently soluble, lose efficacy after administration, or have unfavorable pharmacokinetics[25]. Many of these problems can be improved upon by using drug delivery systems. Among many different types, as described in chapter 3.1, a DDS can, for instance, be composed of hydrophobic polymers and, therefore create a suitable environment by adjusting drug solubility and enhancing protection. Moreover, drug clearance by the kidneys occurs rapidly, necessitating high doses or continuous infusion. To counter this, DDS offer a high degree of protection against rapid clearance of small molecules and also reduce toxicity affecting healthy tissues. A key advantage of DDS is their ability to increase drug concentrations in a specific location such as a tumor or infection site [25]. Ligand-mediated targeting by DDS can also improve specific targeting of tissues[26]. To ensure the success of a system, further factors need to be taken into consideration:

- Rapid and easy processing.
- Biocompatibility of materials used.
- High resistance to sterilization, drying, or packaging[27].

3.1 Different types of systems

In addition to conventional oral and intravenous drug delivery, new systems of delivery have been investigated with the intention of devising a system with the ability to control and concentrate drug release at a specific location. For this purpose, several DDS have been created and investigated for various pharmaceutical applications. These DDS make use of liposomes, nanoparticles, hydrogels, micelles, dendrimers, and polymersomes. These systems are briefly described in an overview presented in the following chapter.

3.1.1 Micelles

Polymeric micelles are self-assembled core-shell structures formed by amphiphilic copolymers. Formation of these structures is driven by hydrophobic interactions and hydrogen bonds, which lead to a decrease of free energy, leading to the formation of micelles. This formation occurs when the concentration reaches a specific concentration: critical micelle concentration (CMC). At the CMC, hydrophobic segments begin to aggregate to minimize contact with water, leading to the formation

of micelles[28]. Most micelles are fabricated by an amphiphilic copolymer with one or more hydrophobic component, such as the following:

- AB-type diblock copolymer[29]
- ABA-type triblock copolymer[30]
- ABC-type triblock copolymer[31].

According to the literature and amoung many others, polyesters as the hydrophobic segment, such as poly(lactide), poly(lactide-co-glycolide), poly(lactide-co-caprolactone), poly(p-dioxanone), poly(p-dioxanone-co-lactide), and poly(orthoester) could be used. As hydrophilic moiety, poly(ethylene glycol), poly(vinyl alcohol), poly(N-(2-hydroxypropyl) methacrylamide), poly(N-vinylpyrrolidone), poly(acrylic acid) and chitosan are widely employed[32].
The most common methods for preparing micelles are the following:

- Solvent evaporation: typically, the block copolymer is dissolved in an organic solvent such as aceton, and then the solution is added dropwise into distilled water. Afterwards, the organic solvent is evaporated under reduced pressure to obtain the micelle solution[33].
- Oil in water emulsion: This consists of dissolving the polymer and the drug in an organic solvent. The resultant solution is then emulsified in an aqueous phase containing a surfactant. This latter process prevents the organic solvent droplets from coalescing. The micelles are formed through stirring under appropriate temperature conditions[34].
- Dialysis methods: If the solvent is, for instance, water/dimethylformamide (DMF) miscible, the DMF solvent can be exchanged by dialysis against water, and this consequently generates the micelles[34].

Micelles have the ability to encapsulate poorly water-soluble drugs through various methods:

- Direct dissolution and complexation: a charged drug is incorporated into micelles through electrostatic interaction with ionic block segments.
- Direct dissolution and physical entrapment: hydrophobic drugs are solubilized with the copolymer and encapsulated into the hydrophobic core during the micellization process.

- Chemical conjugation: the drug is conjugated to the block copolymer through pH or enzyme-sensitive linkers that can be cleaved to trigger drug release[35][36].

In addition to the ability to encapsulate molecules, polymeric micelles are able to protect loaded drugs from harsh conditions, extend the circulation time of a drug in the body, and cause the accumulation of drugs at a localized site of action[37]. In conclusion, micelles have become an appealing structure in which hydrophobic drugs can be encapsulated and which have been demonstrated to be responsive to various exogenous (magnetic field, ultrasound intensity, electric field, variations in temperature, magnetic field, or light) or endogenous stimuli (enzyme concentration, changes in pH or redox gradients)[38].

3.1.2 Hydrogels

A hydrogel comprises three-dimensional cross-linked networks of water-soluble polymers capable of absorbing a high amount of water or biological fluid. The networks are generally made of chemically or physically cross-linked polymers, providing highly satisfactory stability and insolubility in aqueous solution.

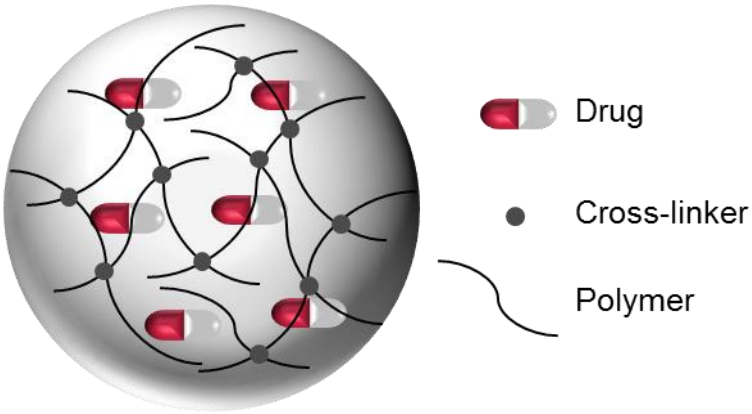

Figure 3-1 Schematic representation of hydrogel as drug delivery system.

Furthermore, hydrogels can be formulated in a variety of physical forms such as nanoparticles, microparticles, coatings, and films[39]. They are commonly used in a range of medical applications such as tissue engineering[40], diagnostics[41], cellular immobilization[42], separation of biomolecules[43], and DDS[44]. The physical properties of hydrogels have aroused particular interest within the drug delivery field. In fact, their mesh-size can be tuned by the cross-link density, which allows for control over the rate of diffusion of encapsulated molecules through the hydrogel[39]. This enables the system to maintain a high local concentration of the drug in the surrounding tissues

over an extended period[45]. A major advantage of hydrogel is its similarity to the extracellular matrix and its capacity to absorb a high amount of water, thus providing good biocompatibility[46]. In addition, biodegradability may be incorporated into hydrogel using different strategies. Enzymatic, hydrolytic pathways or naturally occurring environmental variations in pH and/or temperature[47][48][49] can be used to trigger the degradation and release of a drug. Due to the hydrophilic properties of hydrogels, hydrophilic drugs are the most suitable for encapsulation. The homogeneity and loading capacity of the encapsulation of hydrophobic substances are limited[50]. Because of their high water absorption and porosity, hydrogels are also limited by an effect called burst release[51]. This effect can be described as a high rate of release that occurs rapidly at the beginning of the release process and represents the main drawback of hydrogels.

3.1.3 Nanoparticles[52]

In the field of delivery systems, nanoparticles (NPs) are defined as structures with a diameter ranging from 10 to 100 nm[53][54]. They can be obtained among others from biopolymeric materials such as chitosan, alginate, xanthan gum, and cellulose or synthetic polymers such as poly(ε-caprolactone), poly(acrylamide), and poly-acrylate[55]. According to their structural organization, nanoparticles are classified as nanocapsules or nanospheres[52] (Figure 3-2). Nanocapsules are core-shell structures that are similar to micelles and liposomes. In such systems, the drug is confined or contained within the core cavity, which is surrounded by a polymer membrane. Nanospheres are matrices, where the encapsulated drug is physically and uniformly dispersed in the polymer matrix. Both hydrophobic and hydrophilic substances can be entrapped with high efficiency. Lipophilic drugs are encapsulated in the entire polymer matrix, and hydrophilic compounds are adsorbed at the particle's surface. For both systems, release in a targeted tissue occurs through the processes of diffusion and degradation. These processes are directly related to the biodegradability and permeability of the particle matrix. If diffusion occurs more quickly than degradation, this implies that the mechanism of release is governed by the diffusion process and can be used to maintain a high drug concentration at a specific location over an extended period of time. The rapid initial burst release is the main challenge faced by such systems and is mainly caused by weak interactions between the active ingredient and the NP[56]. Another strategy is to control drug releases by a targeted degradation of the DDS. This has led to novel investigations of synthetic methods, bioconjugation

techniques, and a rapid proliferation of strategies using targeted chemical reactions and degradation processes to trigger changes in structure, shape, chemistry, and degradation rates of DDS. Degradation can be triggered, with high specificity, by enzyme release, temperature or pH changes, electromagnetic radiation, the influence of a magnetic field, ionic strength variation, or reduction-oxidation reactions[57]. For instance, in pathological conditions (tumors or inflammation), the expression of specific enzymes (protease, phospholipase, or glycosidase) is observed and used to release the drug at a desired location[58]. Such stimuli-responsive systems are further discussed in chapter 3.2.

Furthermore, NPs offer many other advantages such as the ability to travel through capillaries, avoid drug clearance by the immune system, penetrate cells, and reduce the side effects of the drug[59].

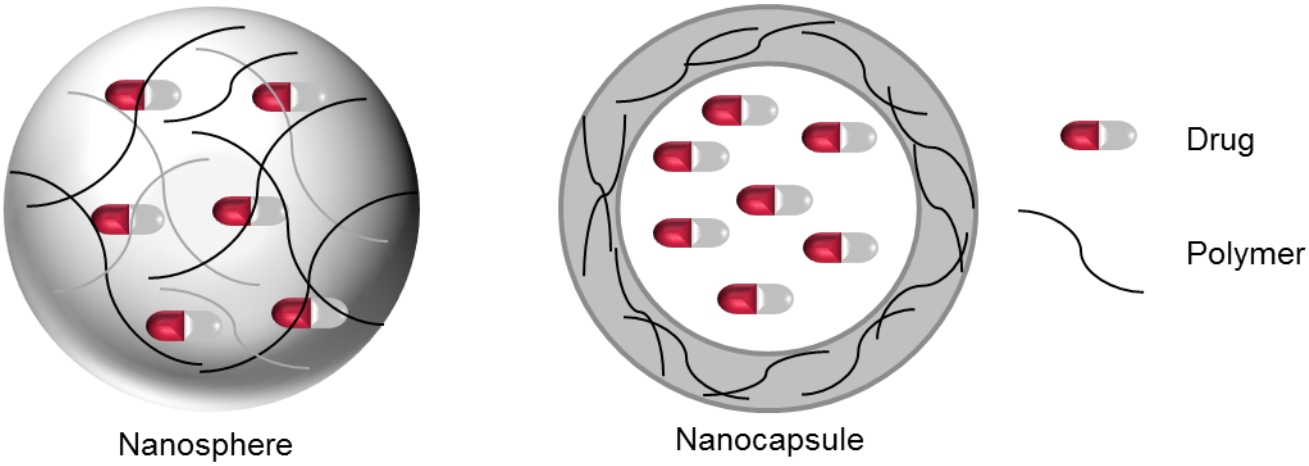

Figure 3-2 Schematic representation of a nanoparticle.

Particle formation can proceed through various mechanisms[60]:

- desolvation
- emulsion/solvent extraction
- electrospraying
- self-assembly through hydrophobic interactions
- ionic gelation

Ionic gelation has many advantages because of the simple procedure and mild conditions for particle formation. In fact, the use of hazardous organic solvents and high shear forces are avoided, which minimizes the risk of affecting the activity of encapsulated active ingredients[61].

3.1.4 Liposomes[62]

Liposomes were called a “magic bullet” by the German bacteriologist Paul Ehrlich because of their unique property to selectively kill abnormal cells without any effect on healthy ones[63]. This specificity has been improved through various approaches based on physical and chemical properties.

Liposomes are formed by lipids, which are amphiphilic molecules with hydrophilic (head) and hydrophobic (tail) parts. Due to hydrophobic and hydrophilic interactions, they are able to generate bilayer-structured vesicles with a hydrophilic compartment in the core and hydrophobic compartments in the lipid bilayers (Figure 3-3)[62].

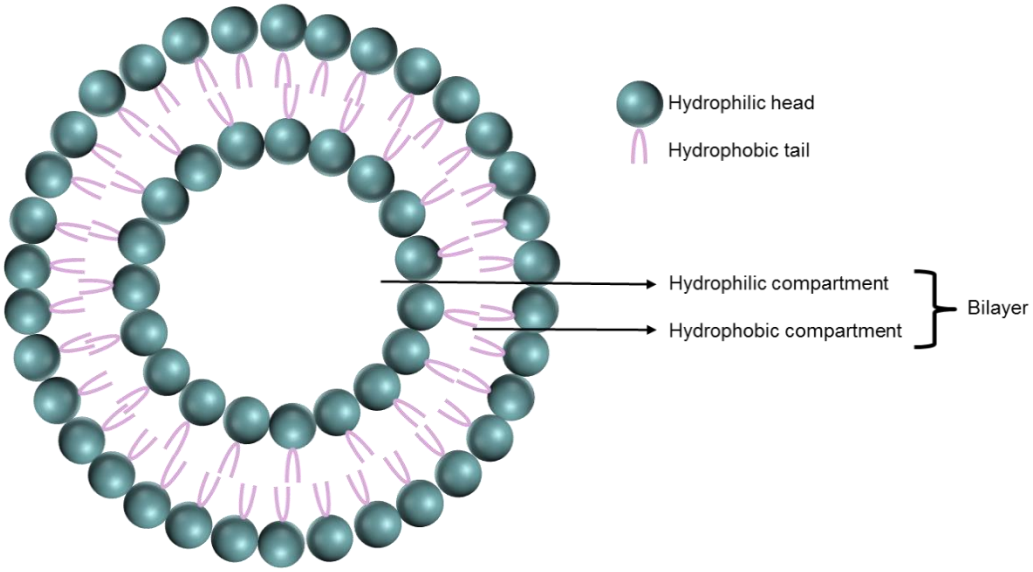

Figure 3-3 Schematic representation of the structure of a liposome.

Liposomes can be classified according to their size, number of bilayers, charge, lipid composition, and surface modification with polymers and ligands able to govern their stability in vitro and in vivo[64][65][66][67].

They are categorized either as unilamellar or multilamellar, depending on their single bilayer and multibilayer separated by a hydrophilic compartment. Unilamellar liposomes are subdivided into small (20-100 nm), large (>100 nm) and giant (10-1000 µm) vesicles[68][69]. From a chemical point of view, Bangham et al. defined liposomes as vesicles with a small size and spherical shapes that can be generated from phospholipids, cholesterols, nontoxic surfactants, and even membrane proteins. Those phospholipids can occur naturally, such as the well-known phosphotidylcholine, or can be synthetic molecules inspired by the natural ones[68]. Many studies concerning

liposomes have shown their advantages for use as delivery systems because of the capacity to carry a variety of compounds in the core section[70]. In fact, the multicompartment structures enable a high drug loading and can deliver both hydrophilic and hydrophobic substances[68]. Additionally, they can increase the stability and efficacy of the drug[71] and reduce both the toxicity of the encapsulated agent and the exposure of sensitive tissues to toxic drugs. Moreover, liposomes offer other benefits such as biocompatibility, physicochemical and biophysical properties through which to control and adapt their biological characteristics[72]. They can be modified to improve stability, enhance their circulation time in the bloodstream, or generate a ligand-targeted liposome. For instance, hydrophilic polyethylene glycol has been an interesting moiety to stabilize liposomes in-vivo [73]. The incorporation of polyethylene glycol as steric barrier improves the efficacy of encapsulated agents by reducing the rapid recognition and uptake by the mononuclear phagocyte system. In addition to reducing the elimination of drugs by prolonging blood circulation and providing accumulation at pathological sites, liposomes also attenuate side effects of drugs[73].

3.1.5 Dendrimers[74]

Dendrimers are a polymeric system with a well-defined structure, high water solubility, and polyvalence, which have made them an object of considerable attention and a possible system for use in biomedical applications. Dendrimers are three-dimensional branched molecules that have a low polydispersity index. The name dendrimer is derived from the Greek word “dendron,” which means “tree,” and refers to the tree-like branching structure of dendrimers. The architecture can be distinguished into a core moiety that is followed by branched sections, which are called generations. Each generation is limited by junction points (Figure 3–4)[75].

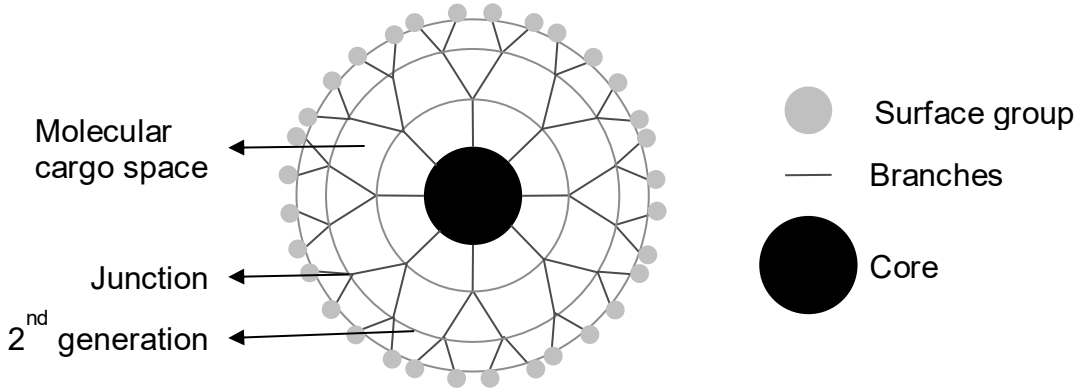

Figure 3-4 Schematic representation of dendrimers.

Moreover, functional groups can be found at the external surface of a dendrimer. The higher the number of generations, the more groups are available for further modifications. The molecular size and surface groups offer considerable potential for making several surface modifications. For instance, multivalency has enabled the appearance of many guest-host complexes, with a wide range of applications[75] and possibilities to target their actions in various body locations. Applications can be achieved by multifunctionalizing the dendrimer with vector devices[76][77]. Additionally, dendrimers also have the capacity to encapsulate drugs in their molecular hydrophobic and hydrophilic cargo spaces through physical or chemical bonds (Figure 3–4). For example, Kannan et al. designed a poly(amidoamine) dendrimer-N-Acetylcystein conjugated with a cleavable disulfide linkages for use as delivery vehicles[78]. One key advantage, when used as a delivery system, is their ability to cross cell barriers via both paracellular and transcellular pathways, allowing these nanocarriers to efficiently deliver drugs into cells[79]. Furthermore, their nanoscopic scale ranges in size (1 to 100 nm), and a low polydispersity index enables them to overcome the macrophage system[80].

Even though dendrimers possess a wide range of applications in the field of biomedicine, their toxicity was reported as a considerable obstacle in their usage[81]. Furthermore, dendrimers remain challenging systems due there high degree of complexity in the synthetic preperation[82] and the low control over the attachement of active substance[83]. Indeed, there is mainly a random conjugation of drug and targeting ligand to the surface of dendrimers results in poorly-defined compound mixtures that are unlikely to pass regulatory revision and translate into the clinical trials[83]. Therefore, dendrimer's mixtures might have significant batch-to-batch variations of active ingredient that leads to non-reproducible pharmacokinetic behavior[83]. To advance dendrimer-based materials into clinical trials it is necessary to develop well-defined multifunctional dendrimers with controlled number and location of drugs[83].

3.1.6 Polymersomes

Similar to liposomes, polymersomes are structures based on amphiphilic molecules and consist of hydrophobic components, which minimize direct exposure to water, and hydrophilic components delimiting the two interfaces of a typical bilayer membrane. Unlike liposomes and as the name suggests, the polymerome is composed of amphiphilic polymers, which are thermodynamically driven into self-assembled ordered structures such as, bilayer or multilayer structures[84][85]. Factors such as the

characteristics of hydrophilic groups, weight percent, the length and chemistry of the hydrophobic components play a crucial role in the shape of the polymer aggregate. Assembly into those different structures is governed by the packing parameter (*p*), which can be used to predict the shape formed during the self-assembly process. The (p) is related, to (*V*), the volume of the hydrophobic chain, to (a), the interfacial area per molecules, and (l) the length of the hydrophobic chain via the following formula[86][87]:

$$p = \frac{V}{a.l}$$

(V): volume of the hydrophobic chain
(a): interfacial area per molecule
(l): length of the hydrophobic chain

Depending on the (p) value, three different structures might be generated, polymersome, worm-like micelles and spherical micelles.

Each structure can be defined by p values:

if $p < \frac{1}{3}$, spherical structures are formed;

if $\frac{1}{3} < p < \frac{1}{2}$, cylinders are formed; and

if $\frac{1}{2} < p < 1$, polymersomes are generated[87][88]

In other words, the hydrophilic part (f) is a determining factor in the formation of different structures and can also be predicted by the balance between hydrophilic and (f). For instance, if the (f) value in the structure is higher than 50%, the formation of spherical micelles is possible, and with an (f) value between 40% and 50%, worm-like structures are more likely. Finally, if the (f) value is between 25% and 40%, which is similar to natural phospholipids, polymersome formation is more favorable[89].

The structure of polymersomes can be described as a bilayer-based core-shell structure with a hydrophobic compartment and hydrophilic core (Figure 3-5). Hence, one of their beneficial attributes for use as drug carriers is the ability to incorporate hydrophilic (Figure 3-5, A) and hydrophobic (Figure 3-5, B) drugs with a high loading capacity[90][91].

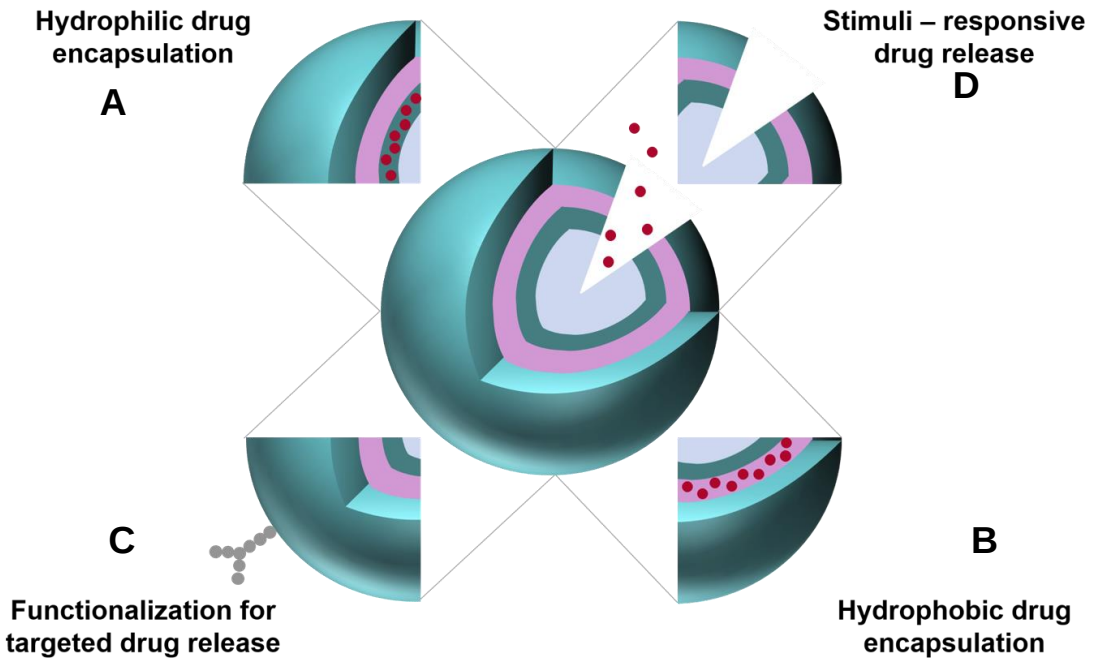

Figure 3-5 Schematic representation of liposome structure: purple, hydrophobic tail; blue, hydrophilic head and its compartments.

Loading capacity is one of the most important factors for any drug delivery system. For instance, DDS with low encapsulation efficiency would require a higher quantity of polymeric materials to achieve the appropriate drug concentration and can lead to a stronger immune response. Besides polymersomes were proven to be more stable and less water-permeable compared to liposomes like phospholipid vesicles[85]. Indeed, liposomes have been described as leaky structures with poor retention efficiencies. On the other hand, polymersomes offer the possibility to control the diffusion rate by varying the amount/length of the hydrophobic segment[92][93]. Moreover, natural and synthetic lipids, to generate liposomes, cannot be easily functionalized. Even small modifications at the head group can have a significant impact on the properties and thus on the self-assembly into liposomes. On the other hand, modification of the lipid tails requires often several synthetic steps[94]. On the contrary, polymersomes surface-functionalization can be achieved by using polymers that carry functional groups on their chains[85]. The ability to functionalize the surface with specific targeting groups or ligands offers a range of possible targeted release sites in the body and thus minimizes unwanted side effects of a drug (Figure 3-5, C). For instance, targeting groups or ligands can be biotin receptors, insulin, or antibodies such as Anti-ICAM-1, which is used to target inflammatory tissues[95]. Moreover,

responsiveness (Figure 3-5, D) can be incorporated and the polymersome designed to release an active ingredient only under specific conditions or upon the application of a particular stimulus[96].

3.2 Stimuli-responsive DDS

An ideal drug delivery system must first demonstrate biocompatibility, efficiency, and then controlled-release functions. Therefore, many studies have focused on DDS that integrate stimuli-responsive characteristics. Stimuli responsiveness is especially important for disease pathologies, in which specific conditions occur. For instance, biological stimuli that can be exploited to target solid tumors include pH, temperature, and the enzyme and redox microenvironment[97][98][99][100]. Another strategy is to physically trigger the release by external stimuli such as a magnetic field[101], ultrasound[102], or light[103].

3.2.1 pH-responsive DDS

It is well known that the physiological pH is approximately 7.4. However, due to different situation or location, the pH might diverge from the pysiological pH. For instance, decrease in pH is observed in pathological tissues upon inflammatory conditions or tumor environment[90]. Under normal conditions, the pH might also vary, in endosome and lysosome compartments with a variation range of 4.5 to 5.5. For this reason, the pH may be an interesting means of triggering the release of an active ingredient. The pH of an infected environment; primary tumor, or metastasized tumors is lower than that in normal tissue[104]. In fact , it can drop from 7.4 to 6.5, after an inflammatory reaction[105]. A tumor environment exhibits pH fluctuations ,ranging from 5.7 to 7.8[106][107].

Anticancer treatments are generally associated with unwanted side effects because of the nonspecific distribution of drugs into normal tissue. Therefore, selective drug targeting is of high interest for treating cancer. As mentioned previously, the pH is significantly lower in a tumor mass than in normal tissues and could therefore be used to release drugs in a localized manner. One reason for this is that tumors proliferate very rapidly and their vascularization is often insufficient to supply adequate nutrients or oxygen; leading to hypoxia and production of lactic acid. The hydrolysis of adenosine triphosphate also contributes to acidification of tumor environments[108]. One approach for triggering drug release is to introduce ionizable chemical groups such as amine or carboxylic acids. Those groups can accept or donate protons and therefore undergo

pH-dependent physical or chemical changes[109]. For instance, weak polyacids such as poly(methacrylic acid) accept protons at a low pH and release protons at a neutral or high pH. Conversely, weak polybases such as poly[(2-dimethylamino)ethyl methacrylate] accept protons at a low pH and generate a positively charged polymer chain. The consequence of these modifications is a variation in the swelling or solubility, causing drug release. Kocak et al. summarized many other examples for pH responsive polymers[109].

Another approach is to use acid-labile chemical bonds to attach drug molecules to nanocarriers, which can be incorporated into the system. These bonds are stable at a neutral pH but hydrolyze under acidic conditions. The bonds usually used are orthoester[110], acetal, hydrazine[111][112], and imine[113] (Figure 3-6).

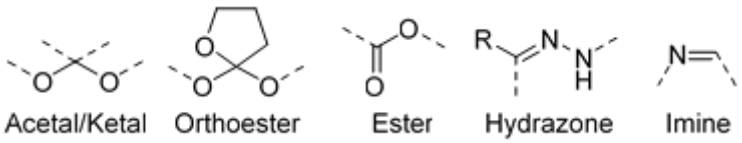

Figure 3-6 Acid-labile chemical bonds.

For example, under acidic conditions, the oxygen of the acetal group is protonated. This facilitates the attack of a water molecule and leads to the cleavage of the bond through formation of an aldehyde and an alcohol[114][115][116].

Several pH-sensitive delivery systems have been developed, including polymersomes[117], polymeric micelles[118], nanospheres[119], hydrogels[120], liposomes[121], and dendrimers[122]. Griset et al. cross-linked NPs using hydrophobic acrylate polymers, which integrate hydroxyl functions protected by an acid labile group. The NPs are stable at a neutral pH, but at a lower pH, the protecting group is cleaved, liberating the hydroxyl group. As a consequence, the polymer becomes hydrophilic, leading to the swelling of NPs and drug release. Drug release was shown to be under 10% at pH 7.4. However, at pH 5, nearly all the encapsulated drug was released within 24 hours[123].

Zhang et al. developed pH-sensitive micelles by linking tretinoin and dextran via a hydrazone bond[124]. The micelles were able to encapsulate doxorubicin (DOX) as an antitumor substance and an accelerated drug release, under acidic conditions, was shown. Under this condition, the cleavage of the hydrazone bond occurs, leading to the disruption of particles. Systems that integrate cleavable acid bonds to link drugs

and polymers have also been used to control drug release. Bae et al.[125] developed a system that conjugates DOX to an amphiphilic block copolymer, poly(ethylene glycol) poly(aspartate hydrazone DOX via a hydrazone bond and that is able to generate polymeric micelles. The DOX is conjugated to the side chain of the poly(aspartate) segment. The pH dependence of DOX release was confirmed and used to accumulate the drug in the nuclei of cancer cells. To conclude, harnessing the acidic conditions of the cancer environment or infection site has proven to be a powerful and effective strategy for drug delivery nanosystems.

3.2.2 Thermoresponsive DDS

In addition to pH, temperature-sensitive DDS are one of the most widely explored classes of environmentally sensitive polymers. They are easy to control, to prepare, and to handle. Generally, thermosensitive systems exhibit a shape and volume change at a specific temperature, leading to a drug release[126]. A slight shift in the temperature causes a significant transformation in their macroscopic properties, which makes them valuable in the biomedical[127][128], pharmaceutical[129][130], and engineering[131] fields.

Temperature variations naturally occur in pathological tissues, and varying temperature is an intriguing means of triggering the release of active ingredients. Thus, various thermo-responsive DDS have been developed to release a drug at a specific temperature. Such systems should be able to protect the active ingredient in the circulatory system and accumulate the drug in locally heated regions. The main characteristics of sensitive polymers are the presence of hydrophobic components such as methyl, ethyl, or propyl groups, which are responsible for the appearance of a critical solution temperature[132]:

- Lower critical solution temperature (LCST): the temperature below which the polymers are miscible in the solution.
- Upper critical solution temperature (UCST): the temperature above which the polymers are miscible.

In the case of LCST polymers, their solubility decreases with an increasing temperature, and systems based on such polymers shrink as the temperature increases above the LCST. This swelling/deswelling effect occurs because of an increasing number of hydrophobic interactions[132][133]. As mentioned previously, these polymer chains contain a mixture of hydrophilic and hydrophobic segments. At lower temperatures, hydrogen bonds between the hydrophilic component and water

enhances dissolution, but at a higher temperature, hydrophobicity increases, resulting in hydrogel shrinking[132].

One of the most studied synthetic thermosensitive polymers is poly(N-isopropylacrylamide), which is also used in DDS[132]. The advantage of this polymer is its LCST at body temperature. For the purpose of a DDS, the phase-transition can be adjusted to the specific temperature of 40°C, which occurs in pathological tissues. This is achieved by incorporating into the polymer hydrophilic comonomers such as N, N-dimethylacrylamide[134][135].

3.2.3 Redox-responsive DDS

Disulfide is a well-known bond that is subject to rapid cleavage by glutathione (GSH)[136]. Therefore, it is an interesting tool that can be used to integrate redox sensitivity into DDS. GSH is an antioxidant capable of preventing cellular damage caused by heavy metals and reactive oxygen species (ROS) such as free radicals, peroxides, or lipid peroxides[137]. GSH also controls the cellular oxidation-reduction environment mainly through the formation or fragmentation of disulfide bonds and the reaction with ROS.

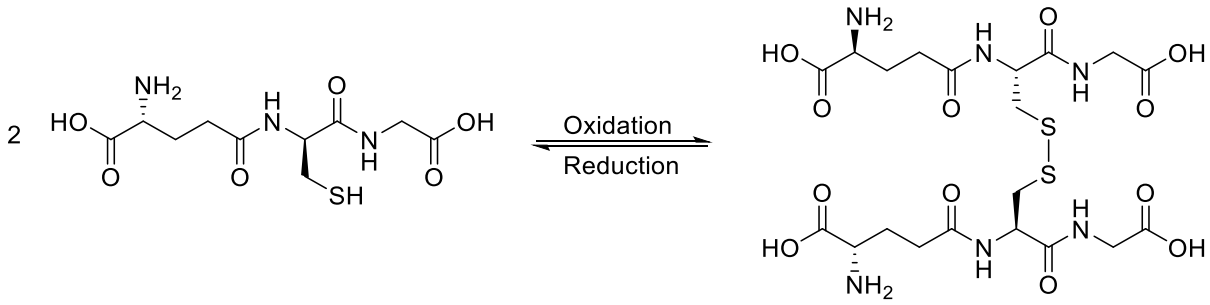

Figure 3-7 Metabolism of glutathione into glutathione disulfide.

Studies have demonstrated that GSH/glutathione disulfide is an abundant redox couple in mammalian cells (Figure 3-7). In the cytosol and nuclei, the concentration of GSH reaches 10 mM, and outside the cell, the concentration drops to 2-20 µM[138]. Moreover, in vivo studies have reported that the concentration of GSH in tumor cells was at least fourfold higher than GSH concentrations in normal tissue[139]. The same variation can be observed in humans[140]. Thus, differences in reducibility of the environment between normal and tumor cells provide strategies for targeted therapy against cancer progression[141]. Specific environmental traits of tumors were used to develop a unique means of degrading redox-sensitive nanocarriers in tumor cells and releasing encapsulated molecules in a localized manner. Three main advantages to

such an approach can be highlighted. First, redox-sensitive nanocarriers exhibit satisfactory stability in a healthy environment, which reduces toxicity and side effects of the drug simultaneously. Then, the nanocarriers exhibit a specific response to the high GSH concentration in tumor cells, which enables a triggered release. Finally, compared with other locations, cytoplasm is often expected to achieve superior therapeutic results[142][143]. In the last decade, many reductive-sensitive systems have been developed on the basis of polymers containing disulfide links that connect polymer blocks together[144]. Disulfide bonds can be easily cleaved by GSH into sulfhydryl functions, subsequently leading to degradation of the DDS and the release of the encapsulated drug. For instance, Navath et al. synthesized two conjugates based on a cationic and an anionic poly(amidoamine) dendrimer with a N-acetylcysteine payload of 16 and 18 per dendrimer. N-acetylcysteine is an antioxidant and anti-inflammatory agent. Their results indicated that the system generated a higher local N-acetylcysteine concentration inside the cells[78]. This strategy enabled many other system such as liposomes[145] or disulphide cross-linked nanogels[146].

Moreover, accumulation of ROS in inflammatory tissues has also been intensively explored for generating redox-responsive systems. Indeed, thioketals are frequently used as a protection group for a carbonyl group as well as a reagent in organic chemistry and can be cleaved by oxidation. For instance, Wilson et al. developed thioketal-based NPs for oral delivery to inflamed intestinal tissues that exhibit abnormally high levels of ROS[147]. In addition to disulfide bonds, diselenide (Se-Se) bonds have been explored. Indeed, they have a similar redox-responsive behavior as disulfide bonds[148][149]. Se-Se and C-Se bonds have lower energy bonds than S-S, making them even more redox sensitive[150].

To conclude, redox-responsive DDS have been recognized as a valuable strategy for achieving efficient drug delivery. The differences between the microenvironments of tumor cells and normal cells appear to be sufficient to generate stable and powerful redox-responsive delivery systems.

3.2.4 Enzyme-responsive DDS

The expression of specific enzymes (protease, phospholipase, or glycosidase) is observed under pathological conditions (tumors or inflammation)[58] and can be used to generate DDS to transport the drug to a desired location[151]. Most of these systems exploit the presence of enzymes in the extracellular matrix as the trigger for drug release, and this has the advantage of exhibiting selectivity to their substrates. For

instance, nanocarriers that incorporate these substrate moieties can significantly improve drug accumulation at the tumor site, reducing nonspecific uptake by other tissues and allowing a specific and controlled release[26]. Drug release can be triggered through integration of specific enzymatic cleavable moieties in the main or side chains of materials, making them enzyme responsive (Figure 3-8). A wide number of polymers have been designed to generate different enzyme-responsive DDS[152][153]. Encapsulation of the drug is achieved through different methods, including the following:

- Covalent attachment of the drug through an enzymatic cleavable peptide sequence (Figure 3-8, B).
- Physical encapsulation involving cross-linking by an enzymatic cleavable peptide sequence (Figure 3-8, C).
- Encapsulation into a nanocarrier based on a block copolymer linked through an enzymatic cleavable peptide sequence (Figure 3-8, A).

In all these cases, release is driven by the cleavage of the peptide. Drug carriers can also be activated by a specific enzyme capable of exposing targeting ligands that are needed for internalization into the cells (Figure 3-8, D).

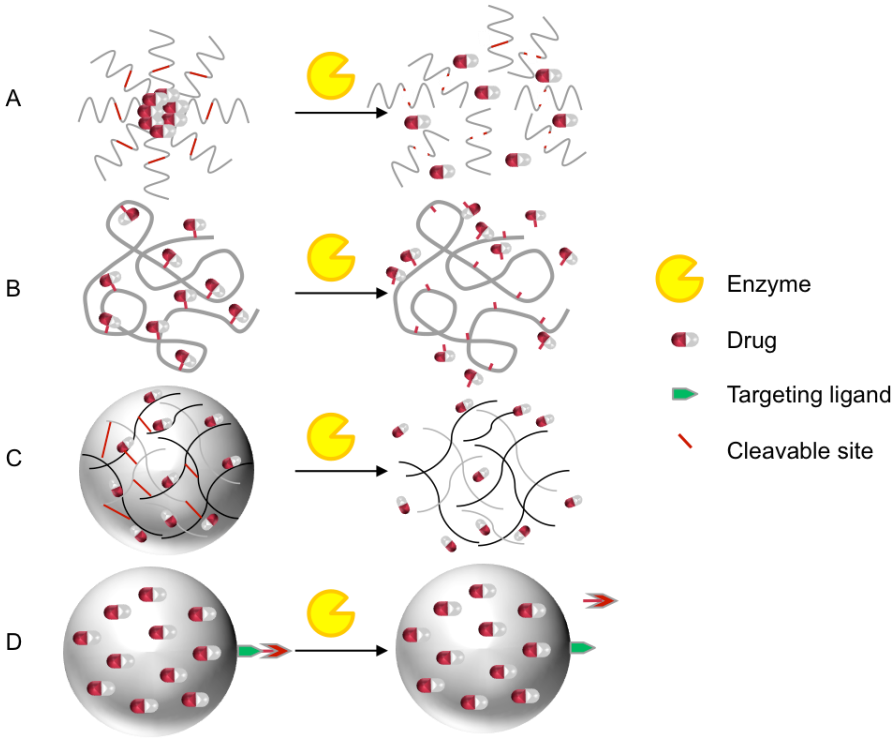

Figure 3-8 Schematic of enzyme-responsive nanomaterials for controlled drug delivery. (A-C) Drugs can be directly released from different carriers upon specific cleavage by enzymes. (D) Drug carriers can be activated by enzymes to expose targeting ligands for a subsequent cellular delivery.

Hahn et al. described self-assembled systems that incorporate enzyme-responsive linkers that are recognizable by a biocatalyst to execute drug release with spatial and temporal control[154]. Ge et al. generated an enzyme-responsive polymeric micelle, by integration of a matrix metalloprotease (MMP)-responsive peptide linker into the block copolymer chains[155]. The MMP-responsive block copolymer, PEG-*GPLGVRGD*G-P(BLA-co-Asp), was synthesized through copper click chemistry, which was followed by ring-opening polymerization (ROP) of N-carboxyanhydride and a partial hydrolysis of poly(β-benzyl L-aspartate). The micelles generated from the copolymer were able to encapsulate DOX with a high loading capacity. Controlled drug release inside the tumor cells was successfully achieved through the cleavage of the GPLGVRGDG peptide linker. The lysosomal cysteine protease called cathepsin B is overexpressed in tumor cells and was used in the system of Kern et al.[156] to trigger release from NPs. They developed enzyme-cleavable micelles based on a diblock copolymer with the aim of delivering a proapoptotic peptide into the intracellular compartment. The first block was composed of a macro-chain transfer agent and a pH responsive endosomolytic copolymer made of N,N-diethylaminoethyl methacrylate and butyl methacrylate. The second polymer block was made of the cleavable peptide BIM capped with a four amino acid cathepsin B substrate (FKFL) and polyethylene glycol methacrylate. BIM is a peptide that was recently described as antitumor substance. The copolymer was able to self-assemble into polymeric NPs. The change of pH in the tumor environment led to the destabilization of the polymeric micelle and subsequent cleavage of the FKFL peptide sequence, resulting in the release of the BIM proapoptotic peptide.

Enzyme-responsive systems can be used to detect various diseases. Schiffer et al. created an enzyme-responsive polymer for microbial infection detection. The use of proteins, polysaccharides, and mixed polymers in a system provides a sensitive tool for identifying a low concentration of protease and glycosyl hydrolases produced in response to an infection[157].

In conclusion, enzyme-responsive systems exhibit therapeutic and detection potential for cancer and other diseases that involve enzymes. The systems described here are mainly based on polymers, which are modified into an enzyme-responsive system. Moreover, they appear to be very promising for overcoming the limitations and drawbacks of conventional infection and tumor responsive systems through their abilities with respect to specificity and early-stage detection[157][158].

3.2.5 Physically responsive DDS

In addition to chemical stimuli-responsive DDS, physically responsive systems sensitive to light, temperature and magnetic field have been intensively used for medical applications. In the case of magnetic field-sensitive systems, two mechanism for treatment have been reported. One mechanism involves magnetic field-induced hyperthermia[159], to release substances, and the other one involves magnetic field to guide the encapsulation system at a specific location and then have a targeted drug delivery[160]. The main advantage of such a system is the ability to target a specific location in the body, where the drug is accumulating without causing collateral damages to the surrounding tissues. Moreover, such systems do not require any specific cell-receptor recognition[161]. Magnetic-responsive systems are based on materials such as magnetite, maghemite, iron, nickel, cobalt, and samarium-cobalt, and respond to the application of a magnetic field to drive and trigger drug releases.

Alexiou et. al describe magnetic nanoparticles labelled with a chemotherapeutic agent. The particles can be injected intraarterially into the tumor-supplying artery and were driven to the tumor region thanks to an external magnetic field. Hence the chemotherapeutic agent was guided and released towards the specific tumor area[162]. Indeed, magnetic fields can then heat magnetic responsive particles, inducing hyperthermia and thus, trigger the drug release by using thermoresponsive materials[163]. Nguyen et. al, have synthesized paramagnetic iron oxide (core) and alginate (shell) based NP, for the encapsulation of doxorubicin. In a magnetic field, the Fe_3O_4 core was able to generate enough heat for doxorubicin release from the alginate shell for chemotherapy[164].

Moreover, electric fields can also be used in drug delivery systems to trigger and regulate drug release. DDS responsive to electrical fields can be composed of positively and negatively charged polyelectrolyte polymers. Those ionizable groups promote responsiveness to an electric field stimulus. A weak electric field can be applied to achieve pulsed and sustained drug release. For instance, NPs based on conductive polymers (polypyrrole) showed triggered drug release as a result of electrochemical reduction-oxidation under the influence of an electric field[165]. The major challenge of such systems is the low tissue penetration of the stimulus and the possibility of undesired tissue damages[103].

Additionally, light-triggered and ultrasound-triggered DDS also may represent effective and minimally invasive methods. Ultrasound waves can trigger drug release, for

instance, through hyperthermia or cavitation phenomena. Hyperthermia generally promotes the fusion of the nanocarrier and the heating of the surrounding tissue, enhancing drug permeation[166]. Moreover, in the field of cancer treatment, the hyperthermia produced through ultrasound improves the efficacy of chemotherapy and radiotherapy. The cavitation process can be described as the formation of microscopic gas bubbles in a medium exposed to ultrasound. The bubble formation leads to a compression that generates an increase in pressure and temperature at the site of action, leading to the release of the drug[167]. Finally, light-responsive systems are of considerable interest because of their possible spatiotemporal characteristics and specific drug release activities after radiation at a specific wavelength. The drug release is based on a one-time or repeatable on-off event triggered by photosensitiveness, which induces structural modification of nanocarriers[168].

3.3 Solution approach

Enzyme-responsive systems have shown to be promising DDS thanks to the overexpression profile of specific enzymes observed in pathological conditions such as inflammation. The research described in this dissertation, explored two enzyme-responsive systems designed as smart DDS, for an implant coating, to prevent implant-associated infections. In both cases, the aim was to encapsulate an antibiotic into a nanocarrier and trigger its release upon inflammation or infection of the environment surrounding the implant.

Chapter 4 describes the synthesis of an enzyme-sensitive chitosan-g-[poly-L-lysine-b-ε-caprolactone] copolymer that is able to self-assemble into polymersomes and to encapsulate hydrophilic and hydrophobic substances in different compartments of the system (Chapter 3.1.6). Its particularity is the presence of an enzyme-cleavable peptide linker between the main hydrophilic chitosan chain and the hydrophobic poly-ε-caprolactone side chain. The peptide was incorporated to intend the degradation of the system by enzymes and subsequently induce the drug release.

Chapter 5 outlines the second system, based on previous studies on alginate, cross-linked via an enzyme-cleavable peptide sequence, which is covalently linked to an antibiotic. The resulting system has the advantages of being enzyme degradable, of avoiding unspecific release and of preventing unwanted drug diffusion across the system.

Both systems were analyzed using dynamic light scattering and scanning electron microscopy (SEM) in order to determine the size distribution and morphology of the

particles. Moreover, the degradation of particles in solution was observed and measured by incubating them with various relevant enzymes and by monitoring the size distribution during the degradation process. Furthermore, the transfer from particles in solution into a coating of titanium materials was investigated. Indeed, titanium is known as a relevant material for implant. Morevoer, ellipsometry was used to determine the thickness of the coating and to study its degradation.

Finally, with respect to the system described in Chapter 5, an antibiotic was modified in order to link it to the polymeric system. Partners at Hannover Medical School cooperated to test the antibacterial efficacy of the different drugs and to assess the consequence of their modifications.

4 Biopolymer-based polymersomes: chitosan-g-[poly-L-lysine$_{20}$-ε-caprolactone]

Polymersomes are of great interest because of there low permeability and high loading capacity which allow them to have an efficient drug encapsulation. Moreover, as described previously, their core-shell structures have the interesting ability to encapsulate hydrophobic and hydrophilic substances. They have been used for the development of controlled release to encapsulate therapeutics ranging from small molecule anti-cancer drugs to siRNA and therapeutic proteins [169]. More information concerning polymersome formation, applications and advantages can be found in Chapter 3.1.6. Based on these advantages and for the development of an enzyme-responsive system, a copolymer has been designed to self-assemble into polymersome. To achieve that end, three components were required to generate the copolymer: chitosan, poly-ε-caprolactone and a peptide. Chitosan is a well etablished and known biopolymer for many different drug delivery systems. It is hydrophilic and biocompatible, which is required for a drug delivery system. Poly-ε-caprolactone is a hydrophobic and biocompatible polymer, which can be easily functionalized by ring opening polymerization. An enzyme cleavable peptide sequence has been used to integrate enzyme responsivness to the system. For instance, Tolle et al. have incorporated a peptide sequence into an alginate/poly-L-lysine DDS to make the system enzyme and inflammation responsive[24]. Based on the same strategy, the peptide sequence was used and integrated into the polymeric system. Indeed, chitosan and poly-ε-caprolactone have been linked through the peptide sequence, to create an amphiphilic graft copolymer. Hydrophobic poly-ε-caprolactone was grafted onto chitosan with a specific amount to generate the core-shell structures. The intergration of a peptide sequence as a linker has been investigated, to study the degradation of the graft copolymer based polymersome through enzymatic cleavage of the peptide. Specific peptidases that are released as a result of an inflammation could be exploited to trigger drug releases by cleavage of a specific sequence. All materials used are described below.

4.1 Chitosan

After cellulose, chitosan is the second most abundant semisynthetic biopolymer. This amino polysaccharide naturally occurs as a partially deacetylated form of chitin. Chitin, which is extracted from sea animals, insects, and microorganisms, is deacetylated

through an alkaline or enzymatic reaction, resulting in chitosan with varying degrees of acetylation[170]. As depicted in Figure 4-1, chitosan is a linear copolymer composed of 2-amino-2-deoxy-glucose (D-glucosamine) and β-D-(acetylamino)-2-deoxy-glucopyranose (N-acetylglucosamin) units.

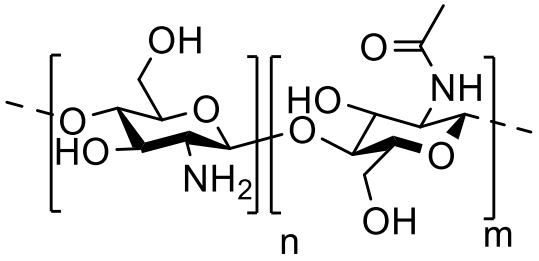

Figure 4-1 Structural formula of chitosan with n) D-glucosamine and m) N-acetylglucosamine units.

The solubility and properties of chitosan are usually strongly influenced by the degree of N-acetylation (DA), which is determined by the ratio of N-acetylglucosamin and glucoamine moiety[171]. The DA process frees amino groups that can be protonated in acidic conditions, thereby increasing chitosan's solubility, which is contrary to the situation regarding chitin, which has a high DA (over 50%) and is poorly water soluble. In addition to amino groups, two hydroxyl groups also contribute to chitosan's hydrophilicity and can be used to functionalize the chitosan. For instance, De Cassan et al. used them to initiate polymerization of PCL, thereby generating a chitosan-grafted PCL copolymer[172].

Furthermore, amine groups offer huge opportunities for additional functionalization, such as amidation, which has been accomplished to introduce thiols[173], dyes[174][175], fatty acids[176], or other polymers[177]. Therefore, chitosan is one of the most used biopolymers for various applications, such as DDS, seed and fertilizer coatings in the agriculture field, immobilizing enzymes for biotechnology applications, promoting tissue growth, and various uses in the cosmetics and food industries[178].

Polycationic chitosan often served as a carrier in polymeric NPs for DDS[179]. It can form NPs upon ionic gelation with polyanions such as sodium triphosphate[24] or through hydrophilic-hydrophobic interaction in aqueous solution[180].

Moreover, because of its good biocompatibility and biodegradability, chitosan is used in many biomedical applications and offers various opportunities for in vivo application. Chitosan biocompatibility is due to its structural similarities to hyaluronic acid and glycosaminoglycan extracellular matrix molecules[181]. Ikada et al. and Thanou et al.[182][183] described the biodegradability of chitosan in the human body. In the case of

the systemic absorption of a hydrophilic polymer, such as chitosan, molecular weight (Mw) plays a crucial role. If chitosan does not have a suitable Mw, it undergoes degradation, resulting in small fragments suitable for renal clearance. Various possibilities exist for degrading chitosan: chemical degradation through acid-catalyzed degradation in the stomach, oxidation-reduction depolymerization, or free radical degradation[182][184]. Furthermore, chitosan can be degraded by enzymes such as lysozyme, which occurs in body fluids (blood, saliva, tears, or wound secretions) and hydrolyzes the glucosamine-N-acetyl-glucosamine/N-acetyl-glucosamine-N-acetyl-glucosamine linkage. Ikada et al. demonstrated the possibility of controlling degradation by using different deacetylated chitosans[184].

Thanks to its good biocompatibility, availibility and functionalization possibilites, chitosan was chosen to generate the encapsulation system. Indeed, through amide coupling, chitosan has been modified by amide coupling with maleimide functions, used to link the peptide sequence. The strategy will be further described in the course of this dissertation. The amide coupling can be illustrated by the following mechanism:

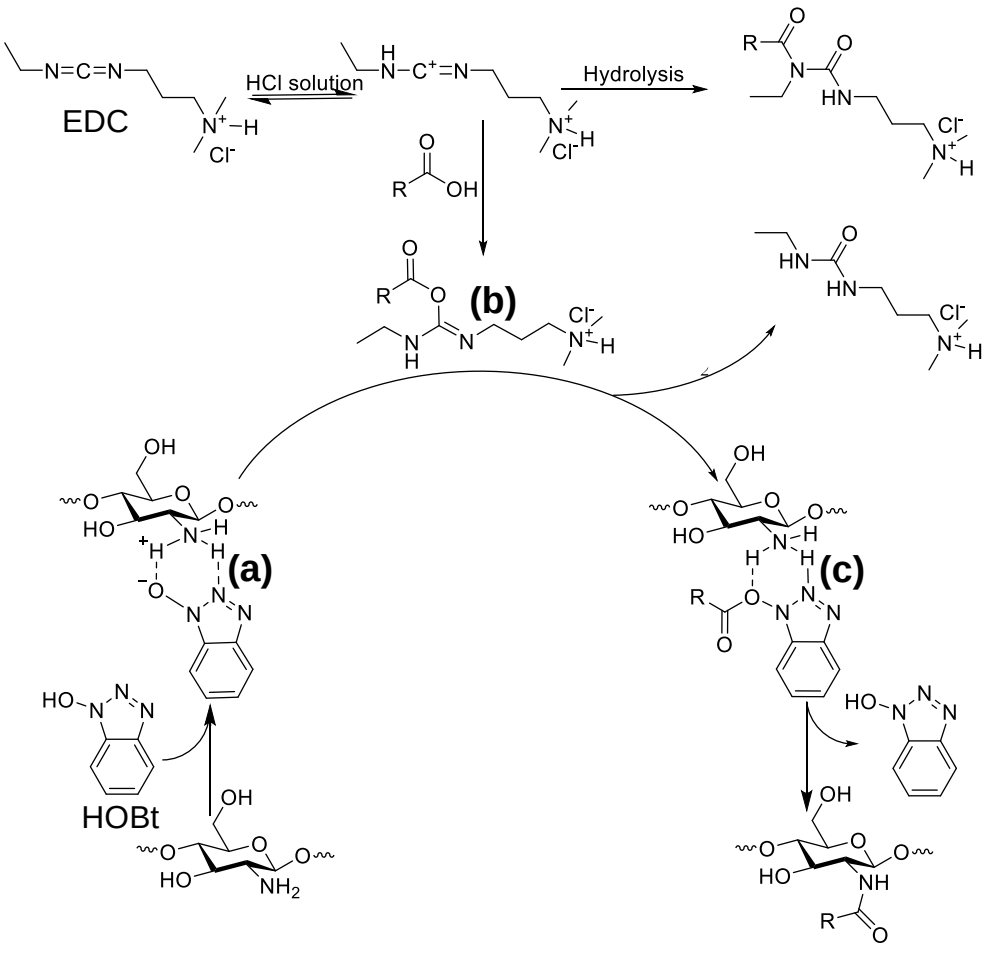

Figure 4-2 Reaction mechanism proposed by Chirachanchai et al.[185].

To begin the catalytic cycle, Hydroxybenzotriazol (HOBt) and chitosan were stirred overnight to form a water-soluble complex (**a**)[186] between HOBt and amines of chitosan. Next, Dimethylaminopropyl)carbodiimide (EDC) was added and protonated by HCl to form a reactive carbocation intermediate, which was described by Cox et al.[187][188] as $EDClH_2^{2+}$. Following this step, two possible reactions were considered: the hydrolysis of the compound and the reaction with 3-maleimidopropionic acid to form O-acylisourea (**b**). Subsequently, the active O-acylisourea (**b**) reacts with the complex (**a**), generating the HOBt-active ester (**c**) and urea as a byproduct. Finally, the rearrangement of the complex (**c**) leads to the final modified chitosan (Figure 4-2). All byproducts as well as the non-reacted carboxylic acid were removed during the dialysis step.

4.2 Poly-ε-caprolactone

During the years 1970s and 1980s, poly-ε-caprolactone (PCL) has received attention because of its high potential for applications within the biomaterials field and for drug-delivery devices. Its popularity has declined due to the arrival of faster resorbable polymers. Consequently, PCL has been percieved as the forgotten polymer. However, recently, FDA approval as well as inexpensive production routes have propelled PCL back into the biomaterials-arena such as medical devices, drug delivery and tissue engineering[189]. For instance, it can be used in in-vivo or in-vitro porous scaffolds to support cell attachment for tissue formation. These scaffolds provide a suitable porous structure in which to encapsulate growth factors to create a cell-friendly environment with physical and biochemical stimuli to promote optimal cell growth[190][191]. As mentioned previously, PCL is also used to build vehicles for drug encapsulation through different methods, such as emulsion evaporation[192], solvent extraction[193], spray drying[194], and melt encapsulation[195]. To generate NPs, PCL is combined with hydrophilic polymers to form various amphiphilic copolymers. For instance, Jelvehgari et al. developed micelles based on poly-ε-caprolactone-co-polyethylene glycol-co-poly-ε-caprolactone to enhance the ocular bioavailability of poorly water-soluble drugs. The resulting micelles are interesting for decreasing the dose frequency by having a sustained release and fulfilling the patient compliance for ocular delivery[196]. Two routes can be considered for the synthesis of PCL: the condensation of hydroxycarboxylic acids[197] and the ring opening polymerization (ROP)[198]. A few studies have described the polycondensation of 6-hydroxy-hexanoic by removing water molecules formed during the reaction, which consequently shifts the equilibrium

towards polymer formation. The reaction is usually performed without catalyst at temperatures between 80°C and 150°C.

ROP of ε-caprolactone can be performed through four different methods:

- anionic ROP, involving the formation of an anionic molecule capable of attacking the carbonyl carbon of the monomer;
- cationic ROP, involving a cationic species, which can be attacked by the carbonyl oxygen the monomer;
- monomer-activated ROP, involving the activation of the monomer molecules by a catalyst; and
- coordination-insertion ROP[199].

The last method (coordination-insertion ROP), is the most common approach for synthesizing functionalized PCL and has been used in this study. It proceeds through the coordination of ε-caprolactone to a metal-based catalyst. The ROP mechanism has been reported by Albertsson et al. for 1,5-dioxepan-2-one and l-lactide as monomers and Sn(Oct)2 as catalyst[200]. The ROP of ε-caprolactone can be described by the same mechanism and is presented in Figure 4-3. The first step involves the coordination of alcohol, the initiator and Sn(Oct)2, which forms the structure (**a**) (Figure 4-3). During this step, two six-membered rings are generated through hydrogen bonds that include octanoate and the alcohol. Then, ε-caprolactone coordinates with the Sn^{2+} in this complex and forms a five-coordinated complex (**b**) (Figure 4-3). Subsequently, the alcohol O and the carbonyl C of the ε-caprolactone react and a ring structure with four members (**c**) is formed (Figure 4-3). Following this step, the bond between the carbon of the carbonyl function and the oxygen of the alcohol increases, and the Sn-O(alcohol) and the double (C=O) bond decrease to form structure (**d**) (Figure 4-3). In the final step, the ring opening occurs, which forms structure (e) (Figure 4-3), and the π system of C=O is restored to generate a new alcohol. The catalytic cycle can then restart.

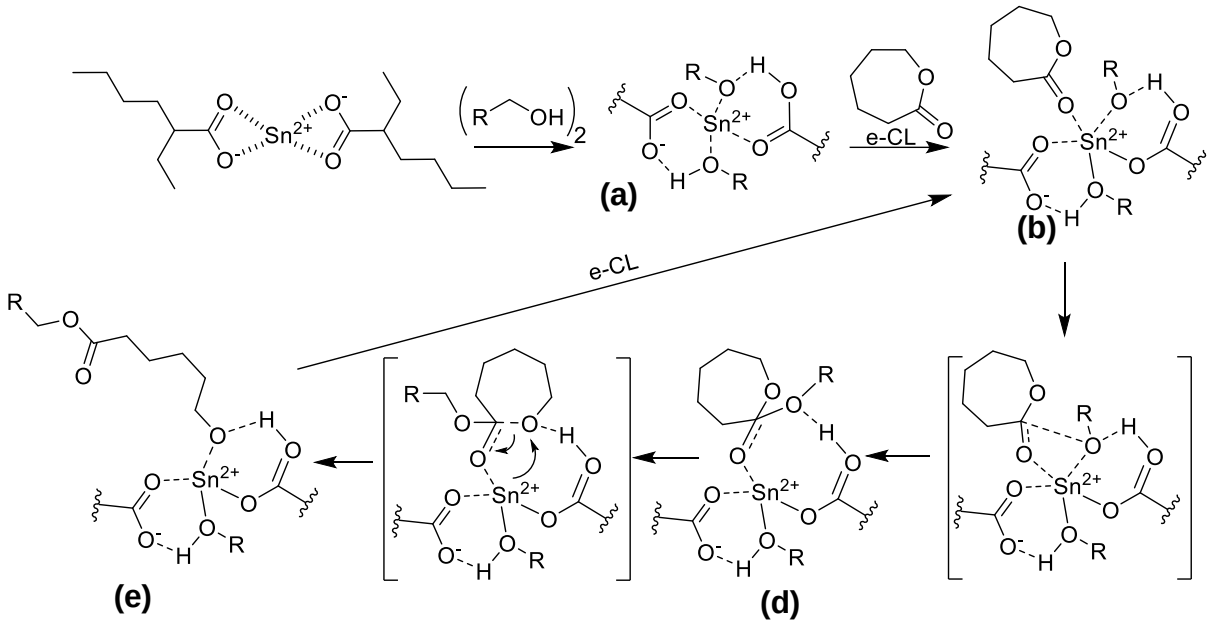

Figure 4-3 Reeaction mechanism of ROP of ε-caprolactone based on the mechanism described by Albertsson et al. for 1,5-dioxepan-2-one and l-lactide as monomer.

Moreover, via coordination-insertion ROP the PCL can easily be end-functionalized by using functionalized alcohols as initiators. In Figure 4-3, R- can be different functional groups. For instance, Bach et al. synthesized a clickable alkyne end-functional PCL by using stannous octanoate as the catalyst and propargyl alcohol as initiator[201]. To conclude, PCL can be easily synthesized, functionalized and has been proved to be biocompatible. Therefore, it is employed in many biomedical applications[202][203] and for this study, it serves as the hydrophobic component of the copolymer. To ensure the binding to chitosan, PCL has been modified with an alkyne function through the same mechanism described above.

4.3 Peptides

Peptides and proteins are fundamental components of cells that perform crucial biological functions. Peptides can be defined as short chains of amino acid monomers linked by peptide bonds. The main difference between proteins and peptide is their size and structure. Peptides are defined as molecules that contain between 2 and 50 amino acids, whereas proteins are made up of over 50 amino acids. Furthermore, peptides tend to have less defined and complex structures than proteins, which are able to adopt conformations known as secondary, tertiary, and quaternary structures. Depending on their size, peptides can be subdivided into oligopeptides and polypeptides. Proteins are formed from polypeptides[204] that interact through disulfide bonds, hydrogen bonds, ionic bonds, and hydrophobic or pi-stacking interactions[205].

Peptide sequences are increasingly perceived to be a powerful tool in biomedical applications such as the replacement of antibiotics or diagnosing and preventing diseases. Many antimicrobial peptides have been described[206][207], and many of them have demonstrated efficacious activity against microorganisms resistant to conventional antibiotics; they have been shown to be able to kill bacteria at concentrations ranging from 0.25 to 4 µg/mL^{-1}[208]. Stayton et al. generated enzyme-cleavable polymeric micelles for the intracellular delivery of proapoptotic peptides. A peptide was directly integrated into a diblock copolymer capable of assembling into polymeric micelles[156]. The peptide was composed of a sequence called BIM and a four amino acid sequence cleavable by the enzyme cathepsin B. This four amino peptide sequence was capable of releasing the BIM sequence into the cell to accomplish intracellular drug release[156]. BIM peptide was recently described as antitumor substance. Tolle et al. incorporated an aggrecanase-labile sequence ARGSV↓NITEGE into an alginate/poly-L-lysine DDS. In this case, the peptide integrated an aggrecanase-labile sequence, a spacer (RGD), and positively charged l-lysine units to generate NPs with negatively charged alginate. Exposure to inflammation-related protease led to the degradation of particles and the subsequent release of encapsulated drugs[24]. Therefore, the final goal is to integrate the aggrecanase-labile sequence ARGSV↓NITEGE into an encapsulation system in order to make it enzyme and consequently inflammation responsive.

4.4 Poly-L-lysine

In a preliminary study, poly-L-lysine (PLL) (Figure 4-4), as readily available and cleavable peptide, was introduced to investigate the feasibility to generate a system which can be degraded by the cleavage of the peptide.

PLL can be cleaved by various enzymes such as trypsin, chymotrypsin, or proteinase K[209][210] and can be synthesized through various methods. The first method employs ring opening polymerization of the corresponding N-carboxyanhydride (NCA)[211]. Second, peptide sequences can be synthesized on a preactivated resin. Here, the first step consists of coupling a protected Fmoc amino acid to the resin[212]. Subsequently, a base is used to deprotect the Fmoc-protected group, to enable the coupling of another amino acid. The coupling reagent HCTU (2-(6-Chlor-1H-benzotriazol-1-yl) together with Diisopropylethylamin are often used to activate this amide coupling[213]. Finally, the peptide and protecting groups are removed with a TFA-containing cocktail[214].

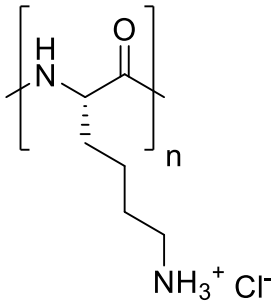

Figure 4-4 Structural formula of poly-L-lysine.

Poly-L-lysine (PLL) was used and integrated as a linker to investigate the feasibility of the system. Both C-terminus and the N-terminus side of the poly-L-lysine were functionalized with an azide and thiol function. The thiol function enables the conjugation to chitosan through thiol-ene reaction with maleimide. Generally, the reaction between thiol and a double bond can be initiated with different catalysts, such as organometallics, bases, Lewis acids, metals, and nucleophiles[215]. Light[216], heat[217], or radical initiators[217] are also used to initiate the reaction by generating a thiol radical capable to undergo the reaction[218].

A uniqueness of the maleimide function is the presence of carbonyl groups in cis-conformation coupled with ring-strain/bond-angle distortion, which increases the reactivity of the double bond towards the thiol function with the help of the solvent. In fact, it is common for such reactions to be performed in the presence of, e.g. DMF as solvents and catalyst[219]. Solvents such as DMSO and DMF possess a high dielectric constant, which promotes the spontaneous dissociation of thiol into nucleophilic thiolate anion. Subsequently, the thiolate is able to react with the double bond of the maleimide function[220]. Choudhary et al.[221] reported the mechanism of thiol-ene-Michael addition between a maleimide derivative and a thiol**.** The reaction starts with the formation of a nucleophilic thiolate anion **(a),** formed by the DMF (Figure 4-5). Two other methods exist to generate thiolate ions: one method entails the addition of a base and the other entails the addition of nucleophiles[222]. In the next step, a thiolate anion undergoes an attack by the π-bond of mal function, resulting in a basic enolate intermediate **(b)** (Figure 4-5). The compound **(b)** deprotonates a thiol into thiolate to form the product. Finally, the cycle restarts with the newly formed thiolate.

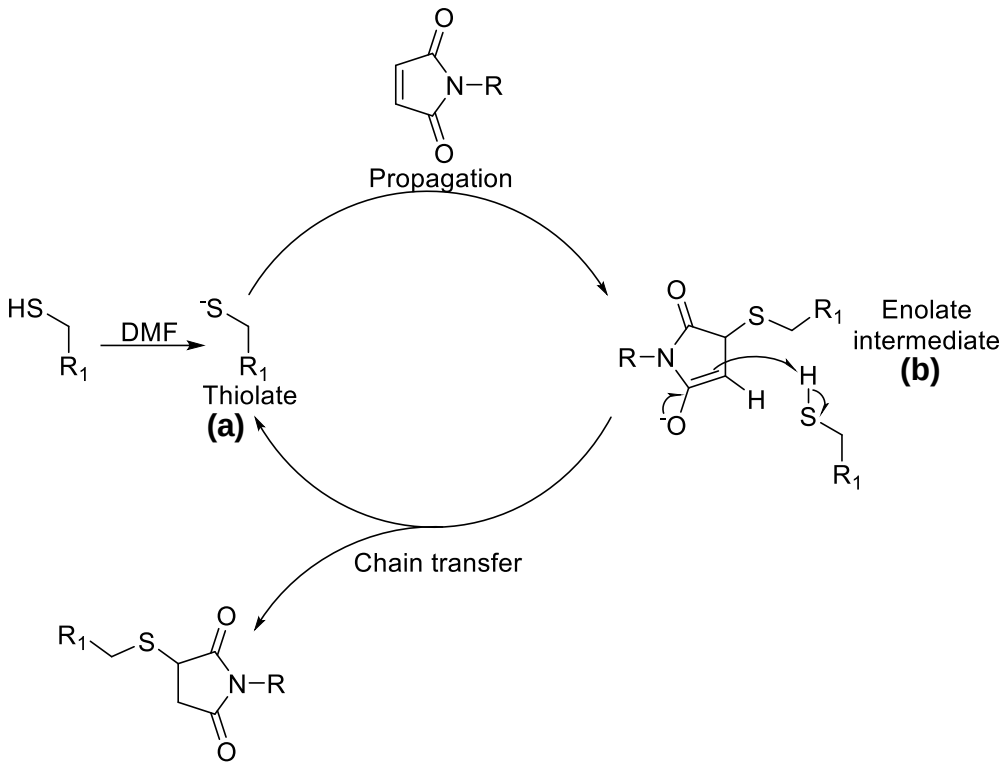

Figure 4-5 Reaction mechanism of thiol-ene-Michael addition.

The azide function of the PLL enables the ligation to poly-ε-caprolactone through a copper-catalyzed Azide-alkyne Huisgen cycloaddition with the alkyne function and can be described by the following mechanism. Hein et al.[223] reported the mechanism of copper-catalyzed azide-alkyne cycloaddition. The first step entailed the π-coordination of an alkyne to copper. This subsequently acidified the terminal hydrogen of the alkyne (**Step 1**, **A**, Figure 4-6). Afterwards, the proton was deprotonated to form the σ-acetylide intermediate (**Step 2**, **B**). In **step 3**, the azide function was coordinated to copper to generate complex **C** (Figure 4-6). During this step, the σ-acetylide became more nucleophilic and the azide function more electrophilic. This synergic effect led to a C-N bond to form the copper metallacycle **D** (Figure 4-6, **Step 4**). Then, **D** underwent a rearrangement by releasing a copper to generate the triazole complex **E** (Figure 4-6, **Step 5**). Finally, the protonation of **E** intermediate produced the final triazole (Figure 4-6, **Step 6**).

Despite many studies on the topic, the mechanism of copper(I)-catalyzed alkyne-azide cycloaddition is still highly controversial.

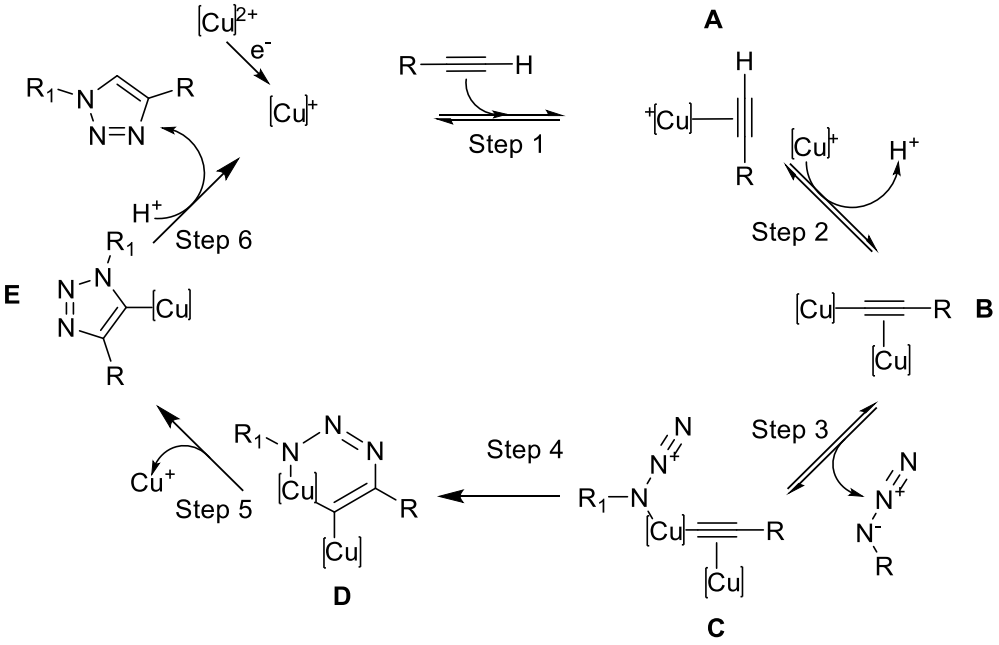

Figure 4-6 Reaction mechanism of 1,3-Huisgen dipolar cycloaddition catalyzed by copper.

Among the several advantages of Azide-alkyne Huisgen cycloaddition, two important features make this reaction particularly attractive for the drug conjugation. Firstly, this cycloaddition proceeds well in aqueous medium and, therefore, may efficiently performed under mild conditions. Moreover, it is an extremely chemoselective reaction and thus, can be used for modifying highly functional biomolecules such as polypeptides, nucleic acids or polysaccharides[224][225][226].

5 Alginate/peptide NPs system

Ionic gelation is a very advantageous method for the preparation of nanogel particles due to the mild conditions. It is considered as a simple and efficient way to obtain nanoparticles, which allow encapsulation of sensitive therapeutic proteins[227]. Moreover, tunability through functionalization of the surface enables a wide range of application in the field of drug delivery system. Biopolymers are preferred for forming such systems and possess advantageous properties, including biocompatibility, biodegradability, low immunogenicity and can be easily modified thanks to their functionalities. Among them, polyions such as chitosan, hyaluronic acid, heparan sulfate or alginate are widely used to generate bio-based NPs. Alginate is considered as a good candidate for drug delivery systems: it is readily available and relatively inexpensive in comparison to other biopolymers. The use of alginate as a matrix for the encapsulation and delivery of biomolecules like proteins, DNA, or cells has been intensively studied[228][229][230]. Moreover, this polyanion has the capacity to generate particles via ionic gelation with cations such as chitosan, calcium and positively charged peptide. Tolle et al. described nanoparticles prepared via an ionic gelation of negatively charged alginate and a positively charged enzyme cleavable peptide[24]. The cleavage was triggered by a specific enzyme released during an inflammation and induced the drug release. However, the retention of the model protein interferon β was limited and a strong burst release was observed[24].

Based on the advantage of alginate and enzyme cleavable peptides, an enzyme-responsive system made of alginate and a peptide-conjugated drug has been designed, in this study. The system was able to self-assemble into nanoparticle as a potential drug delivery system (Figure 5-1).

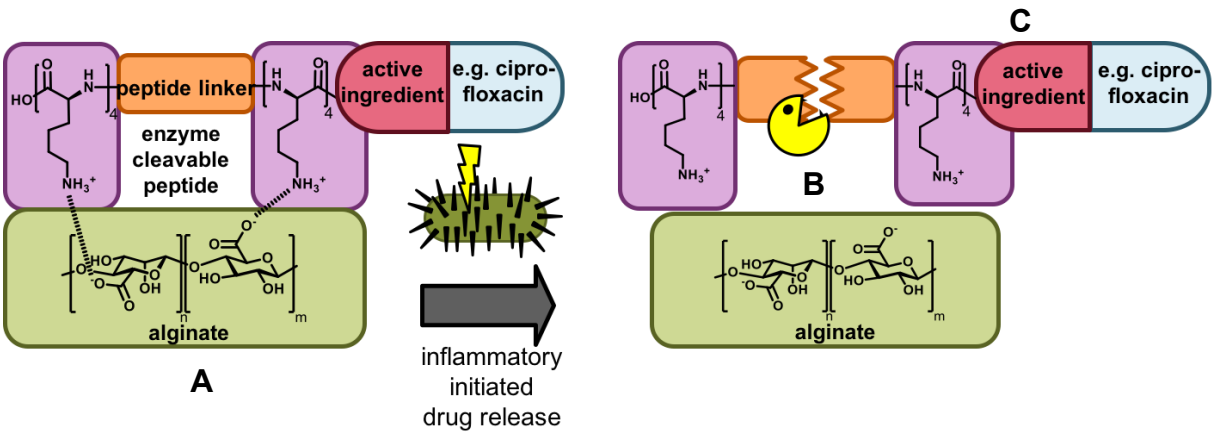

Figure 5-1 Schematic representation of alginate/peptide NPs with A) ionic gelation process, B) enzyme-triggered release, and C) the residue released from the particle.

Based on these promising results and in an effort to address the main drawback of unspecific burst release, this study presents a new enzyme-responsive alginate/peptide nanogel, in which the model drug ciprofloxacin is conjugated to the peptide linker. Hence, ciprofloxacin was modified and conjugated with an enzyme-cleavable peptide sequence. Since this was an early-stage study, poly-L-lysine (PLL) was used as a peptide sequence to identify the ability of conjugated peptide to generate nanoparticles with alginate (Figure 5-1, **A**). The integration of a peptide sequence as a linker has been investigated to study the degradation of the particles through enzymatic cleavage of the peptide (Figure 5-1, **B**) and the release of active ingredient (Figure 5-1, **C**). All materials used are described below.

5.1 Alginate

Alginate is a naturally occurring anionic polymer that can typically be extracted from brown seaweed including *Laminaria hyperborea*, *L. digitate*, *L. japonica*, *Ascophyllum nodosum*, and *Macrocystis pyriferaolav*[231].

It is known to have low toxicity, good biocompatibility and low cost[228]; therefore, alginate has been successfully demonstrated in many biomedical applications. Alginate is a linear copolymer of (1-4)-linked β-D-mannuronate and its C-5 epimer α-L-guluronate residues are randomly distributed along the chain (Figure 5-2).

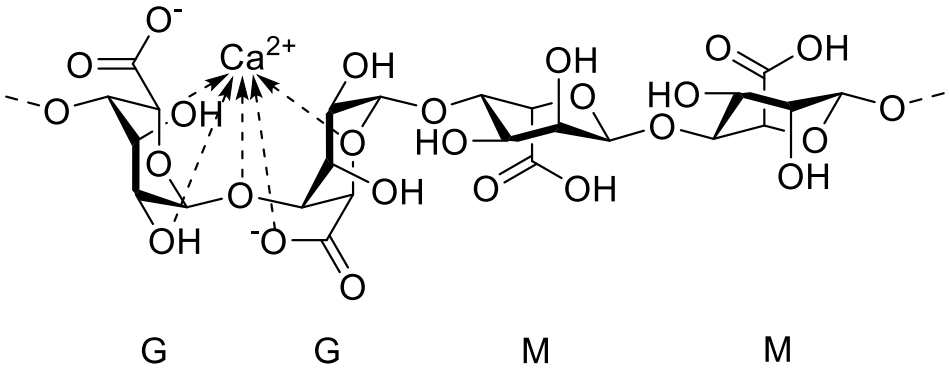

Figure 5-2 Structural formula of alginate and probable binding mode between calcium ions.

Furthermore, water-soluble sodium alginates have the capacity, through carboxylic acid, to produce hydrogels with multivalent cations, such as calcium and peptides such as PLL[232][233][234]. The ions exhibit different affinities with alginate, depending on the alginate's guluronic acid (G) block content. A high amount of G generates hydrogels with higher mechanical strength than alginate rich in mannuranate (M) moiety. One of the reason for it is that G residues exhibit stronger interaction with divalent ions (e.g. Ca^{2+}) than M residues and, therefore, appear to support the formation of junction zones (Figure 5-2)[235][236]. The gelation ability and the structural similarity to extracellular matrices of alginate enable a wide range of applications; for instance, wound healing, which is achieved through maintenance of a physiologically moist microenvironment and minimization of bacterial infection. It is also used for the delivery of bioactive molecules like drugs and proteins[237][238]. Biocompatibility has been intensively evaluated in vitro as well as in vivo, and the debate is ongoing regarding the influence of alginate composition on biocompatibility. For instance, Espevik et al.[239] reported that high M content is immunogenic and approximately ten times more efficient in inducing cytokine production than low M content alginate. Yet, other studies have found low or no immunoresponse around alginate implants[240]. Such absence of or minimal response might be due to impurities remaining in raw alginates such as heavy metals, endotoxins, proteins, or polyphenolic compounds that are present in nature. Therefore, in vivo use requires purification of alginate through a multistep extraction procedure. After purification, alginate does not induce any significant reaction in the body when implanted into animals[236]. Furthermore, no significant inflammatory response was observed in a study[241].

Regarding degradability, no enzyme in the human body can degrade alginate. The only option for degrading alginate-based hydrogels is to exchange multivalent ions with

surrounding monovalent sodium ions. Afterwards, dissolved alginate chains are removed by kidney clearance if the molecular weight is under 50 KDa[242]. One drawback, is that, at a higher Mw, renal clearance cannot occur and alginate remains in the body[243]. A possible approach for making alginate biodegradable under physiological conditions is to partially oxidize the alginate chains. Slightly oxidized alginate can be degraded in aqueous media and has been demonstrated to have potential as a drug delivery vehicle in various applications[244].

In conclusion, thanks to low toxicity, good biocompatibility and its ability to generate hydrogels with multivalent cations, alginate has been chosen to generate the encapsulation system. Indeed, alginate was used in combination with a positively charged peptide to self-assemble into nanoparticle. The peptide sequence is described in the following chapters.

5.2 Peptide NVTEGE↓ALGSV aggrecanase-labile sequence[24][245][246]

In addition to PLL, another peptide with the enzyme cleavable sequence NVTEGE↓ALGSV has been studied in order to integrate it in an alginate/peptide-NP system. This sequence can be cleaved by enzyms such as aggrecanase. The protease aggrecanase belongs to the family of ADAM (a disintegrin and metalloprotease) proteins and will be described further below. This enzyme is mainly secreted during the early stages of inflammations, for instance, in osteoarthritis and leads to the degradation of cartilage. Tolle et. al demonstrated the ability of customized aggrecanase-labile sequence, with a spacer and lysine units to generate nanoparticle with alginate[24].

As the aim of this study is to covalently link ciprofloxacin to a nanoparticle system, the peptide of Tolle et. al have been redesigned. The aggrecanase-labile sequence is equipped with tripeptide spacers, lysine units on each side and a functional group. This peptide is designed to generate nanoparticle and link a bioactive substance through the functional group. The complete sequence is described in Figure 5-3.

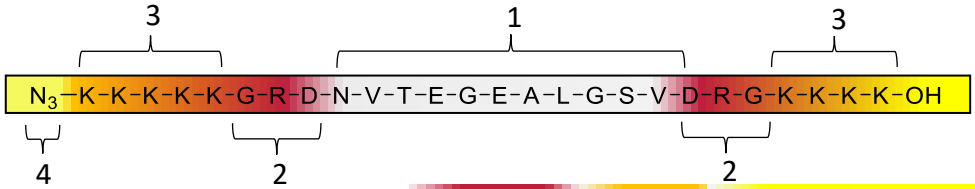

Figure 5-3 Amino acid sequence of the aggrecanase-labile sequence with K – lysine, G – glycine, R – arginine, D – aspartic acid, N – asparagine, V – valine, T – threonine, E – glutamic acid, A – alanine, and S – serine. This sequence represents the mouse aggrecanase-labile sequence.

The right side of the sequence represents the C-terminus, and the left side represents the N-terminus tail. On the N-terminus side, a lysine unit functionalized with an azide group was coupled to four other lysine units. The azide function enables an extremely chemoselective reaction conjugation of bioactive molecules through azide-alkyne Huisgen cycloaddition[224][225][226], whereas the lysine units provide positive charges to generate NPs through ionic gelation, with negatively charged polymers (e.g. alginate). Then, GRD or DRG sequence acts as a spacer between the lysine units and the cleavable sequence (Figure 5-3). Regarding the aim of this study, sequence (1) (Figure 5-3) was chosen because of its property whereby it can be cleaved by an enzyme released during an inflammation (e.g. aggrecanase). This enzyme can cleave the sequence between glutamic acid and alanine amino acids. The linker can also be cleaved by thermolysin or trypsin. The cleavage sites are represented by arrows in Figure 5-4.

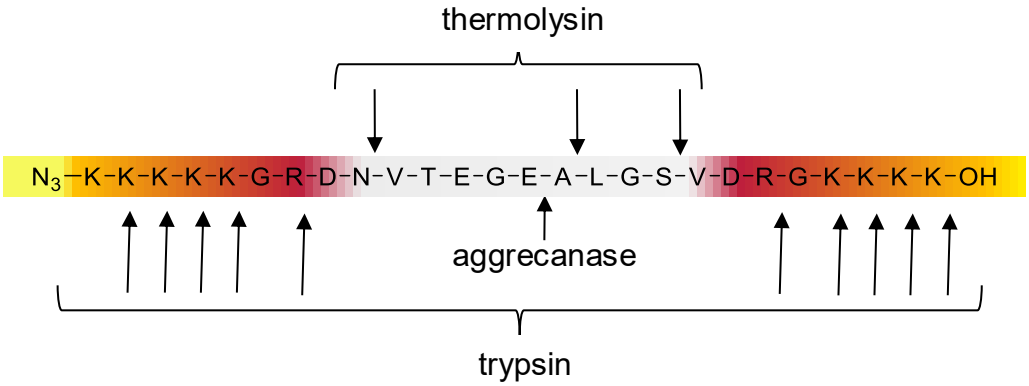

Figure 5-4 Cleavage site of thermolysin, trypsin, and aggrecanase enzymes on the aggrecanase-labile sequence.

Trypsin can potentially hydrolyze bonds on the C-terminus side of a lysine and arginine unit and have therefore ten cleavage sites. Thermolysin is a thermostable metalloproteinase enzyme produced by the gram-positive bacteria *Bacillus thermoproteolyticus*. The cleavage sites can be found at the N-terminus side of hydrophobic amino acids such as isoleucine (I), leucine (L), valine (V), and phenylalanine (F). According to the sequence, there are three possible sites to cleave the peptide (Figure 5-4). Finally, aggrecanase can specifically hydrolyze at one cleavage site. Therefore, it was interesting to integrate this sequence in an encapsulation system to generate a specific and triggered drug release.

5.3 Aggrecanase

The aggrecanases are metalloproteases that belong to the family of extracellular proteases and are also known as ADAMTS. Two different aggrecanases, ADAMTS-4 and ADAMTS-5, appear in higher concentrations in arthritis, which are members of the "A Desintegrin And Metalloproteinase with ThromboSpondin motifs" gene family[245]. Both of them cleave aggrecan at five different sites, and all the resultant fragments have been identified in cartilage explants undergoing matrix degradation. Aggracan is one of the most important components of the extracellular matrix in joint cartilage and is responsible, together with collagen fibrils, for elasticity[247]. The ability to accept highly compressive force is due to the water absorption capacity of aggrecans[248]. Figure 5-5 presents a schematic of the protein that holds three globular domains: G1 and G2 on the N-terminus side and a G3 domain on the C-terminus side. The amino acid sequence between G2 and G3 possesses a high amount of substituted keratan sulfate (subdomain KS) and chondroitin sulfate (Cs), which is organized into two distinct subdomains, Cs-1 and Cs-2. On the N-terminus part, the gap between G1 and G2 is an interglobular domain with 150 amino acids. The G1 domain has high binding specificity with hyaluronan, a glycosaminoglycan present in the extracellular matrix. The binding is reinforced by a link protein[245].

In a disease environment, like osteoarthritis, the rate at which the extracellular matrix degrades is higher than the production rate, resulting in a decrease of cartilage matrix amount. This degradation can be explained by the release of matrix-metalloproteinases responsible for aggrecanolysis. Thus far, two aggrecanase isoforms have been identified: ADAMTS-4 and ADAMTS-5. Along their substrate, multiple sites can be cleaved. The most critical one is located between the G1 and G2 domains and is called the interglobular domain (Figure 5-5).

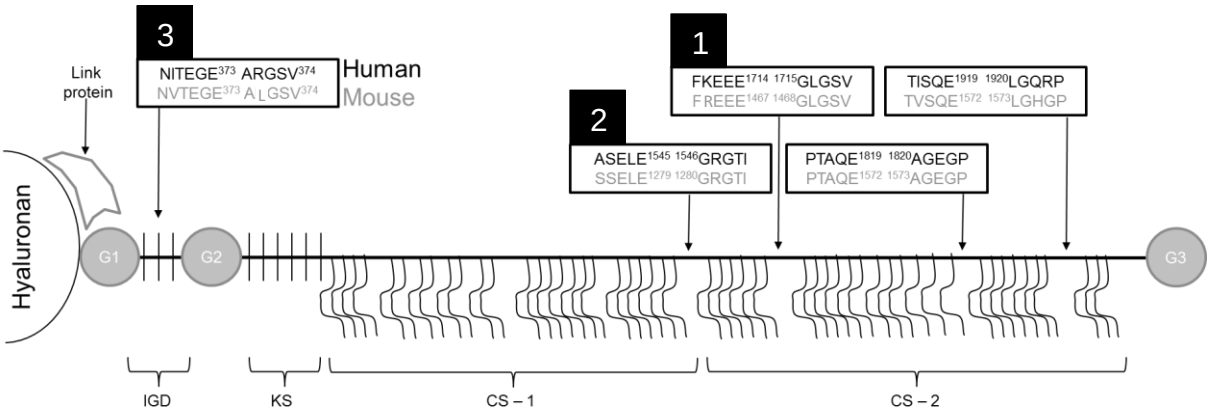

Figure 5-5 Aggrecanase cleavage sites in aggrecan protein.
Schematic showing aggrecan protein with globular G1, G2, and G3 domains. The core protein is substituted with chondroitin sulfate (Cs; wavy lines) and keratan sulfate (KS; straight lines) chains. The aggrecanase cleavage sequences are shown for human (human, black character) and mouse (mouse, grey character). The numbers above the boxed sequences denote the preferred order of enzymatic cleavage (interglobular domain). Scheme has been drawn according to Huang et. al [245].

A consequence of the cleavage is a release of the C-terminus part, which is an important element for the mechanical properties of cartilage[247][245]. The cleavage at Glu^{373}-^{374}Ala has been actively studied and is considered to be a signature of aggrecanase activities. Lohmander et al. demonstrated that GAG-containing aggrecan fragments were present in the synovial liquid of patients affected by rheumatoid arthritis and other types of inflammatory arthritis. In all cases, the presence of Ala-Arg-Gly-Ser sequences could be observed and indicated aggrecanase mediated degradation[249]. Moreover, ADAMTS-4 and ADAMTS-5 also hydrolyze, in the human organism, four other peptide sequences belonging to the subdomains CS-1 and CS-2 between the globular domains G2 and G3 (Figure 5-5). These include the cleavage site Glu^{1545}-^{1546}Gly, Glu^{1714}-^{1715}Gly, Glu^{1819}-^{1820}Ala, and Glu^{1919}-^{1920}Leu. The mouse aggrecanase-labile sequences are slightly different and are described in Figure 5-5[246]. By extending the research of Tolle et al., the aim of the study was to integrate the aggrecanase cleavable sequence -GRDNVTEGE↓ALGSVDRG- in order to generate a drug delivery system responsive only during inflammatory state. For this study, the residue KKKKGRDNVTEGE, which represents the sequence that remains on the drug after peptide cleavage has been linked to an antibiotic to test its influence on the drug efficacy.

5.4 Ciprofloxacin

Ciprofloxacin, depicted in Figure 5-6 is a second-generation fluoroquinolone with good antimicrobial activity, excellent pharmacokinetic properties, and few side effects. It was

introduced a few decades ago for the treatment of various bacterial infections, including those of the lung, skin, bones, and soft tissue[250]. Ciprofloxacin (CIP) was chosen as a model drug with broad spectrum antibacterial activity as it is readily available and deep knowledge of its structure-activity relationships enable structural modification not negatively impacting the antibacterial activity[251].

Regarding its structure, two functionnalities, piperazine and carboxylic acid, provides the opportunity to synthesize ciprofloxacin derivatives. Liu et al. summarized the research progress, made with respect to the discovery of CIP derivatives used as antibacterial agents. Many of them have exhibited considerable in vitro and in vivo potency against both drug-sensitive and drug-resistant organisms. Yet, some of the CIP derivatives have demonstrated reduced efficacy. Indeed, it is known that carboxylic acid and carbonyl are essential for the formation of the bound gyrase complex[252]. If these groups are chemically modified or removed, the antimicrobial activity is strongly reduced[253]. However, modifications at the piperazine ring via alkylation or acylation can result in highly active derivatives[253][251][252][254][255].

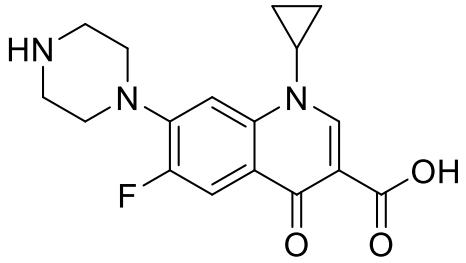

Figure 5-6 Structural formula of Ciprofloxacin.

Since then, numerous CIP derivatives have been developed, with diverse properties and activity against the following: tuberculosis[256][257], bacteria[193], fungi[194], malaria[258], HIV[259], oxidation[260], and tumors[261]. However, the antibacterial effect with a broad spectrum of activity[262] against bacterial infections remains the dominant research field of ciprofloxacin derivatives. CIP is also commonly used for periimplentitis or dental infection treatment[263][264].

To better understand this study, a short overview regarding the mode of action of CIP is necessary. This antibiotic acts by inhibiting the bacterial DNA gyrase and IV topoisomerase, which are necessary for cell division[265]. Bacteria have a circular double-stranded DNA, it contains the unique genetic code for all the proteins required for the bacterial survival[266]. Bacteria replicate through a process known as binary fission and separate into two daughter cells. First, the bacterium generates an identical

copy of its complete circular DNA. DNA replication requires that the two DNA strands separate in order for the genetic code to be read and a complementary strand of each original strand is generated. Various enzymes are involved in this process[267]. DNA helicase breaks the hydrogen bonds between the bases in the DNA strands to separate and stabilize the exposed single strands by preventing them from joining back together[268]. The point where the strands are separated to enable the replication is known as the replication fork. At this location, DNA polymerase is able to move along the DNA strands, synthesizing a new complementary DNA strand. This process generates a superhelical twist in the DNA ahead of the polymerase. The supercoiling must be removed to continue the replication[269]. The bacterial enzyme DNA gyrase is responsible for removing the DNA twist, enabling the DNA replication process to proceed[270]. After completion of replication, two new interlinked double DNA strands are formed. To separate them, the enzyme topoisomerase IV is needed; then, they can be segregated into two new bacterial cells[265]. CIP acts by inhibiting the activity of both DNA gyrase and topoisomerase IV enzymes. For most of the gram-negative bacteria, DNA gyrase is the primary target of CIP[271]. CIP is known to bind specifically to the complex of gyrase and DNA rather than the gyrase alone. CIP appears to stabilize the complex, which in turn results in breaks in the DNA that lead to the death of the bacteria[252]. Furthermore, in most of the gram-positive bacteria, topoisomerase IV is the main target of CIP, which acts by disrupting the separation of the two double DNA strands, leading to bacteria death[252]. The potency of CIP derivatives depends on the affinity for either DNA gyrase or topoisomerase IV[272]. One of the most common mechanisms by which bacteria acquire resistance to CIP is through a spontaneously occurring mutation in the DNA gyrase or topoisomerase gene that modifies the structure of those enzymes. An effective mutation is dependent on the number and location of mutations. A mutation mainly results in a reduction in the affinity for CIP, and this results in resistance[273].

In conclusion, piperazine ring of ciprofloxacin enables modifications through alkylation or acylation for a subsequent conjugation to peptide sequences. Therefore, CIP was chosen as antibacterial agent to develop a drug delivery system for preventing implant-associated infection.

6 Analytical methods

6.1 Dynamic light scattering[274][275][276][277]

Dynamic light scattering (DLS), also known as photon correlation spectroscopy, is the most popular method to determine the size of small particles or macromolecules, in solution. DLS is based on the Brownian motion of dispersed particles. This means that the particles dispersed in a solution are moving randomly in all directions. The principle of Brownian motion is that particles are constantly colliding with solvent molecules. These collisions generate a certain amount of energy to be transferred, inducing the movement of particles. These movements are correlated to their size and shape as well as to the temperature and viscosity of the solution. Therefore, it is crucial to control temperature and viscosity of the solution in order to determine the size by measuring the speed of the particles. The relation between the speed of the particles and their size is described by the Stokes-Einstein equation. Their speed is described by the diffusion coefficient D.

A laser beam can be used to determine the coefficient D and calcule the size of the particles. When entering into direct contact with a particle, the incident laser light gets scattered in all directions. The scattered light intensity is then recorded, over time, at a certain angle and this signal is used to determine the diffusion coefficient and the particle size by the Stokes-Einstein equation. Indeed, the scattered light intensity fluctuates due to the continuous Brownian motion of the particles in solution. This motion gives rise to a Doppler effect and so the scattered light possesses a range of frequencies shifted very slightly from the frequency of the incident light. Due to frequency shifting, the scattered lights will either result in mutually destructive phases and cancel each other out or in mutually constructive phases to produce a specific light-scattering intensity signal. It will constantly fluctuate and the measurement over time will help to determine how rapidly the intensity fluctuates, which can be related to the diffusion behaviour and size of macromolecules.

The main drawback of DLS measurements is that larger particles overwhelm the scattered light of smaller ones. Therefore, DLS is inappropriate for measuring a solution of particles ranging from 10 nm to 1000 nm. The contribution of smaller particles to the intensity of scattered light is extremely low and is, therefore, not taken into account in the determination of size distributions. Indeed, the light-scattering intensity is strongly related to the size of the particles. According to Rayleigh

approximation, the intensity is proportional to d^6, with d = particle diameter. For instance, a 50 nm particle scatters light 10^6 times more than a 5-nm particle.
The Zetasizer Nano ZS is described in the next chapter. In this study, it was used to characterize the size, stability, and degradation of particles.

6.1.1 Zetasizer Nano ZS

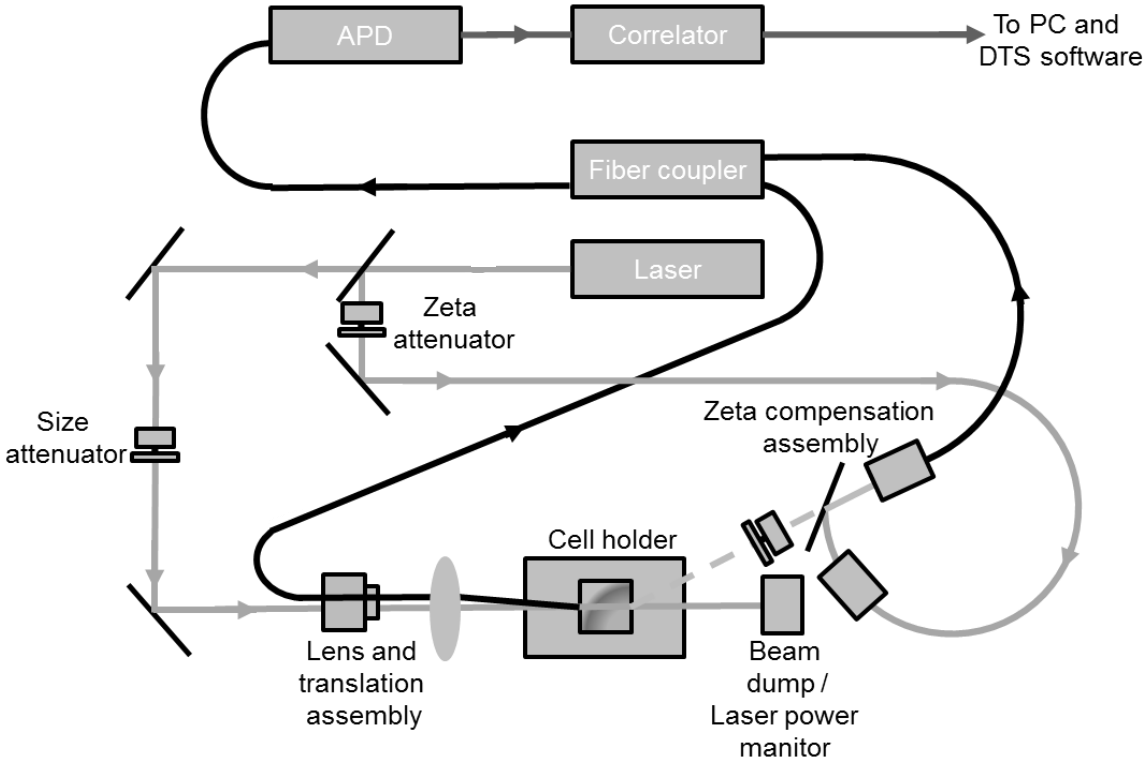

Figure 6-1 Schematic of the Zetasizer Nano ZS (From www.malvern.com)[275].

Figure 6-1 is a schematic representation of the Zetasizer Nano ZS. To measure particle size, a He-Ne laser with a wavelength of 633 nm, is used as light source, which illuminates the particle suspension within the cell holder. When the beam hits the solution, most of the light passes through it and is then neutralized through beam dump. Some of the light is scattered by the particles in all directions. A detector placed at 174.65° for backscatter detection is used to measure the intensity of the scattered light. The analysis at this specific angle helps to minimize the measurement of the light scattered by contaminants such as dust particles. Another critical aspect is the range of intensity received by the avalanche photodiode detector. Samples with small particles or a low concentration result in low intensities and the signal needs to be increased. By contrast, in samples with larger or higher particle concentrations, the scattered light intensity increases and leads to a saturated signal. In this case, the

signal needs to be decreased. Therefore, an attenuator is placed to reduce or increase the intensity of the laser. Then, the signal is transmitted to a correlator that compares the scattering intensity at successive time intervals and determines the rate of the intensity fluctuation. Finally, the signal is forwarded to a computer, which analyzes and translates the signal into size information.

6.1.2 Particle size[274]

The measurement of particle sizes is based on the movement and travel speed of the particles, which are responsible for intensity fluctuation. The movements are governed by Brownian motion, which is the random and uncontrolled movement of particles in a solution, as they constantly collide with the solvent or other molecules. Moreover, speed is strongly affected by the size of the particles. In fact, smaller particles move faster than larger particles, which is reflected in rapid intensity fluctuations (Figure 6-2, A and B).

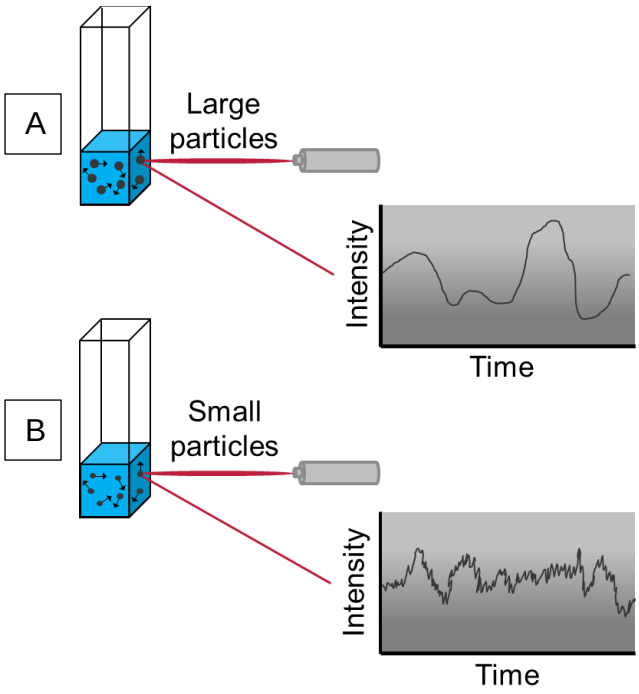

Figure 6-2 Typical intensity fluctuations for large (A) and small (B) particles.

Fluctuation is measured by the correlator, which compares the intensity at different times, I(t) and I(t+τ), with I: intensity and τ: time interval. If the signal intensity is compared after a very short time (τ), a strong relationship, called correlation, can be found. If the signal at I(t) is compared with the intensity at t+2τ, the correlation can be seen to decrease with time. As mentioned previously, the intensity fluctuation is dependent on the speed and the size of the particles. Thus, the presence of large

particles that are moving slowly results in low intensity fluctuation and thus a slow correlation decrease (Figure 6-3, black curve). Small particles that are moving quickly results in a rapid intensity fluctuation and therefore a fast correlation decrease (Figure 6-3, grey curve).

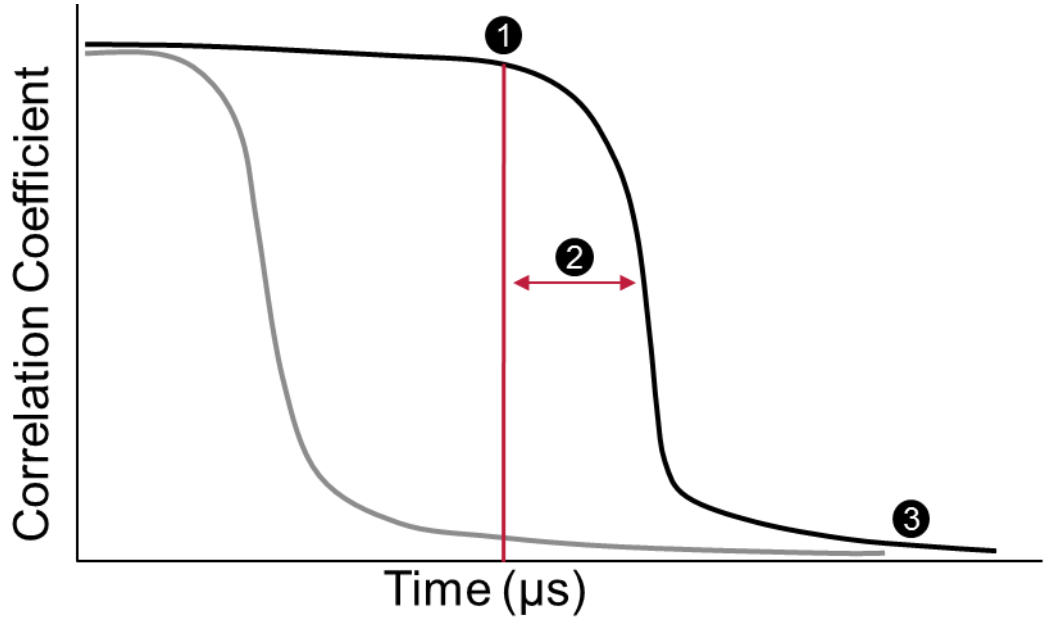

Figure 6-3 Typical correlogram from a sample containing large particles (black curve) and a sample containing small particles (gray curve).

Based on the time and correlation coefficient, correlograms (Figure 6-3) yield different information about the sample. At point (1), the curve starts to decrease and is related to the mean size of the particles. The gradient (2) indicates the polydispersity index of the sample, and the baseline smoothness point (3) represents information about the quality of the measurement. For instance, smoothness can be influenced by the formation of aggregates or dust in the solution. The polydispersity index describes the size distribution of the particles and ranges between 0 and 1. At a value of 0, the particles in the system have a monodisperse size distribution, whereas a value between 0.5 and 1 indicates a polydisperse system with a wide range of particle sizes. Mathematically, the time correlation G(τ) of monodisperse and circular particles in a Newtonian fluid can be described by the following equation:

$$\boldsymbol{G(\tau) = e^{-Dq^2\tau}} \qquad \text{equation 1}$$

D represents the diffusion coefficient, τ the correlator delay time, and q the scattering vector.

The diffusion coefficient (D) is characterized by the Stokes-Einstein equation:

$$d(h) = \frac{k_B T}{3\,\pi\,\eta\,D} \qquad \text{equation 2}$$

where k_B represents the Boltzmann constant, T the temperature, d(h) the hydrodynamic diameter, and η the viscosity of the solution.

Regarding both equations, the time correlation is influenced by external factors such as temperature and viscosity. Additionally, convection and sedimentation processes influence Brownian motion and consequently the time correlation.

In the case of noncircular particles, the equations yield an approximation of the diameter, and the object is perceived as a round object.

6.1.3 Zeta potential[274]

Zeta potential measurement is a technique for determining the surface charge of NPs in solution. A charged particle attracts counter ions and forms a double layer (Stern layer), which travels with the NP. Therefore, a potential difference between the solvent and the double layer occurs. This is known as the zeta potential of particles and has values that typically range from +100 to −100 mV. The magnitude of the zeta potential predicts the particle stability in suspension.

The electrical double layer of negatively charged particles can be described as follows: The first layer is known as the Stern layer, which is generated by positive counterions that are attracted by the particle surface and become closely attached to it through electrostatic force. Due to the different size of ions present in the solution, the negative charges cannot be fully compensated by cations to reach a potential of 0. For this reason, a second layer called the diffuse or Gouy-Chapman layer is formed. The diffuse layer contains free ions, with a majority of counterions. The electrical potential within the electric double layer has a maximum value on the particle surface (Stern layer). Then, it decreases with increasing distance from the surface and reaches 0 at the border of the electric double layer. When a particle moves through the solution, a layer of surrounding ions remains attached to the particle. The boundary of this layer is called the shear plane. The value of the electric potential at the shear plane is called the zeta potential, which is a critical parameter concerning the stability of particles and can be determined by the Zetasizer Nano ZS device.

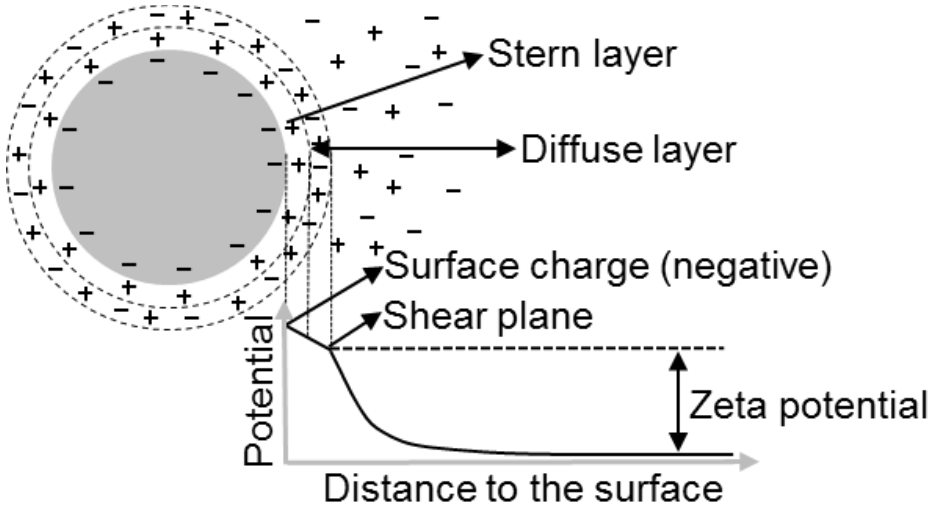

Figure 6-4 Schematic showing of the electrical double layer that surrounds a particle in an aqueous medium and the position of the shear plane. The zeta potential is the electrical potential at this plane.

The Zetasizer Nano series calculates the zeta potential by determining the electrophoretic mobility of particles and then by applying the Henry equation. The electrophoretic mobility can be determined by using an electrophoresis experiment on the sample and measuring the velocity of the particles using Laser Doppler Velocimetry.

In practice, an electric field is applied across charged particles and is consequently attracted towards the electrode of opposite charge. Viscous forces acting on the particles tend to oppose this movement. When the equilibrium is reached, between these two opposing forces, the particles move with constant velocity. The velocity of the particle is dependent on different factors such as the strength of electric field or voltage gradient, the dielectric constant of the medium, the viscosity of the medium and the zeta potential. The velocity of a particle subjected to an electric field is commonly referred to as its electrophoretic mobility. The technique used to determine the velocity is called laser Doppler velocimetry. The light scattered at a specific angle is combined with the reference beam. The movement of particles produces a fluctuating intensity signal where the rate of fluctuation is proportional to the migration speed of the particles. The migration speed can be divided by electric field strength to obtain the electrophoretic mobility (UE).

Zeta potential and UE can be linked via the Henry equation, to define the zeta potential:

$$UE = \frac{2\varepsilon\, z\, f(\kappa a)}{3\eta}$$

With *U*E electrophoretic mobility, ε the dielectric constant, z the zeta potential, f(κa) the Henry´s function and η the viscosity. Two values are used as approximations for f(κa) determination, 1.5 or 1.0. Electrophoretic determinations of zeta potential are commonly done in aqueous solution and moderate concentration. In this case, f(κa) is 1.5 and is referred to as the Smoluchowski approximation. Therefore, calculation of zeta potential from the mobility is straightforward for systems that fit the Smoluchowski model, i.e. particles larger than 0.2 microns dispersed in electrolytes containing more than 10^{-3} molar salt. For small particles, low dielectric constant media f(κa) becomes 1.0 and allows the use of a specific calculation. This is referred to as the Huckel approximation. Non-polar solvent measurements generally use this equation.

6.2 Ellipsometry[278][279]

Ellipsometry is a powerful and nondestructive technique for determining optical properties (refractive index or extinction coefficient) of surfaces and coatings. In addition, it provides information about intrinsic and structural properties of materials. The measurement is based on amplitude changes in polarized light upon light reflection. A light beam, with a known polarization state (mainly linear), is used to radiate a sample (Figure 6-5). The device is composed of a laser, a polarizer, a compensator (λ/4), a rotating analyzer, and a detector. The laser beam is first linearly polarized by the polarizer and subsequently guided to the compensator (C; λ/4). (C) is described as an anisotropic optical device placed at an angle of 45° to the light beam. It transforms a linearly polarized light into a circularly polarized one (Figure 6-5). Afterwards, the light hits the surface of the sample, resulting in a reflected beam with an altered state of polarization. The reflected beam is then guided to a second polarizer (rotating analyzer: RA). The RA is adjusted so that the resulting reflection beam is linearly polarized. The orientation is determined by alternately adjusting the polarizer and the analyzer until the null value is identified.

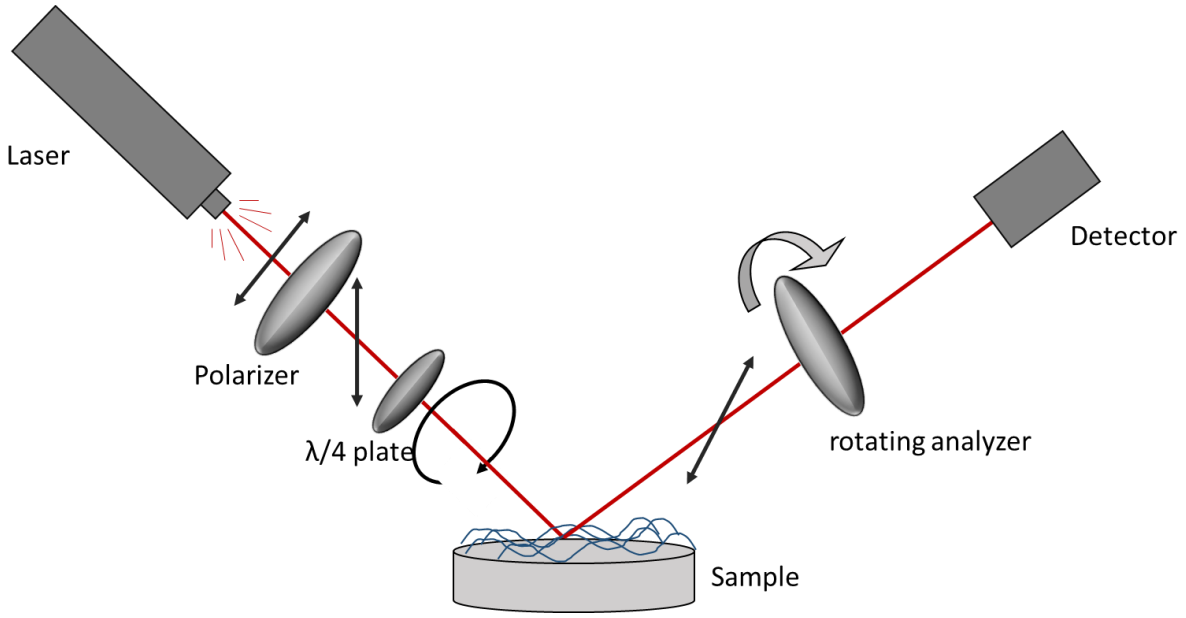

Figure 6-5 Schematic of ellipsometry.

The polarization state of incident and reflected light can be decomposed into s (for perpendicular) and p (for parallel) components (Figure 6-6). The parameters Δ (phase difference) and Ψ (amplitude component) are used to describe the properties of the sample.

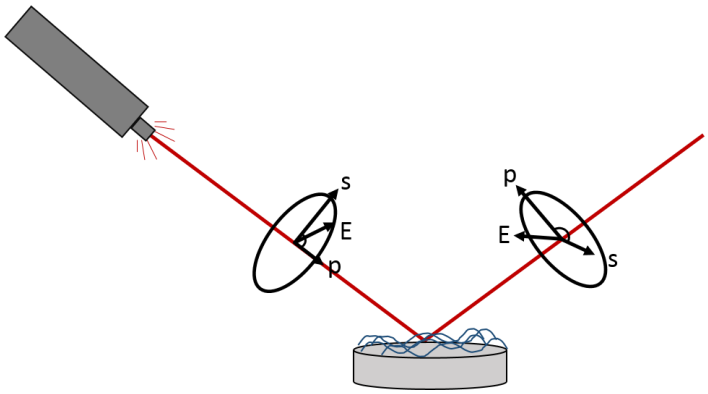

Figure 6-6 Schematic of ellipsometry before and after reflection with E: electric field resolved into its p and s components.

Mathematically, the amplitude can be described by equation 3. The amplitudes s and p of the reflected light are respectively denoted by the reflection coefficients R^s and R^p. The factor tan Ψ represents the magnitude of the reflectivity ratio, with Ψ ranging between 0° and 90°.

$$tan\Psi = \frac{|R^p|}{|R^s|} \qquad \text{equation 3}$$

Moreover, the change in polarization of reflected light is represented by the phase difference Δ (equation 4), with δ1 representing the phase difference between p and s components of the incoming light wave and δ2 representing the outgoing wave.

$$\Delta = \delta 1 - \delta 2 \qquad \text{equation 4}$$

Both parameters Ψ and Δ are defined during measurement and are related to the following equation (equation 5).

$$tan\Psi * e^{i\Delta} = \frac{|R^p|}{|R^s|} * e^{i(\delta 1 - \delta 2)} = \frac{R^p}{R^s} \qquad \text{equation 5}$$

These parameters enable the definition of the refractive index, film thickness, surface roughness and extinction coefficient of the substrate. These properties are found by using the measured Ψ and ∆ in various equations and algorithms to produce a model that describes the interaction between light and sample. After the sample measurement, a model is constructed to describe the sample. The model is used to calculate the predicted response from Fresnel's equations, which describe each material with thickness and optical constants. If these values are not known, an estimation is given for the purpose of the preliminary calculation. The calculated values are compared to experimental data. Any unknown material properties can then be varied to improve the match between experiment and calculation. Finding the best match between the model and the experiment is typically achieved through regression. The measurement of the uncoated substrate is necessary, and the result is compared with the parameters obtained after the coating. More details can be found in the literature[280].

7 Results: chitosan-g-[poly-L-lysine-b-ε-caprolactone]

The scope of this study entailed the synthesis of a chitosan-g-[poly-L-lysine-b-ε-caprolactone] with a specific grafting degree (Figure 7-1, **A**). The graft-copolymer can be self-assembled into polymeric micelles or vesicles through the solvent shift method (Figure 7-1, **B**) and generates well-defined core-shell structures suitable for encapsulation. The hydrophobic (PCL) and the hydrophilic (CS) parts were linked via a biocompatible peptide in order to make it enzyme-cleavable. A suspension of polymersomes was used to coat a titanium plate and resulted in a highly stable coating at body temperature, which is an essential requirement for a drug delivery system. Furthermore, degradability was studied by incubating polymersomes with two enzymes: peptidase and chitosanase. Specific peptidases that are released as a result of an inflammation could be used to trigger drug releases (Figure 7-1, **C**).

First, the synthetic route involves the functionalization of chitosan with maleimide groups[281] and PCL with an alkyne end-group[282]. Thiol-maleimide click-chemistry and azide-alkyne Huisgen cycloaddition were used to link chitosan and poly-ε-caprolactone chains via a thiol- and azide-functionalized peptide (Figure 7-1). For a preliminary study, to investigate the feasibility of the system, PLL was employed as a readily available and cleavable peptide linker. The size, shape, and enzyme-triggered degradability were studied through DLS/cryo-SEM. Finally, the ability to form a coating on a titanium substrate was also analyzed.

Part of the results described in this chapter have been published: Y. Bourgat, B. Tiersch, J. Koetz, H. Menzel, Enzyme degradable polymersomes from Chitosan-g-[poly-L-lysine-b-ε-caprolactone] copolymer Macromol. Biosci. published online 2.12.2020 (2020). DOI: 10.1002/mabi.202000259[198].

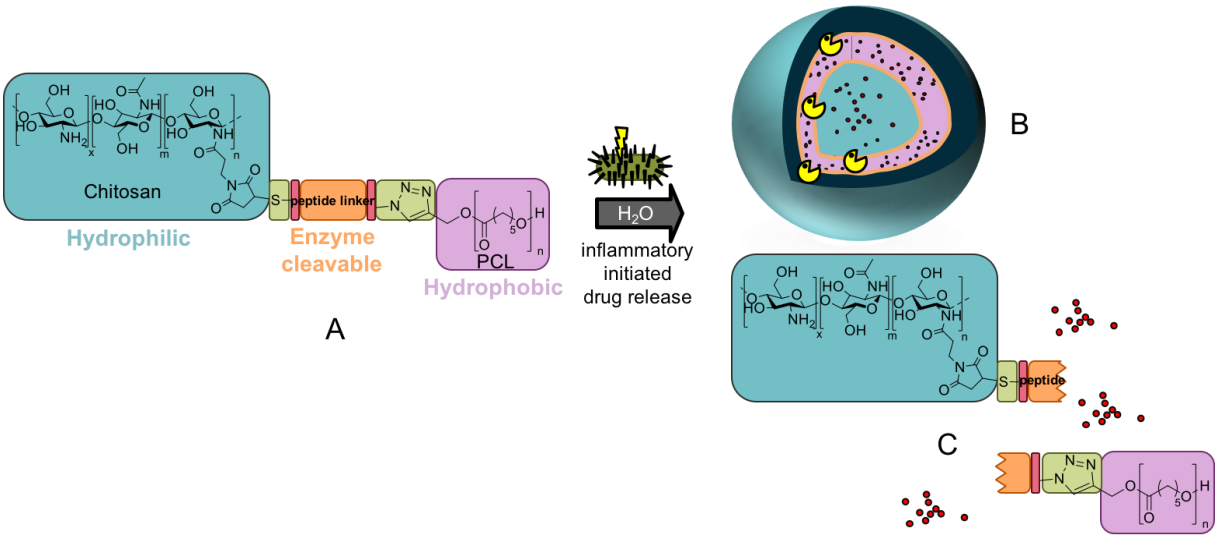

Figure 7-1 Schematic of A) chitosan-g-[poly-L-lysine-b-ε-caprolactone] copolymer, B) polymersome structure, and C) degradation.

7.1 Synthesis of chitosan-g-[poly-L-lysine-b-ε-caprolactone] 4

The graft polymer chitosan-g-[poly-L-lysine-b-ε-caprolactone] (CS-g-[PLL-PCL]) was synthesized in four steps. In the first step, maleimide groups were introduced as side chains at the chitosan backbone, with different degrees of substitution (DS) (Figure 7-2, **step 1**). This step was followed by the synthesis of propargyl-terminated poly-ε-caprolactone (Figure 7-2, **step 2**), the grafting of poly-L-lysine$_{20}$-N$_3$ onto chitosan (Figure 7-2, **step 3**) and finally the link between poly-ε-caprolactone and CS-[poly-L-lysine$_{20}$-N$_3$] (Figure 7-2, **step 4**).

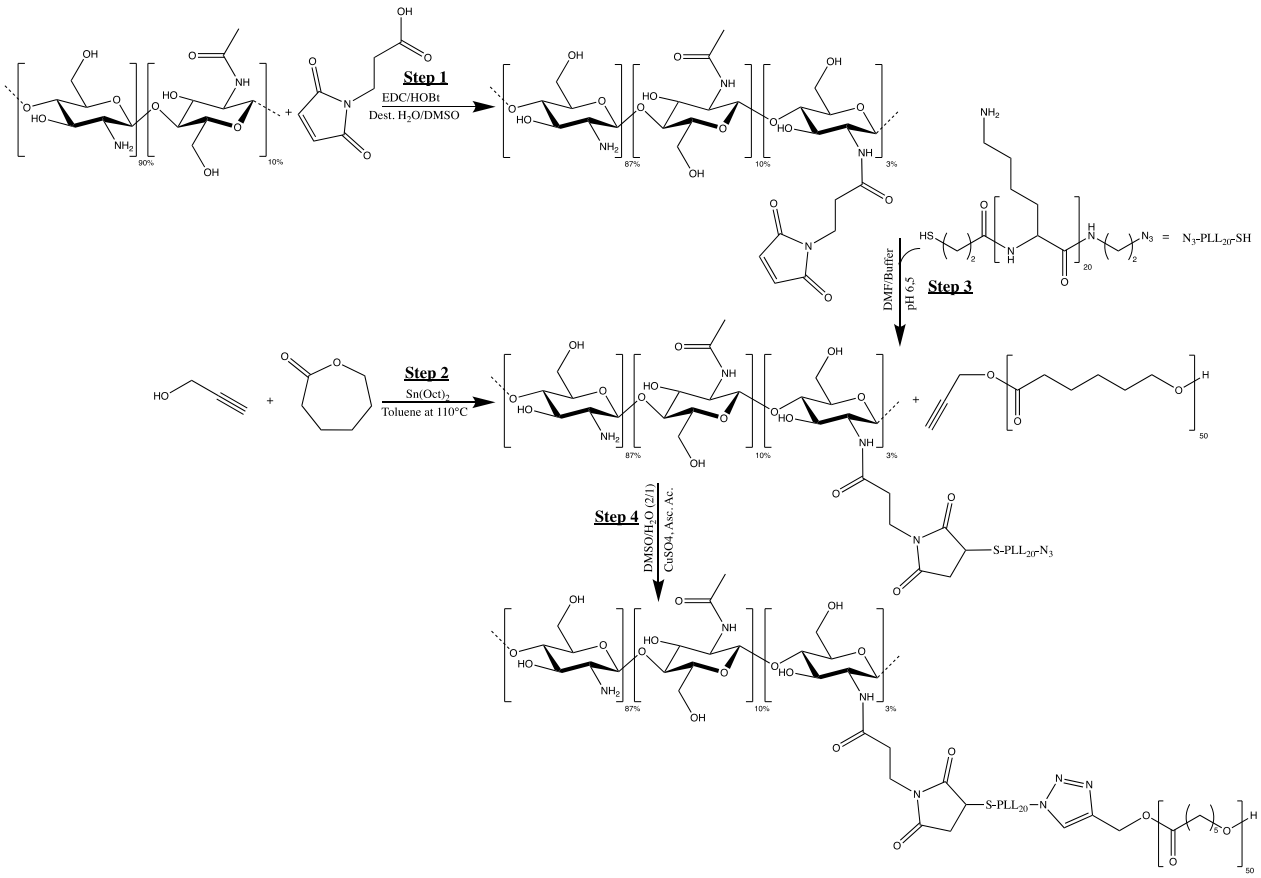

Figure 7-2 Reaction scheme of chitosan-g-[poly-L-lysine-b-ε-caprolactone]$_{3\%}$.

Synthesis of chitosan conjugated with N-maleoyl-β-alanine step 1 (Figure 7-2)

The maleimide group was conjugated to chitosan with varying DS through a reaction between the carboxylic acid of N-maleoyl-β-alanine and the amine function of chitosan. This reaction was optimized, using chitosan from various sources and with various molecular weight, and by exploring different synthetic pathways.

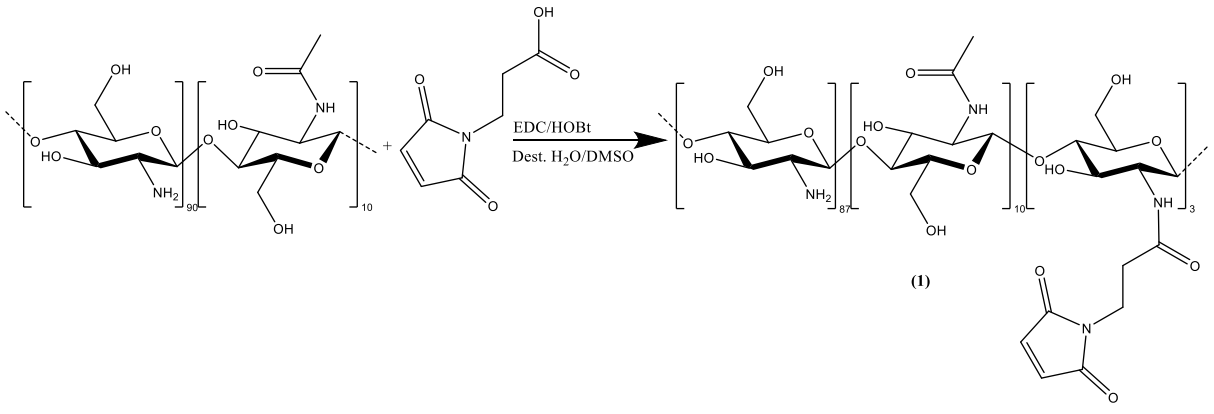

*Figure 7-3 Conjugation of chitosan with N-maleoyl-β-alanine **1**.*

The reaction was first performed with a 4-(4,6-dimethoxy-1,3,5-triazin-2-yl)-4-methyl-morpholinium chloride (DMTMM) as coupling reagent (Table 7-1, CS6) or NHS-activated ester of N-maleoyl-β-alanine (Table 7-1, CS7). Both ways led to insoluble or minimally substituted product. Chirachanchai et al.[281] proposed a pathway using 1-hydroxybenzotriazole (HOBt), 1-Ethyl-3-(3-dimethylaminopropyl)carbodiimide (EDC) as coupling reagents and DMSO as a cosolvent to increase the solubility of the intermediate[281]. When an inappropriate amount of DMSO (lower than 50%) is used, the DS was found to be low and to lead to an insoluble product. This can be explained by the formation of a poorly water-soluble intermediate or the occurrence of a side reaction between grafted maleimide and the amine functions of chitosan during the dialysis process (e.g., 1.4-addition of amino group, transamidation, etc.[283]). This last hypothesis can be validated through infrared spectroscopy. In fact, the peak intensity ratio between the carboxylic groups of chitosan at 1645 nm^{-1} and the double-bond peak of the grafted maleimide increased after dialysis against water.

$$\text{Ratio} = \frac{\text{Intensity (carboxylic group)}}{\text{Intensity (maleimide group)}}$$

A decrease in maleimide groups entails a possible cross-linking with the amine functions of chitosan. Indeed, it is known that at a certain pH (approximately 8), the reactivity of maleimide with amines increases[284]. Therefore, to avoid this side reaction, performing dialysis against acidic solutions was necessary. As described in Table 7-1, several experiments were needed to optimize the reaction. Variations in Dimethylsulfoxid (DMSO) amount (Table 7-1, CS1 and CS3), coupling reagents (Table 7-1, CS4 and CS5), and molecular weight of chitosan (Table 7-1, CS1 and CS2) were relevant factors in obtaining a coupling efficiency (CE) of up to 67%. Moreover, the following conclusions can be drawn from the experiments described in Table 7-1:

- Experiment CS1 and CS2 are using the same DMSO content and theoretical grafting degree but different molecular weight. This leads to an increase of 212% of the CE by using a lower molecular weight chitosan from fungal sources.
- Experiment CS4 and CS5 are using different coupling reagents as EDC and lead to low CE. These two experiments were performed at the very begin of this study and the dyalisis against acidic condition, to avoid side reaction, was not respected. This could explain the low grafting degree.
- Experiment CS3 and CS1 are using different amount of DMSO, respectively 50% and 91% of total volume. This leads to an increase of 34% of the CE by using higher amount of DMSO.

Further investigation will be described in a future publication of Christ et. al[i].

Table 7-1 Comparison of different synthesis conditions: chitosan source, solvent, and coupling agent.

Experiment	Grafting degree (theoretical) (%)	Grafting degree (experimental) (%)	Coupling efficiency (%)	DMSO amount (%)	Coupling reagent	Molecular weight (KDa)
CS1-Fungal	30	15	50	50	HOBt / EDC	110–150
CS2-Shrimp	30	4.8	16	50	HOBt / EDC	190–310
CS3-Fungal	30	20	67	91	HOBt / EDC	110–150
CS4-Shrimp	20	0.05	0.25	0	DMTMM	190–310
CS5-Shrimp	50	2.2	4.4	0	NHS	190–310

Fourier-transform infrared spectroscopy (FT-IR) and proton nuclear magnetic resonance (^{1}H-NMR) spectra were used to prove the conjugation of chitosan with 3-maleimidopropionic acid. In FT-IR spectra a signal assigned to the amide I group at 1645 cm^{-1} was found, which increased with increasing DS (Attached file 2, A). By contrast, the signal at 1511 cm^{-1}, representing primary amine bending, decreased with increasing substitution. These findings were regarded as a consequence of the reaction between amines of chitosan and carboxylic acid, resulting in amide bonds. Furthermore, a signal at 1704 cm^{-1} was found, and is the characteristic vibrational frequency of aromatic -C=C- bending, originating from the maleimide functions.

The protons of the N-acetyl-D-glucosamine, D-glucosamine unit of chitosan and two proton signals of the maleimide double bond (6.85 ppm) were also noticed in the ^{1}H-NMR spectra of maleimide substituted chitosan (Attached file 1). The DS was calculated from the ^{1}H-NMR spectra, using the ratio of maleimide protons at 6.85 ppm and the signal at 2.00-2.08 ppm, which represents 3 protons of the chitosan backbone. By using different sources of chitosan and DMSO content, the highest coupling efficiency that could be reached was 67% (Theoritical grafting degree of 30%). This demonstrates the limitation of this condition to graft malemide functions on chitosan.

[i]H. A. Christ, Y. Bourgat, H. Menzel, Optimization of critical parameters for carbodiimide mediated production of highly modified chitosan *Carbohyd. Polym.* **Submitted.** (2021)

In order to understand the parameters that influence the reaction, a brief overview on the mechanism is discussed in chapter 4.1.

The rate-determining step of the reaction is governed by the reaction between $EDClH_2^{2+}$ and carboxylic acid (see Figure 4-2, page 28). Thus, EDC must be protonated to react with the deprotonated acid. Cox et al. described the reaction of acetic acid and EDCl as a coupling reagent. They observed a maximum conversion rate at pH = ((pKa (RCO_2H) + pKa ($EDClH_2$))/2. Acetic acid and EDCl with a respective pKa of 4.7 and 3.1, have an optimal pH of 3.9 for synthesis. A rapid decrease at pH > 4.7 (reduced levels of $EDClH_2^{2+}$) and pH < 3.1 (reduced the amount of deprotonated carboxylic acid) is evident. Thus, the rate of the reaction is strongly pH dependent.

Another key element to improve the reaction rate is to use additives, which suppresses the formation of N-acylurea and promotes the formation of O-acylisourea (see Figure 4-2, page 28). In fact, N-acylurea is undesirable because it leads to consumption of the 3-maleimidopropionic acid and no further formation of the desired ester. The commonly used N-acylurea-suppressing additives are benzotriazole derivatives, including HOBt and 1-hydroxy-7-azabenzotriazole.

In conclusion, there are three impacting parameters that highly influence amide coupling and can be used to optimize the reaction:

- Hydroxybenzotriazole which acts as a catalyst and an N-acylurea-suppressing substance.
- Dimethylsulfoxid which increases the solubilty of intermediate.
- And the pH, which influences the protonation of amines and carboxylic acid.

Synthesis of propargyl-terminated poly-ε-caprolactone step 2 (Figure 7-2)

The “clickable” side chain was synthesized as propargyl-terminated poly-ε-caprolactone **2** through ROP of ε-caprolactone (ε-CL) by using Tin(II) 2-ethylhexanoate ($Sn(oct)_2$) as the catalyst and propargyl alcohol as the initiator (Figure 7-4).

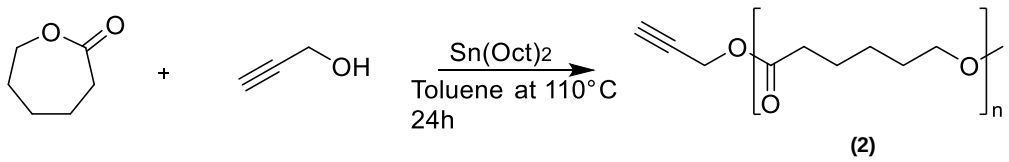

(2)

*Figure 7-4 Reaction scheme of polymer **2**.*

The molar ratio of ε-CL, propargyl alcohol, and $Sn(oct)_2$ was determined to be 83:2:1. More details regarding the synthesis conditions can be found in the experimental part

of Chapter 10. The ^{1}H-NMR spectra (Attached file 3) was used to confirm the presence of both alkyne function and PCL backbone signals. The peaks at 4.68 and 2.43 ppm represent, respectively, HC≡C- and C-CH_2- protons of the propargyl function. The protons at 1.36, 1.62, 2.27, 4.03, and 3.62 ppm represent the PCL backbone protons. Furthermore, FT-IR analysis (Attached file 2, B) was carried out to corroborate the success of the synthesis. The characteristic vibrational bands of **2** appear at 1720 cm^{-1} (C=O stretching) and 1238 cm^{-1} (C-O-C asymmetric stretching). The signal at 3261 cm^{-1} (H-C≡C- stretching) highlighted the end-terminal alkyne function. Finally, the Mw = 5755 g/mol was calculated from the ^{1}H-NMR spectrum. The calcuation was based on the integration of proton peaks of CH from the alkyne function at 4.68 and from the PCL backbone at 4.03 ppm. The theoretical Mw calculated from the ratio of initiator and monomer was Mw_{theor} = 6770 g/mol.

Synthesis of CS-[poly-L-lysine$_{20}$-N$_3$] (CS-g-[PLL$_{20}$-N$_3$]) Step 3 (Figure 7-2)

The ligation between the thiol end-functionalized peptide and the maleimide-functionalized chitosan to synthezise CS-g-[PLL_{20}-N_3] **3,** was carried out by thiol-ene click chemistry, also known as Thiol-Michael addition (Figure 7-5)

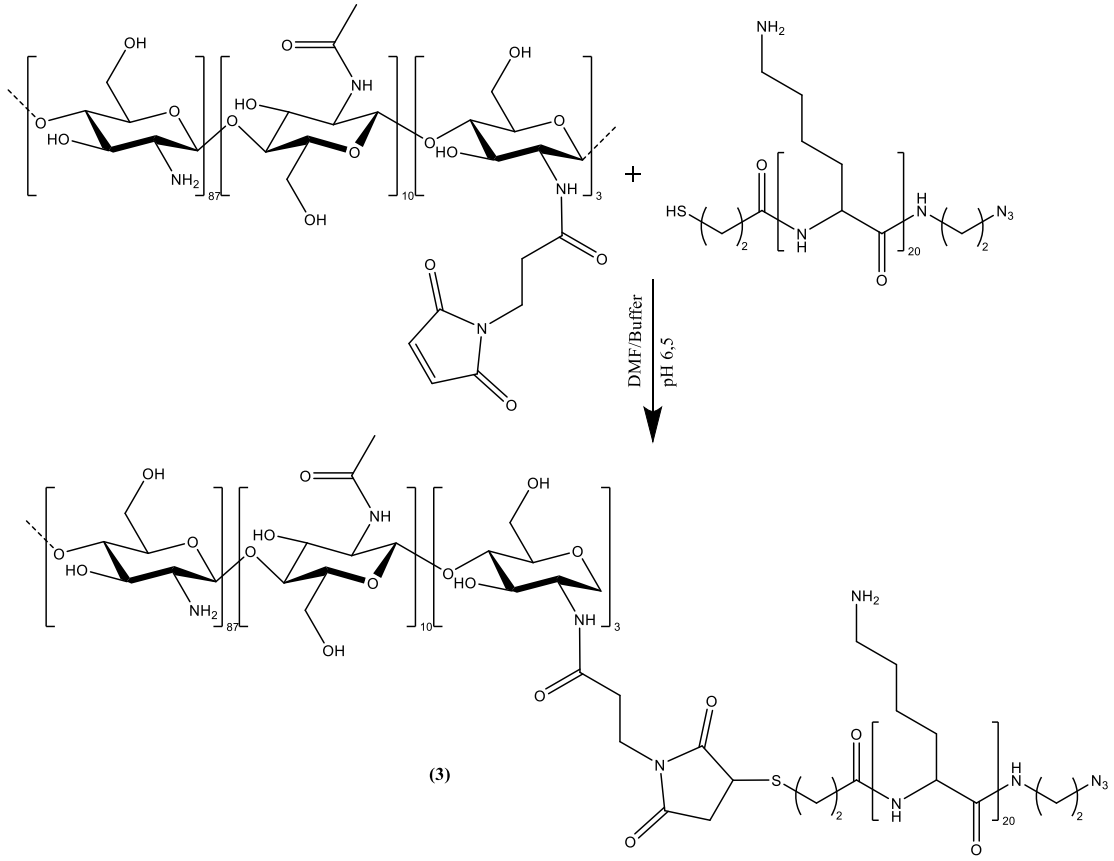

*Figure 7-5 Reaction scheme of CS-[poly-L-lysine$_{20}$-N$_3$] **3**.*

As previously mentioned, It is common for such reactions to be performed in the presence of, e.g. DMF as solvents and catalyst[219]. Solvents such as DMSO and DMF possess a high dielectric constant, which promotes the spontaneous dissociation of thiol into nucleophilic thiolate anion. Subsequently, the thiolate is able to react with the double bond of the maleimide function[220]. Nevertheless, DMSO is also known to catalyze undesired disulfide bond formation[221]; therefore, DMF was chosen as the optimal solvent for this synthesis. In addition to solvent choice, pH plays a crucial role. The reaction between a maleimide and thiol function specifically occurs at physiological pH (6.5-7.5), generating a stable thioester bond. At a pH above 8.0, the reactivity between the double bond and amines of chitosan is significantly increased, which leads to side reactions[283][284].

More details about the synthesis conditions can be found in the experimental section. The reaction was checked by ^{1}H-NMR spectroscopy, which showed the disappearance of the maleimide double bond protons at 6.85 ppm; these protons are involved in the reaction with the thiolate. New signals at 1.43, 1.70, 2.98, and 4.31 ppm characteristic for the protons of the PLL backbone indicated the presence of the peptide (Attached file 4). The FT-IR analysis (Attached file 2, C) was also conducted to confirm the reaction and to demonstrate the appearance of a vibrational band at 2126 cm^{-1}, which is characteristic of the azide function grafted on the chitosan.

Synthesis of chitosan-g-[poly-L-lysine-b-ε-caprolactone] (CS-g-[PLL-PCL]) Step 4 (Figure 7-2)

The ligation between azide functionalized CS-[poly-L-lysine$_{20}$-N_3] and the alkyne-functionalized poly-ε-caprolactone to synthezise CS-g-[PLL-PCL] **4** was carried out by 1,3-Huisgen dipolar cycloaddition, also known as the «copper click reaction».

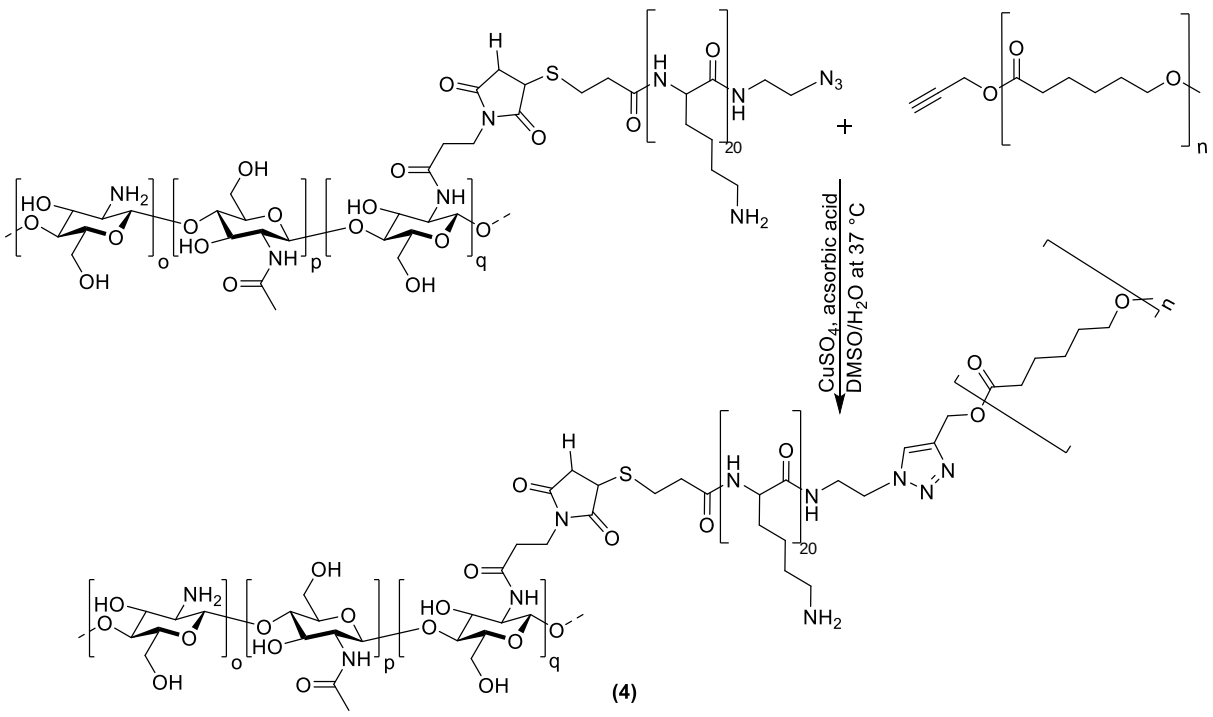

Figure 7-6 Reaction scheme of chitosan-g-[poly-L-lysine-b-ε-caprolactone] 4.

The reaction occurs between the azide function of the peptide already grafted onto CS and the alkyne function of the PCL. The reaction was catalyzed by $CuSO_4 \cdot 5H_2O$ and sodium ascorbic acid as agent to reduce unreactive Cu(II) to Cu(I).

The purification step consisted of a dialysis against tetrahydrofuran (THF), to remove unreacted ε-caprolactone, followed by a dialysis against a saturated aqueous solution of ethylenediaminetetraacetic acid EDTA to remove copper[285]. The alcohol and amine groups on the chitosan are excellent ligands to coordinate with copper to obtain a chitosan-metal complex. Because EDTA is a better ligand than chitosan, the formation of the (EDTA)-copper complex is favored[285] and removed during the dialysis process. More details regarding the synthesis condition can be found in the experimental part, chapter 10.5.5.

^{1}H-NMR spectroscopy, operated at a temperature of 50°C, to ensure the solubility of the copolymer, was carried out to validate the synthesis of chitosan-g-[poly-L-lysine-b-ε-caprolactone] copolymer (Attached file 5). The peaks at 4.24; 2.80; 1.64 and 1.41 ppm are characteristic for PLL protons in DMSO/H_2O mixture. The peaks at 4.95; 3.86-3.73; 2.93; 1.87 ppm are originating from the chitosan backbone. Finally, the peaks at 3.99, 2.27, 1.54, and 1.30 ppm are characteristic for the PCL backbone protons. In addition, the disappearance of the peak at 2121 cm^{-1} in the IR-spectrum confirmed the consumption of the azide groups (Attached file 2, D). The chitosan and PLL backbones

can be characterized by the band at 1646 cm^{-1} (C=O stretching of amide I) and strong bands at 3287, 3340 cm^{-1} that correspond to N-H and O-H stretching. The bands at 1045 cm^{-1} correspond to C-O stretching of chitosan. The DS was calculated from the ^{1}H-NMR spectra, using the ratio of PCL protons at 3.99 ppm and 3 protons of chitosan backbone at 1.87 ppm.

In conclusion, all parts of the copolymer, maleimide modified chitosan and propargyl-terminated poly-ε-caprolactone were succesully synthesized and characterized before they were linked together via a poly-L-lysine sequence.

7.2 Formation and characterization of polymersome

After the successful synthesis of amphiphilic graft copolymer, its self-assembly into polymersomes and their degradability by enzymes were studied. Polymersome formation depends on different factors, an important one is the hydrophilic to hydrophobic ratio. Studies have suggested that a hydrophilic mass fraction from 20% to 45% is a unifying rule for achieving self-assembly into polymersomes[286]. Based on this rule, two graft copolymers, with mass fractions in or near the recommended range, were synthesized: CS-g-$[PLL\text{-}PCL]_{3\%}$ with a hydrophilic mass fraction of 50%, and CS-g-$[PLL\text{-}PCL]_{5\%}$ with hydrophilic mass fraction of 40%. As described in the experimental part, the polymersomes were generated by the solvent shift method to induce the self-assembly process. Briefly, this method includes the dissolution of the copolymer in DMSO/H_2O and the careful removal of the DMSO by dialysis against H_2O. During this process, the hydrophobic and hydrophilic parts self-assembled into polymersomes through hydrophobic interactions. DLS was performed to measure the size of the polymersomes.

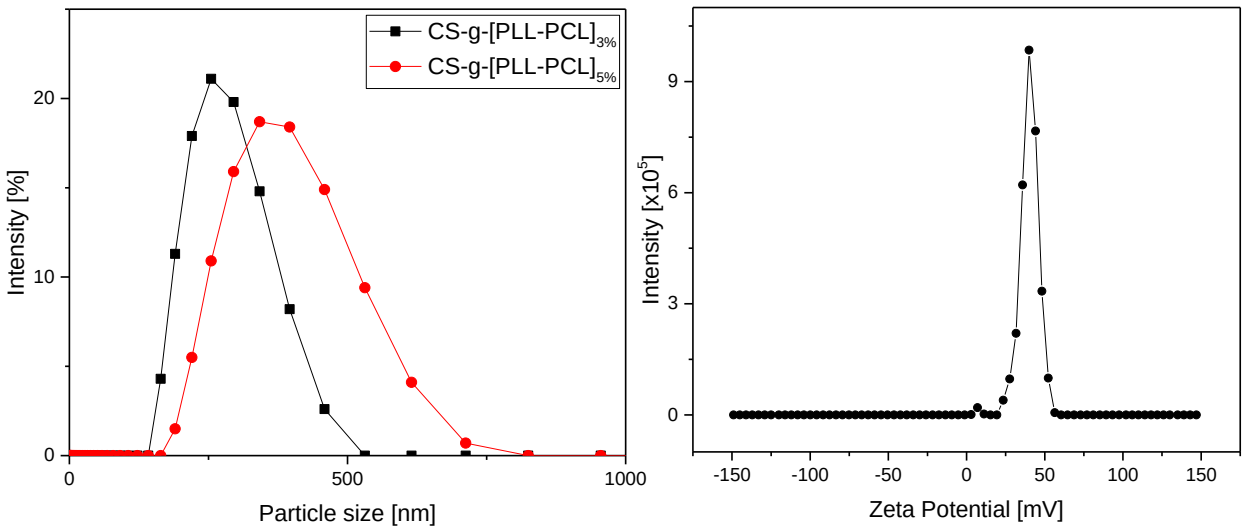

Figure 7-7 DLS size distribution of CS-g-[PLL-PCL]5% and CS-g-[PLL-PCL]3% and Zeta potential of CS-g-[PLL-PCL]3% polymersomes in deinized H_2O at rt.

Both graftpolymers gave polymersomes with a monomodal size distribution. Compared with polymersomes prepared from CS-g-[PLL-PCL]3%, with a mean size of 258 nm, CS-g-[PLL-PCL]5% leads to particles with an average size of 427 nm (Figure 7-7). The increase can be explained by the relation between shape, weight fraction of the hydrophilic part, Mw, and the interaction strength of the hydrophobic fraction with water. Furthermore, polymersomes can be predicted according to the equation $p = v/a \cdot l$, where "*p*" is the packing parameter, "*v*" is the volume of the hydrophobic chains, "*a*" is the optimal area of the head group, and "*l*" is the length of the hydrophobic tail[87]. Therefore, the ratio between hydrophilic and hydrophobic fraction affects the size/shape of polymersomes. With the increase in size, the polydispersity index (PDI) also increased from 0.129 for 3% to 0.351 for 5%. Drug delivery systems applications, using carriers with PDI of 0.3 and below, are considered to be acceptable and indicates an homogeneous population of particles[287]. Moreover, DLS measurements (Figure 7-7) indicated a positive zeta potential of approximately +41 ± 4.3 mV. This is an indication that amine functions of chitosan are oriented toward the outer water phase, as represented in Figure 7-8 **II**. Cryo-SEM was used to confirm the shape and morphology of polymersomes in suspension.

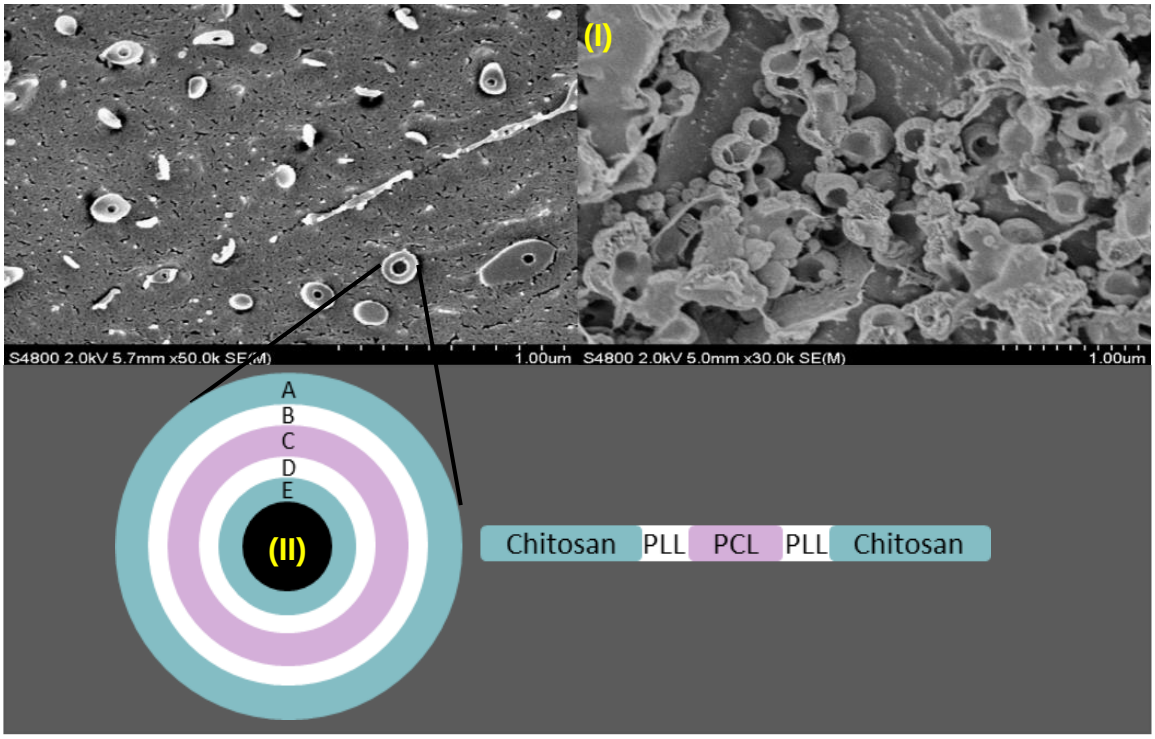

Figure 7-8 SEM micrographs of cryo-fractured surface of I) CS-g-[PLL-PCL]$_{3\%}$ polymersomes solution in ultrapure water and II) schematic representation of polymersomes with A/E, chitosan; B/D, poly-L-lysine; C, poly-ε-caprolactone.

Cryo-SEM micrographs (Figure 7-8 (**I**)) revealed well-defined core-shell structures for the polymersomes (Figure 7-8 (**II**)), with a size range centered around 300 nm, which is consistent with the size measured by DLS.

For testing the colloidal stability, the particle size was monitored via DLS while polymersomes were incubated in H_2O at pH 5.6 (Figure 7-9). The tests were performed at 37°C. Compared with room temperature measurements (Figure 7-7), CS-g-[PLL-PCL]$_{3\%}$ polymersomes at 37°C exhibited an increased initial size (Figure 7-9, Time = 0), which is a consequence of measuring at a higher temperature. During the incubation period, the size decreased slightly at a rate of approximately 0.43 nm/h (Figure 7-9). This is due to some sedimentation of larger, probably aggregated particles, during the DLS measurements. However, this is not attributed to a chemical degradation of the graft-polymers, as coatings prepared from the particle suspensions are very stable (vide infra). Similar tests were performed in a 63 mM sodium phosphate buffer, at pH 7.6, to observe the stability of polymersomes at physiological pH. Again, some decrease in particle size were observed after 6 days, which is very similar to the situation at pH 5.6 (Figure 7-10).

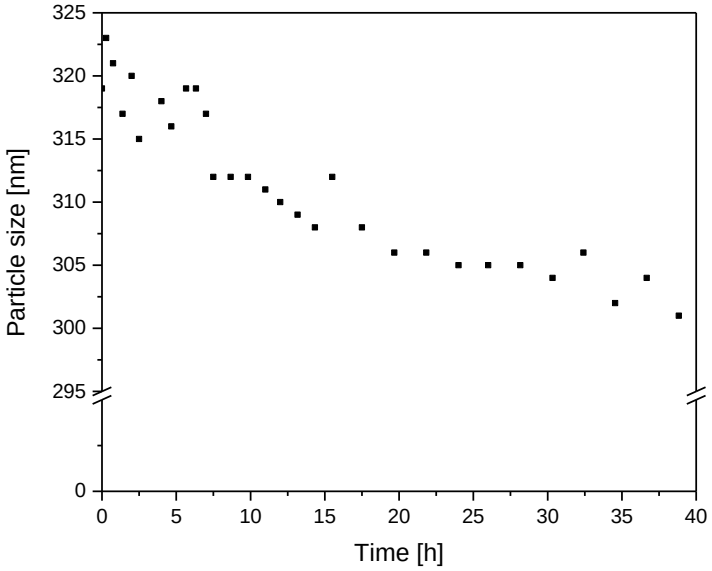

Figure 7-9 Particle size of chitosan-g-[poly-L-lysine-b-ε-caprolactone]$_{3\%}$ incubated in ultrapure H_2O for 40 hours at 37°C.

In conclusion, CS-g-[PLL-PCL]$_{3\%}$ was found to be the ideal copolymer, with a specific amount of hydrophobic fraction, to enable the formation of polymersomes with a well defined core-shell structure.

As the system is supposed to be degraded by specific peptidases, stability and degradability toward different enzyme is studied in the following chaper.

7.3 Enzymatic degradation of polymersome

The degradability of the well-defined polymersome was studied by incubating them with different enzymes, namely trypsin, which is able to cleave poly-L-lysine[209] and chitosanase, which endohydrolyzes β-1,4-linkages of partially acetylated chitosan[288]. As described in the experimental part, the polymersome suspension was treated with a 4 µg/mL trypsin solution and a 5 µg/mL chitosanase solution. DLS measurements were performed to determine particle sizes before and after incubation (Figure 7-10 and Figure 7-11).

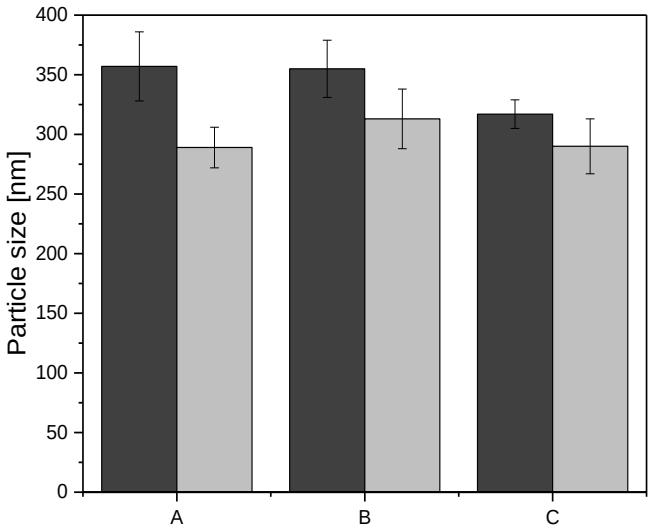

Figure 7-10 Particle size before ■ *and after* ■ *incubation of CS-g-[PLL-PCL]$_{3\%}$ polymersome at 37°C for 6 days in different media. A: H_2O pH = 5.6; B: H_2O, pH = 5.6 with trypsin (4 µg/mL) and C: 63 mM sodium phosphate buffer pH = 7.6.*

Incubation tests (Figure 7-10, B) with trypsin indicated no relevant variation in particles size, compared to the incubation in water (Figure 7-10, A) or buffer (Figure 7-10, C). In fact, in experiments A and C, without trypsin (Figure 7-10), a similar slight decrease in size was observed after 6 days, which was probably due to the sedimentation of larger aggregated polymersomes. Thus, polymersomes were stable against trypsin. However, incubation with chitosanase (Figure 7-11, A) resulted in a significant increase in particle size, while for incubation without chitosanase, again, a slight decrease was observed (Figure 7-11, B). Counterintuitive increase in particle size, link with the degradation, can be explained by the reduction in the hydrophilic part (chitosan), hydrolyzed by chitosanase, which consequently results in an increase in the hydrophobic fraction in the graft copolymer. Since shape and size of the polymersomes depend on the weight fraction of the hydrophilic part, Mw, and the interaction strength of the hydrophobic fraction with water[87]. As a consequence, a change in the hydrophilic amount, formed due to the degradation of the chitosan, results in variations of the aggregation or shape of particles, inducing in both cases a change in particle size.

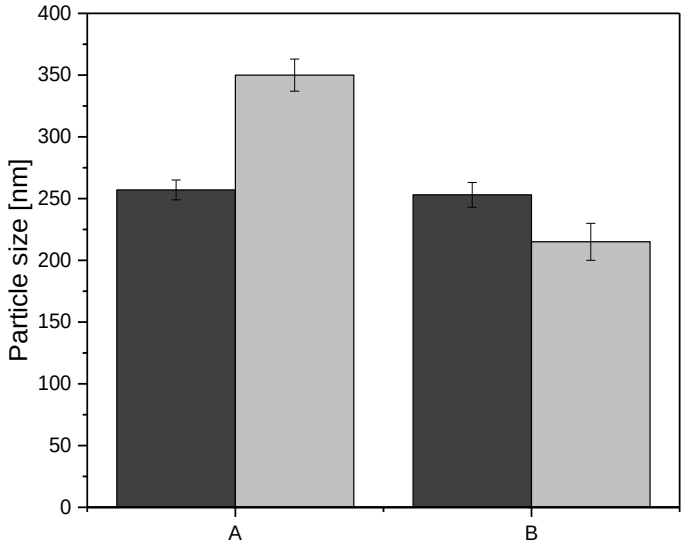

Figure 7-11 Particle size before ■ and after 72h incubation ■ of CS-g-[PLL-PCL]$_{3\%}$ polymersome at rt. A: with chitosanase (5 µg/mL) and B: without.

A further stability test was carried out with films, on titanium substrates, prepared by spray-coating: a suspension of polymersomes (chitosan-g-[poly-L-lysine-b-ε-caprolactone]$_{3\%}$. After drying, the films were incubated in water and in a mixture of water and chitosanase or trypsin. After certain incubation times, the dry thickness of the films was determined via ellipsometry. Figure 7-12 depicts the variation in layer thickness during incubation with either water (blue curve), water with chitosanase (5 µg/mL; red curve) or with trypsin (4 µg/mL; black curve) for 11 days. The solutions were refreshed daily to ensure the degradation capability of enzymes.

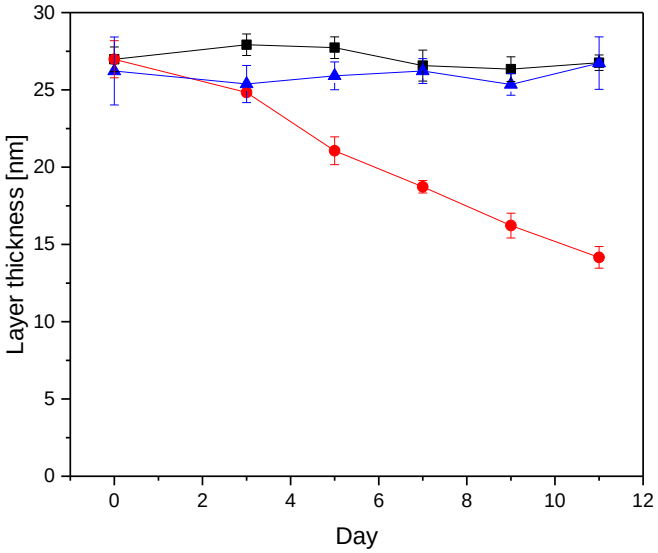

Figure 7-12 Layer thickness of chitosan-g-[poly-L-lysine-b-ε-caprolactone]$_{3\%}$ coated on Ti plate during incubation with chitosanase ● (5 µg/mL) and trypsin ■ (4 µg/mL), and without enzyme ▲ at 37°C.

After 11 days of incubation, with just water or a trypsin solution, no significant decrease in dry thickness was noticed; these observations confirmed a stable coating. However, after incubation in a chitosanase solution, a decrease, by 52%, in the layer thickness was noted (Figure 7-12). Contrary to the particle size increase, observed for the polymersomes in suspension (Figure 7-10), here, indeed, a decrease in film thickness is noticed. This is due to the degradation of the chitosan chains resulting in less material being bound to the surface. A similar behavior (particle growth and film thickness reduction) has been identified before for chitosan/tripolyphosphate nanoparticles and coatings, respectively[289]. The degradation of the polymersomes via a specific cleavage of the PLL-linker by trypsin was not confirmed. This might be explained by the difficulty of the enzyme to reach the PLL layer: (Figure 7-13 (B) and/or (D)). PLL is located at the border of the polymersome compartments, between the hydrophobic PCL (C) layer and hydrophilic chitosan (A) and (E) layer (Figure 7-13). For this reason, trypsin must diffuse through the chitosan layers (A) or (C) (Figure 7-13), to reach the substrate (PLL). According to Buck et al. bovine trypsin has an isoelectric point (pI) of 10.5[290] and thus, is positively charged at pH<7.6, which is the highest pH for the degradation tests. Consequently, the enzyme is subjected to repulsive interactions with the positively charged chitosan. On the other hand, chitosanase has an isoelectric point (pI) of 9.6 and at a pH of 5.6, has therefore a net

positive charge and is still able to reduce the thickness of a coating prepared with the polymersomes[291]. An explanation for these findings is that chitosan is localized at the surface of the polymersome and thereby is easily accessible for enzymes. In conclusion, with the chitosan outer layer, the linker region is not easily accessible for proteases like trypsin. Likewise, the chitosan layer will protect any peptide in the inner compartment from degradation by trypsin or other proteases. The chitosan shell, however, can be enzymatically degraded by specialized enzymes like chitosanase. In human body, due to the lack of chitosanase, chitosan can be very stable depending on the degree of deacetylation[292].

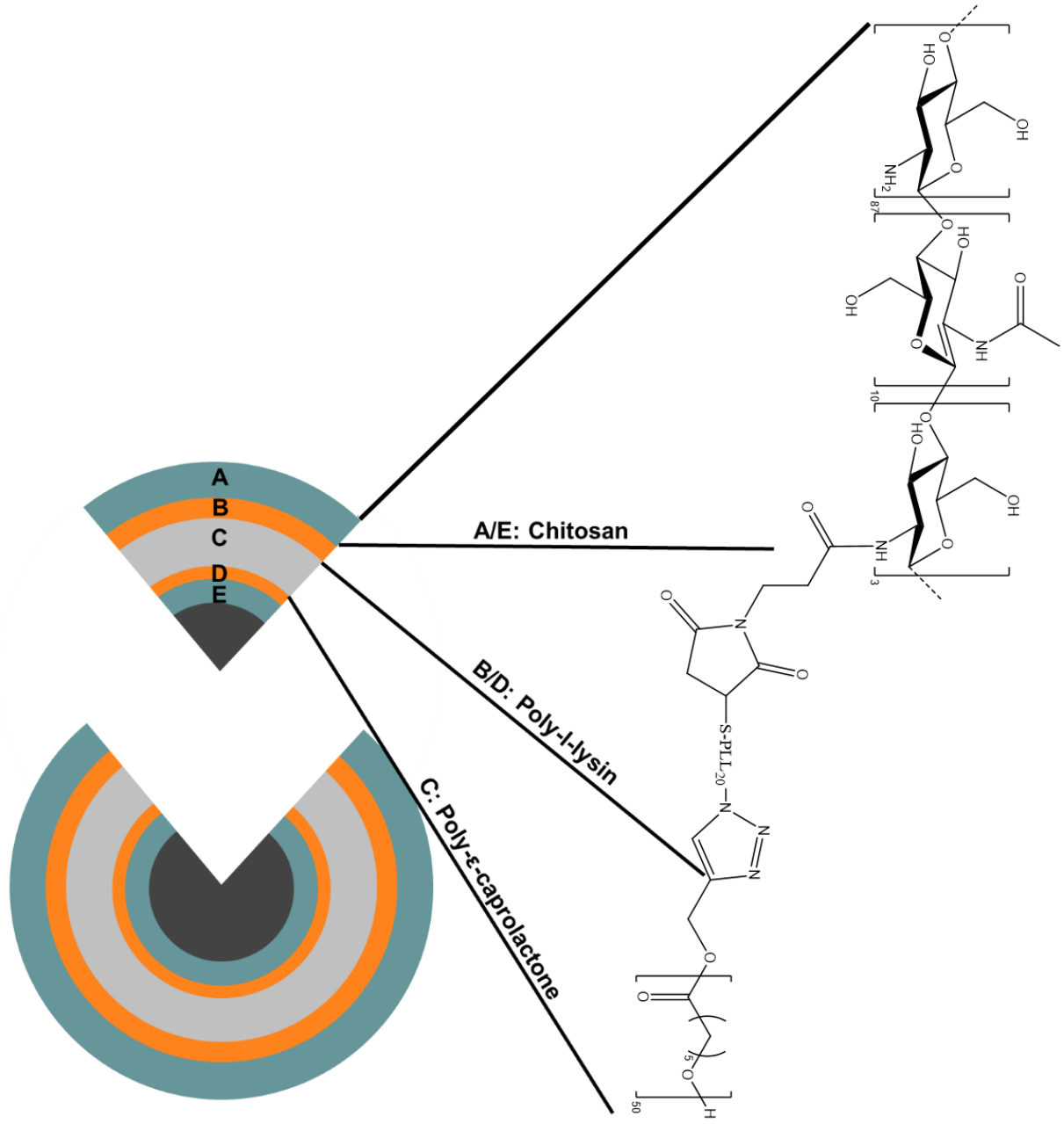

Figure 7-13 Schematic representation of polymersomes based on cryo-SEM micrographs.

7.4 Conclusion

A new amphiphilic graft-copolymer, based on two biocompatible polymers, has been synthesized. Chitosan (CS) and poly-ε-caprolactone (PCL) were linked via a peptide to form a graft-polymer, which is able to self-assemble into polymersomes, using the solvent shift method. A relationship between the particle size and the amount of hydrophobic PCL was demonstrated. This might be interesting for optimizing the encapsulation and diffusion rate of encapsulated drugs. These polymersomes were characterized via dynamic light scattering and cryo-SEM. Cryo-SEM images highlighted well-defined spherical core-shell structures. The stability of the polypeptide linker, against degradation by trypsin, was proved for both the polymersomes and the coatings prepared therefrom. The stability was attributed to the chitosan layer which cannot be penetrated by the trypsin. However, incubation with chitosanase, known for hydrolysis of chitosan, led to a degradation of the graft-polymer as indicated by an increase in particle size for the polymersomyes and a reduction of the layer thickness. To conclude, the graft-copolymer shows good stability against peptidases such as trypsin and therefore, can be used to generate a chitosanase-responsive drug delivery system against plant fungal diseases. For instance, Okazaki et al., purified chitosanase produced from the pathogenic plant fungus, *Fusarium solani* f. sp. *phaseoli*[293]. An infection of the plant by this fungus, would lead to the release of chitosanases, which can degrade the chitosan based responsive delivery system. Furthermore, the polymersome system could also be employed as a blocking layer, to control the drug release of multilayer delivery systems. However, further investigations are needed to better understand and improve the capability of the system.

8 Aginate/peptide-NPs

The scope of this study entailed the synthesis of modified ciprofloxacin in order to build an enzyme-responsive drug delivery system as described in chapter 5. The system is based on three different components: a positively charged peptide functionalized with an azide group, a modified ciprofloxacin and a negatively charged alginate. Through the positive and negative charges, the system was able to self-assemble into nanoparticle. The process is know as ionic gelation and is described in chapter 3.1.3.

Tolle et al. have described NPs that are generated through ionic gelation of negatively charged alginate and positively charged enzyme-cleavable peptide[24]. The cleavage was triggered by a specific enzyme, released during an inflammation state, inducing the release of a model substance. However, the retention of the model protein interferon β was limited and a strong burst release was observed, leading to a low encapsulation efficiency. This low yield could be explained by the complicated interplay of electrostatic and entropic forces, mediated by van der Waals interactions and hydrogen bonding, which have to be taken into account to understand the binding and release of polymeric carrier and protein[294]. Based on the promising results of inducing drug release by enzymatic cleavage of a peptide and in an effort to counter the main drawback of premature and not triggered release, this chapter presents a new enzyme-responsive alginate/peptide nanogel, in which the model drug ciprofloxacin is conjugated to the peptide linker.

Ciprofloxacin has two functional groups: carboxylic acid and piperazine, which have been used in many studies for its modification[253]. In order to graft ciprofloxacin to a peptide sequence, it has been modified, on the piperazine side, with different functional groups. More details about the modification of ciprofloxacin on the piperazine side is described in chapter 5.4.

As the conjugation of ciprofloxacin may affect its antibacterial efficacy, the conjugated ciprofloxacin **5** and other derivatives of ciprofloxacin (**11, 12b**, **13b** and **14b**, Figure 8-1) were tested for their antimicrobial activity against *Staphylococcus aureus*. S. aureus was used because it is one of the pathogens that often caused orthopedic implant-associated infections[295].

At first, ciprofloxacin was modified with a terminal alkyne moiety by alkylation (Figure 8-1, **5**), which allow conjugation with PLL or other peptides via copper(I) catalyzed 1,3 dipolar cycloaddition leading to a 1,2,3-triazol link. Then, to propose a copper click free chemistry strategy, ciprofloxacin was modified with a cyclooctyne function (Figure 8-1,

7). A 6-aminohexanoic acid linker has also been integrated between the ciprofloxacin and the cyclooctyne to reduce any sterical hinderance, which could affect the antimicrobial efficacy (Figure 8-1, **10**).

Subsequently, the modified drugs were linked to different peptide sequences. Since this was an early-stage study, PLL was used as an enzyme cleavable peptide sequence to identify the ability of conjugated peptide **11** to generate nanoparticles with alginate. The literature suggests that non-conjugated PLL has the capacity to generate NPs with alginate[24].

Finally, several moieties were conjugated to ciprofloxacin to study the effect of the resulting triazol link on drug efficacy. Compound **10** was used to graft a peptide sequence and to synthesize **12b** (Figure 8-1). This peptide would represent the part which remains on the active ingredient after release from the encapsulation system, generated with the peptide described in chapter 5.2 and 5.3. Therefore, by testing the antimicrobial activity of **12b** (Figure 8-1), the final active ingredient released from the drug delivery system can be analyzed. More details about the cleavage site of the peptide sequence can be found in chapter 5.2 and 5.3.

Then, two other moeities: polyethylene glycol and homoalanine, respectivily compound **13b** and **14b** (Figure 8-1), were grafted onto ciprofloxacin. Both molecules were used to understand the relation between modification and antimicrobial efficacy.

Particle size, enzymatic degradation, and drug release were studied by DLS measurements and ultraviolet-visible spectroscopy (UV-Vis). UV-Vis was performed to determine the amount of ciprofloxacin released during the degradation process. The NP suspension was used to coat titanium substrates, a material commonly employed for dental implants. Ellipsometry was carried out to measure the layer thickness and degradability of the coating. Finally, the antimicrobial efficacy of conjugated CIP was tested in cooperation with partners at Hannover Medical School.

Part of the results described in this chapter have been published: Bourgat, Y.; Mikolai, C.; Stiesch, M.; Klahn, P.; Menzel, H. Enzyme-Responsive Nanoparticles and Coatings Made from Alginate/Peptide Ciprofloxacin Conjugates as Drug Release System. Antibiotics (2021). DOI: 10.3390/antibiotics10060653.

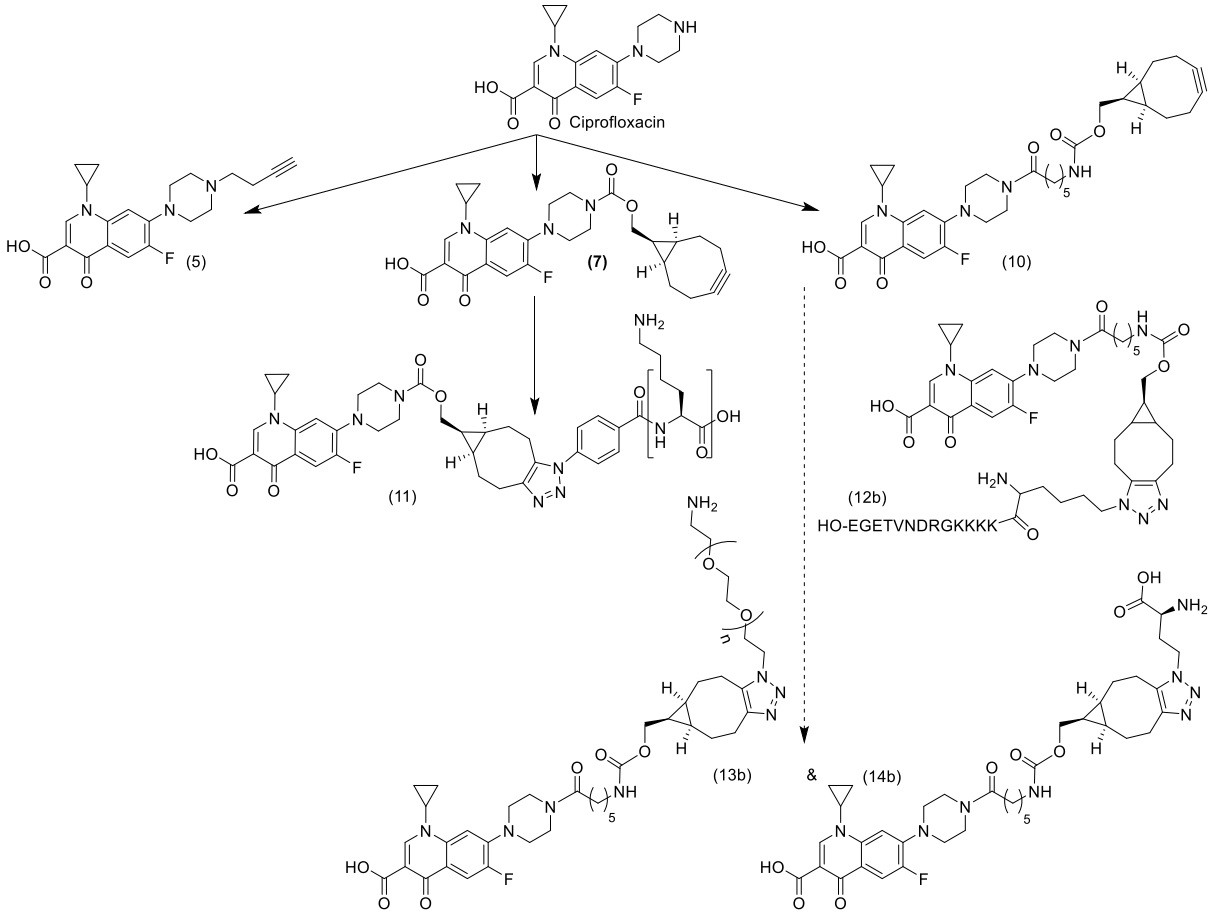

Figure 8-1 General overview of the synthesis of modified ciprofloxacin.

8.1 Alkyne-functionalized Ciprofloxacin 5

As described in chapter 5, many ciprofloxacin derivatives, with diverse properties, have been developed via the modification on the carboxylic acid or piperazine function[251]. As mention in chapter 5.4, if these the carboxylic acid is chemically modified or removed, the antimicrobial activity is strongly reduced[253]. However, modifications at the piperazine ring via alkylation or acylation can result in highly active derivatives [251,255]. Therefore, the conjugation was carried out by modification of the piperazine ring.

In this study new ciprofloxacin derivatives have been synthesized and linked to different peptide linkers. In order to specifically link azide functionalized peptides, ciprofloxacin was modified with alkyne function. Both peptide and ciprofloxacin can then be linked via copper click chemistry. Indeed, as mentioned previously, click chemistry is an extremely chemoselective reaction and can therefore be used to specifically link two molecules [224][225][226]. The antimicrobial efficiencies of conjugated ciprofloxacin derivatives were then tested on *S. aureus,* to study the effect of the modification.

Synthesis of alkyne modified ciprofloxacin (CIP-alkyne) 5

Herczegh et al. described the synthesis of 1-hydroxybisphosphonate derivatives of ciprofloxacin (CIP), gatifloxacin and moxifloxacin, synthesized by using Cu(I) catalyzed azide-alkyne through a 1,3-dipolar cycloaddition reaction[296]. The 1,2,3-triazol derivative of CIP exhibited antibacterial activity, comparable to the parent antibiotic. Therefore, alkyne modified CIP **5** has been considered as a strong candidate and synthesized, with the aim of conjugating CIP to the peptide sequence through a 1,2,3-triazol link.

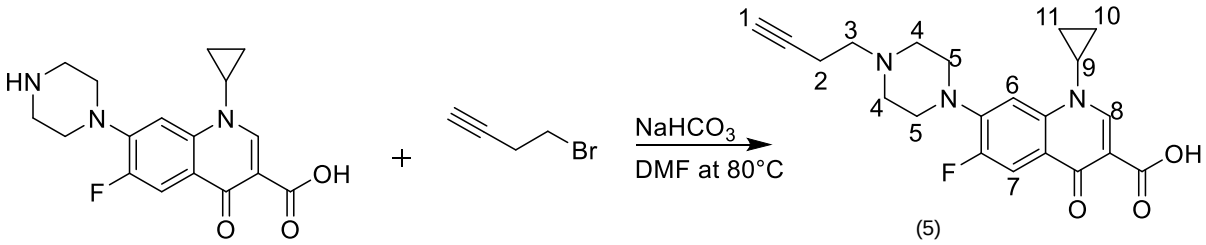

*Figure 8-2 Reaction scheme of CIP-alkyne **5** with numbered protons.*

Mechanism for the synthesis of 5 (Figure 8-3)

According to Herczegh et al., the synthesis required an alkylation between the amine of CIP and or 4-Bromo-1-butyne[297]. More details about the synthesis conditions can be found in the experimental part of chapter 10.6.1.

As mentioned above, the alkylation of CIP is a nucleophilic substitution (Type Sn2). The nucleophilic amine attacks the carbon next to the bromide (Figure 8-3, **a**) and the bromide is then displaced to form an ammonium salt intermediate (Figure 8-3, **b**). Finally, the ammonium salt intermediate is deprotoned by a base $(NaHCO)_3$, yielding the final product **5**.

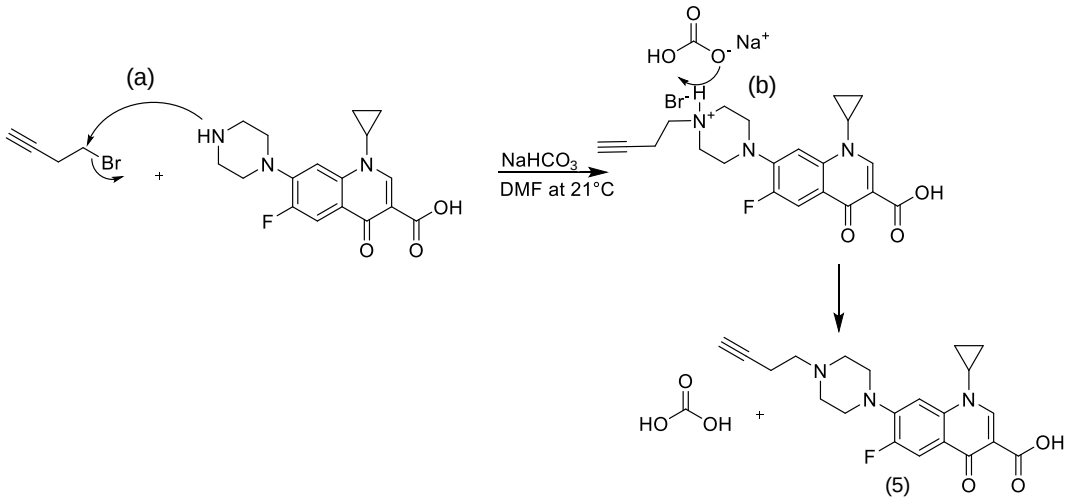

Figure 8-3 Reaction mechanism of ciprofloxacin alkylation.

Characterisation of 5

^{1}H-NMR was performed to confirm the synthesis success. Numbers have been assigned to each protons in order to facilitate the characterization (Figure 8-2). The signals at 8.7, 7.96, 7.3, 3.48, 3.38-3.28, 2.8-2.7, 1.38-1.27, and 1.14 ppm represent the framework protons of CIP (Attached file 6). Moreover, the presence of five protons at 2.25 (H2), 2.39 (H3), and 1.95 (H1) ppm confirmed the presence of the grafted butyne.

Hence, after this successful synthesis, efficacy tests have been performed on molecule **5**. The CIP derivative **5** exhibited antibacterial activity, comparable to commercial ciprofloxacin. For concentration ranging from 1.7 to 13.3 µg/mL, a bacterial growth of 0% was observed.

8.2 Synthesis of modified CIP for copper-free click chemistry

As previously described, ciprofloxacin was modified with an alkyne in order to link it to the peptide via Cu(I) catalyzed cycloaddition. The reaction between **5** and PLL_9-N_3 has been tested, but the copper catalyst could not be fully removed from the product. Indeed, copper ions forms very stable complexes with peptides. For instance, Ottaviani et al. studied PLL dendrigraft-Cu(II) complexes, which are of particular interest for their application in bio catalysis[298]. However, the copper is antibacterial and cytotoxic and mediates the generation of reactive oxygen species[299][300], therefore any activity tests or further investigation with copper containing samples are not meaningful.

Cyclooctynes are reported to react selectively with azides without any copper(I) catalyst avoiding cytotoxic effect of copper(I) in the product[301]. Therefore, it has been selected to be grafted onto ciprofloxacin to link an azide-functionalized peptide via Copper-free click chemistry.

Influence of the modification on the antimicrobial efficacy, has been studied by synthezising different ciprofloxacin derivatives, one with (**10)** and one whitout (**7)** linker in between cyclooctyne and ciprofloxacin (Figure 8-1). The aim of the linker was to minimize the risk of reducing efficacy by separating the bulky triazole-cyclooctyne bond and the ciprofloxacin.

8.2.1 Cyclooctyne-functionalized ciprofloxacin without linker **7**

The synthetic route for the preparation of the ciprofloxacin derivative **7** to enable the link with poly-L-lysine is depicted in Figure 8-4. (1R,8S,9S)-bicyclo[6.1.0]non-4-yn-9-

ylmethanol (BCN-OH) was reacted with *p*-nitrophenyl chloroformate in the presence of pyridine (Figure 8-4, **step 1**) to obtain the *p*-nitrophenyl carbonate **6**. Subsequently, the BCN-moiety was installed at the free amino function of ciprofloxacin by reaction with the *p*-nitrophenylcarbonate **6** in the presence of *N*-methyl morpholine (NMM) as a base to form compound **7** (Figure 8-4, **step 2**).

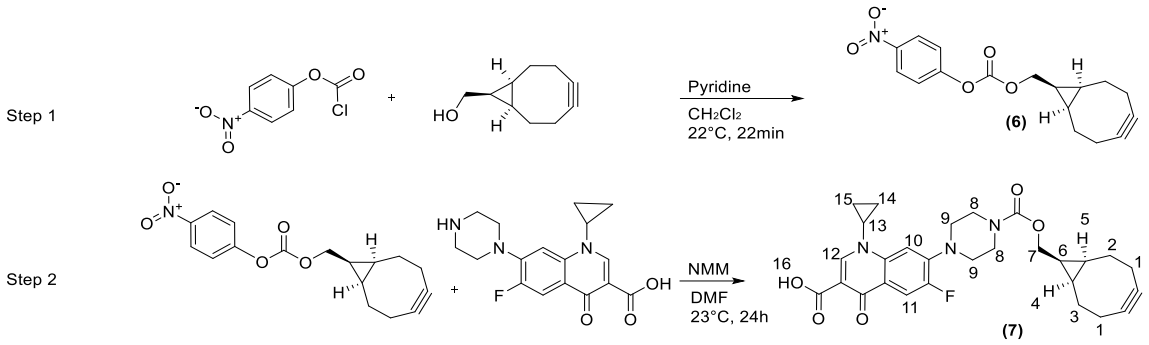

*Figure 8-4 Reaction scheme of cyclooctyne-functionalized ciprofloxacin **7** with numbered protons.*

Mechanism of step 1

The first step of the mechanism (Figure 8-5) involves a nucleophilic attack of pyridine on the positive carbon atom of the acyl chloride (Figure 8-5, **I**) (Schotten-Baumann conditions). Known for its basicity, pyridine is also an excellent nucleophile. In fact, pyridine is more nucleophilic than the alcohol and therefore, rapidly attacks the acyl chloride. Subsequently, a displacement of the chloride occurs, leading to a highly electrophilic intermediate (Figure 8-5, **a**), which undergoes a nucleophilic attack by the alcohol (Figure 8-5, **II**), a deprotonation by a pyridine (Figure 8-5, **III**), and a displacement of the pyridine (Figure 8-5, **IV**), forming the final carbonate ester **6**.

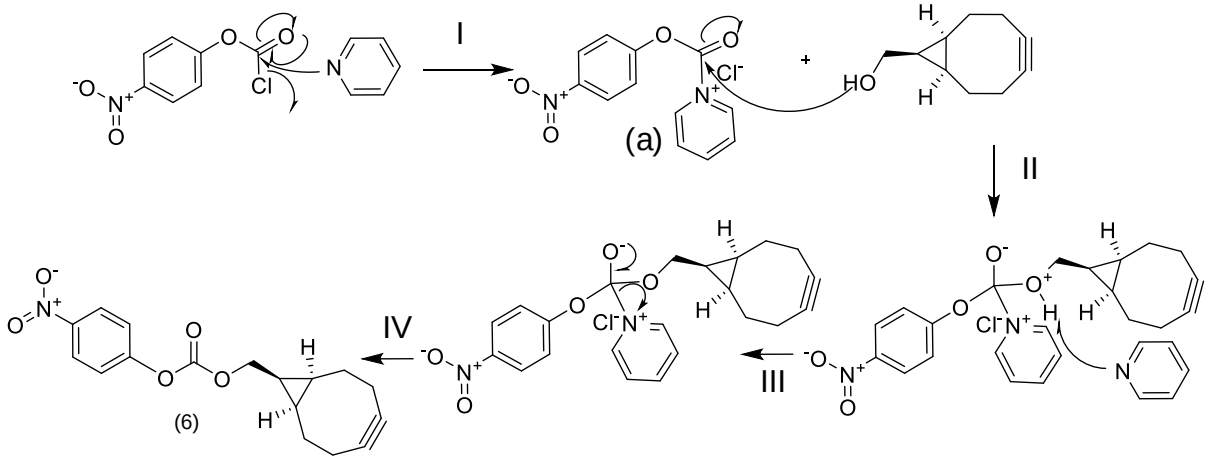

*Figure 8-5 Reaction mechanism of BCN-O(CO)O(4-NO2-Ph) **6**.*

Characterization of 6

The ^{1}H-NMR was consistent with previous work[302], and all signals could be assigned to the corresponding protons (Attached file 7).

Mechanism of step 2

Ciprofloxacin was functionalized with a bicyclooctyne through a reaction between the amine of ciprofloxacin and the carbonate ester **6** (Figure 8-4, **step 2**). In order to avoid thermal degradation of the BCN moiety, ciprofloxacin was first dissolved at 82°C and the solution cooled down to 23°C before the compound **6** was added.

The mechanism of **step 2** (Figure 8-4), can be described as follow: it involves a nucleophilic attack of the ciprofloxacin amine on the positive carbon of the carbonate **7** (Figure 8-6, **I**). Next, a deprotonation by N-methylmorpholine (Figure 8-6, **II**) occurs, and finally, elimination (Figure 8-6, **III**) of the nitrophenyl group occurs to generate the final product **7**. Flash chromatography through silica gel was performed to purify the residue.

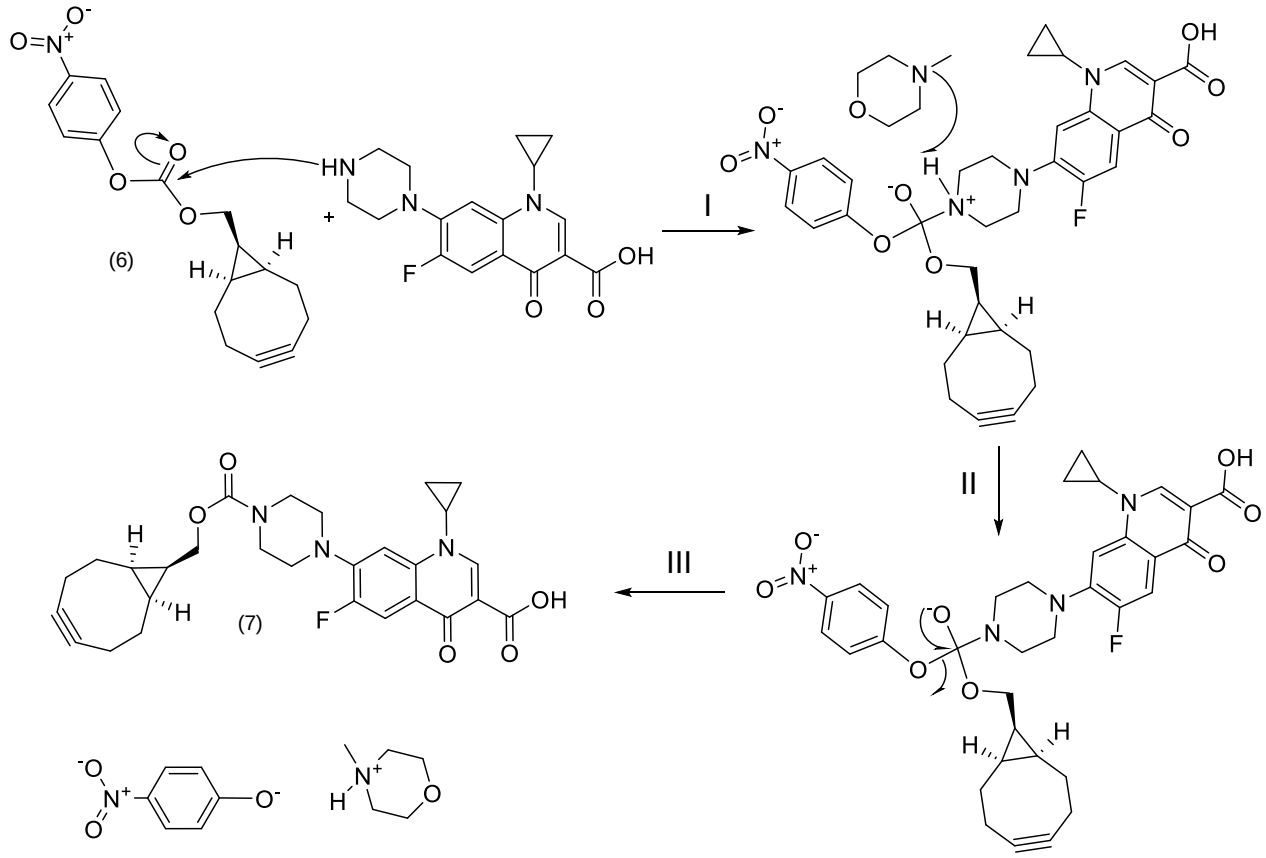

*Figure 8-6 Reaction mechanism of BCN-O(CO)HN-CIP **7**.*

Characterization of 7

^{1}H-NMR spectroscopy was performed to prove the reaction and the structure of compound **7**. Numbers have been assigned to each protons in order to facilitate the characterization (Figure 8-4). In ^{1}H-NMR spectra of the product, the signals of ciprofloxacin and bicyclooctyne proton were detected, which demonstrates the successful synthesis of the compound **7** (Attached file 8**)**. The signals at 8.67 (H12), 7.92 (H11), and 7.29 (H10) ppm represent the quinolone framework protons of ciprofloxacin. The presence of a doublet at 4.17 (H7) ppm confirmed the presence of BCN moiety. Moreover, four protons of the nitrophenyl-leaving group disappeared. Finally, the expected number of protons and their signal correlations were also determined (Attached file 8). Electrospray Ionisation Mass Spectrometry (ESI-MS) was used to further confirm the synthesis. Peaks were found at 508.22, 530.20, and 1037.42 m/z, which represent the following ions: $[M + H]^+$ = 508.22 m/z, $[M + Na]^+$ = 530.20 m/z, $[2M + Na]^+$ = 1037.42 m/z. M represents the calculated mass for $C_{28}H_{30}FN_3O_5$ = 507.22 g/mol.

The predominant ions observed were $[M + Na]^+$ and a dimer species. McNair et al[303] have studied pseudo-molecular ion formation, in electrospray ionization mass spectrometry (ESI-MS), of six anti-inflammatory pharmaceuticals with similar functionality as in ciprofloxacin. Some of the compounds were able to form dimers, during the measurement, through the interaction of their carboxylic acid function and sodium ion. This behavior was observed during ESI-MS measurements of ciprofloxacin **7**.

8.2.2 Cyclooctyne-functionalized ciprofloxacin with spacer **10**

The synthesis route of cyclooctyne-functionalized ciprofloxacin with spacer **10** is illustrated in Figure 8-7. The compound **9** was first synthesized through nucleophilic attack of the ciprofloxacin amine on the 6-((tert-butoxycarbonyl)amino) hexanoic acid (Boc-6-Ahx-OH), in presence of the phosphonium salt PyAOP, Trimethylsilyl chloride (TMSCl) and N,N-Diisopropylethylamine (DIPEA) (Figure 8-7, **step 1**). PyAOP salt is a coupling reagent mainly used in peptide synthesis to activate the reaction between amine and carboxylic acid. Then, the tert-Butyloxycarbonyl protecting group of Boc-6-Ahx-OH was cleaved, by trifluoroacetic acid, to obtain the compound **9** (Figure 8-7, **step 2**). Subsequently, the BCN-moiety was installed at the free amino function of ciprofloxacin **9** by reaction with the *p*-nitrophenylcarbonate **6** in the presence of NMM as a base to form compound **10** (Figure 8-7, **step 3**).

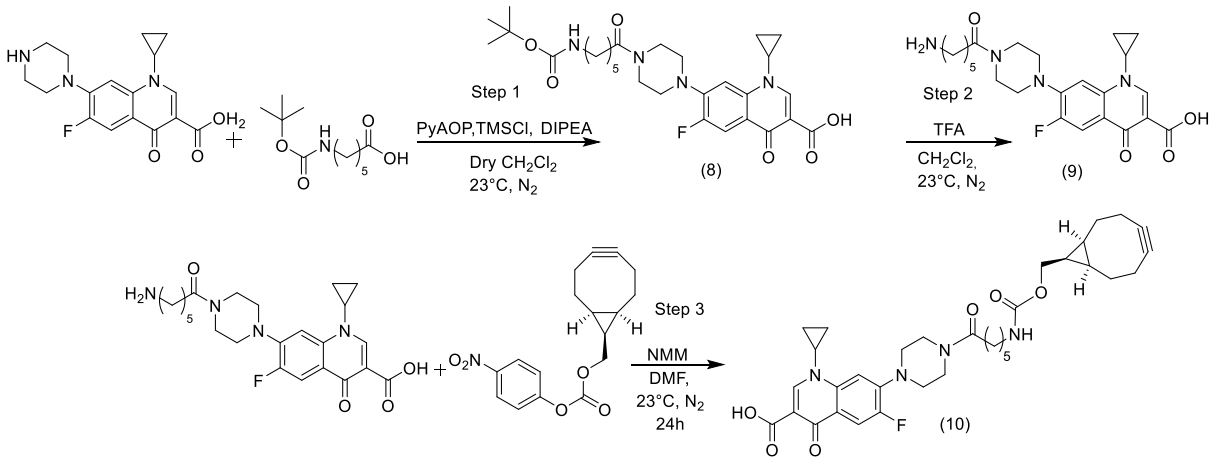

Figure 8-7 Reaction scheme of cyclooctyne-functionalized ciprofloxacin with spacer.

Mechanism of step 1 and step 2 (Figure 8-7)

The mechanism involves a deprotonation of the carboxylic acid before it undergoes a reaction with the phosphonium salt PyAOP. Subsequently, a nucleophilic attack of oxybenzotriazol **(a)** (Figure 8-8) takes place, forming an activated ester **(b)** (Figure 8-8). Ciprofloxacin was separately mixed with a base and trimethylsilyl chloride (TMSCl) to protect the carboxylic acid and avoid any side reactions. Then, the protected ciprofloxacin was added to the compound **(b)** (Figure 8-8) to undergo a nucleophilic attack, after which the elimination of the oxybenzotriazol group yields the product **8** (Figure 8-7, **step 1**). The final product **9** was obtained through deprotection of Boc-protected amines using trifluoroacetic acid (Figure 8-7, **step 2**). More details about the synthesis can be found in the experimental part in Chapter 10.6.1. Mechanism to form compound **10** (Figure 8-7, **step 3**) can be described by the mechanism presented in Figure 8-6. The synthesis was performed under the same conditions as the synthesis of compound **7**.

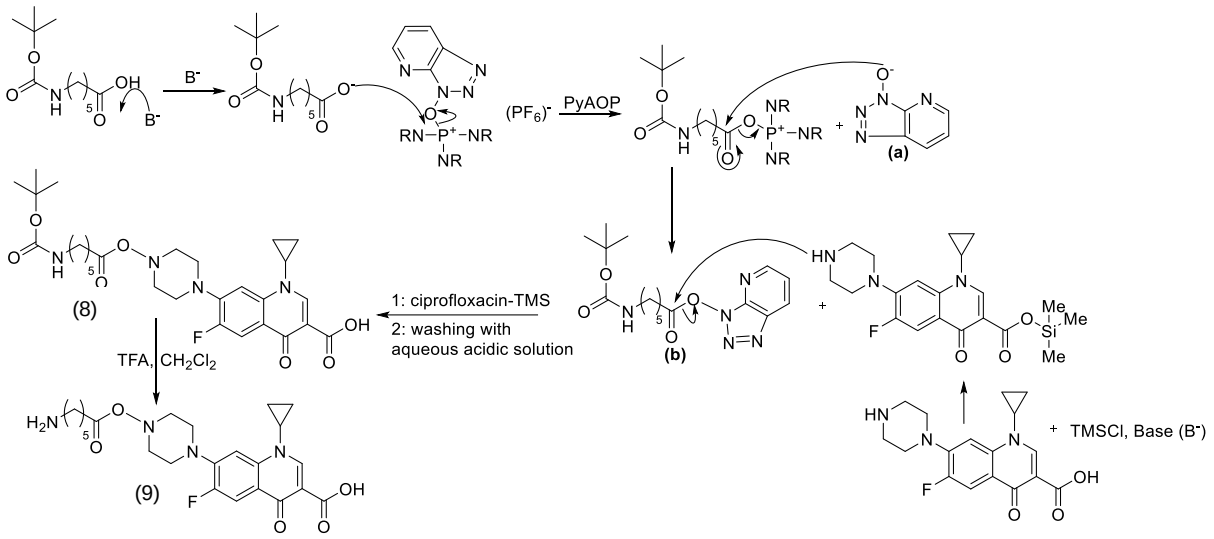

*Figure 8-8 Reaction mechanism of **9**.*

Characterization of 9

The ^{1}H-NMR spectrum was used to identify signals of ciprofloxacin and 10 protons that match with the protons of the linker (Attached file 10). The deprotection of tert-Butyloxycarbonyl protecting group was proven by the disappearance of methyl protons at 1.36-1.56 ppm. All signals could be assigned to the corresponding protons and can be found in Attached file 10.

Characterization of 10

The ciprofloxacin derivate **10** was analyzed and validated using various NMRs, heteronuclear multiple bond correlation (HMBC, Attached file 16), heteronuclear single quantum coherence (HSQC, Attached file 15), correlation spectroscopy (COSY, Attached file 13), nuclear Overhauser effect spectroscopy (NOESY, Attached file 14) and ^{1}H-^{15}N heteronuclear multiple bond correlation (NH-HMBC, Attached file 12). Besides conventional ^{1}H-NMR analysis, two-dimensional NMR methods were used to clearly confirm the structure of the molecule. Indeed, those analyses revealed the correlation between protons, carbons, proton-carbon and nitrogene-proton, which helps to define the structure of complex molecules. Numbers have been assigned to each protons in order to facilitate the characterization (Figure 8-9).

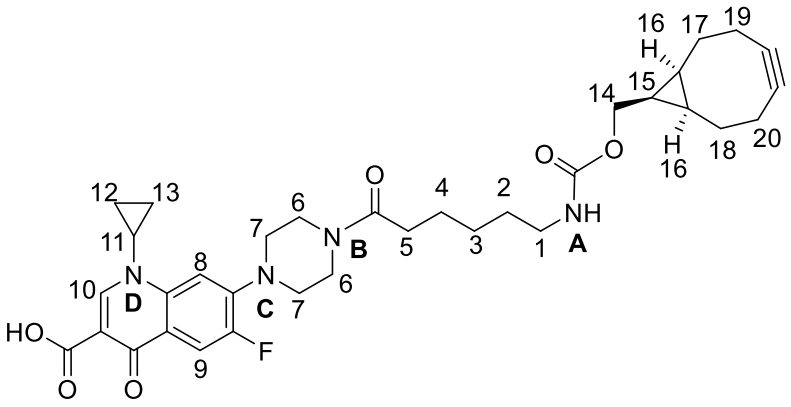

*Figure 8-9 Chemical structure of **10** with numbered protons.*

NH-HMBC was used to identify the signal of the NH proton at 7.00 ppm (Attached file 12). COSY (Attached file 13) was performed to reveal the direct correlation between NH (A) and the proton H1 at 3.11 ppm. H1 correlates to the signal at 1.52 ppm, which corresponds to H2. Protons H3 to H5 were identified by their direct correlation. The next challenge was to find a correlation between H5 of the grafted linker and H6 belonging to ciprofloxacin. NOESY (Attached file 14) was used to identify the correlation of H5 with four protons representative of H6 protons, which have a direct correlation with four other protons, expected to be H7. This proposition was supported by the correlation of H7 with a doublet at 7.73 ppm, representing the proton H8 (NOESY). Furthermore, proton H8 was correlated with two nitrogens, (C) and (D). (C) was correlated with H6 and a doublet at 7.97 ppm (H9). (D) was correlated with three unidentified signals at 8.74, 1.45 and 1.33 ppm (NH-HMBC, Attached file 12). According to the literature, 8.74 ppm represents proton H10. The signals at 1.45 and 1.33 ppm have a direct correlation with a proton at 3.94 ppm, which was expected to be H11[304]. The signals at 1.45 and 1.33 ppm, respectively, were determined to represent H13 and H12. HSQC (Attached file 15) and HMBC (Attached file 16) were used to identify the correlation between protons H1 and H14. The latter is part of the bicyclooctyne moiety. HSQC was used to identify the direct correlation of proton H1 with carbon at 41.90 ppm. Furthermore, HMQC was utilized to reveal a correlation between H1 and the carbon at 158.18 ppm; because no direct correlation with any protons was identified, it was speculated to be the carbon of the carbamate link. Moreover, the signal at 158.18 ppm correlates with the doublet at 4.09 ppm, standing for a methyl group. It was suspected to be the proton H14 of the BCN moiety. Furthermore, a correlation between the signals at 4.09 (H14) and 1.31 ppm indicated

the proton H15. The proton H15 correlates with two protons at 0.89 ppm, and they were expected to be H16. The latter directly correlates with protons at 1.56 and 2.17 ppm, representing H17 and H18. In addition, protons at 1.56 ppm correlate with the signals at 2.17 and 2.25 ppm, standing for H19 and H20. The correlation between the protons H18 and H19-H20 cannot be clearly defined. Finally, HMBC was used to reveal the correlation between protons H19-H20 and carbons at 100.25, which are not directly correlated with any proton. These carbons, appeared in the shifting range of triple bonds of cyclooctynes[87], and clearly demonstrated the successful synthesis of **10.**

Electrospray Ionisation Mass Spectrometry (ESI-MS) was used to further confirm the synthesis. Peaks were found at 333.14, 643.29, 1263.59, and 1574.24 m/z, which represent the following ions: $[M + Na]^+$ = 333.14 m/z (z = 2), $[M + Na]^+$ = 643.29 m/z (z = 1), $[M + Na]^+$ = 1263.59 m/z (z = 1/2) and $[M + Na]^+$ = 1574.24 m/z (z = 1/3). M represents the calculated mass for $C_{35}H_{43}FN_4O_6$ = 620.3 g/mol.

The predominant ions observed were $[M + Na]^+$ = 643.29 m/z (z = 1) and a dimer species $[M + Na]^+$ = 1263.59 m/z (z = 1/2). McNair et al[303] have studied pseudo-molecular ion formation in electrospray ionization mass spectrometry (ESI-MS) of six anti-inflammatory pharmaceuticals with similar functionalities found in ciprofloxacin. During the measurement, some of the compounds were able to form dimers through the interaction of their carboxylic acid function and a sodium ion. This behavior is observed during ESI-MS measurements of ciprofloxacin derivative **10**.

8.3 Synthesis and analysis of peptide conjugated ciprofloxacin

In this study, PLL_9 **11** or KKKKGRDNVTEGE **12a** peptide sequences and molecules such as polyethylene glycol **13a** or homoalanine **14a** were grafted onto ciprofloxacin (Figure 8-1). The goal was to analyse the feasability of the system and to have a deeper understanding on why the grafting is affecting the antimicrobial efficacy of ciprofloxacin. Further details can be found in each concerned parts below.

8.3.1 General mechanism of copper-free click chemistry

Molecules **11**, **12b**, **13b**, and **14b** were all synthesized through the same type of reaction, called 1,3-dipolar cycloaddition, between a cyclooctyne and an azide function. The reaction occurs rapidly and selectively due to ring strain in the cyclooctyne function. Moreover, in comparison with the copper-catalyzed Huisgen cycloaddition, copper-free click chemistry is an attractive approach to click chemistry that is free of cytotoxic transition metal catalysts [301].

It is known that the stability of cyclic alkynes decreases with decreasing ring size. This is because the stability is directly correlated with the C-C≡C-C bond angle. In the cyclic alkynes, the ideal angle of sp-hybridized carbons is 180°. As shown in Figure 8-10, the angles of C-C≡C-C increases with the ring size, leading to more stable compounds.

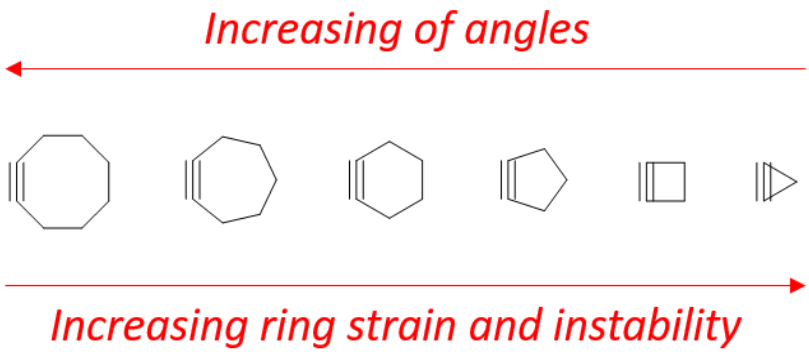

Figure 8-10 Stability of cycloalkynes

Cyclooctyne has a good balance between stability and reactivity. The ideal bond angle of 180° cannot be adopted for cyclooctyne (Figure 8-11, **a**). For this reason, it has a high ring strain and thus, instantly reacts with azide functions to generate a triazole bond. The newly formed double bond (Figure 8-11, **b**) exhibited a stable bond angle of 120°, which is ideal for sp^2-hybridized carbons. Therefore, the reaction is strain-promoted.

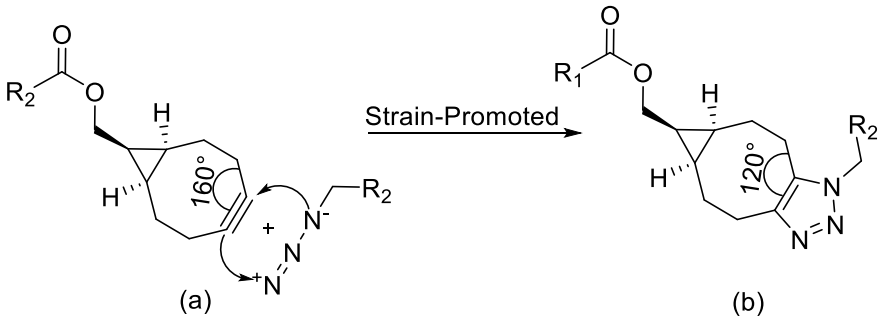

Figure 8-11 Reaction mechanism of copper-free click chemistry

8.3.2 Synthesis and analysis of poly-L-lysine-ciprofloxacin **11**

The aim of this study is to synthesize a peptide, which has the ability to link a bioactive substance and to generate nanoparticles, with alginate, through ionic gelation. Therefore, in the presentation of the peptide design (chapter 5.2, Figure 5-3), lysine units have been integrated which can bear positive charges. Since this was a

preliminary study, a single PLL sequence was used to link ciprofloxacin and develop nanoparticles with alginate. Hence, the hindrance of the conjugated drug to produce the nanoparticle could be identified with this experiment.

As described and explained in chapter 5, copper-free click chemistry was implemented to link poly-L-lysine to ciprofloxacin. The reaction described in Figure 8-12, instantly occurs between the azide function of poly-L-lysine and the cyclooctyne function of ciprofloxacin derivative **7**.

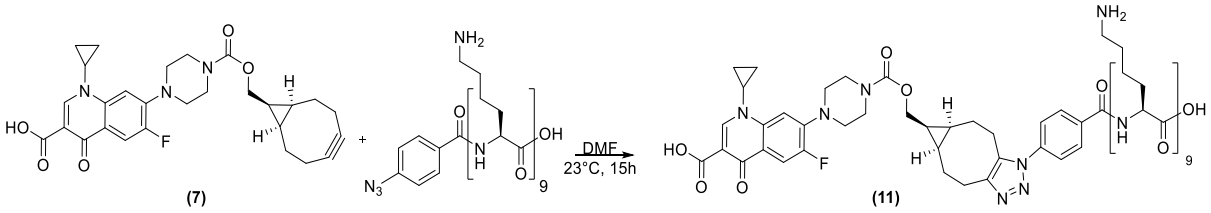

*Figure 8-12 Reaction scheme of CIP-PLL **11**.*

8.3.2.1 Characterization of ciprofloxacin-poly-L-lysine **11**

^{1}H-NMR (Attached file 27), FT-IR, and UV-Vis were used to characterize compound **11**. Numbers have been assigned to each proton in order to facilitate the characterization (Figure 8-13). ^{1}H-NMR spectra revealed the presence of protons which can be assigned to ciprofloxacin and poly-L-lysine. Protons H8, H7, H6, and H10/H9 belong to ciprofloxacin and the signal at 1.87-1.25 ppm represented protons of PLL (H3/4 and H5).

In addition, FTIR of PLL_9-N_3 and Poly-L-lysine-Ciprofloxacin was performed to prove the disappearance of the signal at 2121 cm^{-1}, which belongs to the reacting azide of PLL_9-N_3 (See Attached file 28). Finally, UV-Vis was used to confirm the presence of ciprofloxacin. An absorption peak was observed at 278 nm, which is characteristic for ciprofloxacin. The measurements proved the synthesis of compound **11**. Compound poly-[L-lysine]$_9$ conjugated ciprofloxacin **11** was then used with alginate to demonstrate the ability of conjugated peptide to generate nanoparticle.

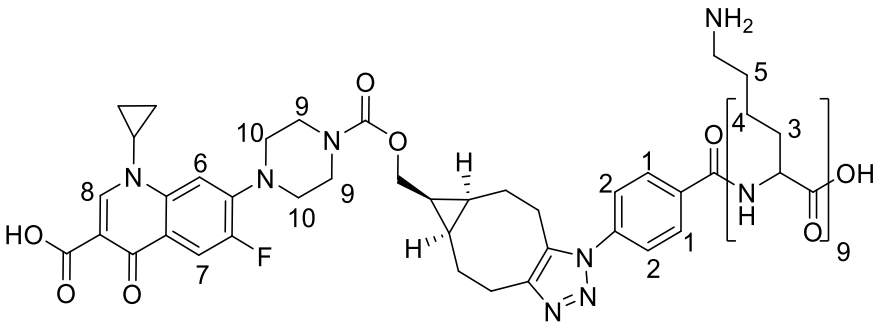

*Figure 8-13 Chemical structure of **11** with numbered protons.*

8.3.2.2 Alginate/Peptide-Ciprofloxacin Nanoparticles

Nanoparticle formation and characterization

Similar to chitosan/TPP nanoparticles system, the alginate/peptide-ciprofloxacin nanoparticles were formed by ionic gelation in an aqueous solution by mixing a solution of purified alginate and PLL-ciprofloxacin **11**. More information can be found in the experimental part (chapter 10.6.3). In the final system, as described in chapter 5, L-lysine residues will be integrated at both sides of the NVTEGE↓ALGSV peptide sequence. Due to ionic interactions between the components (lysine and alginate), they were able to self-assemble into nanoparticles. As described in chapter 3.1.3, various parameters such as the PLL-ciprofloxacin/alginate ratio, the pH, and the concentration influenced the particle formation. The influence of the PLL-ciprofloxacin/alginate ratio was tested by mixing a solution of **11** and alginate at different ratios. The concentration of both solutions was fixed at 1 mg/mL in deionized H_2O. Dynamic light scattering measurements were used to determine particle sizes. PLL-ciprofloxacin/alginate ratios of 1:4, 1:3, 1:2 and 1:1 were tested (Figure 8-14).

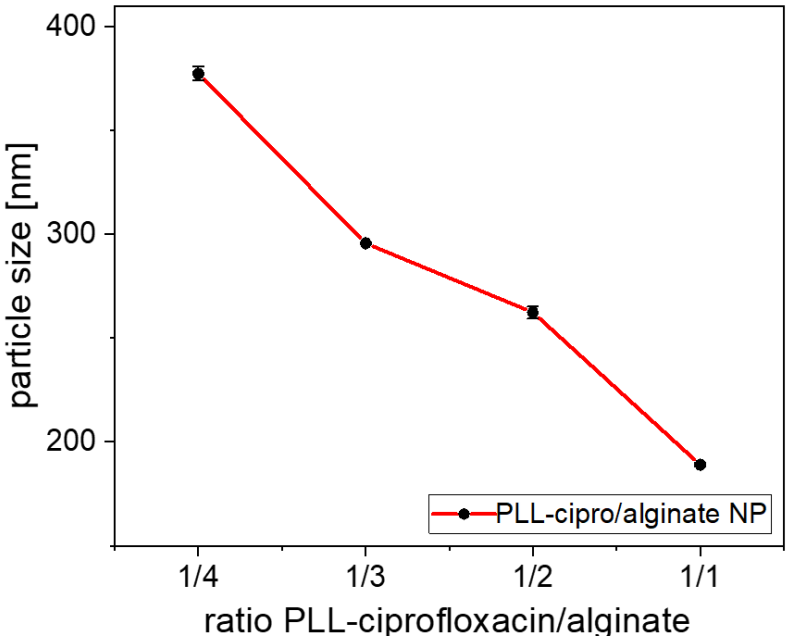

Figure 8-14 Dependence of the size of nanogels prepared with different PLL-ciprofloxacin/alginate ratios at RT in deionized water.

In all cases, monomodal particles-size distributions were obtained. As shown in Figure 8-14, the size decreased as the amount of PLL increased. Indeed, it is known that the size of the particle is influenced by different parameters such as concentration of the polycation and the polyanion [63]. Giri et al.[305] explained that ionic gelation is based on the capability of polyelectrolytes to generate crosslinks with respective counter ions to form nanoparticles. In this case, PLL acts as a cross-linker to bind the alginate chains to each other. At the same time PLL compensates the negative charges of alginate. Therefore, by increasing the amount of positive PLL, negative charges are compensated and the repulsive force inside the system is reduced. The direct consequence is a decrease of the particle size.

The polydispersity index for 1:4, 1:3, 1:2, and 1:1 mixtures were found to be 0.488, 0.225, 0.247, and 0.171, respectively. It is clear that the PDI tends to decrease with an increasing amount of polycation. This behavior has been observed by Hiorth et al. with Zn2+as polycation[306]. This might be explained by the transition from free alginate to cross-linked alginate chains. In order to maximize the cost effectiveness while keeping a low polydispersity index for the NP a ratio of 1:3 was chosen to perform the stability and degradation tests. The stability was tested by incubating the nanoparticles for 50 h at 37 °C inin phosphate buffered saline (Figure 8-15).

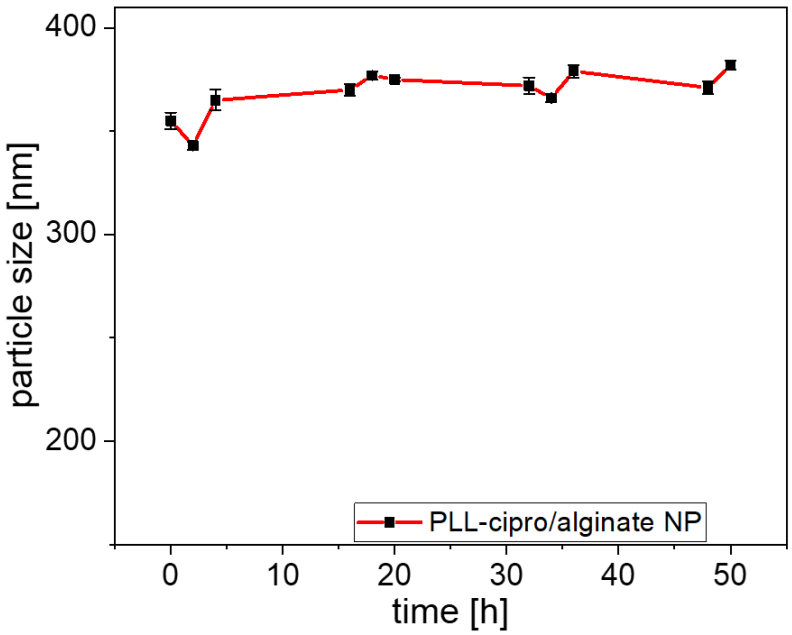

Figure 8-15 Size of the nanoparticles (PLL-ciprofloxacin/alginate 1-3) as function of incubation time in phosphate buffer saline (pH 7.4) at 37°C. The particle size for the 1-3 mixture here was somewhat higher because of the buffer and the higher temperature.

Due to the different conditions (pH, temperature, and salt concentrations) the particle size for the 1-3 composition was somewhat higher than in the previous experiment (Figure 8-15, 355 nm instead of ~300nm). There was a slight further increase in particle size from 355 to 380 nm. However, in general the stability of the nanoparticles was confirmed.

Enzymatic degradation of nanoparticles

The degradability and release of ciprofloxacin were tested by incubating the system with trypsin (2.5 µg/mL). This enzyme is known to cleave PLL sequences[209]. The incubation led to a substantial increase in particle size (Figure 8-16). As was shown in Figure 8-14, a decrease in the amount of poly-L-lysine, thus a reduced PLL to alginate ratio led to an increase in nanoparticles size. Indeed, during incubation, trypsin converted PLL into monomer moieties, reducing the PLL concentration and as a direct consequence an increase in nanoparticle size was observed.

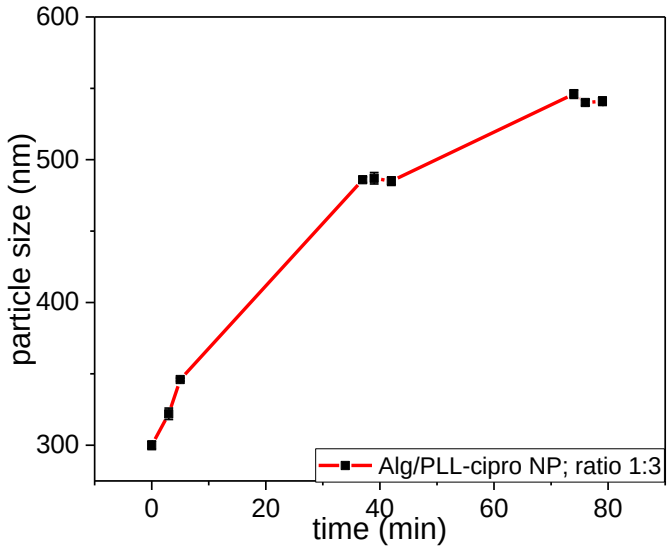

Figure 8-16 Size of the nanoparticles (PLL-ciprofloxacin/alginate 1/3) as function of incubation time in phosphate buffer saline (pH 7.4) at 37°C after addition of trypsin (final concentrations of 2.5 µg/mL).

Release study of Ciprofloxacin from nanoparticles

The triggered release of ciprofloxacin by cleavage of the peptide sequence was confirmed by the following investigations. Different suspensions of nanoparticles were incubated with trypsin in PBS at 23°C and dialyzed to filtrate the solutions. The aim was to remove the non-degraded particles and to extract the released ciprofloxacin. The dialysate was investigated by UV-Vis to quantify the ciprofloxacin at 278 nm. To study the influence of trypsin, the experiment was tested with different concentrations (Figure 8-17). With regard to the incubation without trypsin (Figure 8-17, blue curve), a small amount of the conjugated ciprofloxacin **11** remained unbound in the solution and therefore was detected in the dialysate. However, incubation with 2 µg/mL and 5 µg/mL of trypsin (Figure 8-17) induced a strong increase of the ciprofloxacin concentration. During the process, PLL is degraded, causing the release of conjugated ciprofloxacin from the nanoparticle. Incubation with higher trypsin concentration led to quicker degradation (Figure 8-17, black symbols) and confirmed the possibility of controlling the drug release. The nanoparticle suspensions was then used to coat the surface of titanium plates, which is a common implant material.

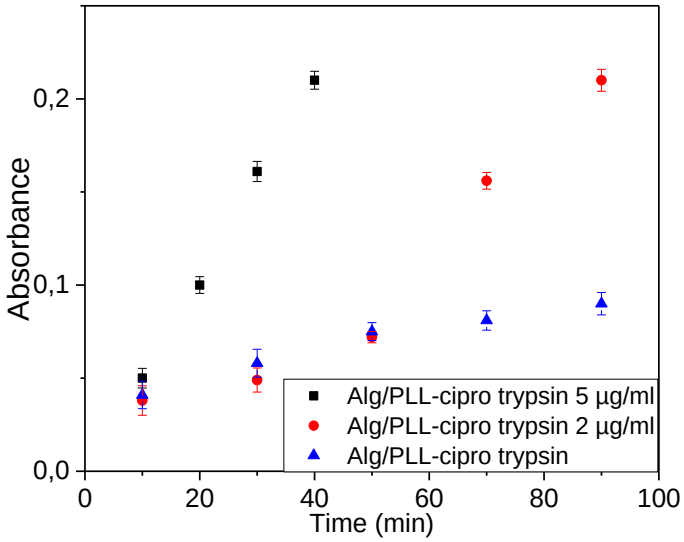

Figure 8-17 Absorbance at 278 nm, which corresponds to the ciprofloxacin concentration in the dialysate as function incubation time in PBS buffer (pH 7.4) without, with 2 µg/ml or 5 µg/ml trypsin, respectively, at 37°C.

Coating of titanium samples and its stability / degradation

In addition, to ensure the possibility to employ the system for dental implants, the particles were used to coat the surface of titanium plates. Afterwards, stability and degradation of the coating were studied. The coating process comprises a spray or spin coating, drying and rising[24][307]. During the coating the nanoparticles form a homogeneous layer [24][307][308]. More information about the coating process can found in chapter 10.6.4.

While chitosan based nanoparticles directly bind to the negatively charged titanium surface [307], for alginate based nanoparticles with a negative zeta potential a surface charge reversal is necessary[24]. Here, adsorption of polyethyleneimine was used to obtain a positively charged surface. The thickness of the polyethyleneimine layer was determined by ellipsometry to be around 3.0 ± 1 nm. Subsequently a PLL-ciprofloxacin/alginate (ratio 1:3) nanoparticle suspension was spray-coated resulting in a dry layer thickness of around 40 ± 6.5 nm. The coating on the titanium was then used for degradation. For this purpose, coated titanium plates were incubated in PBS buffer with or without addition of trypsin (5 µg/ml) at pH 7.4 and at 37°C. In the absence of enzyme the layer thickness does not change, and thicknesses between 35-40nm are determined by ellipsometry for the dried coatings (Figure 8-18, red curve). For the incubation in buffer with trypsin another coating was prepared, which is slightly thicker at the beginning (~45 nm, Figure 8-18, black symbols). Indeed, those differences can occur due to the coating process. In this case, the incubation caused an increase in

the thickness of the layer in the first few hours (Figure 8-18, black symbols). This was interpreted to be due the diffusion of trypsin into the layer. Then, over 109 hours, a decrease of 45% of the initial layer thickness was observed, clearly indicating the enzymatic degradability of the coatings.

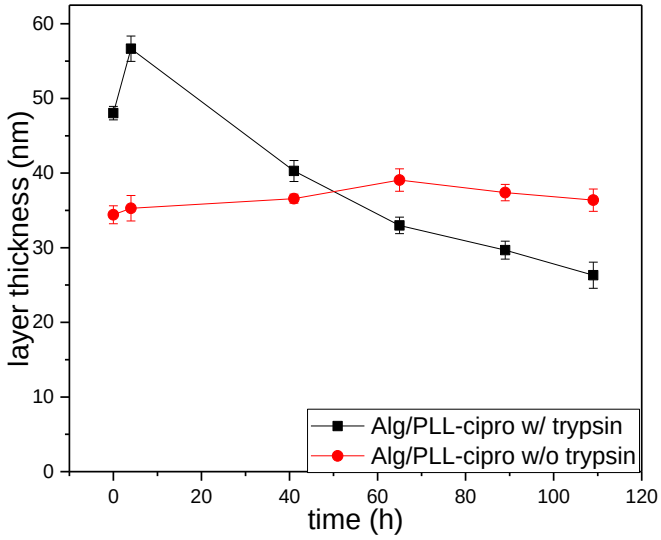

Figure 8-18 Dry layer thickness of PLL-cipro/alginate coatings as determined by ellipsometry after incubation in PBS buffer with or without addition of trypsin (5 µg/ml) at pH 7.4 and at 37°C.

In conclusion, degradation and release results discused above, demonstrate a controlled degradation (by enzymatic activity) of the system and its capacity to trigger drug release by enzymatic degradation (Figure 8-17).

8.3.3 Synthesis, analysis and antimicrobial efficacy of the conjugated ciprofloxacin.

KKKKGRDNVTEGE **12a** peptide sequences and molecules such as polyethylene glycol **13a** or homoalanine **14a** were grafted onto ciprofloxacin to gain a deeper understanding on how the grafting is affecting the antimicrobial effeciency of ciprofloxacin.

8.3.3.1 Binding of [N_3KKKKGRDNVTEGE] **12a** to ciprofloxacin **12b**

The peptide residue KKKKGRDNVTEGE represents the sequence that remains on the drug after peptide cleavage. Therefore, to test the efficacy of the released compound, peptide **12a** was linked to ciprofloxacin (Figure 8-19). The reaction described in Figure 8-19 instantly occurs between the azide function of petpide **12a** and the cyclooctyne of ciprofloxacin **10**.

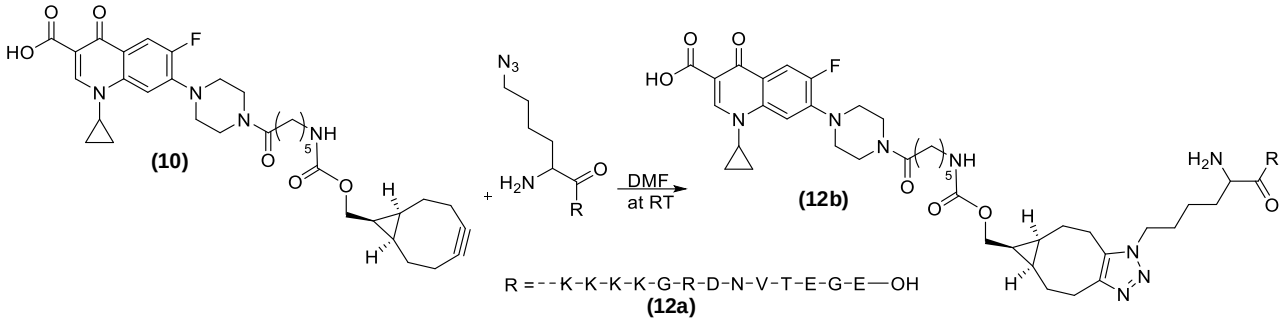

Figure 8-19 Reaction scheme of CIP-[KKKKGRDNVTEGE] ***12b****.*

Characterization of ciprofloxacin derivate 12b

Electrospray Ionisation Mass Spectrometry (ESI-MS) was used to further confirm the synthesis of **12b**. Peaks were found at 453.64, 566.80, 755.40, and 1132.60 m/z, which represent the following ions: $[M + H]^+$ (z = 5), $[M + H]^+$ (z = 4), $[M + H]^+$ (z = 3), and $[M + H]^+$ (z = 2). M represents the calculated mass for $C_{101}H_{160}FN_{29}O_{29}$ = 2262.19 g/mol)]. After successful synthesis, the antimicrobial efficacy of the conjugated ciprofloxacin **12b** was investigated against *Staphylococcus aureus*.

Antimicrobial efficacy of the 12b

The molecule **12b,** expected to be the active ingredient released during the degradation process, showed a decrease of antimicrobial efficacy. Indeed, for the ciprofloxacin conjugated to KKKKGRDNVTEGE a strong reduction in the inhibition of bacterial growth is observed. At a concentration of 12 µg/mL of **12b** a bacterial growth of 50% was observed. At the same concentration, bacterial growth in the presence of commercial ciprofloxacin was 0%. Therefore, to understand the reason of this decrease, **13b** and **14b** have been synthesized.

As previously mentioned, ciprofloxacin have been grafted to polyethylene glycol and L-azidohomoalanine to have a deeper understanding and investigate on why the grafting is affecting the antimicrobial efficacy of ciprofloxacin.

8.3.3.2 Binding of N_3(polyethylene glycol)NH_2 **13a** to ciprofloxacin

The efficacy tests were performed in the tryptic soy broth medium, containing proteins. Interactions between the peptide chain of **12b** and the proteins might have affected the efficacy. Therefore, ciprofloxacin was conjugated to PEG (Figure 8-20, **13b**), which is known not to interact specifically with proteins. Thence, by testing **13b**, the hypothesis concerning the involvement of peptide / protein interactions can be clarified. The reaction described in Figure 8-20 instantly occurs between azide of polyethylene glycol **13a** and cyclooctyne of ciprofloxacin **10**.

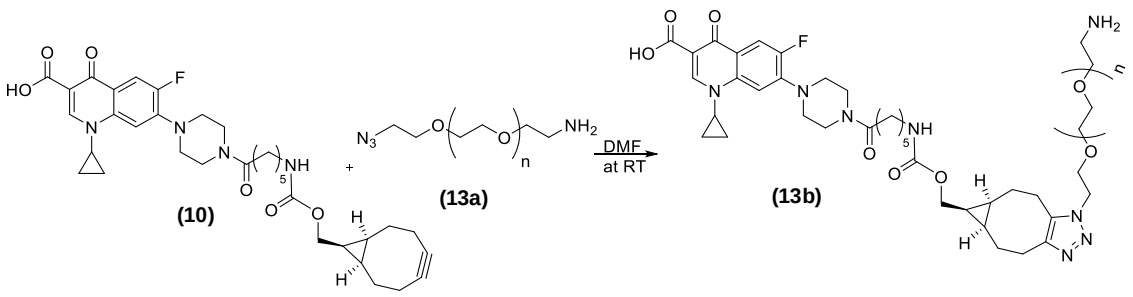

*Figure 8-20 Reaction scheme of CIP-(PEG)NH₂ **13b**.*

Characterization of 13b

With the help of two-dimensional NMR methods, the coupling of the ciprofloxacin and **13a** was established. Indeed, those analyses revealed the correlation between protons, carbons, protons-carbons and nitrogene-protons, which helps to define the structure of complex molecules. Numbers have been assigned to each protons in order to facilitate the characterization (Figure 8-21). HMBC (Attached file 21), HSQC (Attached file 22), COSY (Attached file 19), NOESY (Attached file 20) and NH-HMBC (Attached file 18) were performed to analyze and validate the synthesis of molecule **13b**.

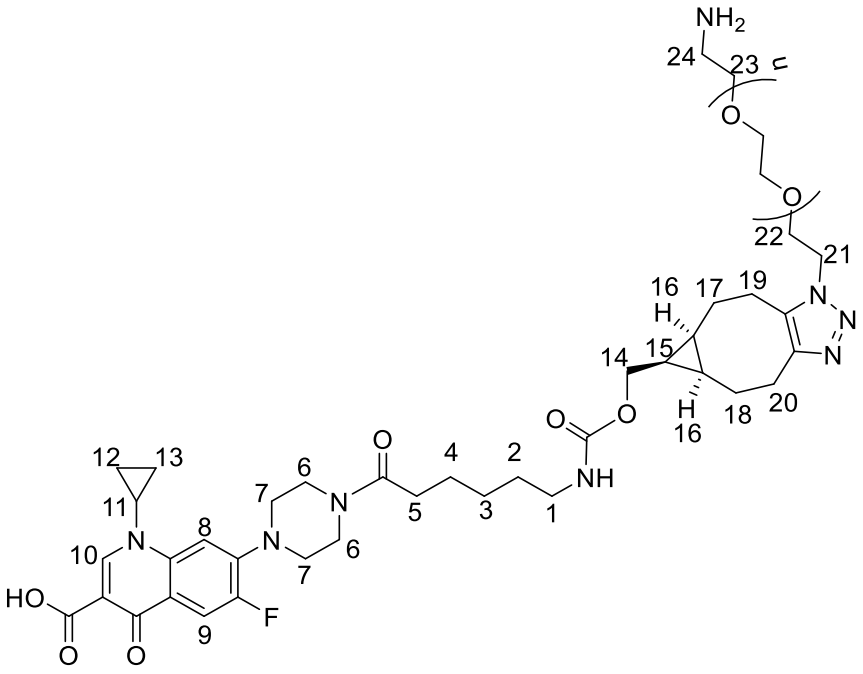

*Figure 8-21 Chemical structure of **13b** with numbered protons.*

The same starting point as that for the analysis of **10** was used to identify compound **13b**. Briefly, the NH signal of the carbamate was analyzed to define the protons H1

and H14. Atoms H15 to H20 were identified by means of the correlation with the H14 protons. After the reaction, a shift of all those protons was observed. The most affected protons were H19 and H20, which shifted from 2.17-2.25 ppm to 3.03 and 2.79 ppm. Furthermore, HSQC was performed to highlight the direct correlation of H19-H20 with the carbons at 24.26 and 27.52 ppm (Attached file 22), which correlate with two other carbons at 135.34 and 144.93 ppm and are not directly correlated with any proton (Attached file 21). These carbons appear in the shift range of the double bond of triazoles. In fact, the synthesis of **13b** implies the formation of a triazole ring. NH-HMBC (Attached file 18) and COSY (Attached file 19) analyses were performed to identify the proton in PEG chains. As evident in the analysis of compound **10**, the nitrogen at −230.03, −298.01 and −314.84 ppm were identified respectively as (D), (A), and (C). The nitrogens of PEG chains (G) and (F) were characterized by the correlation with the same protons at 4.49 ppm. Regarding the structure of **13b**, the protons at H21 correlate with two nitrogens: (F) at −25.56 ppm and (G) at −136.76 ppm. Therefore, the protons at 4.49 ppm were defined as H21, directly correlating with signals at 3.83 ppm, which is expected to be H22. ^{1}H-NMR and the NH-HMBC spectrum of N_3-PEG-NH_2 were needed to reveal the nitrogen (H) at −353.33 ppm and protons H24 at 3.78 ppm. Moreover, H24 correlates with protons at 3.25 ppm, which are supposed to be H23. Finally, three different points confirmed the bonding of the PEG chains (**13a**) and ciprofloxacin derivate **10**. First, the carbon at 135.34 ppm was identified to be part of the generated double bond and part of the BCN-CIP, and it correlates with protons at 4.49 ppm, which was identified as H21 of PEG chains (Attached file 22). Second, NOESY (Attached file 20) was carried out to identify the correlation between H21 and H19-H20 of **10**. Third, nitrogen (F) is shifted at −25.56 ppm (Attached file 18), which typically characterizes a shifting of triazole nitrogens[309]. Finally, the analysis highlighted the disappearance of the triple bond signal at 100.25 ppm and the appearance of C=C double bond signals at 135.34 and 144.93 ppm (Attached file 21). After successful synthesis, efficacy tests have been performed on the molecule **13b**.

Antimicrobial efficacy of the 13b

The molecule **13b** showed a decrease of antimicrobial efficacy. Indeed, for the ciprofloxacin conjugated to PEG a strong reduction in the inhibition of bacterial growth is observed. At a concentration of 6 µg/mL of **13b** a bacterial growth of 75% was observed. At the same concentration, bacterial growth in the presence of commercial ciprofloxacin was 0%. In conclusion, as **13b** did not show a significant efficacy, it can

be speculated that interactions between the peptide chain of **12b** and the proteins is not responsible for the bacterial growth.

8.3.3.3 Binding of L-azidohomoalanine hydrochloride **14a** to ciprofloxacin

Ciprofloxacin was conjugated to L-azidohomoalanine **14b**, which represents the smallest amino acid that can be linked. By testing its efficacy the influence of peptide length can be studied. The reaction described in Figure 8-22, instantly occurs between azide of L-azidohomoalanine hydrochloride **14a** and cyclooctyne of ciprofloxacin **10**.

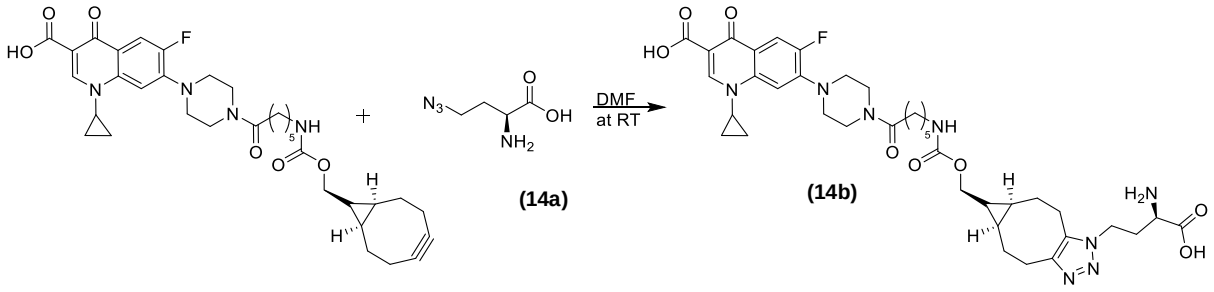

Figure 8-22 Reaction scheme of CIP-L-homoalanine hydrochloride 14b.

Characterization of 14b

With the help of two dimensional-NMR methods, the coupling of the ciprofloxacin and **14a** was established. Indeed, those analyses revealed the correlation between protons, carbons, protons-carbons and nitrogene-protons, which helps to define the structure of complex molecules. HMBC (Attached file 26), HSQC, COSY (Attached file 24), NOESY and NH-HMBC (Attached file 25) were performed to analyze and validate the synthesis of molecule **14b**. Numbers have been assigned to each protons in order to facilitate the characterization (Figure 8-23).

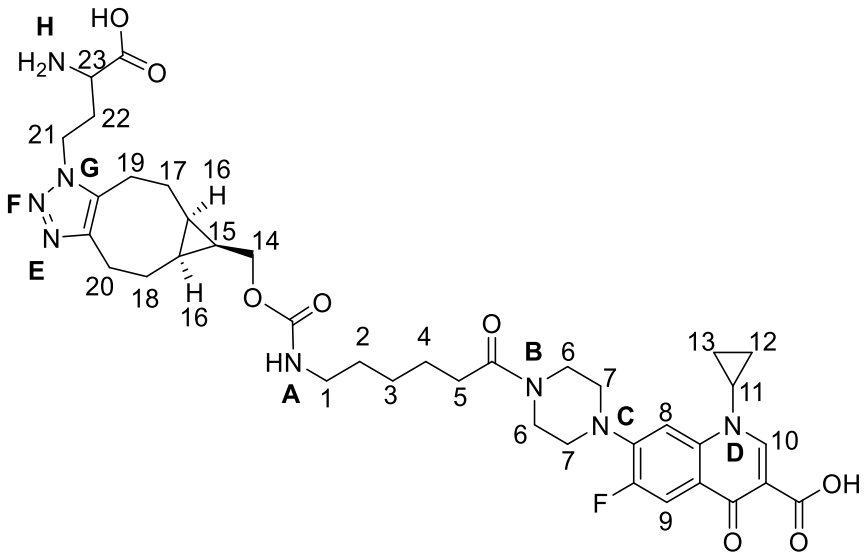

Figure 8-23 Chemical structure of 14b with numbered protons.

The synthesis of molecule **14b** was confirmed through the same evidence that helped to characterize the compound **13b**:

- Shifting of protons H19 and H20 (Attached file 23, ^{1}H-MNR).
- Disappearance of triple bond signals at 100.25 ppm, confirming the reaction of cyclooctyne (HMBC, Attached file 26).
- Appearance of C=C double bond signals of 1,2,3-triazoles bond, formed during the synthesis of **14b**, at 135.34 and 144.93 ppm. (HMBC, Attached file 26).
- NOESY was used to highlight the correlation between H21 of the grafted L-azidohomoalanine and H19-H20 of ciprofloxacin derivate **10**.
- Finally, nitrogen (F) was found to be shifted to −26.63 ppm, which is a typical shift for triazole nitrogens[309].

The spectrums shows some remains of the reagent L-azidohomoalanine, which could not be removed completely by precipitation of the polymer. For L-azidohomoalanine no antibacterial effect was observed, therefore, **14b** with the small amounts of impurities was used for the experiments.

Antimicrobial efficacy of the 14b

The molecule **14b** showed a decrease of antimicrobial efficacy. Indeed, for the ciprofloxacin conjugated to 4-azido-homoalanine a strong reduction in the inhibition of bacterial growth is observed. At a concentration of 1 µg/mL of **14b** a bacterial growth

of 80% was observed. At the same concentration, bacterial growth in the presence of commercial ciprofloxacin was 0%.

These results strongly suggest a hindrance due to the resulting bicyclononatriazole bond between ciprofloxacin and peptides. In fact, even the binding of a single amino acid leads to a reduction of the antibacterial efficacy. This compound **14b** did not have a KKKKGRDNVTEGE chain, but the same linking group, thus it can be concluded that the acylation of the piperazine ring with a bicyclononatriazole as in the linking group of compounds **14b** and **12b** hindered the drug from reaching or interacting with the target in the bacteria. While acylation of the secondary amino function has been found to be dentrimental for activity against a wide range of Gram-negative bacteria[310][251], in which the zwitter ionic structure of ciprofloxacin is important to pass the outer membrane pore OmpF, acylation is mostly tolerated for activity in Gram-positive bacteria like *S. aureus* having no outer membrane. In this case acylation can even lead to improved antibacterial activities [251]. However, the mechanism of action of ciprofloxacin involves an interaction with gyrase and bacterial DNA. Ciprofloxacin stabilizes the gyrase and bacterial DNA complex, which results in a DNA break [311]. It can be speculated that the linker with its structure of three annelated rings systems are too bulky to allow the formation of the complex with gyrase and DNA.

The residual efficacy of **12b** can be explained by the antimicrobial properties of the peptides, rich in cationic lysine residues. In general, they act by disrupting the structural integrity of the microbial membranes [312][313][314].

8.4 Conclusion

In this study, a new nanogel system was prepared by ionotropic gelation of alginate with PLL conjugated with ciprofloxacin. The conjugation of the ciprofloxacin was carried out by modification with a cyclooctyne-group suitable for a copper-free 1,3-cycloaddition with an azide at the peptide sequence. This is a versatile method to link small drug molecules to peptide sequences. Ciprofloxacin was therefore modified with cyclooctyne to enable the reaction with the azide function attached to different peptide sequences and molecules. Ciprofloxacin was modified, both with and without a linker comprising five methylene groups. This linker aimed at separating the bulky triazole-cyclooctyne bond and the ciprofloxacin, to minimize the risk of an efficacy loss. However, despite the integration of this linker the antimicrobial activity was affected as well. Further derivatives of ciprofloxacin were evaluated to elucidate the role of the conjugation chemistry. All of them showed a lower efficacy, suggesting the bulkiness

of triazole-cyclooctyne or the acyl conjugation as a possible cause, by hindering interactions of ciprofloxacin with the gyrase.

Then, a poly-L-lysine functionalized with an azide group was bond to ciprofloxacin to demonstrate the ability of conjugated peptide to generate stable nanoparticles with alginate. The PLL with conjugated ciprofloxacin forms nanoparticles with alginate solutions by ionotropic gelation as evidenced by dynamic light scattering. The nanoparticles are stable in aqueous suspension, but are degraded upon addition of trypsin. The ciprofloxacin was released from the nanoparticles only when the PLL sequence was enzymatically cleaved by trypsin. Moreover, the nanoparticle suspensions were used to prepare coatings on titanium by spray coating and characterized by ellipsometry. The coating was stable and degradable by enzymatic activity only. The results clearly demonstrated the intrinsic capabilities of the systems for application as triggered release systems for antibacterial agents. In conclusion, despite drug efficacy reduction, the introduced system was able to deliver on-demand molecules without any burst release. Any active substance with amine function can be modified through the same procedure and incorporated into the nanoparticle system.

9 Conclusion

Once external materials are implanted into the body, bacteria can attach to their surface, grow in biofilms and cause chronic inflammation. As a consequence, it can lead to the implant's failure and implementation of further surgical treatments, generating additional costs. To avoid this, smart drug delivery systems, which enable the encapsulation and triggered release of a drug substance, in a targeted and sustained way, were examined and presented in this study.

The main focus was to develop a system with a specific release occurring within particular enzymatic conditions or inflammatory state. To build up a stable and cleavable encapsulation system, different steps were established: 1) the integration of a model enzyme-labile peptide into two different polymer-based systems 2) generation of particles 3) the implementation of the particles into a coating, on titanium surfaces 4) the study of stability and degradability of those systems 5) the release of ciprofloxacin as model substance.

The first system was chitosan based (system 1). Chitosan-g-[poly-L-lysine-block-ε-caprolactone] copolymer was synthesized in four steps: functionalization of chitosan, grafting of a poly-L-lysine linker, synthesis of functionalized polycaprolactone, and binding of polycaprolactone to the chitosan via the linker. For the second system, based on alginate (system 2), a poly-L-lysine cross-linker and a model drug substance have been synthesized/modified to enable the binding of both components through a bicyclononatriazole link.

Systems 1 and 2 were able to generate polymersomes and nanoparticles in aqueous solution, respectively. Polymersomes (system 1) were formed by a solvent shift method, using DMSO as organic solvent. The relationship between the particles size and the amount of hydrophobic PCL was demonstrated and revealed an increase of the size by increasing the hydrophobic PCL amount. The peptide-alginate nanoparticles (system 2) were formed in aqueous solution by ionic gelation between positively charged drug-conjugated peptide linker and negatively charged alginate. The particle size and structure were characterized by Dynamic Light Scattering and/or Cryo-Scanning Electron Microscopy. Cryo-SEM images highlighted well-defined spherical and bi-layered core-shell structures of polymersomes. However, for the first system, a specific degradation through the cleavage of the polypeptide linker by the enzyme trypsin was not demonstrated. Its stability was attributed to the first chitosan layer which cannot be penetrated by the trypsin. This was confirmed by the capability

of chitosanase to degrade the polymersome by cleaving the external chitosan layer. In contrast to the system 1, for the alginate based nanoparticles (system 2), a change in particle size could be observed after adding trypsin and was explained by the degradation of the nanoparticles through the cleavage of the poly-L-lysine cross-linker. Indeed, an influence of the cross-linker amounts could be demonstrated and an increase in particle size was observed at lower cross-linker amount.

Both nanoparticle suspensions were used to prepare coatings on titanium, employing a spray coating process. The coating formation was confirmed and characterized by using ellipsometry. For both systems, the coating was stable at body simulated conditions and degradable by a specific enzymatic activity only. Regarding the coating of the second system, a specific decrease in layer thickness could be observed after adding trypsin. This enzyme is well known to have poly-L-lysine as substrate. On the other hand, for the first system, as for the polymersome in solution, the degradability of the coating was revealed only after adding chitosanase, well known to have chitosan as substrate.

As the degradability of the system 2 was directly related to the cleavage of the peptide, the triggered drug release by an enzymatic activity has been further investigated. Hence, it has been noted that the drug was only released, from nanoparticles, after trypsin was added, allowing the poly-L-lysine sequence cleavage. The specificity towards trypsin was demonstrated by using different concentrations of the enzyme. The increase in concentration revealed an accelerated drug release. This result clearly demonstrated a dependence of the system towards enzymatic activities and in other words, its capability to trigger specific release.

Moreover, for the second system, the antimicrobial efficacy of the drug after release has been studied. In a view of integrating the aggrecanase (an inflammation relevant enzyme) labile peptide, the drug substance was linked to a peptide, which represents the sequence that potentially remains conjugated to the drug after the peptide cleavage. The activity of the drug conjugated with peptide was strongly affected. Further ciprofloxacin derivatives were evaluated to better understand the role of the conjugation chemistry. First, a linker has been integrated between the drug and the peptide to analyze the influence of the bicyclononatriazol link on the efficacy. Second, a PEG chain with no affinity towards proteins has been grafted to the drug in order to check if a potential efficacy reduction happened due to the affinity of peptide and proteins. Finally, one single amino acid has been grafted on the drug to confirm the

influence of the peptide length on the efficacy. However, all 3 derivatives led to a lower efficacy of the drug. It can be deduced that the acylation of the piperazine ring of the ciprofloxacin, by a bicyclononatriazole linking group, hindered the drug from reaching or interacting with the target in the bacteria. It is known from literature that the acylation of the secondary amino function can be detrimental for the activity against a wide range of gram-negative bacteria[251][310]. Indeed, the zwitter-ionic structure of ciprofloxacin is affected and known to be important to pass the outer membrane pore OmpF. Nevertheless, acylation is mostly tolerated for activity in gram-positive bacteria, like *S. aureus,* which have no outer membrane.

In this study, as the acylation had a negative impact on the drug efficacy, alkylation of the drug substance could be preferred for further investigations. As a preliminary study, the binding via an alkylation at the drug substance showed the same efficacy against *S. aureus,* as the non-modified drug. However, this modified drug was not further studied due to the use of copper catalyst to achieve the binding. To avoid copper chemistry, the ciprofloxacin could be alkylated and functionalized with bicyclooctyne, through the following steps: i) alkylation of the secondary amino function with 6-(Boc-amino)hexyl bromide, ii) deprotection of tert-butoxycarbonyl protecting group and iii) bicyclooctyne functionalization using the same procedure used in this study.

For future research, in order to avoid the loss of zwitter-ionic structure of ciprofloxacin, the drug could be linked to the carrier through a self-immolative spacer in which, the system would release the drug without any residue on the drug-substance. Waldmann et. al have designed a new linker which undergo an enzyme-catalysed modification, combined with a subsequent intramolecular cyclization, leading to the release of the attached substance[315]. For this, the linker embodies three functional groups, i) a group or attachment to the polymeric support, ii) a group for the binding of the drug-substance and iii) a group which recognized and attacked by penicillin G acylase. Thereby, the enzyme releases an intermediate which cyclizes and deliver the target compound in its original structure. The example shown by Waldmann et. al proved an interesting chemoselectivity of penicillin G acylase, since the enzyme attacks only the phenylacetamide unit[315]. The system should then be tested in presence of bacteria related to implant associated infection, as well as the kinetic of cyclization leading to the release of the drug.

10 Experimental part

10.1 Materials

10.1.1 Chemicals

Chemicals	Purity	Supplier
Chitosan	-	Sigma-Aldrich
Acetic acid	100%	Sigma-Aldrich
Propargyl alcohol	99%	Sigma-Aldrich
Tin (II)-2-ethylhexanoate	92.5-100%	Sigma-Aldrich
ε-caprolactone	97%	Sigma-Aldrich
Hydroxybenzotriazole	≥97.0%	Sigma-Aldrich
1-Ethyl-3-(3-dimethylaminopropyl)carbodiimide	≥98.0%	Sigma-Aldrich
Sodium chloride	99.0%	Fisher scientific
Azido-$[Lys]_{20}$-SH	-	Nanosoft Polymers
Natrium hydrogen carbonate	≥99.0%	Roth
Ciprofloxacin	≥98.0%	Sigma-Aldrich
Propargyl Chloride	98%	Sigma-Aldrich
4-Bromo-1-butyne	97%	Sigma-Aldrich
Nα-Acetyl-L-lysine methyl ester hydrochloride	98%	Sigma-Aldrich
4-(4,6-dimethoxy-1,3,5-triazin-2-yl)-4-methyl-morpholinium chloride	≥96.0%	Sigma-Aldrich
(1R,8S,9s)-bicyclo6.1.0non-4-yn-9-yl) methanol	-	Sigma-Aldrich
Pyridine	99.8%	Sigma-Aldrich

4-nitrophenyl chloroformiate	96%	Sigma-Aldrich
Ammonium chloride	≥99.5%	Sigma-Aldrich
Sodium sulfate	≥99%	Alfa aesar
N-Methylmorpholine	99%	Sigma-Aldrich
N,N-Diisopropylethylamine	≥99%	Sigma-Aldrich
Trimethylsilyl chloride	≥99%	Sigma-Aldrich
6-((tert-Butoxycarbonyl)amino)hexanoic acid	≥99.0%	Sigma-Aldrich
7-Azabenzotriazol-1-yloxy)tripyrrolidinophosphonium hexafluorophosphate	98%	Carbolution
Citric acid	≥99.5%	Sigma-Aldrich
Trifluoroacetic acid	≥99.0%	Sigma-Aldrich
[EGETVNDRG]-N_3	-	CASLO ApS
[EGETVNDRGKKKK]-N_3	-	CASLO ApS
Azido-$[Lys]_9$	-	Klahn Lab
Alginate	-	Sigma-Aldrich
Poly(ethyleneimine) solution	-	Sigma-Aldrich
Trypsin	-	Sigma-Aldrich
Phosphate-buffered saline	-	Sigma-Aldrich
Sodium hydroxide	≥99.0%	Roth
Deuterium oxide	99.9%	Deutero
Deuterated chloroform	99.98%	Deutero
Copper sulfate pentahydrate	≥98%	Sigma-Aldrich
Chitosanase from Streptomyces griseus	-	Sigma-Aldrich

Deutered Methyl alcohol	99.98%	Deutero
Copper bromide	98%	Alfa aesar
3-maleimidopropionic acid	95%	Alfa Aesar

10.1.2 Solvents

Solvent	**Purity**	**Supplier**
Toluol	HPLC (99.8%)	Sigma-Aldrich
Methanol	HPLC (99.8%)	Fisher scientific
Tetrahydrofuran	HPLC (99.8%)	Sigma-Aldrich
Dimethyl sulfoxide	99.99%	Honeywell
Hydrochloric acid	37%	Sigma-Aldrich
Dimethylformamide	HPLC (99.9%)	Fisher scientific
Dichloromethane	HPLC (99.8%)	Sigma-Aldrich
Ethanol	99.8%	Sigma-Aldrich
Chloroform	99.96%	Fisher scientific
Ethyl acetate	HPLC (99.8%)	VWR
Petroleum ether	Analytical reagant grade	Fisher scientific
Diethyl ether	99.8%	Sigma-Aldrich
Ultrapure water	-	-

10.1.3 Titanium substrate

Titanium plates, with a diameter of 1.1 cm (medical grade 4), provided by BRASSELER (Lemgo, Germany) were used as substrates for polymer films. Before being coated, the Ti plates were polished with a Phoenix 4000 device (BUEHLER, Esslingen, Germany) using the following protocol. The plates were treated with SiC abrasive paper (P400) and polished with a polycrystalline diamond suspension (9 µm) on an

Ultrapad polish paper and a MestMet colloidal silica polishing suspension (0.02-0.06 µm) on ChemoMet paper. BUEHLER provided all suspensions and papers used for the above procedure. Once polished, the plates were cleaned by ultrasonification, in water followed by dichloromethane, acetone, methanol, and, finally, in MilliQ water. Afterwards, the plates were dried under nitrogen flow and stored in the refrigerator. Prior to each coating process, the plates were thermally treated overnight in order to obtain the desired negatively charged titanium oxide layer.

10.2 Molecule Characterization

10.2.1 NMR-Spectroscopy

Instruments AV III HD 300N, AV III 400 and AV 600 supplied by BRUCKER (Billerica, USA) were used to perform H-NMR, C-NMR, F-NMR, N-NMR spectroscopy. Those instruments applied magnetic fields strength of 300, 400 and 600 MHz, respectively. The different deuterated solvents were purchased from DEUTERO (Kastellaun, Germany). The evaluation was carried out with the analytical software MestReNova from MESTRELAB (Santigo de Compostela, Spain).

10.2.2 FT-IR-Spectroscopy

A FT-IR Equinox 55 instrument from BRUKER (Billerica, MA, USA) equipped with a mercury cadmium telluride detector, and an attenuated total reflection accessory with a zinc selenide crystal from HARRICK SCIENTIFIC PRODUCTS (Pleasantville, NY, United States) was used to perform FT-IR spectroscopy. The following conditions were used: wavelength range between 4000 and 550 cm^{-1}, 10 kHz and 32 scans per sample. The evaluation was carried out with the software OPUS from BRUKER (version 4.0.24).

10.2.3 Mass-spectroscopy

Dr. Ulrich Papke from the Institute of Organic Chemistry-University TU Braunschweig conducted the Mass Spectroscopy measurements. LTQ-Orbitrap Velos spectrometer was used to perform Electrospray Ionisation Mass Spectrometry. A voltage of 2.3 to 2.8 kV (positive) or 1.7 to 2.5 kV (negative) was applied. The sample was dissolved in methanol (C = 50 µg/mL) and 0.1 mg/mL trimethyltetradecylammonium bromide were added. A flow rate of 0.1 µL/min was used.

10.2.4 Gel permeation chromatography (GPC)

THF GPC column and a Shodex RI-101 Refractive Index Detector from SHODEX (Munich, Germany) were used for measurements:

- Precolumn 1 PSS SDV,
- Column 2 PSS SDV 5 µm - 1000 Å,
- Column 3 PSS SDV 5 µm-1000 Å.

THF was used as eluent with a flow rate of 1 mL/min. was used. Before injections, the samples were filtrated with a PTFE 0.22 µm filter. A 100 µl solution was injected with a concentration of 2 mg/mL. The evaluation was done with the software WinGPC UniChrom of the company PSS (Mainz, Germany).

10.3 Characterization of nanoparticles

10.3.1 Particle size

Particle size and stability measurements were carried out using a Zetasizer Nano ZS from MALVERN INSTRUMENTS (Malvern, UK) as well as to study the degradation of nanoparticle. A 12mm Square Disposable sizing cuvettes (DTS0012) were used for size measurements. Degradation tests were performed at 37°C. Malvern Zetasizer Software Version 7.03 was used for data evaluation.

10.3.2 Zeta-potential

Zeta potentials of the nanoparticles were determined using a Zetasizer Nano ZS from MALVERN INSTRUMENTS (Malvern, UK). Disposable Capillary Cells (DTS1070) were used for zeta potential measurements. The evaluation was done with the Malvern Zetasizer Software Version 7.03 from MALVERN INSTRUMENTS.

10.3.3 Cryo-SEM

For the morphological characterization the samples were cooled by plunging into nitrogen slush at atmospheric pressure and freeze fractured at −180 °C and etched for 60 s at −98 °C. After sputtering with platinum in the GATAN Alto 2500 cryo preparation chamber the samples were transferred into the Hitachi S-4800 microscope (Chiyode, Japan).

10.4 Coating process and Characterization

10.4.1 Dip coating with PEI solution

Before further treatment, the titanium substrate was coated with a polyethylenimine (PEI) layer to obtain a positively charged layer. The substrate was immersed for one minute in 5% (w/w_{H2O}) PEI solution, washed with pure water, and dried under nitrogen. With regard to the PEI sctructure (Figure 10-1), amine functions enable a positively charged coating.

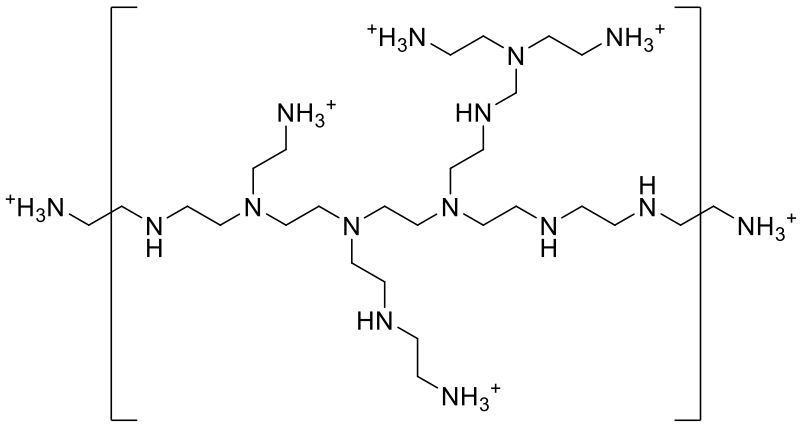

Figure 10-1 Chemical structure of poly(ethyleneimine).

10.4.2 Spray coating process of Titan plate

The titanium substrates were then spray-coated for 180 seconds with an airbrush Aztek A470 from TESTORS (Vernon Hills, IL, USA), depositing ≈20 µL of the polymersome suspension with a concentration of 1 mg/mL^{-1}. Subsequently, the Ti plates were washed with 0.1% acetic acid (AcOH) and H_2O in an ultrasonic bath for 15 min. Subsequently, the plates were dried under nitrogen flow. During the process, the plates were gently manipulated to avoid any scratches and residues on the polished surface. Ellipsometry was used to measure coating thickness.

10.4.3 Ellipsometry

The optical properties of coatings and thickness were determined using a Multiskop from OPTREL (Sinzing, Germany) in the ellipsometry mode. Uncoated titanium plates were used as reference. Data were collected in the x, y-mode at 70° as mean value of 16 data points in total to determine optical constants and the thickness layers. Evaluation of the data was carried out using Elli Version 3.2 from OPTREL.

10.5 Synthesis for chitosan-g-[poly-L-lysine-b-ε-caprolactone]

10.5.1 Purification of chitosan

Season, origin, supplier and conditions of deacetylation are reasons which, cause variations of commercial chitosan quality. To overcome this problem and to obtain chitosan with a highest purity and integrity, Gan et al. proposed an additional purification process. Briefly, 1 g of purchased chitosan (Medium MW, 190-310 kDa, 75-85% DDA) was soaked in 10 mL 1M sodium hydroxide solution. The suspension was then heated at 70°C for 2 hours before the chitosan was filtered off and washed with deionized water. Afterwards, the chitosan was dissolved in a 1% acetic acid solution. After complete dissolution of chitosan, the solution was filtered, and dialyzed against 0.1 M NaCl solution, and deionized water. Freeze drying was used to remove the water and to obtain a dried product. The resulting chitosan was dissolved in a mixture of D_2O/DCl (500/1) and ^{1}H-NMR was used to analyse chitosan and determine the degree of deacetylation (DDA). The follwing equation was used to calculate the DDA.

$$\text{DDA} = 1 - \frac{Integral\,H8*2}{Integral\,(H2-H6)+Integral\,H7}$$

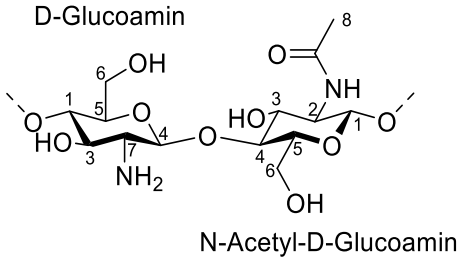

Figure 10-2 Chemical structure of chitosan.

^{1}H-NMR (400 MHz, D_2O) δ [ppm] = 2.00-2.16 (m, CH_3, GlcNAc); 3.37-3.03 (s, 1H); 3.37-4.23 (m, 6H); 5.04-4.78 (m, 1H)

10.5.2 Sysnthesis of chitosan-maleimide **1**

Chitosan-maleimide was synthesized according to Chirachanchai et al.. Briefly, CS (100 mg) and HOBt (91 mg, 0.5 mmol) were dissolved in 3 mL of ultrapure water and stirred overnight. To the CS solution, 33 mL of DMSO and a variable amount of 3-Maleimidopropionic acid were added. Afterward, EDC (114 mg, 0.5 mmol) HCl solution (200 µL, pH = 4-5) was added, and the solution was stirred for 24 hours at

room temperature. Finally, the reaction mixture was dialyzed against a solution containing 10 mM HCl, 1 wt% NaCl, and then against 10 mM HCl. Subsequently the solution was lyophilized to obtain **1**. The coupling efficiency was optimized by adjusting the amount of DMSO, HOBt, chitosan (from shrimp and fungi) and different coupling reagents (Table 7-1, chapter 7.1). ^{1}H-NMR and FT-IR spectroscopy were used to characterize **1**. Degree of substitution was calculated from the ^{1}H-NMR spectra, using the ratio of maleimide protons at 6.85 ppm and the signal at 2.00-2.08 ppm which represents 3 protons of the chitosan backbone. The degree of acetylation of unmodified chitosan was measured by ^{1}H-NMR and was found to be 10%.

^{1}H-NMR (400 MHz, D_2O) δ [ppm] = 2.00-2.08 (m, 3H, CH_3 of GlcNAc); 3.07-3.24 (m, 1H, CH of GlcN); 3.43-4.09 (m, 5H, CH on chitosan backbone); 4.52-5.01 (m, 1H, O-CH-O); 6.85 (s, 2H, HC=CH). (Attached file 1)

FT-IR [cm^{-1}]: 3248 (O-H); 2875 (C-H); 1704 (C=C); 1645 (C=O); 1556 (N-H); 1422 (CH-OH), 1699 (C=C), 1045 (C-O)). (Attached file 2)

10.5.3 Synthesis propargyl-terminated poly-ε-caprolactone **2**

propargyl-terminated poly-ε-caprolactone was synthesized via a general procedure for ring-opening polymerization of poly(ε-caprolactone)[201]: ε-caprolactone, propargyl alcohol, and Tin (II)-2-ethylhexanoate were dissolved in dry toluene. The solution was stirred at 110°C under dry nitrogen gas for 24 hours. The solution was then cooled down to room temperature. After cooling, tetrahydrofuran was added to dilute the solution. Finally, **2** was precipitated, in a significant excess of methanol, filtered, washed with methanol, and dried in a vacuum oven at 40°C for 48h. Molecular weight was calculated to M_n = 5755 g/mol by the integration of terminal proton of CH_2 at 3.62 ppm and the corresponding protons of CH_2-groups in the chain at 4.03 ppm. ^{1}H-NMR and FT-IR spectroscopy were carried out to characterize **2**. ^{1}H-NMR and FT-IR spectroscopy were performed to characterize **2**.

^{1}H-NMR (400 MHz, $CDCl_3$) δ [ppm] = 1.36 (m, 90H, CH_2 on PCL backbone); 1.62 (m, 180H, CH_2 on PCL backbone); 2.27 (m, 90H, CH_2C=O on PCL backbone); 2.45 (s, 1H, CH_2−C≡CH); 3.62 (t, 2H, CH_2OH); 4.03 (m, 88H, CH_2O on PCL backbone); 4.65 (s, 2H, CH_2−C≡CH). (Attached file 3)

FT-IR [cm^{-1}]: 3265 (C≡C-H); 2944 (C-H); 2855 (C-H); 2098 (C≡C); 1721 (C=O); 1469 (C-H); 1238 ((C=O)-O); 1171 (C-O-C). (Attached file 2)

10.5.4 Synthesis of CS-[poly-L-lysine$_{20}$-N$_3$] **3**

Chitosan-maleimide with a DS of 3% or 5% and a molar equivalent amount of Azido-poly-L-Lysine$_{20}$-SH were dissolved in a mixture of DMF and phosphate buffer saline (ratio: 1-6) with a final pH of 6.5. After the complete dissolution, the mixture was stirred for 24 hours at room temperature. Subsequently, the solution was dialyzed against a solution containing 10 x 10^{-3} M HCl and 1 wt% NaCl, and 10 x 10^{-3} M HCl solution. Finally, the solution was lyophilized to obtain CS-[poly-L-lysine$_{20}$-N$_3$]. ^{1}H-NMR and FT-IR spectroscopy were performed to characterize **3**.

^{1}H-NMR (400 MHz, D$_2$O) δ [ppm] = 2.00-2.08 (m, 3H, CH$_3$ of GlcNAc); 3.07-3.24 (m, 1H, CH of GlcN); 3.43-4.09 (m, 5H, CH on chitosan backbone); 4.52-5.01 (m, 1H, O-CH-O); Poly-L-lysine 4.31 (m, 1H, CH); 2.98 (t, 2H, CH$_2$); 1.7 (m, 4H, -CH$_2$); 1.43 (m, 2H, CH$_2$). (Attached file 4)

FT-IR relevant peaks [cm^{-1}]: 2121 (-N$_3$). (Attached file 2)

10.5.5 Synthesis of poly-[L-lysine-b-ε-caprolactone] **4**

2 (1.79 µmol) and CS-[poly-L-lysine$_{20}$-N$_3$]$_{3\%}$ (0.01 g) were dissolved in 2 mL DMSO and in 1 mL H$_2$O at 37°C, respectively. After dissolution, a mixture of CuSO4·5H$_2$O (3.57 µmol) and ascorbic acid (8.93 µmol) were added to the reaction mixture. The solution was stirred overnight at 37°C. Finally, the resulted copolymer was dialyzed against THF in order to remove unreacted **2**, against a saturated aqueous solution of EDTA disodium salt, 10 x 10^{-3} M HCl solution 1 wt% NaCl solution, and against 10 mM HCl solution. After lyophilisation, the copolymer was obtained. ^{1}H-NMR and FT-IR spectroscopy were performed to characterize **4**.

^{1}H-NMR (400 MHz, D$_2$O/DMSO) δ [ppm] = PCL backbone: 1.30 (m, CH$_2$ on PCL backbone); 1.54 (m, 2x CH$_2$ on PCL backbone), 2.27 (m, CH$_2$C=O on PCL backbone); 3.99 (m, CH2); Chitosan backbone: 1.87 (m, 3H, -CH$_3$ of GlcNAc); 2.93 (m, 1H, CH of GlcN); 3.73-3.86 (m, 5H, CH on chitosan backbone), 4.95 (m, 1H, O-CH-O); Poly-l-lysine: 4.24 (m, 1H, CH); 2.80 (m, 2H, CH$_2$); 1.64 (m, 4H, CH$_2$); 1.41 (m, 2H, CH$_2$). (Attached file 5)

FT-IR [cm^{-1}] relevant peaks: Chitosan component: 3287 (O-H); 2876 (C-H); 1646 (C=O);1526 (N-H); 1045 (C-O); PCL component: 2928 (C-H); 2862 (C-H); 1724 (C=O); 1466 (C-H)); 1239 ((C=O)-O); 1175 (C-O). (Attached file 2)

10.5.6 Polymersome formation

For polymersome formation, 1 mg/mL CS-graft-copolymer was dissolved in a mixture of H_2O or 63 x 10^{-3} M sodium phosphate buffer pH of 7.6 and DMSO (ratio: 1-20) at 37°C. After dissolution, the solution was dialyzed (molecular weight cut-off 14.000 g/mol) three times against deionized H_2O or 63 mM sodium phosphate buffer pH of 7.6. After 15 hours, the solution turned turbid, and the polymersomes were obtained. Then, particle size, zeta potential and stability measurements were carried out using a Zetasizer Nano ZS from MALVERN INSTRUMENTS (Malvern, UK). Disposable sizing cuvettes (DTS0012) and disposable folded capillary cell (DTS1070) were used for size / zeta potential measurements. Malvern Zetasizer Software Version 7.03 was used for data evaluation. Cryo-SEM images were used to inspect the shape and morphology of polymersomes using a HITACHI S-4800 instrument (Chiyode, Japan).

10.5.7 Spray coating of Titanium plates

The titanium substrates were then spray-coated for 180 seconds with an airbrush Aztek A470 from TESTORS (Vernon Hills, IL, USA), depositing approximately 20 µL of the polymersome suspension with a concentration of 1mg/ml. Subsequently, the Ti plates were washed with 0.1% acetic acid (AcOH) and H_2O in an ultrasonic bath for 15 minutes. Subsequently, the plates were dried under nitrogen flow. Ellipsometry was used to determine the coating thickness.

10.5.8 Stability / degradation experiment of polymersomes and coatings

The degradation studies of the coatings on the Ti plates were carried out by the incubation in trypsin (4 µg/ml) or chitosanase (5 µg/ml) containing solution. The tests have been performed in distilled water at pH between 5.6-5.8. The solutions were renewed daily to ensure degradation capability of trypsin. Before each thickness measurement, the samples were washed with 0.1% acetic acid (AcOH) and H_2O solutions in an ultrasonic bath for 15 minutes and dried under nitrogen flow.

The degradation of the polymersomes was investigated by the addition of trypsin or chitosanase to the suspension. The tests have been performed in 63 mM sodium phosphate buffer pH of 7.6 and distilled water (pH = 5.6-5.8). Briefly, 1 mL polymersome suspension were filled in a sizing cell. Trypsin or chitosanase solution was added in order to obtain respectively final concentrations of 4 and 5 µg/mL. The degradation process was then monitored via consecutive size measurements using the Zetasizer Nano ZS.

10.6 Aginate/Peptid-nanoparticles

10.6.1 Synthesis of ciprofloxacin derivates

Synthesis of alkyne-functionalized ciprofloxacin 5

$NaHCO_3$ (0.187 g, 0.0022 mol) and ciprofloxacin (0.5 g, 0.0015 mol) were dissolved in 150 ml of dry DMF at 80°C. Once a clear solution is obtained, the reaction mixture was degassed with N_2 for 15 minutes. Finally, 4-Bromo-1-butyne (1 g, 0.0075 mol) was added and the solution was stirred 24 hours at 21°C. After 24 hours, the DMF was removed under reduced pressure by adding toluene as co-solvent. The resulting solid was purified by flash chromatography on silica gel. A mixture of CH_2Cl_2 and MeOH (97-3) was used for the chromatography. A white solid was obtained: 172 mg. Yield = 29%

^{1}H-NMR (700 MHz, $CDCl_3$) δ [ppm] = 8.70 (s, 1H); 7.95 (d, *J* = 13.1 Hz, 1H); 7.29 (d, *J* = 7.2 Hz, 1H); 3.47 (tt, *J* = 7.1, 3.9 Hz, 1H); 3.35-3.25 (m, 4H); 2.65 (m, 6H); 2.39 (m, 2H); 1.95 (t, *J* = 2.6 Hz, 1H); 1.36-1.27 (m, 2H); 1.13 (m, 2H). (Attached file 6)

Synthesis of BCN-O(CO)O(4-NO_2-Ph) 6

First, 100 mg (0.666 mmol) (1R,8S,9s)-bicyclo6.1.0non-4-yn-9-yl-methanol (BCN-OH) was dissolved in 17 mL dry CH2Cl2. 134 µL (1.664 mmol) of pyridine and 168 mg (0.831 mmol) of 4-nitrophenyl chloroformiate was added to the solution. The mixture was stirred for 20 minutes at 22°C before being quenched by the addition of 20 mL of saturated ammonium chloride solution. The mixture was extracted with CH2Cl2 (3x20 mL). The combined organic layers were dried over Na2SO4 and concentrated under reduced pressure. Flash chromatography through silica gel was performed to purify the residue. A mixture of light petroleum-EtOAc (95-5) and (90-10) were used for the chromatography.

A white solid was obtained: 180 mg. Yield = 85%

^{1}H-NMR (300 MHz, $CDCl_3$) δ [ppm] = 8.26-8.31 (m, 2H); 7.37-7.42 (m, 2H); 4.4 (d, 2H); 2.38-2.26 (m, 4H); 2.25-2.21 (m, 2H); 1.66-1.57 (m, 2H); 1.49 (p, 1H); 1.11-1.02 (m, 2H). (Attached file 7)

Synthesis of BCN-O(CO)HN-Ciprofloxacin 7

At 82°C, 42 mg (0.127 mmol) of ciprofloxacin was dissolved in 7 mL of dry DMF. After the complete dissolution, 38 mg (0.38 mmol) of *N*-methylmorpholine (NMM) and a solution of 40 mg (0.127 mmol) BCN-O(CO)O(4-NO_2-Ph) in 2 mL DMF were added. The solution was stirred for 24 hours at 23°C. Then, DMF was evaporated under

reduced pressure. It is important to stop the evaporation before the end to keep 0.5 ml of the solution. The residue was purified by flash chromatography through silica gel. A mixture of CH_2Cl_2/MeOH (95-5 and 90-10) were used. After vacuum drying, a yellow solid was obtained: 45 mg. Yield = 70 %.

^{1}H-NMR (300 MHz, $CDCl_3$) δ [ppm] = 4.17 (d, J = 8.2 Hz, 2H), 3.70-3.63 (m, 4H); 3.48 (tt, J = 7.1, 4.0 Hz, 1H); 3.29-3.21 (m, 4H); 2.32-2.10 (m, 6H); 1.62-1.46 (m, 2H); 1.37-1.29 (m, 3H); 1.17-1.10 (m, 2H); 0.96-0.86 (m, 2H). (Attached file 8)

MS-ESI (m/z): calculated 507.22 g/mol; found 508.22 $[M + H]^+$; 530.20 $[M + Na]^+$; 1037.42 $[2 M + Na]^+$ (calculated for $C_{28}H_{30}FN_3O_5$= 507.22 g/mol)

$_2$HN-$(CH_2)_5$-Ciprofloxacin 9

Ciprofloxacin 165.5 mg (0.5 mmol) and N,N-Diisopropylethylamine 0.5 mL (2.9 mmol) were mixed in 3 mL of dry CH_2Cl_2 and 185 µL trimethylsilyl chloride. The solution turned yellow. Separately, 6-((tert Butoxycarbonyl)amino)hexanoic acid 173 mg (0.75 mmol), PyAOP 417 mg (0.8 mmol) and DIPEA 350 µL (2 mmol) were dissolved in 2 mL of dry CH_2Cl_2. The two solutions were combined and stirred overnight at 23°C. 60 mL H_2O were added and the aqueous solution was extracted with 3x80 mL CH_2Cl_2. The combined organic layers were washed with 60 mL H_2O, 10 % w/w citric acid in water, saturated aqueous $NaHCO_3$ solution, brine and 2x50 mL H_2O. The organic phase was dried over Na_2SO_4 and concentrated under reduced pressure. A yellow solid was obtained: 190 mg. Yield = 70 %.

^{1}H-NMR ($CDCl_3$, 300 MHz), δ 1.18-1.23 (2H, m), 1.36-1.56 (15H, m), 1.63-1.74 (2H, m), 2.39 (t, J = 7.5 Hz, 2H), 3.12 (dt, J = 6.7 Hz, 2H). 3.25-3.39 (4H, m), 3.51-3.59 (1H, m), 3.67-3.90 (4H, m), 4.56 (1H, bs), 7.36 (d, J = 7.1 Hz, 1H), 7.99 (d, J = 12.9 Hz, 1H), 8.72 (s, 1H), 14.9 (1H, bs).

MS-ESI (m/z): calculated 545.28 g/mol; found 567.82 g/mol (z=1, $[M + Na]^+$); 1111.53 (z=1/2, $[M + Na]^+$), (z=1/3, $[M + Na]^+$).

The trifluoroacetic acid (TFA) salt was obtained by stirring it overnight, in 16.7 % TFA/CH_2Cl_2, at room temperature and by removing the solvent with methanol as co-solvent. The resulting solid was re-precipitated with diethyl ether. A yellow pale solid was obtained: 110 mg. Yield = 90 %

^{1}H-NMR (CD_3OD, 300 MHz), δ 1.22 (m, 2H) 1.54-1.37 (m, 4H), 1.63-1.77 (m, 4H), 2.52 (t, J = 7.3 Hz, 2H), 3.05-2.86 (m, 2H), 3.46-3.33 (m, 4H), 3.87-3.70 (m, 5H), 7.55 (d, J = 7.2 Hz, 1H), 7.81 (d, J = 13.2 Hz, 1H), 8.72 (s, 1H). (Attached file 10) ^{19}F-NMR ($CDCl_3$, 282 MHz), δ -75.36, -121.56.

Synthesis of BCN-O(CO)HN-$_2$HN-$(CH_2)_5$Ciprofloxacin 10

100 mg (0.127 mmol) of **9** was dissolved in 2.65 mL dry DMF. After complete dissolution, 78 µL (mmol) NMM and a solution of 56.5 mg (mmol) BCN-O(CO)O(4-NO2-Ph) in 2 mL DMF were added and stirred for 24 hours at 23°C. DMF was evaporated under reduced pressure (it is important to stop the evaporation before the end in order to keep 0.5 mL of the solution). The residue was purified by flash chromatography through silicagel. Solvent: CH_2Cl_2/MeOH (95-5 and 90-10).

A yellow solid was obtained: 50 mg. Yield = 45%

^{1}H-NMR (DMF, 600 MHz), δ 8.75 (s, 1H), 7.97 (d, J = 13.2 Hz, 1H), 7.73 (d, J = 7.4 Hz, 1H), 7.00 (t, J = 5.8 Hz, 1H), 4.09 (d, J = 8.1 Hz, 2H), 3.94 (tt, J = 7.3, 4.1 Hz, 1H), 3.79 (m, 4H), 3.42 (m, 4H), 3.11 (td, J = 7.1, 5.8 Hz, 2H), 2.45 (t, J = 7.5 Hz, 2H), 2.30-2.14 (m, 6H), 1.66-1.22 (m, 15H), 0.95-0.85 (m, 2H). (Attached file 11) ^{13}C-NMR (DMF, 600 MHz): 9.15, 19.5, 21.47, 22.41, 26.39, 27.96, 30.5, 31.42, 34.09, 37.64, 42.06, 42.42, 46.54, 51.17, 51.79, 62.92, 100.21, 108.41, 108.88, 112.62, 141.13, 146.99, 149.67, 154.23, 155.88, 158.38, 167.66, 172.48, 178.51. ^{14}N-NMR (DMF, 600 MHz): -314.56, -298.18, -266.90, -229.85.

10.6.2 Synthesis of Ciprofloxacin conjugated peptides/substances

Synthesis of ciprofloxacin-poly-L-lysine 11

PLL_9-N_3 was synthesized using automated standard solid phase supported peptide (SPPS) synthesis utilizing a Syro II Peptide synthesizer from MultiSynTech. The first Fmoc-protected lysine was loaded onto a 2-chlorotrityl resin (capacity 0.48 mmol/g) in the presence of Triethylamine in dichloromethane at 23°C over 12 h. The loading of the resine was determined after Fmoc-cleavage in the presence of a solution of 20 w% piperidine in DMF analysing the concentration of the fulvene-piperidine adduct at 309 nm by UV-Vis spectrometry. Coupling of further Fmoc-protected lysines and 4-azidobenzoic acid was achieved after Fmoc-cleavage (Piperidine 20w% in DMF) using the acid as well as DIC/HOBt/DiPEA:1/1/1 as coupling mixture in 4-fold excess. Between all cleavage and coupling steps the resin was washed with DMF. Final cleavage of the peptide from the resine was achieved in the presence of TFA at 23°c over a period of 5 min and PLL_9-N_3 was obtained from the cleavage solution by precipitation with cold diethylether.

For this synthesis of **11**, 40 mg of PLL_9-N_3 were added to a solution of 18 mg BCN-O(CO)HN-Ciprofloxacin (0.035 mmol) in 4 mL. The mixture was stirred overnight at

23°C before the product was precipitated with diethyl ether, re-dissolved in DMF, and re-precipitated. Finally, the solid was washed with diethyl ether until a white powder was obtained. Yield = 81 %

^{1}H-NMR (700 MHz, D_2O) δ [ppm] relevant peaks: 8.55 (s, 1H, CIP); 7.89 (m, 2H, PLL); 7.13-7.49 (m, 4H, CIP/PLL); 2.99 (m, 24H, PLL); 1.98-1.29 (PLL). (Attached file 27)

UV-Vis: Absorption peak at ~278 nm.

Synthesis of Peptide 12a conjugated Ciprofloxacin 12b

0.01 mg (0.009 mmol) of peptide: [EGETVNDRGKKKK]-N_3 **(12a)** was added to a solution of 5.5 mg BCN-O(CO)HN-2HN-$(CH_2)_5$Ciprofloxacin (0,009 mmol) in 1 mL (DMF),. The solution turned from yellow to transparent. The mixture was stirred over night at 23°C before the product was re-precipitated with diethyl ether, re-dissolved in DMF and re-precipitated. Finally, the solid was washed with diethyl ether.

A white-yellow solid was obtained: 13 mg. Yield: 65%.

MS-ESI (m/z): calculated 2263.56 g/mol; found, 566.80 (z = 4, [M + H^+]); 755.40 (z = 3, [M + H^+]); 1132.60 (z = 2, [M + H^+]).

UV-Vis: Absorption peak at ~278 nm.

Synthesis of 13a or 14a conjugated Ciprofloxacin 13b or 14b

N3-PEG3500-NH2 (13a) L-Azidohomoalanine hydrochloride (14a)

Figure 10-3 Chemical structure of 13a and 14a.

0.024 mmol of **13a** or **14a** (Figure 10-3) were added to a solution of 15 mg **10** (0.024 mmol) in 1 mL (DMF). The solution turned from yellow to transparent. The mixture was stirred over night at 23°C, before the product was precipitated with diethyl ether, re-dissolved in DMF and re-precipitated. Finally, the solid was washed with diethyl ether and a white-yellow solid (80-90%) was obtained.

A white solid was obtained **(13b)**: 105 mg. Yield: 91%.

A white solid was obtained **(14b)**: 17 mg. Yield: 87%.

Molecule **13b**: ^{1}H-NMR (DMF, 600 MHz), δ 8.76 (s, 1H), 7.98 (d, J = 13.2 Hz, 1H), 7.73 (d, J = 7.4 Hz, 1H), 7.00 (t, J = 5.8 Hz, 1H), 4.49 (t, J = 5.4 Hz, 2H), 4.17-4.07 (m, 2H), 3.94 (tt, J = 7.3, 4.0 Hz, 1H), 3.85-3.76 (m, 8H), 3.41-3.36 (m, 2H), 3.26 (dd, J = 5.7, 4.7 Hz, 2H), 3.14-3.08 (m, 2H), 3.08-3.00 (m, 2H), 2.84-2.76 (m, 2H), 2.45 (t, J = 7.5

Hz, 2H), 2.22-2.07 (m, 2H), 1.66-1.14 (m, 15H), 1.06-0.95 (m, 2H). (Attached file 17) ^{13}C-NMR ($CDCl_3$, 600 MHz): 9.27, 19.43, 21.10, 21.76, 23.49, 24.16, 26.49, 27.49, 27.92, 30.89, 31.45, 34.09, 37.62, 41.38, 42.15, 42.35, 46.54, 49.07, 51.17, 51.84, 62.96, 69.02, 71.36, 71.56, 108.70, 112.69, 119.49, 121.00, 135.26, 141.09, 145.28, 147.03, 149.8, 153.95, 155.7, 158.7, 158.21, 167.87, 172.47, 178.8. ^{14}N-NMR (DMF, 600 MHz): -352.99, -312.78, -298.18, -266.87, -229.85, -136.07, -25.38.
UV-Vis: Absorption peak at ~278 nm.

Molecule **14b**: ^{1}H-NMR (DMF, 600 MHz), δ 8.75 (s, 1H), 7.97 (d, J = 13.2 Hz, 1H), 7.74 (d, J = 7.5 Hz, 1H), 7.05 (t, J = 5.8 Hz, 1H), 4.71 (m, 1H), 4.33 (t, J = 6.3 Hz, 1H), 4.12 (m, 2H), 3.95 (tt, J = 7.3, 4.0 Hz, 1H), 3.83-3.75 (m, 4H), 3.48-3.36 (m, 4H), 3.14-3.08 (m, 2H), 3.08-3.00 (m, 2H), 2.88-2.81 (m, 2H), 2.60 (m, 2H), 2.45 (t, J = 7.5 Hz, 2H), 2.23-2.07 (m, 2H), 1.68-1.31 (m, 14H), 1.16 (m, 1H), 1.00 (m, 1H). (Attached file 23) ^{13}C-NMR ($CDCl_3$, 600 MHz): 7.87, 15.09, 17.9, 19.34, 19.68, 21.73, 22.34, 22.7, 25.04, 26.07, 26.56, 29.94, 31.07, 32.68, 36.33, 40.78, 41.14, 44.46, 45.19, 49.86, 50.08, 50.49, 61.66, 107.27, 111.30, 119.62, 133.46, 139.75, 144.30, 145.74, 148.34, 152.93, 154.66, 157.14, 166.44 170.66, 171.32, 177.31. ^{14}N-NMR (DMF, 600 MHz): -26.63, -135.18, -230.03, -267.4, -298.01, -314.38.
UV-Vis: Absorption peak at ~278 nm.

10.6.3 Nanoparticle formation with alginate

Purification of alginate

Alginate was purified according to the method outlined by Tolle et al.[24] 2 g of commercial alginate were dissolved in 30 mL of deionized H_2O. This solution was dialyzed over three days against deionized H_2O with three medium changes a day (14 kDa MW cutoff). The solution was stirred overnight with a ratio of 0.5 g activated carbon per gram of alginate. After being stirred for 15 hours, the solution was filtered for removal of the activated carbon. Finally, the filtrate was freeze-dried and stored at -20°C to avoid the hygroscopic phenomenon.
^{1}H NMR (D_2O, 600 MHz): 3.96 ppm (m).
FT-IR [cm^{-1}]: 3325, 1596, 1407, 1297, 1088, 1028, 625.

Preparation of Alginate/α-PLL conjugated Ciprofloxacin 11 Nanoparticles

Solutions of 1 mg/ml Alginate (solution 1) and PLL-Ciprofloxacin (solution 2) were prepared in filtered pure water. The nanoparticles were prepared by mixing solutions

1 and 2 at different ratios. The tested ratios were 1:4, 1:3, 1:2, and 1:1 (Alg:PLL-Ciprofloxacin). Then, particle size, stability measurements and degradation study were carried out using a Zetasizer Nano ZS from MALVERN INSTRUMENTS (Malvern, UK). Disposable sizing cuvettes (DTS0012) were used for size measurements. Malvern Zetasizer Software Version 7.03 was used for data evaluation.

10.6.4 Spray coating of Titanium plates

Coating of Alginate / PLL-Ciprofloxacin Nanoparticles on Ti plate

Before being coated with alginate nanoparticles, the substrates were polished, and cleaned through ultrasonification in water, dichloromethane, acetone, methanol, and MilliQ water. The titan substrate was first coated with a Polyethylenimine (PEI) layer. The substrate was immersed for one minute in 5% (w/w) PEI solution, washed with pure water, and dried under nitrogen. Then, the substrates were spray-coated (three minutes) with an airbrush Aztek A470 from TESTORS (Vernon Hills, IL, USA), depositing approximately 20 µL of the Alg/PLL-ciprofloxacin nanoparticle solution. The particle formation process was carried out in MilliQ water with both 1 mg/mL of sodium alginate and peptides. Subsequently, the Ti plates were rinsed with an H_2O solution in an ultrasonic bath for 15 minutes. After the plates were dried under nitrogen flow, ellipsometry was used to measure coating thickness. Layer thicknesses were determined using a Multiskop from OPTREL (Sinzing, Germany) in the ellipsometry mode. Uncoated titanium plates were used as a reference. Data were collected in the x, y-mode at 70° as mean value of 16 data points in total. Evaluation of the data was carried out using Elli Version 3.2 from Optrel. More details about ellipsometry measurement can be found chapter 6.2.

10.6.5 Stability of NP coating and NP solution

Stability of Nanoparticles in aqueous solution

A solution of Alginate / PLL-Ciprofloxacin nanoparticle was prepared with a ratio of 1:3 in Phosphate-Buffered Saline solution (PBS) pH = 7.4 and added to the disposable sizing cuvettes. The particle's behavior was analyzed via dynamic light scattering with a Zeta Nano ZS device at 37°C for 50 hours.

Stability of NP coating on titanium

The coating stability was tested by immersing the coated substrate in PBS, pH = 7.4 at 37°C for 109 hours. The test was performed in triplicate to ensure the reproducibility.

Before each thickness measurement, the samples were washed with H_2O and dried under nitrogen flow.

10.6.6 Enzymatic degradation of Nanoparticles and coatings

The degradation study was carried out by incubation in trypsin containing buffer solution (PBS, pH = 7.4). A PLL hydrolysis reaction was initiated by adding trypsin to obtain a final concentration of 5 µg/ml at 37°C. The solutions were renewed daily to ensure degradation capability of trypsin. Before each measurement, the samples were washed with H_2O and dried under nitrogen flow. The test was performed in triplicate to ensure reproducibility.

The degradation of the Alg/peptide nanoparticles was accomplished through the addition of trypsin to the nanoparticle dispersion. Briefly, 1 mL Alg/PLL-ciprofloxacin nanoparticle suspensions were filled in a sizing cell and maintained at 37 °C. Trypsin solution was added in order to obtain final concentrations of 2.5 µg/mL. The degradation process was monitored via consecutive size measurements using the Zetasizer Nano ZS.

10.6.7 Enzyme-triggered release

For the tests 3 x 6 ml of particle solutions were prepared. Two solutions were treated with a concentration of 2 µg/ml and 5 µg/ml of trypsin. The last, was not treated with enzyme and was used as a control. After trypsin was added, the solutions were incubated at 37°C. Then, every 15 minutes, 1 mL of each sample was collected and inserted into a Vivaspin tube containing two vertical membranes with a cutoff of 5 kDa. The tube was centrifuged, and the ciprofloxacin concentration was determined using a V-630 UV-VIS Spectrophotometer from JASCO and a quartz glass Ultra-Micro Cell. A calibration curve was prepared by plotting different concentration of commercial ciprofloxacin hydrochloride versus their absorbances at λ = 278 nm and found to be linear in the concentration range of 2 to 10 µg/mL. This curve was then used to determine the concentration of ciprofloxacin released during the degradation process.

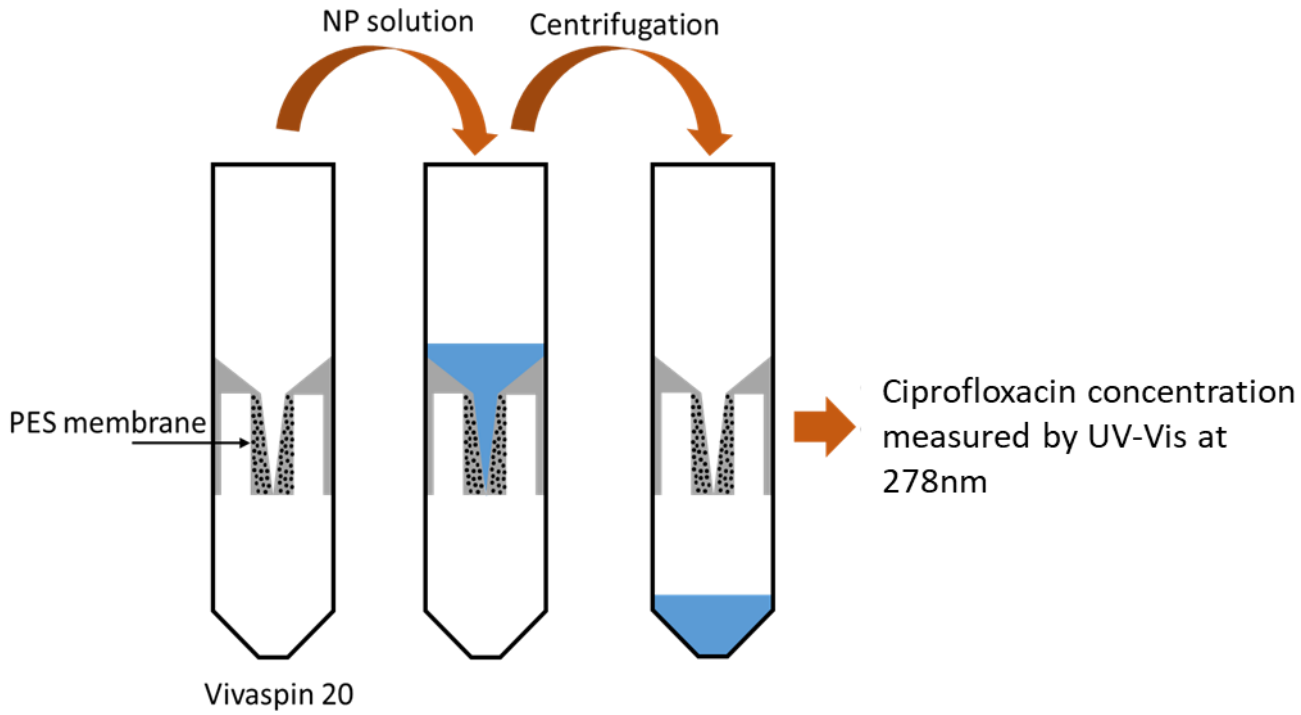

Figure 10-4 Schematic representation of vivaspin 20 tube.

10.6.1 Drug efficacy tests

The antimicrobial efficacy of the conjugated ciprofloxacin were investigated against *Staphylococcus aureus* at different concentrations (DSM 799, German Collection of Microorganisms and Cell Cultures, Braunschweig, Germany). *S. aureus* was cultured in tryptone soya broth supplemented with 10 % yeast extract (TSBY) for 18 hours at 37 °C. The preculture was adjusted to an optical density (600 nm) of 0.001 in TSBY and added to 96-well plate (100 µL/well). The conjugated ciprofloxacin's were diluted 1:2 in TSBY as a 5-fold dilution series. In order to prevent nutrient reduction, the first dilution was prepared in 2-fold TSBY. In the same way, ciprofloxacin and MilliQ water were diluted and served as controls. The dilution series were added to *S. aureus* in 96-well plate (100 µL/well) and cultivated for 24 hours under shaking (400 rpm) at 37 °C. Afterwards, the optical density (600 nm) was measured by microplate reader (infinite M200PRO, Tecan, Männedorf, Switzerland). The absorption values were normalized against the positive control, which was a *S. aureus* culture in TSBY under the same cultivation conditions.

11 Appendix

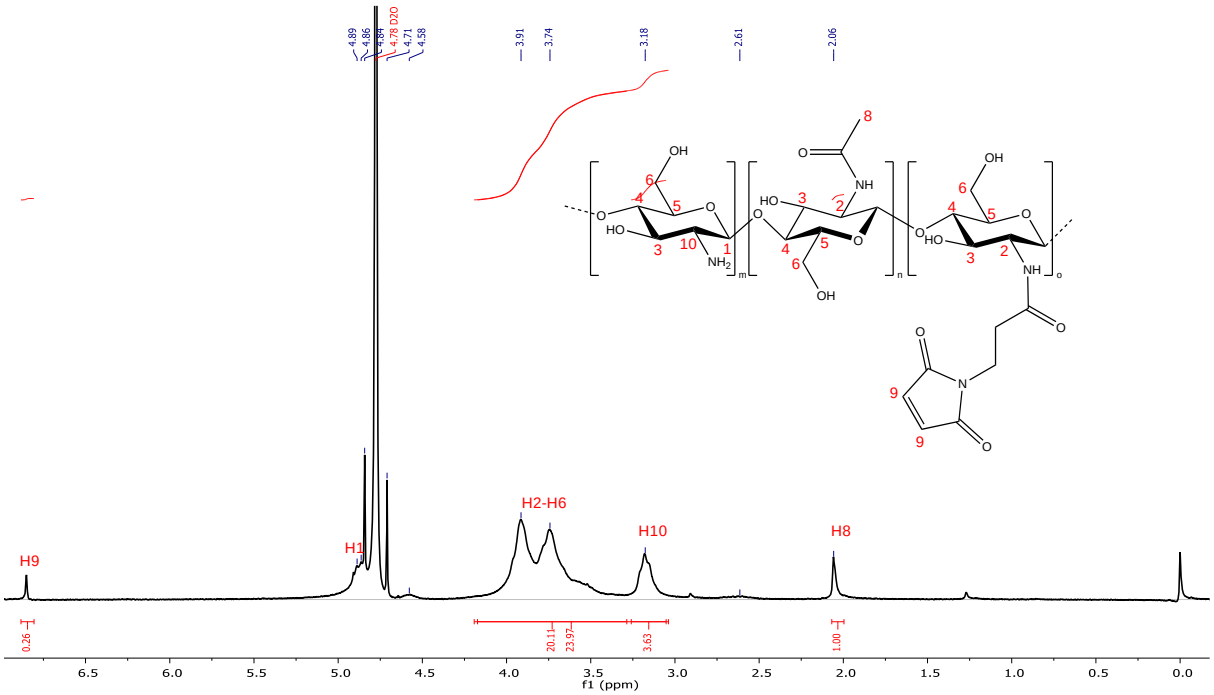

Attached file 1 ^{1}H-NMR-spectrum and peak assignment for Chitosan maleimide in D_2O.

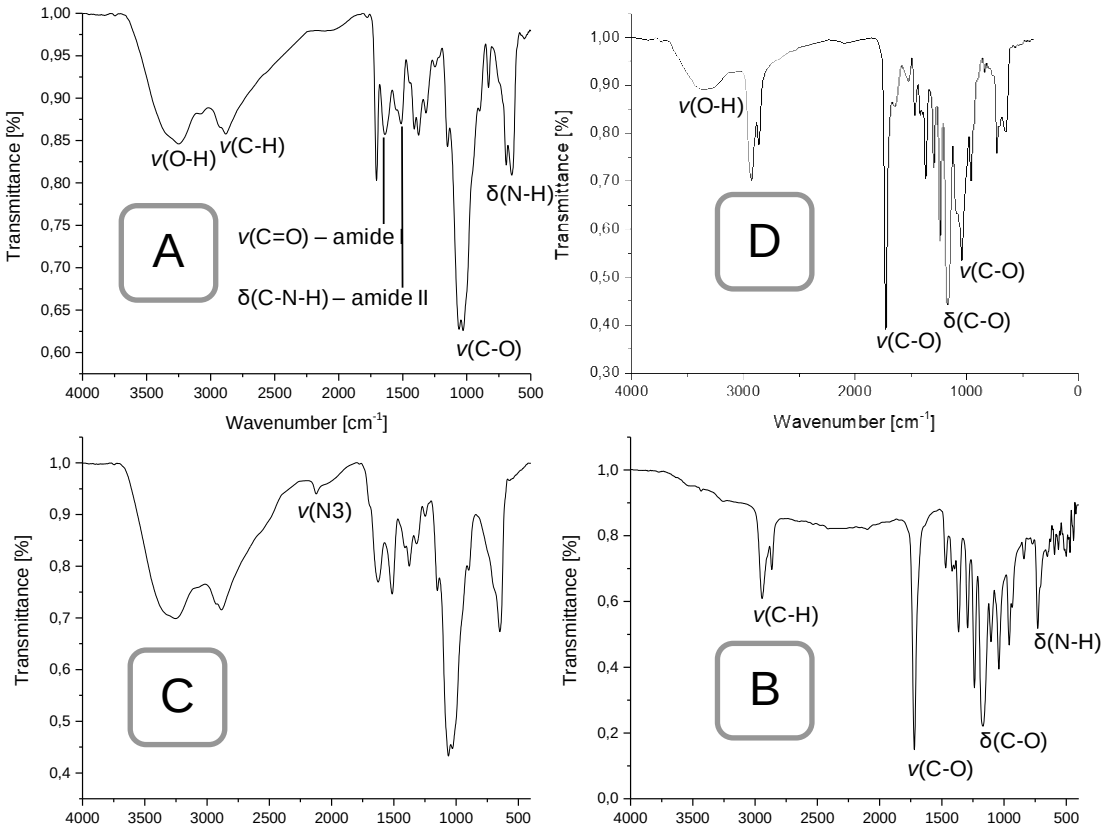

Attached file 2 FT-IR spectrum of A: Chitosan maleimide, B: propargyl-terminated poly-ε-caprolactone, C: CS-[Poly-L-lysine$_{20}$-N$_3$], D: Chitosan-g-[PLL-poly-ε-Caprolactone].

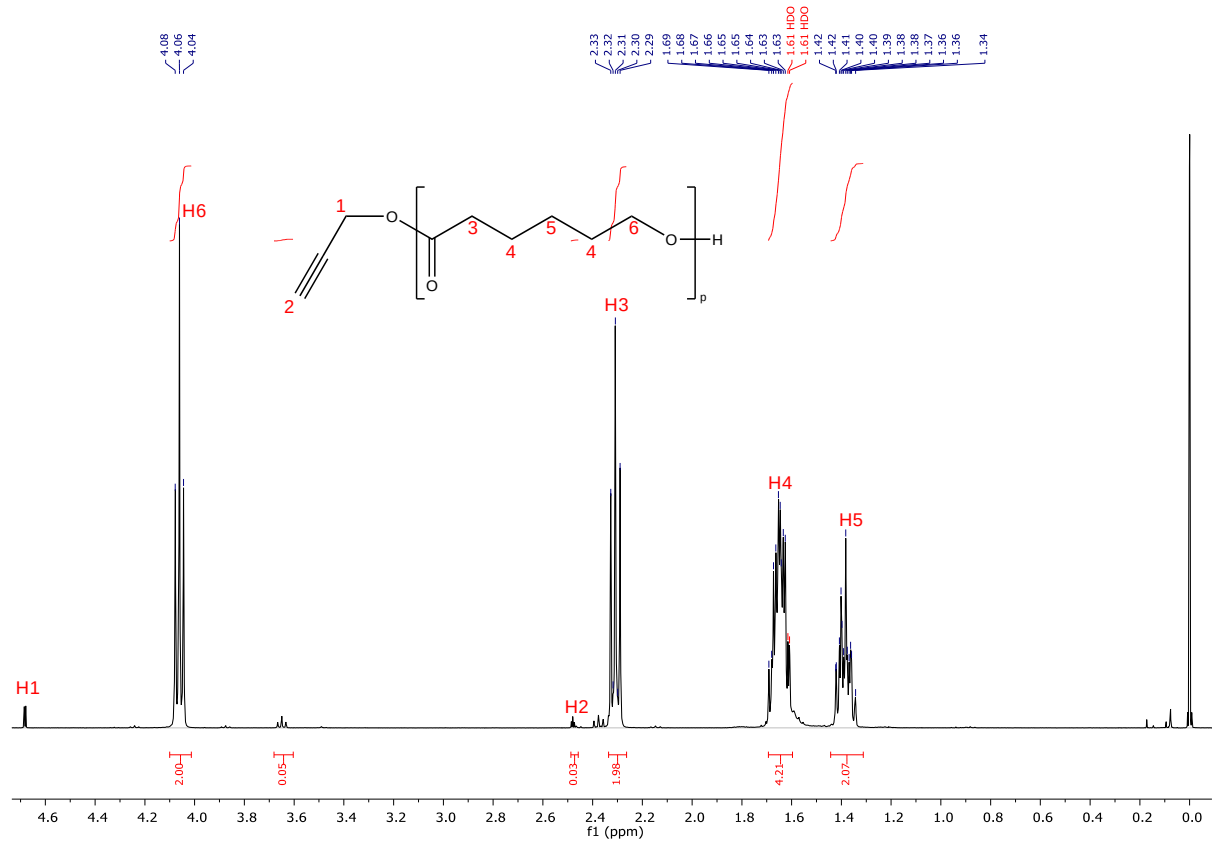

Attached file 3 ^{1}H-NMR spectrum and peak assignment for propargyl-terminated poly-ε-caprolactone in $CDCl_3$.

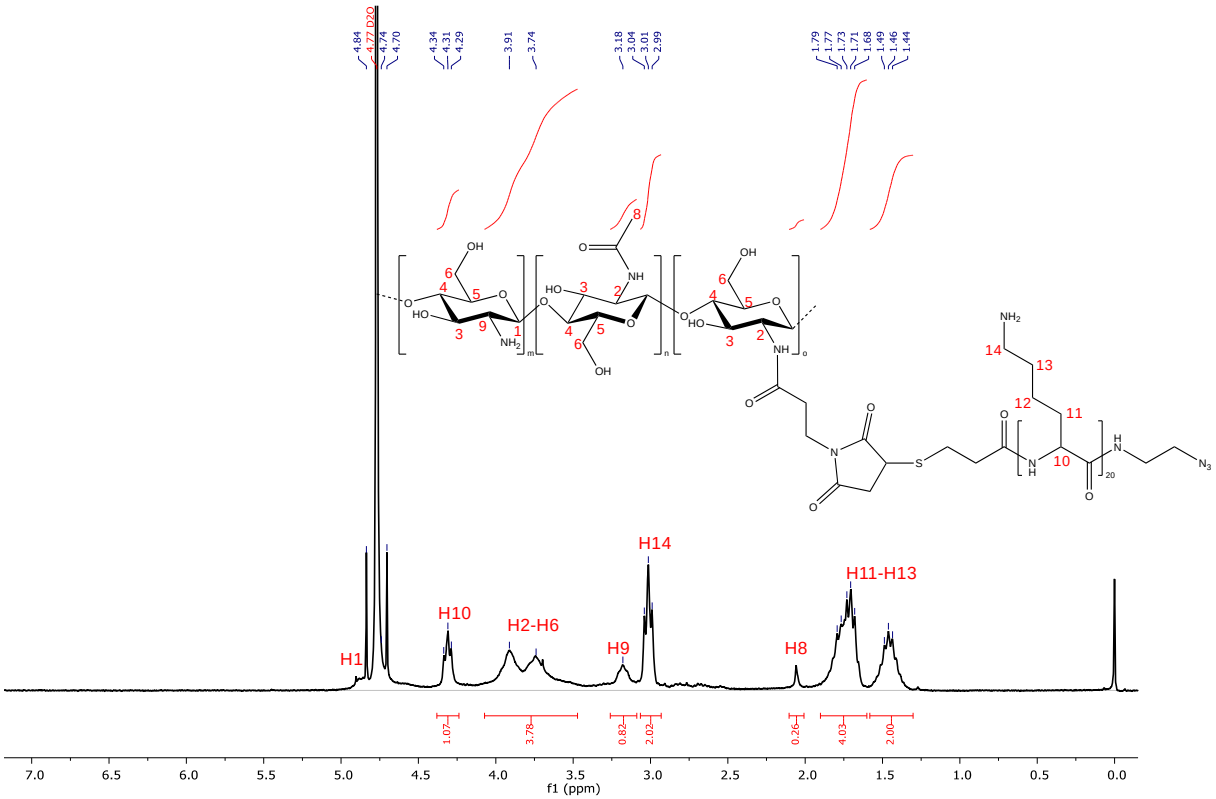

Attached file 4 ^{1}H-NMR-spectrum and peak assignment for CS-[Poly-L-lysine$_{20}$-N_3] in D_2O.

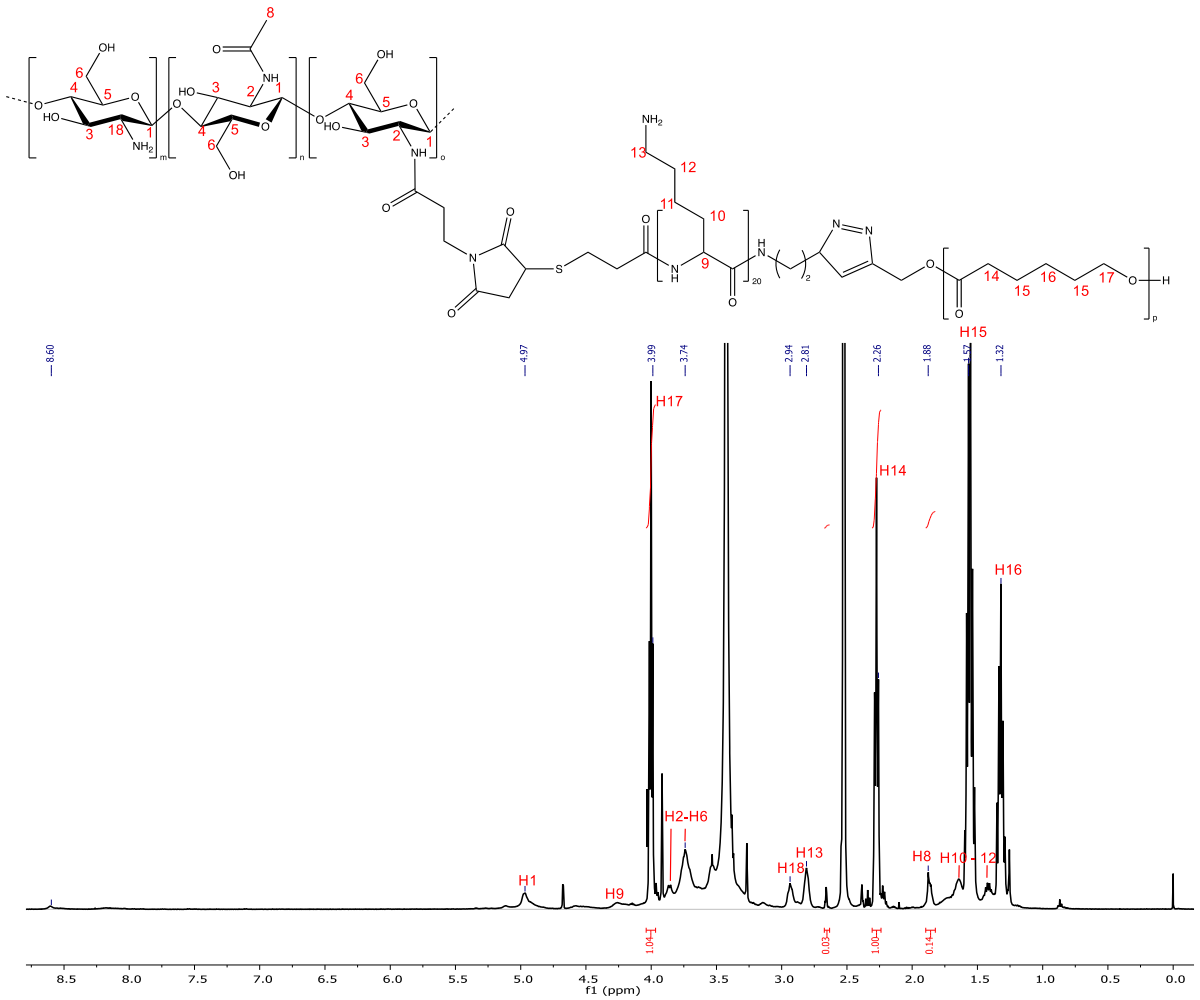

Attached file 5 ^{1}H-NMR spectrum and peak assignment for Chitosan-g-[poly-L-lysine-b-poly-ε-Caprolactone] in deuterated DMSO/D_2O.

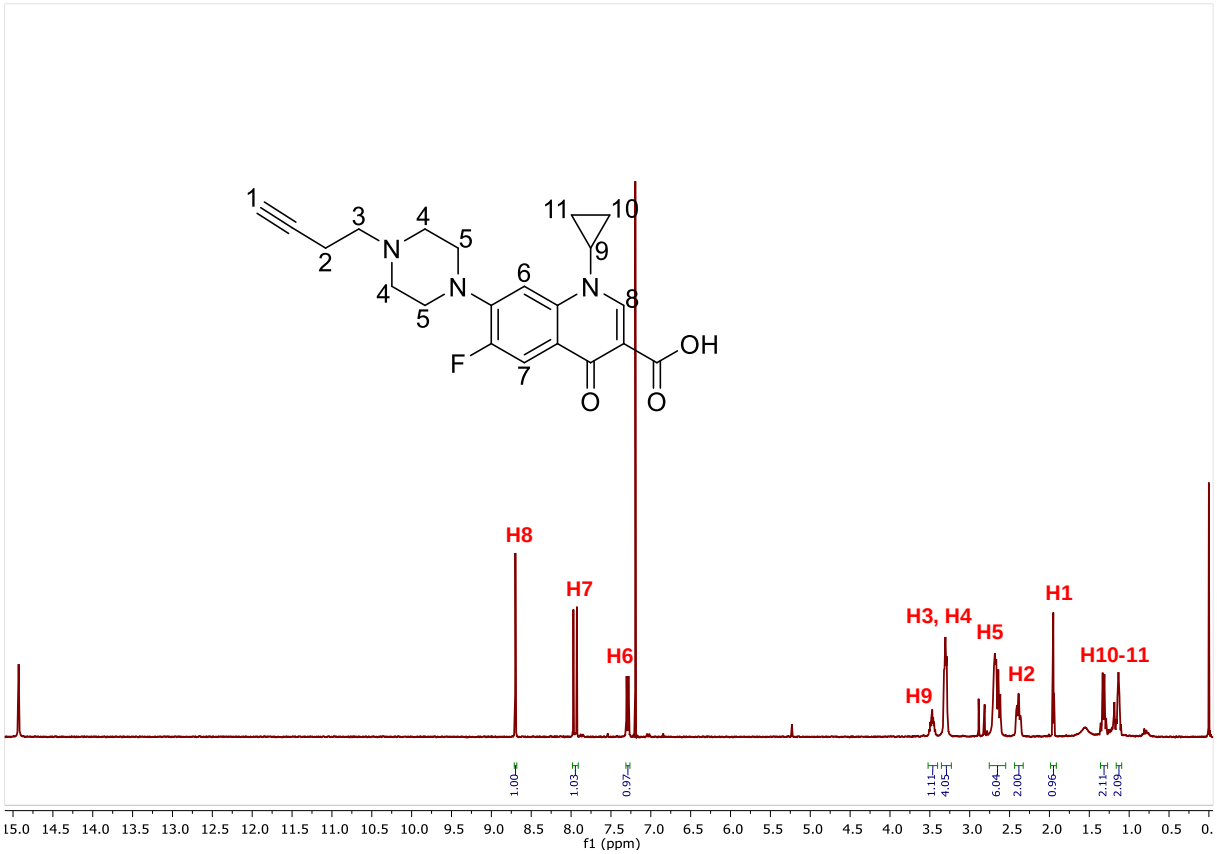

*Attached file 6 ^{1}H-NMR spectrum and peak assignment for modified ciprofloxacin **5** in deuterated $CDCl_3$.*

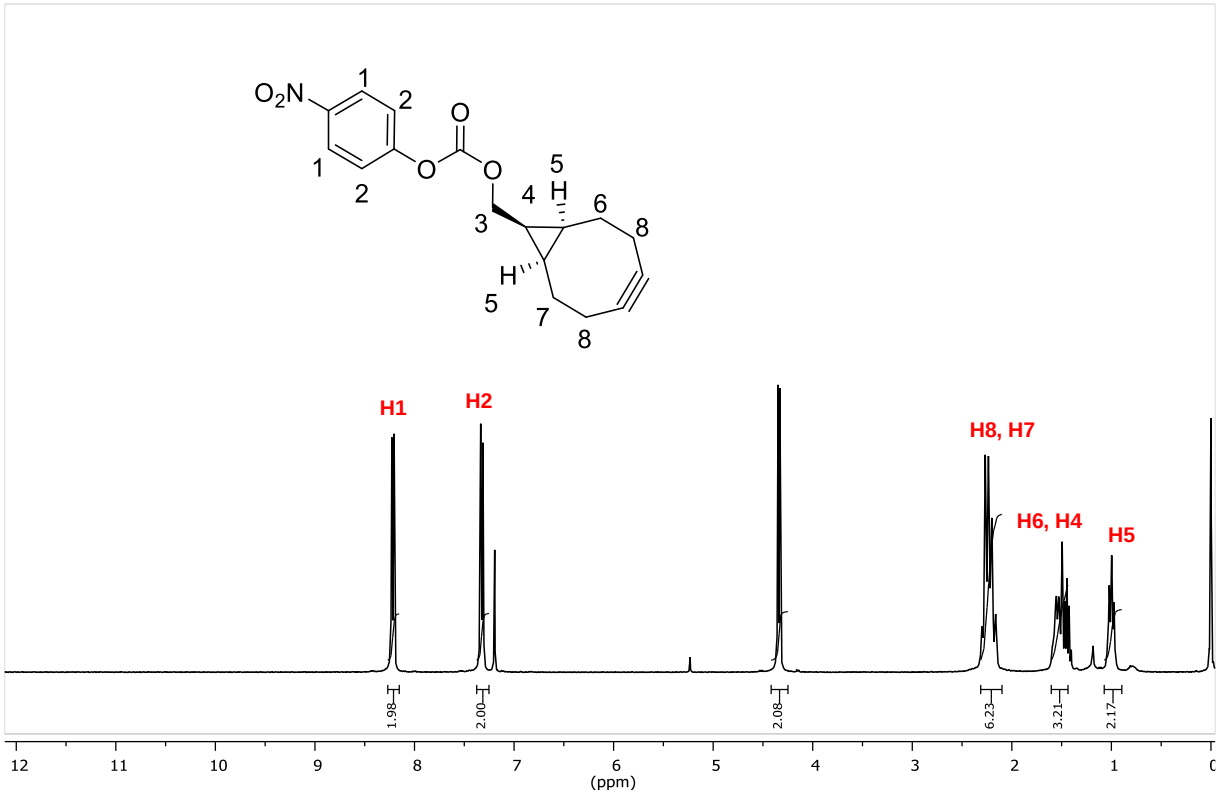

Attached file 7 ^{1}H-NMR spectrum and peak assignment for BCN-O(CO)O(4-NO_2-Ph) in deuterated $CDCl_3$.

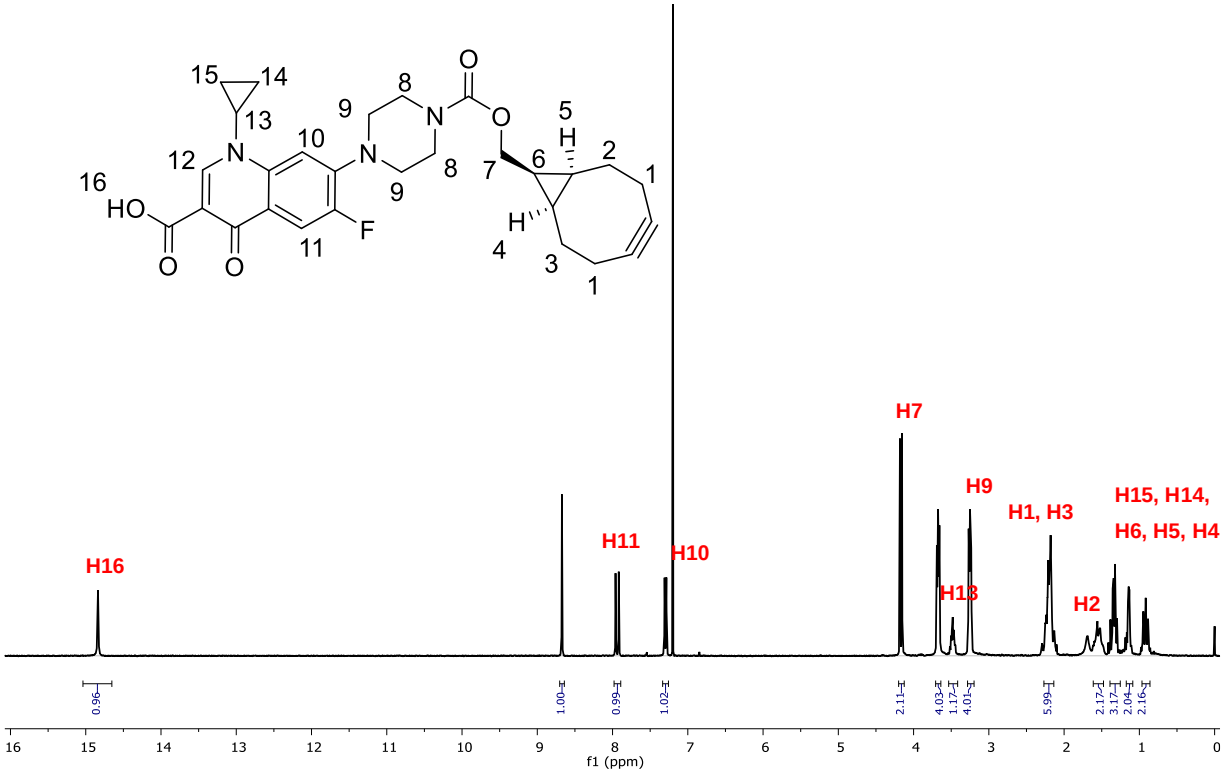

Attached file 8 ^{1}H-NMR spectrum and peak assignment for BCN-O(CO)HN-Ciprofloxacin in deuterated $CDCl_3$.

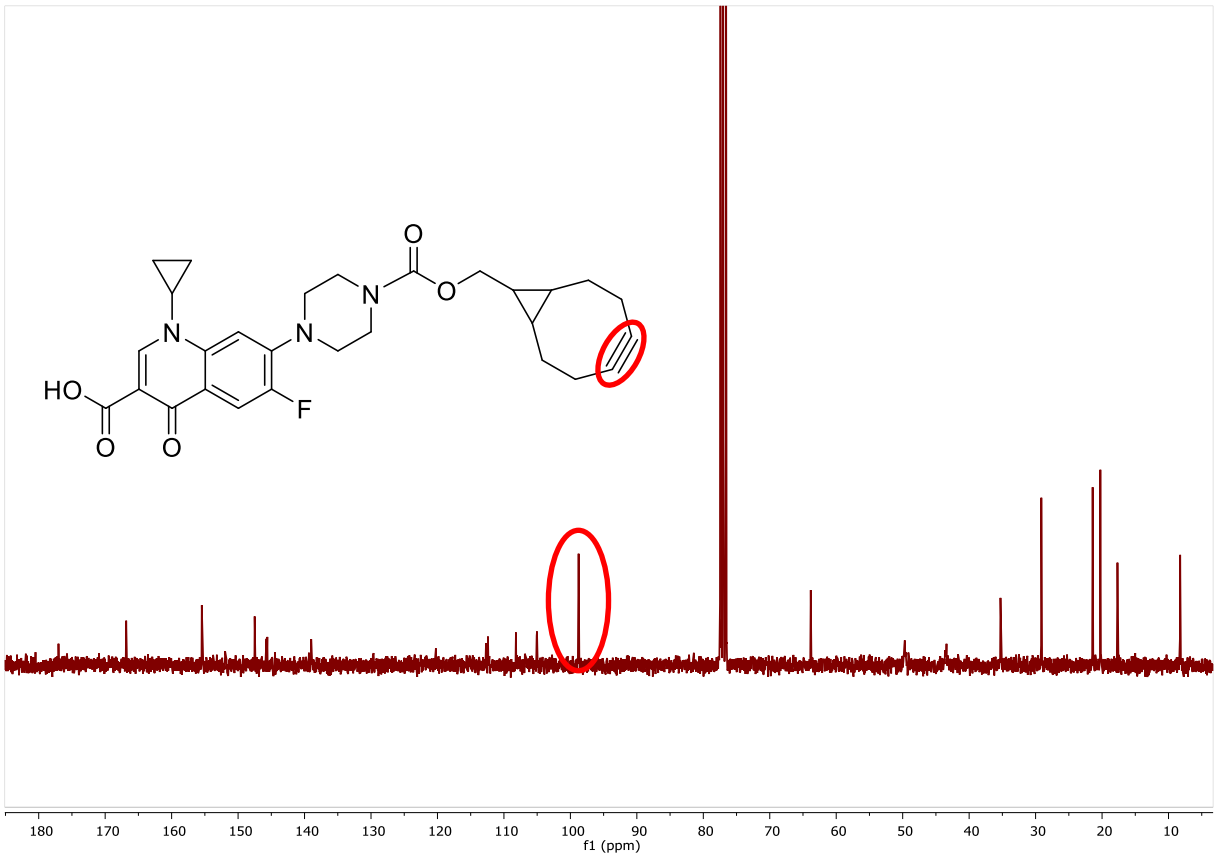

Attached file 9 ^{13}C-NMR spectrum and peak assignment for BCN-O(CO)HN-Ciprofloxacin in deuterated $CDCl_3$.

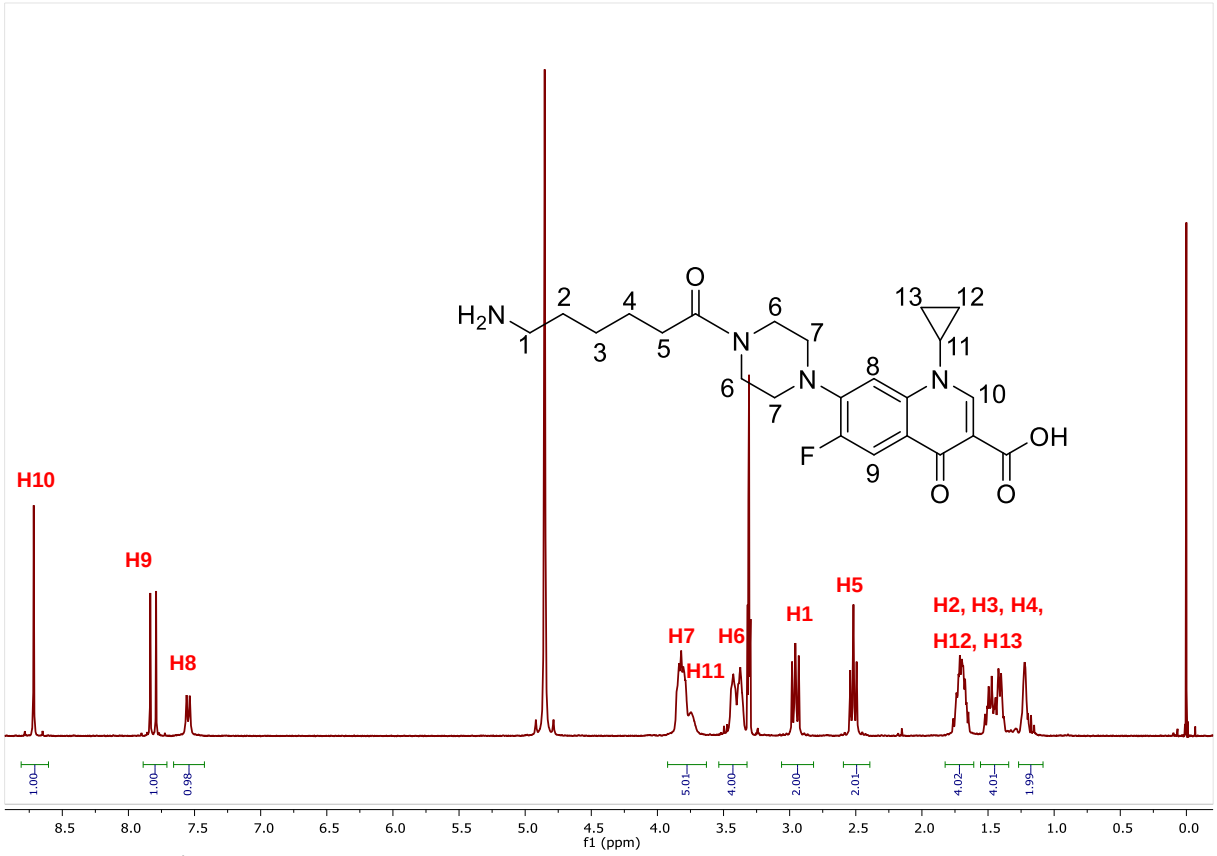

Attached file 10 ^{1}H-NMR spectrum and peak assignment for $_{2}$HN-$(CH_2)_5$Ciprofloxacin in deuterated MeOH.

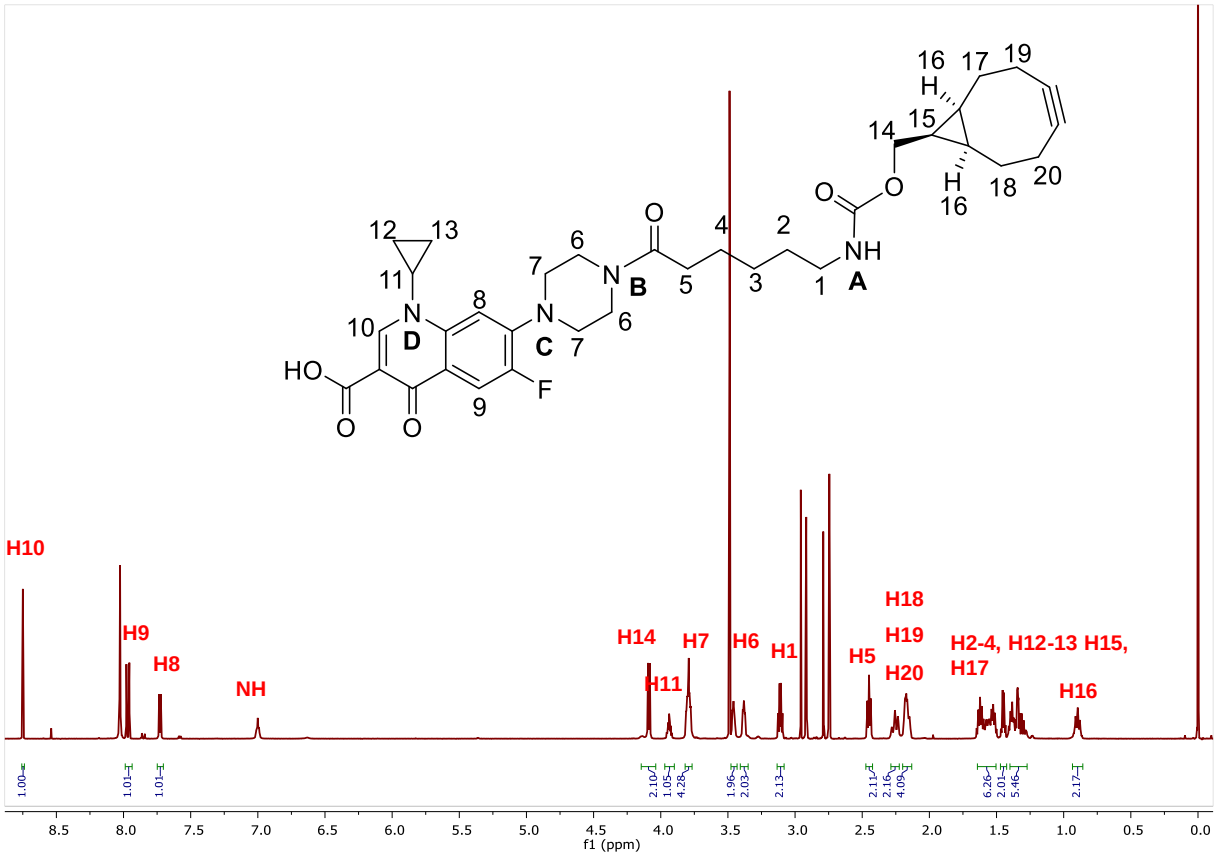

Attached file 11 ^{1}H-NMR spectrum and peak assignment for BCN-O(CO)HN-$_{2}$HN-(CH$_{2}$)$_{5}$Ciprofloxacin in deuterated DMF.

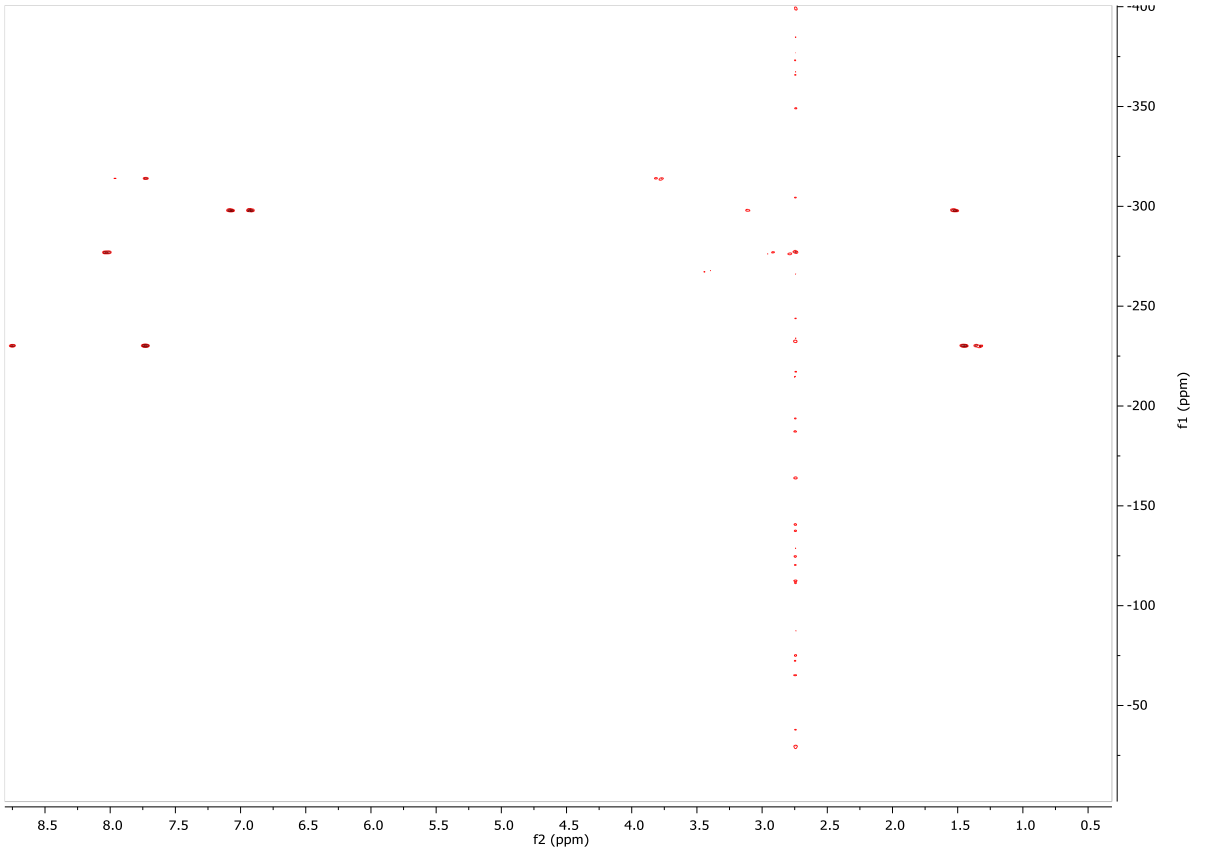

Attached file 12 2D-NH-HMBC spectrum of BCN-O(CO)HN-$_{2}$HN-(CH$_{2}$)$_{5}$Ciprofloxacin in deuterated DMF.

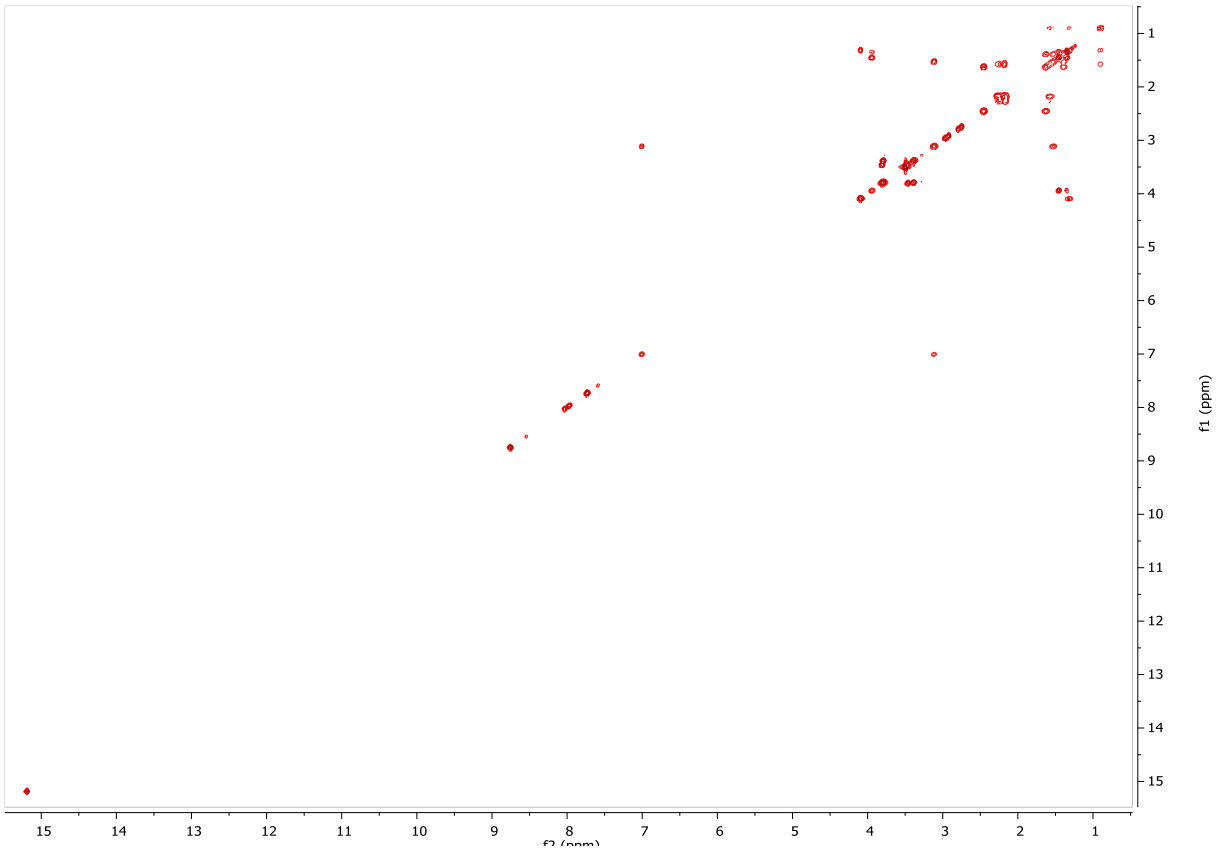

Attached file 13 2D-COSY spectrum of BCN-O(CO)HN-$_2$HN-$(CH_2)_5$Ciprofloxacin in deuterated DMF.

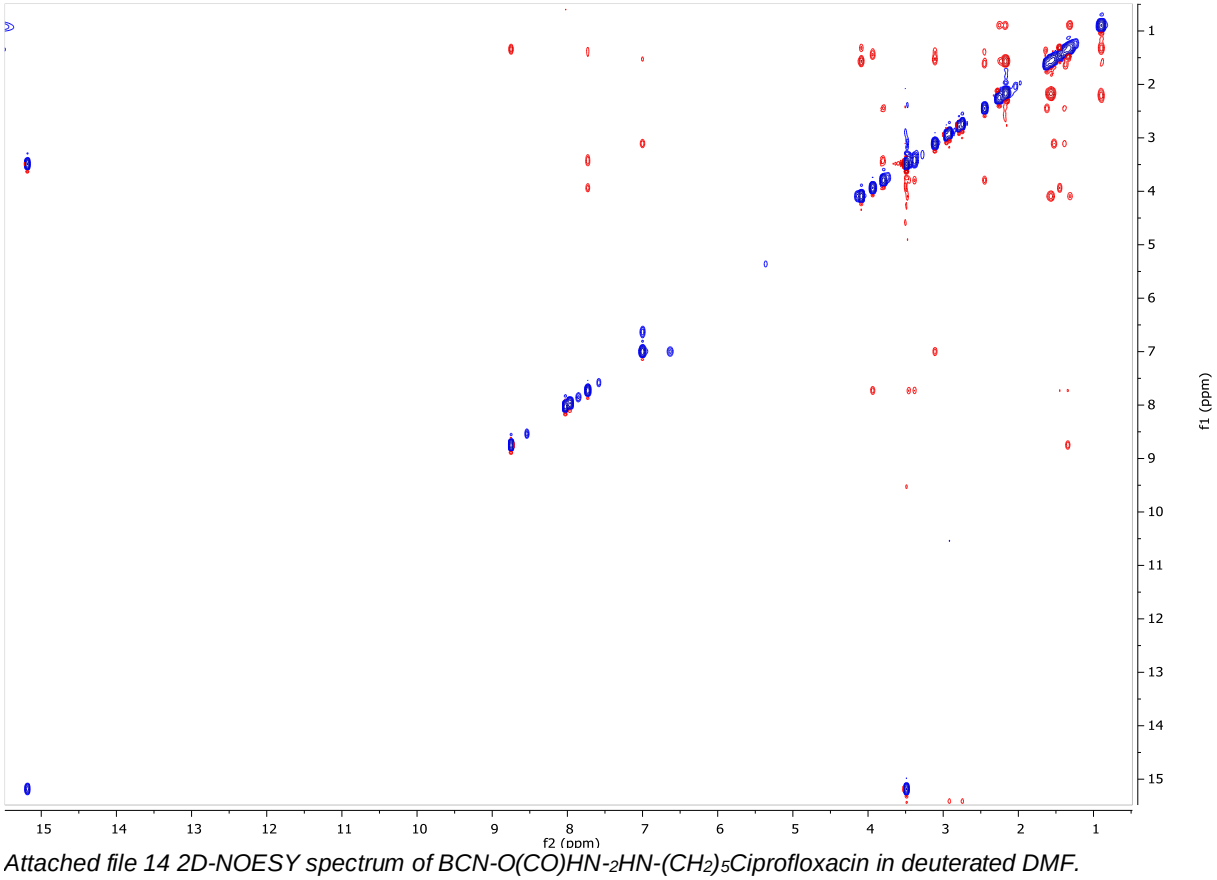

Attached file 14 2D-NOESY spectrum of BCN-O(CO)HN-$_2$HN-$(CH_2)_5$Ciprofloxacin in deuterated DMF.

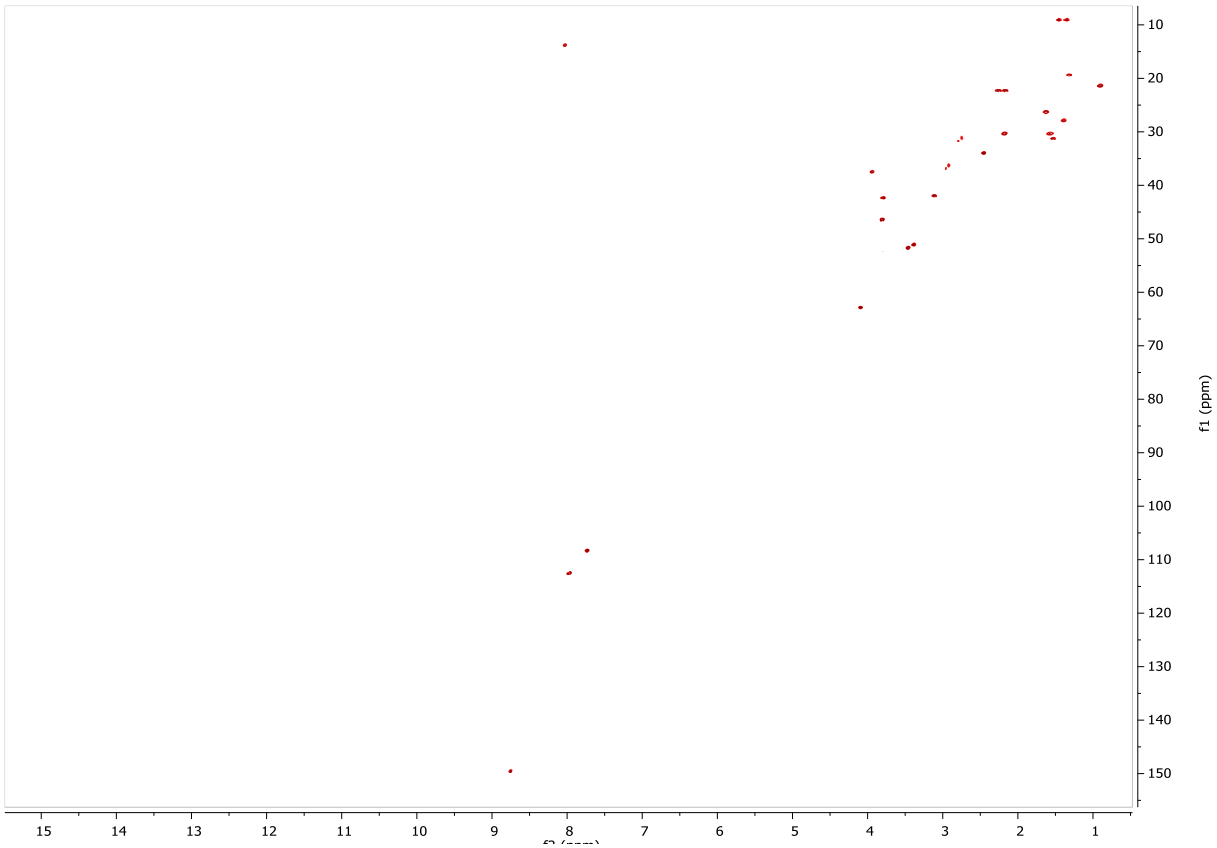

Attached file 15 2D-HSQC spectrum of BCN-O(CO)HN-$_2$HN-$(CH_2)_5$Ciprofloxacin in deuterated DMF.

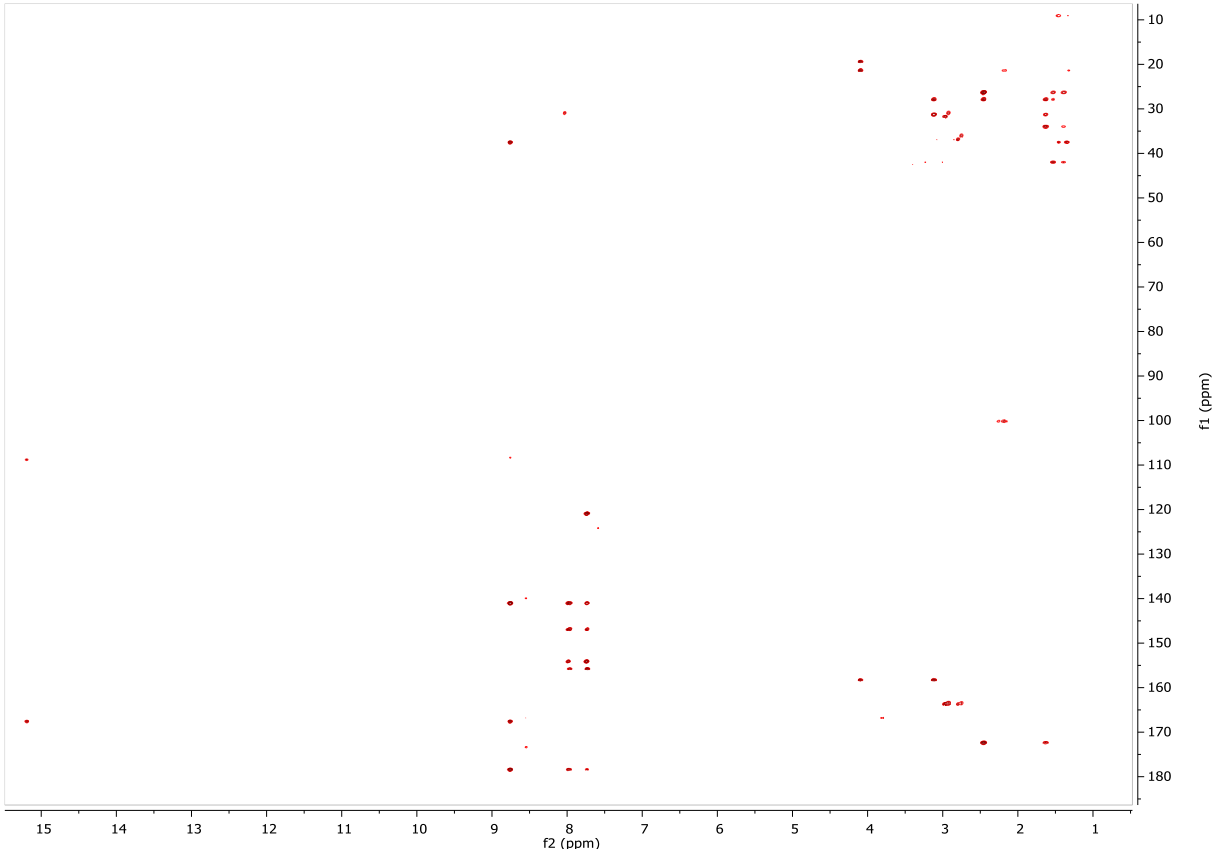

Attached file 16 2D-HMBC spectrum of BCN-O(CO)HN-$_2$HN-$(CH_2)_5$Ciprofloxacin in deuterated DMF.

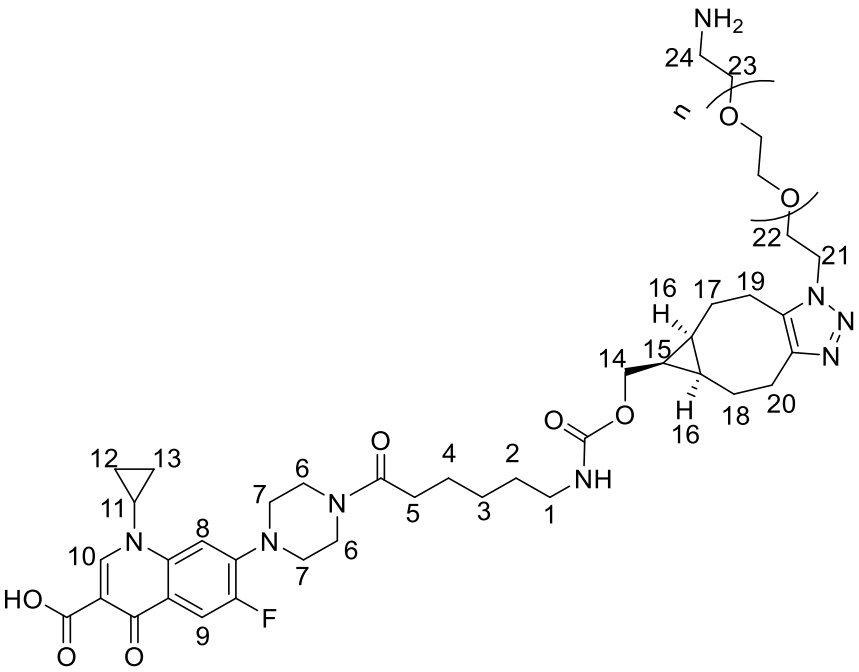

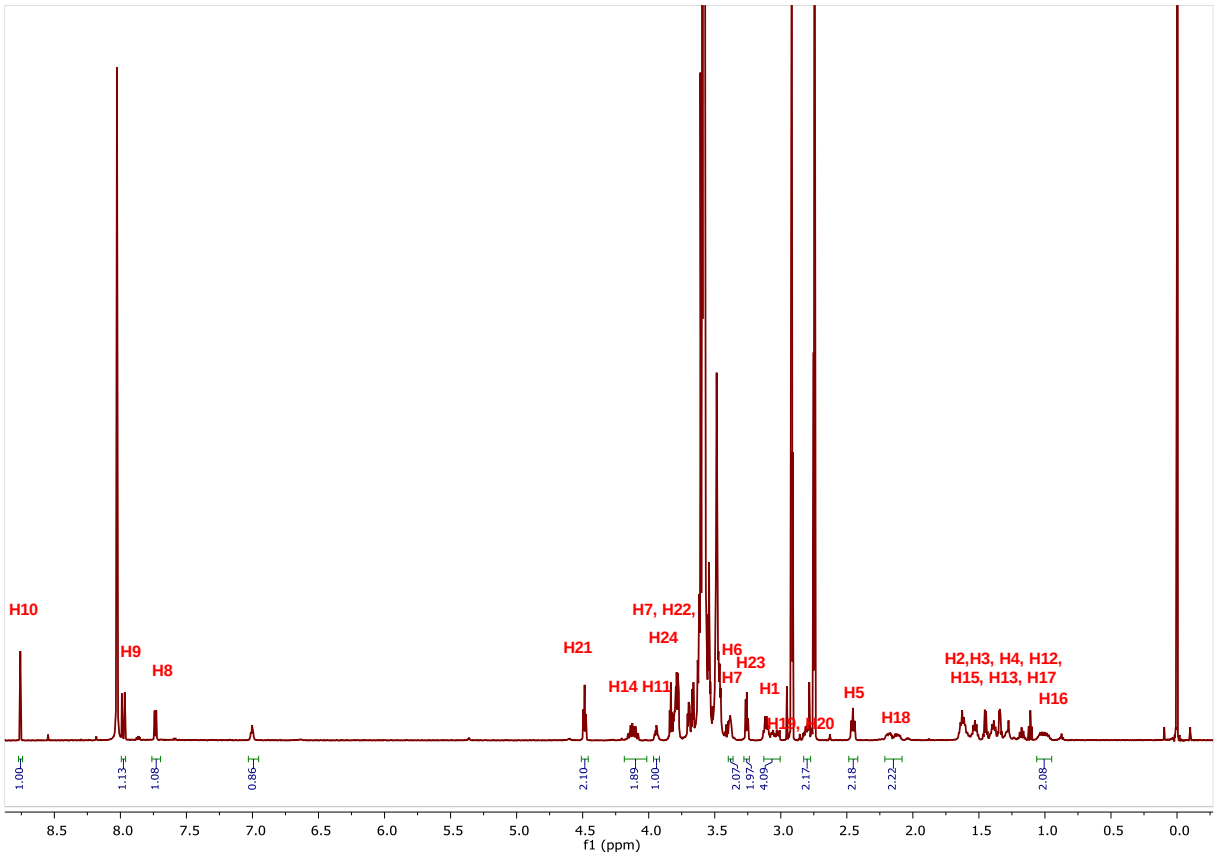

Attached file 17 ^{1}H-NMR spectrum and peak assignment for $_{2}$HN-PEG-BCN-O(CO)HN-$_{2}$HN-(CH$_{2}$)$_{5}$Ciprofloxacin 13b in deuterated DMF.

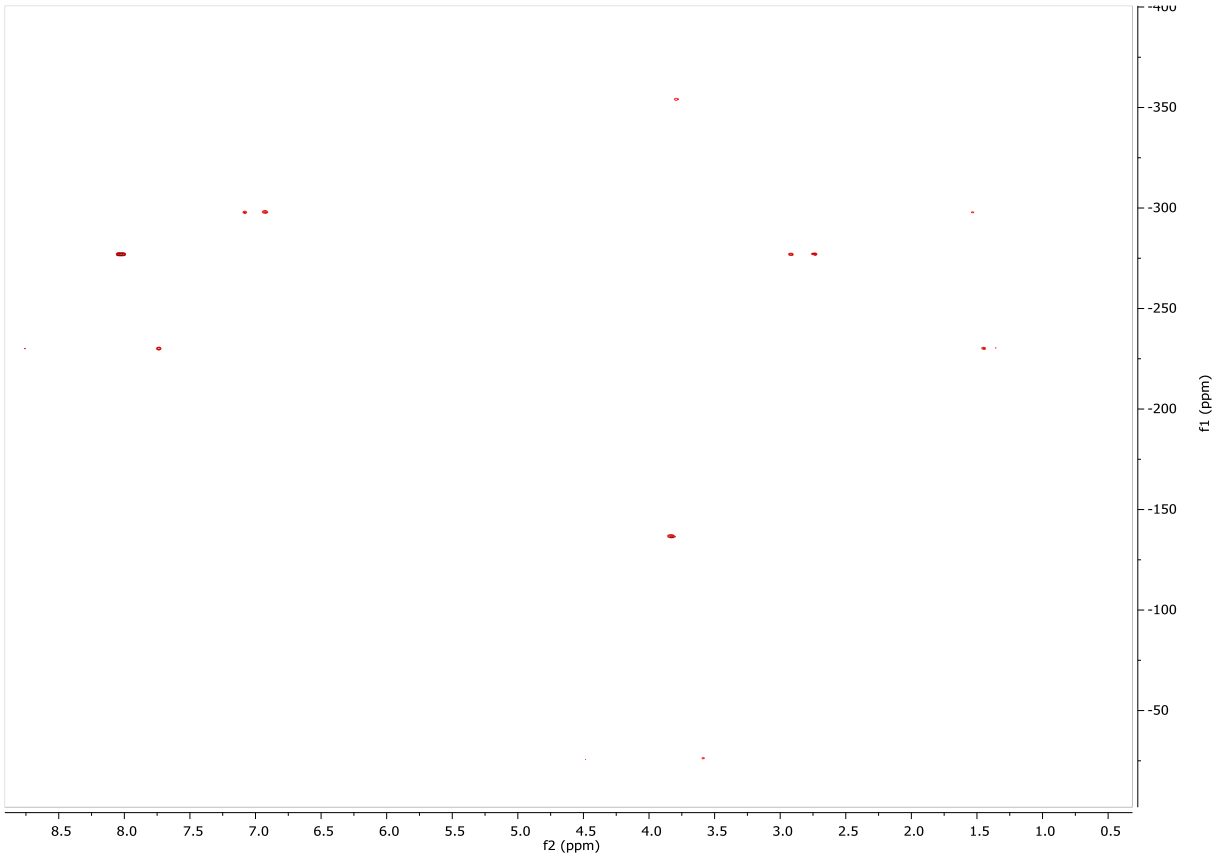

Attached file 18 2D-NH-HMBC spectrum of $_2$HN-PEG-BCN-O(CO)HN-$_2$HN-(CH$_2$)$_5$Ciprofloxacin in deuterated DMF.

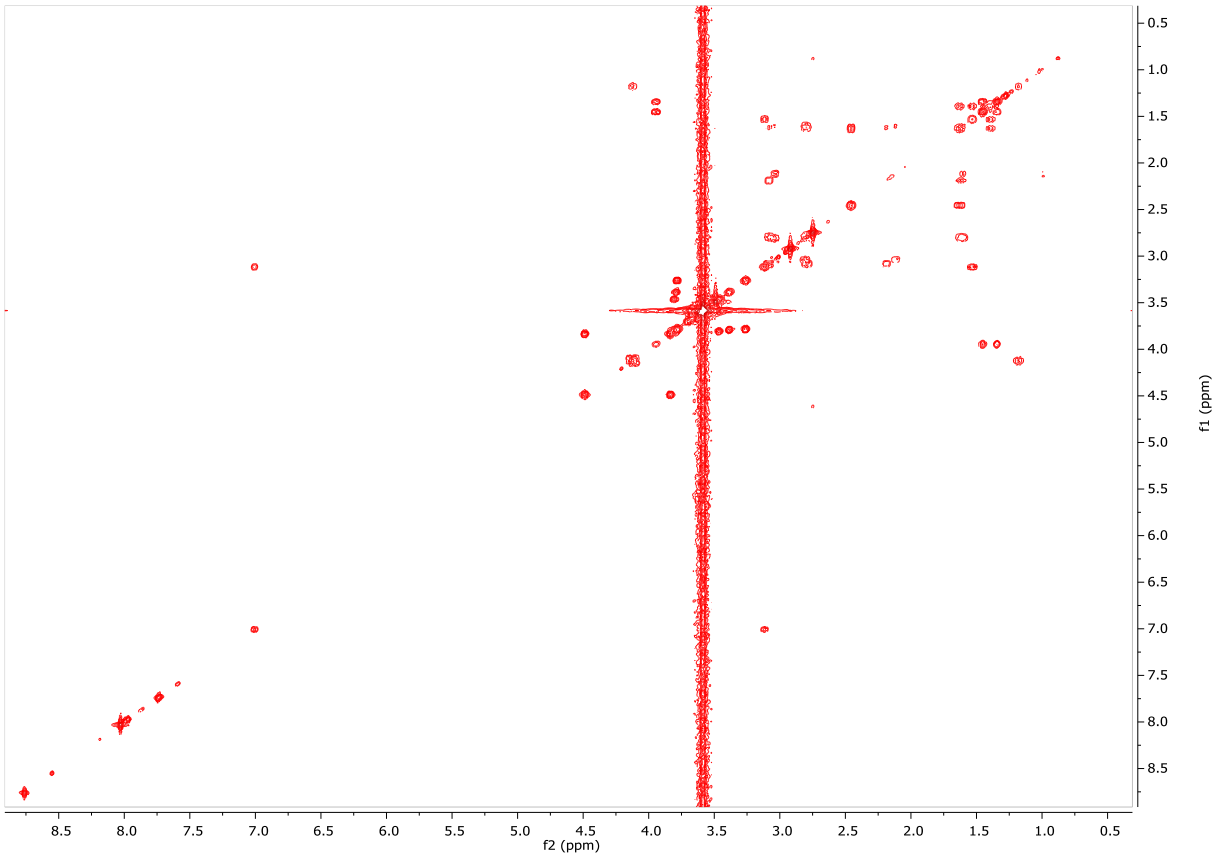

Attached file 19 2D-COSY spectrum of $_2$HN-PEG-BCN-O(CO)HN-$_2$HN-(CH$_2$)$_5$Ciprofloxacin in deuterated DMF.

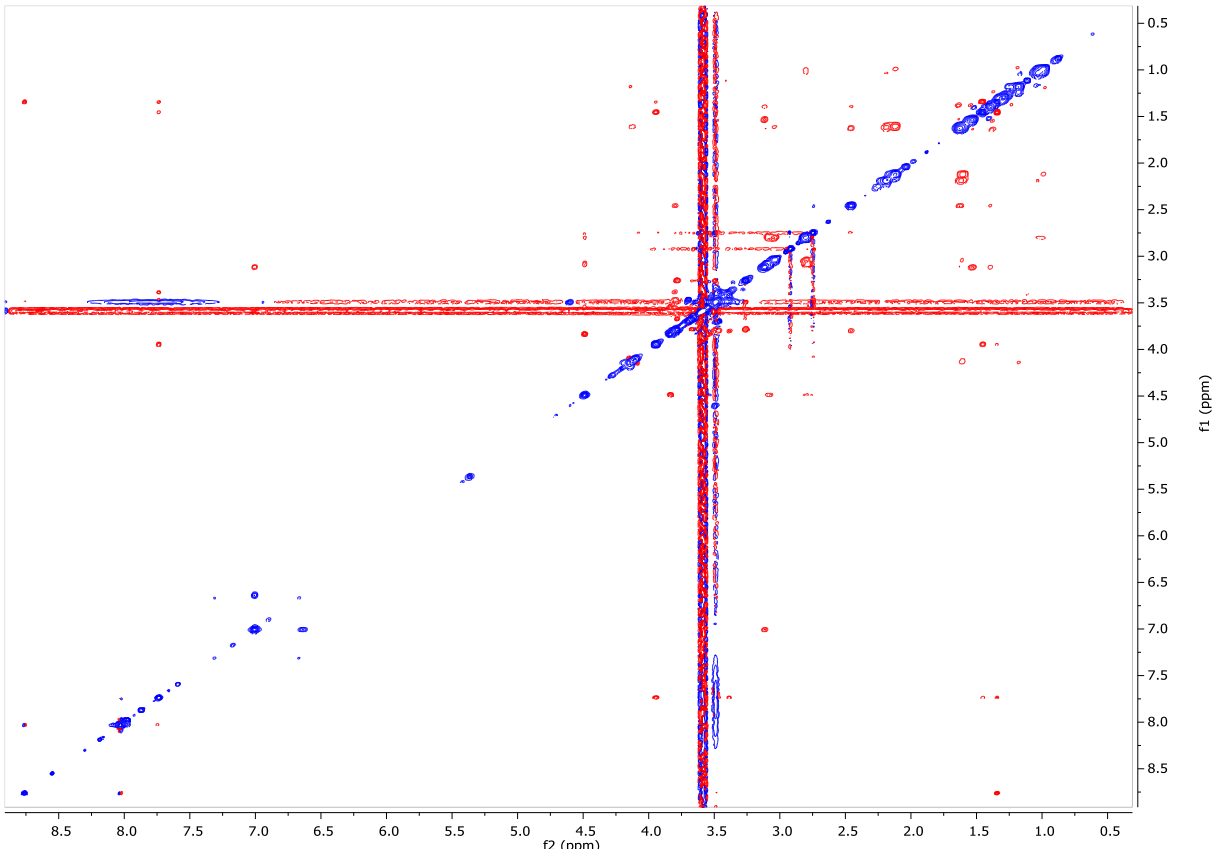

Attached file 20 2D-NOESY spectrum of $_2$HN-PEG-BCN-O(CO)HN-$_2$HN-$(CH_2)_5$Ciprofloxacin in deuterated DMF.

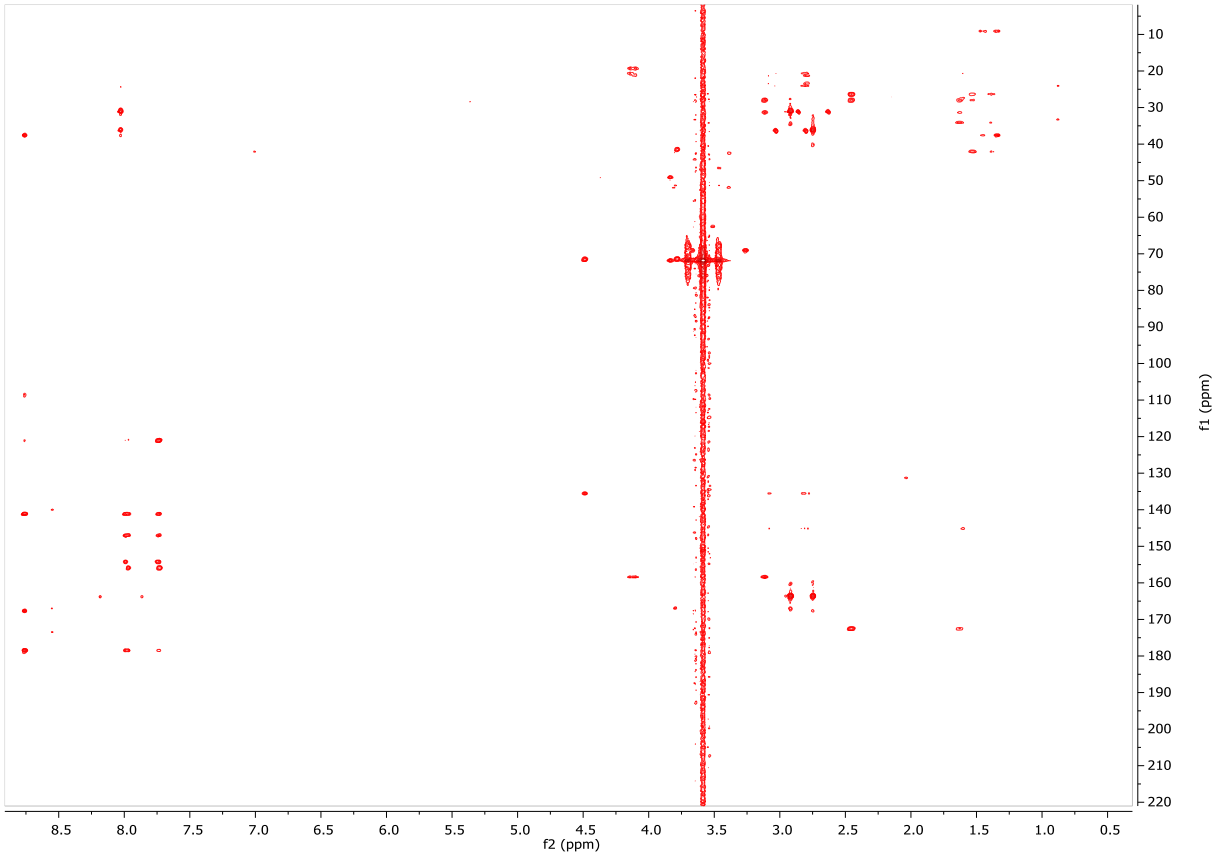

Attached file 21 2D-HMBC spectrum of $_2$HN-PEG-BCN-O(CO)HN-$_2$HN-$(CH_2)_5$Ciprofloxacin in deuterated DMF.

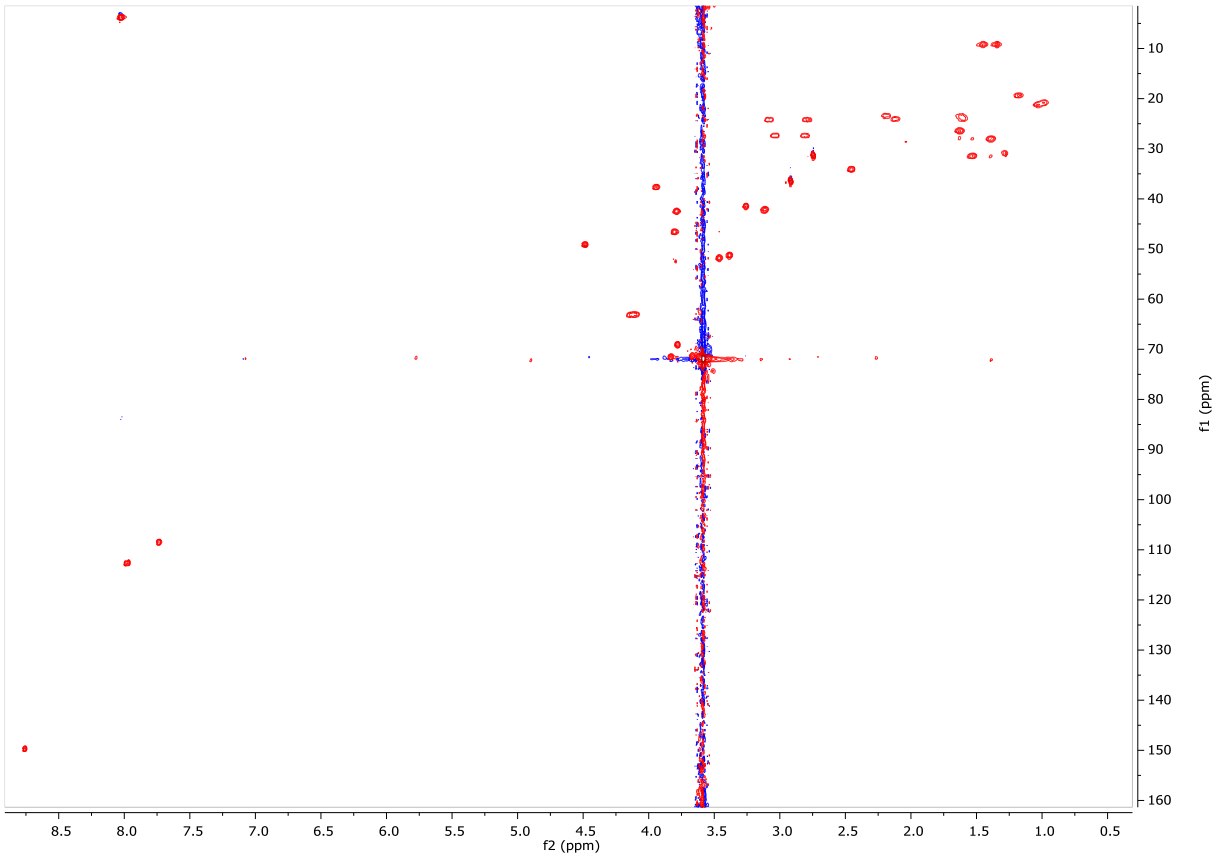

Attached file 22 2D-HSQC spectrum of $_2$HN-PEG-BCN-O(CO)HN-$_2$HN-(CH$_2$)$_5$Ciprofloxacin in deuterated DMF.

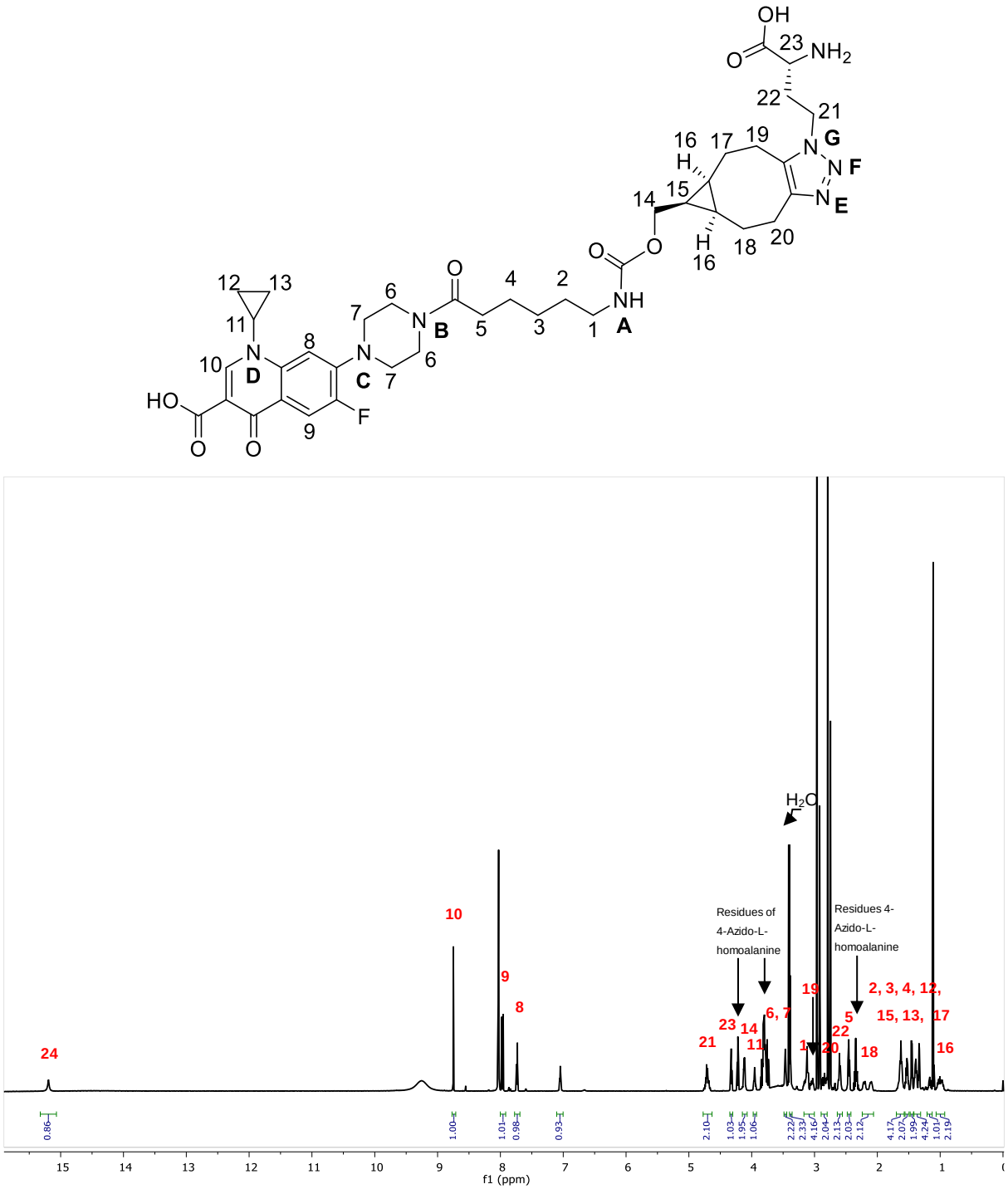

*Attached file 23 ^{1}H-NMR spectrum and peak assignment for substance **14b** in deuterated DMF.*

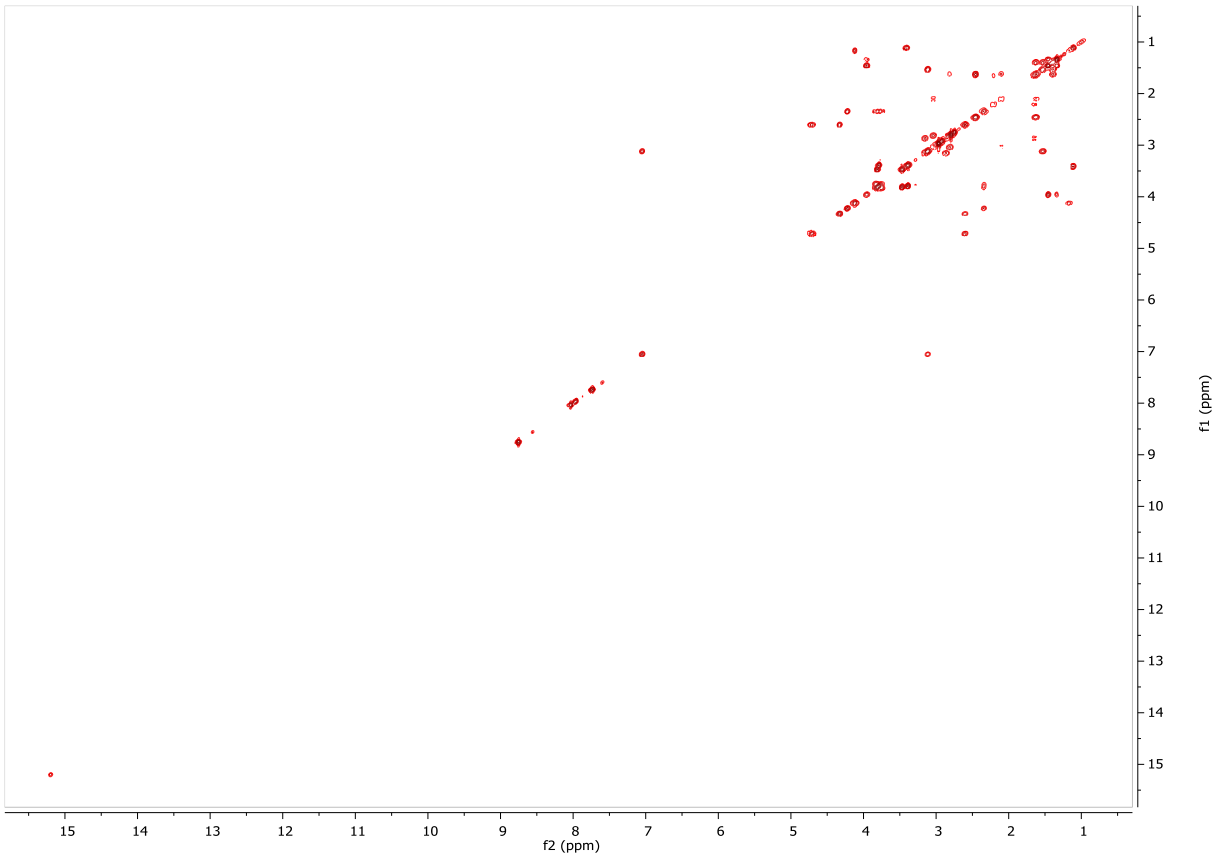

*Attached file 24 2D-COSY spectrum of substance **14b** in deuterated DMF.*

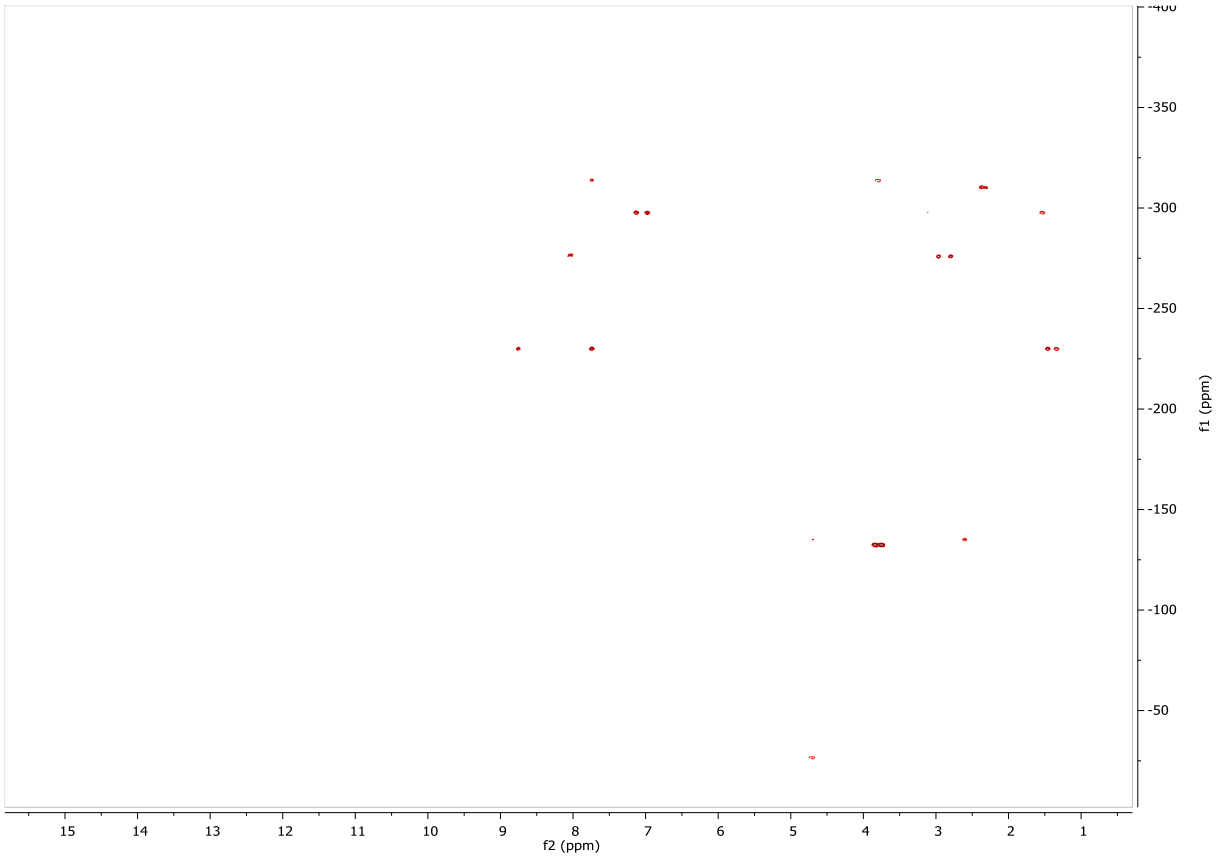

*Attached file 25 2D-NH-HMBC spectrum of substance **14b** in deuterated DMF.*

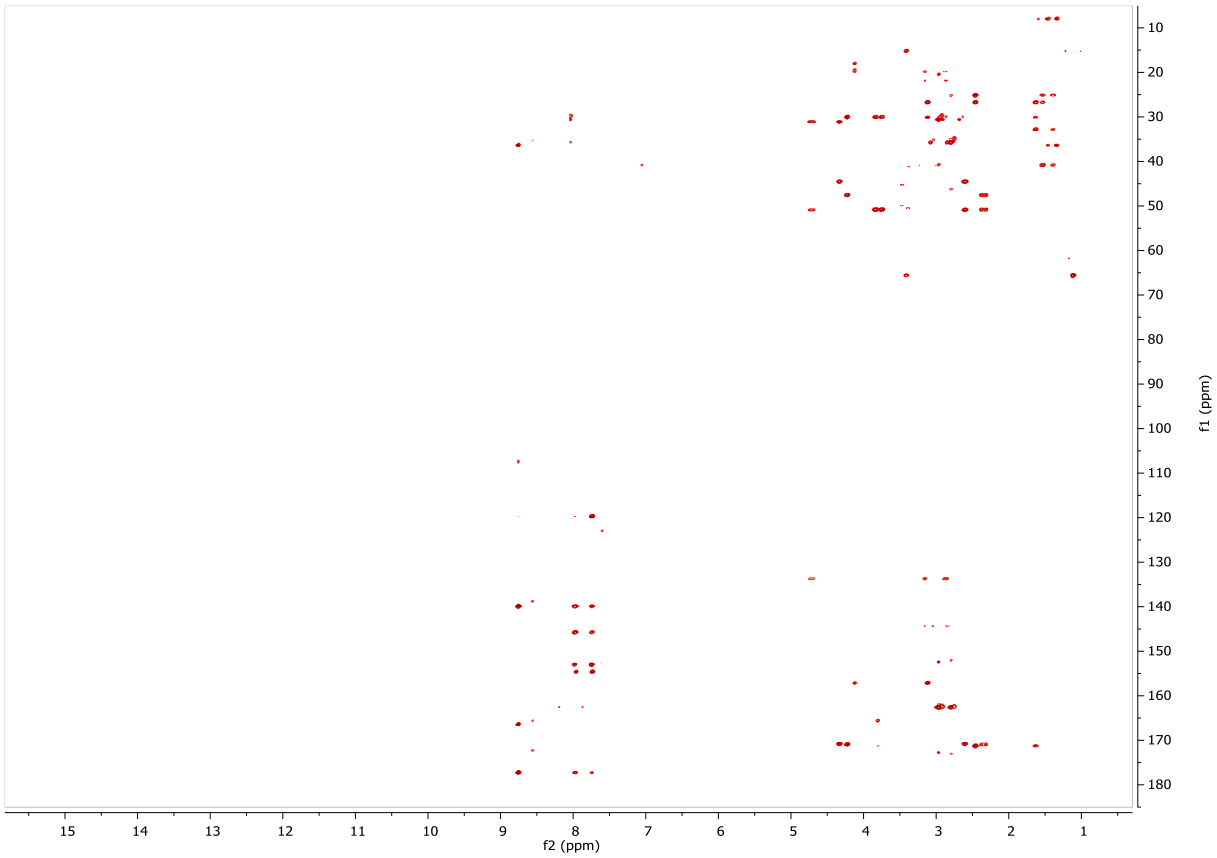

*Attached file 26 2D-HMBC spectrum of substance **14b** in deuterated DMF.*

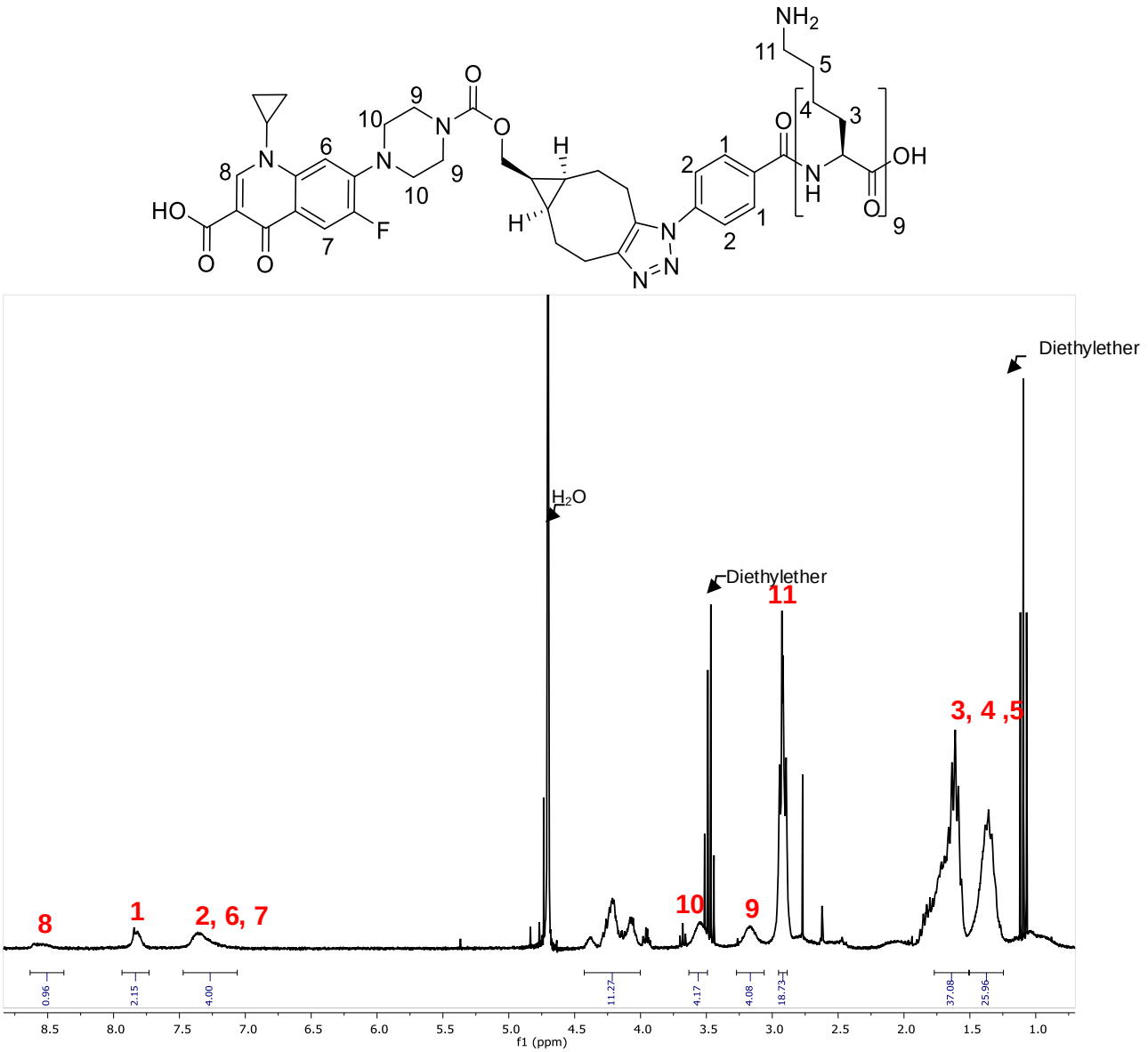

*Attached file 27 ^{1}H-NMR spectrum and peak assignment for Ciprofloxacin-poly-L-lysine **11** in deuterated H_2O.*

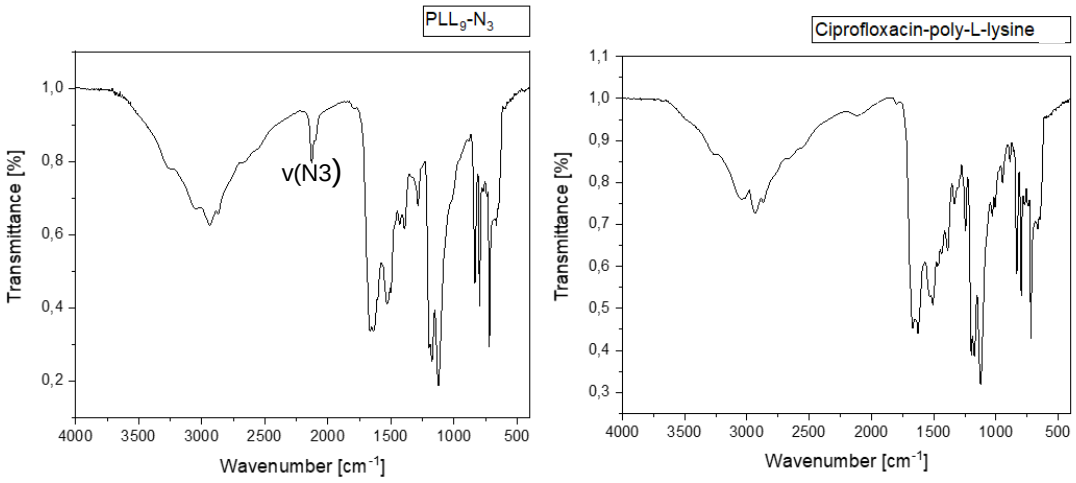

Attached file 28 FT-IR spectra of PLL_9-N_3 and Ciprofloxacin-poly-L-lysine

[1] N. R. Patel and P. P. Gohil, *Int. J. Emerging Technol. Adv. Eng.* **2012**, *2*, 31.

[2] Y. Sato, N. Kitagawa, A. Isobe, *Jpn. Dent. Sci. Rev.* **2018**, *54*, 45–51.

[3] S. Annibali, M. Ripari, G. La Monaca, F. Tonoli, M. P. Cristalli, *Oral Implantol.* **2008**, *1*, 21–33.

[4] T. Bjarnsholt, *APMIS.* **2013**, 1–51.

[5] Z. Khatoon, C. D. McTiernan, E. J. Suuronen, T.-F. Mah, E. I. Alarcon, *Heliyon* **2018**, *4*, e01067.

[6] G. M. Dickinson, A. L. Bisno, *Antimicrob. Agents Chemother.* **1989**, *33*, 602–607.

[7] T. R. Garrett, M. Bhakoo, Z. Zhang, *Prog. Nat. Sci.* **2008**, *18*, 1049–1056.

[8] K. A. Floyd, A. R. Eberly, M. Hadjifrangiskou in *Woodhead Publishing series in biomaterials* (Hrsg.: Y. Deng, W. Lv), WP Woodhead Publishing an imprint of Elsevier, Amsterdam, Boston, Cambridge, Heidelberg, **2017**, S. 47–95.

[9] E. Drenkard, F. M. Ausubel, *Nature* **2002**, *416*, 740–743.

[10] H. Yamamoto, M. Amaike, *Macromolecules* **1997**, *30*, 3936–3937.

[11] Y.-H. Li, X. Tian, *Sensors (Basel, Switzerland)* **2012**, *12*, 2519–2538.

[12] S. Veerachamy, T. Yarlagadda, G. Manivasagam, P. Yarlagadda, *Proc. Inst. Mech. Eng., Part H* **2014**, *228*, 1083–1099.

[13] D. Monroe, *PLoS Biol.* **2007**, *5*.

[14] a) C. Bain, *Dental update* **1997**, *24*, 328–330; b) M. Esposito, J.-M. Hirsch, U. Lekholm, P. Thomsen, *Eur. J. Oral Sci.* **1998**, *106*, 721–764; c) J. E. Hutton, M. R. Heath, J. Y. Chai, J. Harnett, T. Jemt, R. B. Johns, S. McKenna, D. C. McNamara, D. van Steenberghe, R. Taylor, *Int. J. Oral Max. Impl.* **1995**, *10*, 33–42; d) N. P. Lang (Hrsg.) *Quintessence books*, Quintessence Publ, Berlin, London, Chicago, Tokyo, Paris, Barcelona, São Paulo, Moscow, Prague, Warsaw, **2000**; e) L. Sennerby, J. Roos, *Int. J. Prosthodont.* **1998**, *11*, 408–420; f) M. D. Shaffer, D. A. Juruaz, P. C. Haggerty, *Oral Surg. Oral Med. Oral Pathol. Oral Radiol. Endod.* **1998**, *86*, 578–581; g) M. S. Tonetti, J. Schmid, *Periodontol. 2000* **1994**, *4*, 127–138.

[15] H. W. Buchholz, R. A. Elson, E. Engelbrecht, H. Lodenkamper, J. Rottger, A. Siegel, *J. Bone Joint Surg. Br.* **1981**, *63-B*, 342–353.

[16] A. Simchi, E. Tamjid, F. Pishbin, A. R. Boccaccini, *Nanomedicine* **2011**, *7*, 22–39.

[17] R. Konradi, B. Pidhatika, A. Mühlebach, M. Textor, *Langmuir* **2008**, *24*, 613–616.

[18] J. Tsibouklis, M. Stone, A. A. Thorpe, P. Graham, V. Peters, R. Heerlien, J. R. Smith, K. L. Green, T. G. Nevell, *Biomaterials* **1999**, *20*, 1229–1235.

[19] Y. Yang, Z. Cai, Z. Huang, X. Tang, X. Zhang, *Polym. J.* **2018**, *50*, 33–44.

[20] M. S. Ganewatta, C. Tang, *Polymer* **2015**, *63*, A1-A29.

[21] J. He, E. Söderling, M. Österblad, P. K. Vallittu, L. V. J. Lassila, *Molecules* **2011**, *16*, 9755–9763.

[22] R. Pandey, G. K. Khuller, *Chemotherapy* **2007**, *53*, 437–441.

[23] E. Roseeuw, V. Coessens, A.-M. Balazuc, M. Lagranderie, P. Chavarot, A. Pessina, M. G. Neri, E. Schacht, G. Marchal, D. Domurado, *Antimicrob. Agents Chemother.* **2003**, *47*, 3435–3441.

[24] C. Tolle, J. Riedel, C. Mikolai, A. Winkel, M. Stiesch, D. Wirth, H. Menzel, *Biomolecules* **2018**, *8*, 103.

[25] T. M. Allen, P. R. Cullis, *Science* **2004**, *303*, 1818–1822.

[26] T. M. Allen, *Nat. Rev. Cancer* **2002**, *2*, 750–763.

[27] M. M. Villiers, P. Aramwit, G. S. Kwon, *Nanotechnology in Drug Delivery*, Springer New York, New York, NY, **2009**.

[28] S. Rana, J. Bhattacharjee, K. C. Barick, G. Verma, P. A. Hassan, J. V. Yakhmi in *Nanostructures in therapeutic medicine series*, *Vol. 4* (Hrsg.: A. Ficai, A. M. Grumezescu), Elsevier, Amsterdam, **2017**, 177–209.

[29] E. B. Zhulina, M. Adam, I. LaRue, S. S. Sheiko, M. Rubinstein, *Macromolecules* **2005**, *38*, 5330–5351.

[30] H. Shi, T. Qiu, H. D. Ou-Yang, H. Xu, Q. Lu, Y. Zheng, K. Liu, L. He, L. Guo, X. Li, *J. Colloid. Interface Sc.* **2019**, *545*, 220–230.

[31] N. Ghasdian, D. M. A. Buzza, P. D. I. Fletcher, T. K. Georgiou, *Macromol. Rapid Commun.* **2015**, *36*, 528–532.

[32] J. Zhang, S. Li, X. Li, *Nanotec.* **2009**, *3*, 225–231.

[33] C.-L. Peng, M.-J. Shieh, M.-H. Tsai, C.-C. Chang, P.-S. Lai, *Biomaterials* **2008**, *29*, 3599–3608.

[34] K. Cholkar, A. Patel, A. D. Vadlapudi, A. K. Mitra, *Recent Pat. Nanomed.* **2012**, *2*, 82–95.

[35] Y. Bae, N. Nishiyama, S. Fukushima, H. Koyama, M. Yasuhiro, K. Kataoka, *Bioconjugate Chem.* **2005**, *16*, 122–130.

[36] Y. Bae, S. Fukushima, A. Harada, K. Kataoka, *Angew. Chem., Int. Ed.* **2003**, *42*, 4640–4643.

[37] W. Xu, P. Ling, T. Zhang, *J. Drug Delivery* **2013**, *2013*, 340315.

[38] Y. Dai, X. Chen, X. Zhang, *Polym. Chem.* **2019**, *10*, 34–44.

[39] T. R. Hoare, D. S. Kohane, *Polymer* **2008**, *49*, 1993–2007.

[40] K. Y. Lee, D. J. Mooney, *Chem. Rev.* **2001**, *101*, 1869–1880.

[41] H. J. van der Linden, S. Herber, W. Olthuis, P. Bergveld, *Analyst* **2003**, *128*, 325–331.

[42] A. C. Jen, M. C. Wake, A. G. Mikos, *Biotechnol. Bioeng.* **1996**, *50*, 357–364.

[43] K. L. Wang, J. H. Burban, E. L. Cussler in *Advances in Polymer Science*, *Vol. 110* (Hrsg.: K. Dušek), Springer, Berlin, Heidelberg, **1993**, 67–79.

[44] J. Li, D. J. Mooney, *Nat. Rev. Mater.* **2016**, *1*, 16071.

[45] A. Vashist, A. Kaushik, K. Alexis, R. Dev Jayant, V. Sagar, A. Vashist, M. Nair, *Curr. Pharm. Des.* **2017**, *23*, 3595–3602.

[46] Y. Zhang, T. Iwata, K. Nam, T. Kimura, P. Wu, N. Nakamura, Y. Hashimoto, A. Kishida, *Heliyon* **2018**, *4*, e00600.

[47] M. Åhlén, G. K. Tummala, A. Mihranyan, *Int. J. Pharm.* **2018**, *536*, 73–81.

[48] P. Gupta, K. Vermani, S. Garg, *Drug discovery today* **2002**, *7*, 569–579.

[49] R. V. Ulijn, N. Bibi, V. Jayawarna, P. D. Thornton, S. J. Todd, R. J. Mart, A. M. Smith, J. E. Gough, *Mater. Today* **2007**, *10*, 40–48.

[50] E. Larrañeta, S. Stewart, M. Ervine, R. Al-Kasasbeh, R. F. Donnelly, *J. Funct. Biomater.* **2018**, *9*, 13.

[51] H. Hezaveh, I. I. Muhamad, *Chem. Eng. Res. Des.* **2013**, *91*, 508–519.

[52] S. S. Guterres, M. P. Alves, A. R. Pohlmann, *Drug Target Insights* **2007**, *2*, 147–157.

[53] T. C. Yih, M. Al-Fandi, *J. Cell. Biochem.* **2006**, *97*, 1184–1190.

[54] M. Vert, Y. Doi, K. Hellwich, M. Hess, P. Hodge, P. Kubisa, M. Rinaudo, F. Schué, *Pure Appl. Chem.* **2012**, *84*, 377.

[55] A. Z. Wilczewska, K. Niemirowicz, K. H. Markiewicz, H. Car, *Pharmacol. Rep.* **2012**, *64*, 1020–1037.

[56] B. Magenheim, M. Y. Levy, S. Benita, *Int. J. Pharm.* **1993**, *94*, 115–123.

[57] M. Motornov, Y. Roiter, I. Tokarev, S. Minko, *Prog. Polym. Sci.* **2010**, *35*, 174–211.

[58] A. Meirovitz, R. Goldberg, A. Binder, A. M. Rubinstein, E. Hermano, M. Elkin, *FEBS J.* **2013**, *280*, 2307–2319.

[59] Z. Liu, Y. Jiao, Y. Wang, C. Zhou, Z. Zhang, *Adv. Drug Delivery Rev.* **2008**, *60*, 1650–1662.

[60] J. K. Patra, G. Das, L. F. Fraceto, E. V. R. Campos, M. D. P. Rodriguez-Torres, L. S. Acosta-Torres, L. A. Diaz-Torres, R. Grillo, M. K. Swamy, S. Sharma et al., *J. Nanobiotechnol.* **2018**, *16*, 71.

[61] J. Berger, M. Reist, J. M. Mayer, O. Felt, N. A. Peppas, R. Gurny, *Eur. J. Pharm. Biopharm.* **2004**, *57*, 19–34.

[62] N. Monteiro, A. Martins, R. L. Reis, N. M. Neves, *J. R. Soc. Interface* **2014**, *11*, 20140459.

[63] S. Vaezifar, S. Razavi, M. A. Golozar, S. Karbasi, M. Morshed, M. Kamali, *J. Clust. Sci.* **2013**, *24*, 891–903.

[64] B.-S. Ding, T. Dziubla, V. V. Shuvaev, S. Muro, V. R. Muzykantov, *Mol. Interventions* **2006**, *6*, 98–112.

[65] S. Hua, S. Y. Wu, *Front. Pharmacol.* **2013**, *4*, 143.

[66] G. A. Koning, G. Storm, *Drug discovery today* **2003**, *8*, 482–483.

[67] J. M. Metselaar, G. Storm, *Expert Opin. Drug Delivery* **2005**, *2*, 465–476.

[68] M. Alavi, N. Karimi, M. Safaei, *Adv. Pharm. Bull.* **2017**, *7*, 3–9.

[69] A. Salimi, *Asian J. Pharm.* **2018**, *12*.

[70] T. M. Allen, P. R. Cullis, *Adv. Drug Deliv. Rev.* **2013**, *65*, 36–48.

[71] H. Anwekar, S. Patel, A. K Singhai, *Int. J. Pharm. Life Sci.* **2011**, *2*.

[72] L. Sercombe, T. Veerati, F. Moheimani, S. Y. Wu, A. K. Sood, S. Hua, *Front. Pharmacol.* **2015**, *6*, 286.

[73] M. L. Immordino, F. Dosio, L. Cattel, *Int. J. Nanomedicine* **2006**, *1*, 297–315.

[74] B. Noriega-Luna, L. A. Godínez, F. J. Rodríguez, A. Rodríguez, G. Zaldívar-Lelo de Larrea, C. F. Sosa-Ferreyra, R. F. Mercado-Curiel, J. Manríquez, E. Bustos, *J. Nanomater.* **2014**, *2014*, 1–19.

[75] K. Madaan, S. Kumar, N. Poonia, V. Lather, D. Pandita, *J. Pharm. BioAllied Sci.* **2014**, *6*, 139–150.

[76] Jay Prakash Bharti, S. K. Prajapati 1, Manoj K. Jaiswal and Rahul, Deo Yadav, *Int. J. Pharm. Sci. Res.* **2011**, *2*, 1947–1960.

[77] T. Garg, O. Singh, S. Arora, R. Murthy, *Int. J. Pharm. Sci. Rev. Res.* **2011**, *7*, 211–220.

[78] R. S. Navath, Y. E. Kurtoglu, B. Wang, S. Kannan, R. Romero, R. M. Kannan, *Bioconjugate Chem.* **2008**, *19*, 2446–2455.

[79] S. K. Parajapati, S. D. Maurya, M. K. Das, V. K. Tilak, K. K. Verma, R. C. Dhakar, *J. Drug Delivery Ther.* **2016**, *6*, 71–88.

[80] N. Surendra (Hrsg.) *Gene Therapy : Woodhead Publishing Series in Biomedicine*, Woodhead Publishing, Cambridge, **2013**.

[81] K. Jain, P. Kesharwani, U. Gupta, N. K. Jain, *Int. J. Pharm.* **2010**, *394*, 122–142.

[82] J. Njuguna, K. Pielichowski, H. Zhu (Hrsg.) *Engineering professional collection*, Elsevier Science and Technology Books, Cambridge, UK, **2014**.

[83] C. Ornelas, *Macromol. Chem. Phys.* **2016**, *217*, 149–174.

[84] K. Rajagopal, D. A. Christian, T. Harada, A. Tian, D. E. Discher, *Int. J. Polym. Sci.* **2010**, *2010*, 1–10.

[85] E. Rideau, R. Dimova, P. Schwille, F. R. Wurm, K. Landfester, *Chem. Soc. Rev.* **2018**, *47*, 8572–8610.

[86] J. N. Israelachvili, *Intermolecular and surface forces,* 3. Aufl., Academic Press, Burlington, MA, **2011**.

[87] H. Che, J. C. M. van Hest, *J. Mater. Chem.* **2016**, *4*, 4632–4647.

[88] D. E. Discher, V. Ortiz, G. Srinivas, M. L. Klein, Y. Kim, D. Christian, S. Cai, P. Photos, F. Ahmed, *Prog. Polym. Sci.* **2007**, *32*, 838–857.

[89] D. E. Discher, F. Ahmed, *Annu. Rev. Biomed. Eng.* **2006**, *8*, 323–341.

[90] T. Anajafi, S. Mallik, *Ther. Delivery* **2015**, *6*, 521–534.

[91] X. Hu, Y. Zhang, Z. Xie, X. Jing, A. Bellotti, Z. Gu, *Biomacromolecules* **2017**, *18*, 649–673.

[92] J. Leong, J. Y. Teo, V. K. Aakalu, Y. Y. Yang, H. Kong, *Adv. Healthcare Mater.* **2018**, *7*, e1701276.

[93] F. Itel, M. Chami, A. Najer, S. Lörcher, D. Wu, I. A. Dinu, W. Meier, *Macromolecules* **2014**, *47*, 7588–7596.

[94] A. M. Bayer, S. Alam, S. I. Mattern-Schain, M. D. Best, *Chemistry* **2014**, *20*, 3350–3357.

[95] J. S. Lee, T. Groothuis, C. Cusan, D. Mink, J. Feijen, *Biomaterials* **2011**, *32*, 9144–9153.

[96] M. C. García in *Woodhead Publishing series in biomaterials* (Hrsg.: A. S. H. Makhlouf, N. Y. Abu-Thabit), Woodhead Publishing, Cambridge, **2019**, 345–392.

[97] V. P. Torchilin, *AAPS J.* **2007**, *9*, E128-47.

[98] D. Shenoy, S. Little, R. Langer, M. Amiji, *Pharm. Res.* **2005**, *22*, 2107–2114.

[99] S. Kommareddy, M. Amiji, *Bioconjugate Chem.* **2005**, *16*, 1423–1432.

[100] E. Mazzotta, L. Tavano, R. Muzzalupo, *Pharmaceutics* **2018**, *10*, 150.

[101] S. L. McGill, C. L. Cuylear, N. L. Adolphi, M. Osiński, H. D. C. Smyth, *IEEE Trans. Nanobioscience* **2009**, *8*, 33–42.

[102] W. Chen, J. Du, *Sci. Rep.* **2013**, *3*, 2162.

[103] C. S. Linsley, B. M. Wu, *Ther. Delivery* **2017**, *8*, 89–107.

[104] L. E. Gerweck, K. Seetharaman, *Cancer Res.* **1996**, *56*, 1194–1198.

[105] C. A. Hunt, R. D. Macgregor, R. A. Siegel, *Pharm. Res.* **1986**, *3*, 333–344.

[106] K. Engin, D. B. Leeper, J. R. Cater, A. J. Thistlethwaite, L. Tupchong, J. D. McFarlane, *Int. J. Hyperthermia* **1995**, *11*, 211–216.

[107] M. Stubbs, P. M. McSheehy, J. R. Griffiths, C. L. Bashford, *Mol. Med. Today* **2000**, *6*, 15–19.

[108] Y. Kato, S. Ozawa, C. Miyamoto, Y. Maehata, A. Suzuki, T. Maeda, Y. Baba, *Cancer cell international* **2013**, *13*, 89.

[109] G. Kocak, C. Tuncer, v. Bütün, *Polym. Chem.* **2017**, *8*, 144–176.

[110] T. Thambi, V. G. Deepagan, C. K. Yoo, J. H. Park, *Polymer* **2011**, *52*, 4753–4759.

[111] S. J. Sonawane, R. S. Kalhapure, T. Govender, *Eur. J. Pharm. Sci.* **2017**, *99*, 45–65.

[112] M. Prabaharan, J. J. Grailer, S. Pilla, D. A. Steeber, S. Gong, *Biomaterials* **2009**, *30*, 5757–5766.

[113] Y. Tao, S. Liu, Y. Zhang, Z. Chi, J. Xu, *Polym. Chem.* **2018**, *9*, 878–884.

[114] E. R. Gillies, A. P. Goodwin, J. M. J. Fréchet, *Bioconjugate Chem.* **2004**, *15*, 1254–1263.

[115] V. Knorr, V. Russ, L. Allmendinger, M. Ogris, E. Wagner, *Bioconjugate Chem.* **2008**, *19*, 1625–1634.

[116] N. Murthy, J. Campbell, N. Fausto, A. S. Hoffman, P. S. Stayton, *J. Controlled Release* **2003**, *89*, 365–374.

[117] W. Chen, F. Meng, R. Cheng, Z. Zhong, *J. Controlled Release* **2010**, *142*, 40–46.

[118] Y. Liu, W. Wang, J. Yang, C. Zhou, J. Sun, *Asian J. Pharm. Sci.* **2013**, *8*, 159–167.

[119] A. Makhlof, Y. Tozuka, H. Takeuchi, *Eur. J. Pharm. Biopharm.* **2009**, *72*, 1–8.

[120] L. Xu, L. Qiu, Y. Sheng, Y. Sun, L. Deng, X. Li, M. Bradley, R. Zhang, *J. Mater. Chem. B* **2018**, *6*, 510–517.

[121] H. Karanth, R. S. R. Murthy, *J. Pharm. Pharmacol.* **2007**, *59*, 469–483.

[122] M. Zhang, J. Zhu, Y. Zheng, R. Guo, S. Wang, S. Mignani, A.-M. Caminade, J.-P. Majoral, X. Shi, *Pharmaceutics* **2018**, *10*, 162.

[123] A. P. Griset, J. Walpole, R. Liu, A. Gaffey, Y. L. Colson, M. W. Grinstaff, *J. Am. Chem. Soc.* **2009**, *131*, 2469–2471.

[124] Y. Zhang, P. Li, H. Pan, L. Liu, M. Ji, N. Sheng, C. Wang, L. Cai, Y. Ma, *Biomaterials* **2016**, *83*, 219–232.

[125] Y. Bae, N. Nishiyama, K. Kataoka, *Bioconjugate Chem.* **2007**, *18*, 1131–1139.

[126] M. Karimi, P. Sahandi Zangabad, A. Ghasemi, M. Amiri, M. Bahrami, H. Malekzad, H. Ghahramanzadeh Asl, Z. Mahdieh, M. Bozorgomid, A. Ghasemi et al., *ACS Appl. Mater. Interfaces* **2016**, *8*, 21107–21133.

[127] J. E. Key, *Eye & contact lens* **2007**, *33*, 343-5; discussion 362-3.

[128] N. A. Peppas, Y. Huang, M. Torres-Lugo, J. H. Ward, J. Zhang, *Annu. Rev. Biomed. Eng.* **2000**, *2*, 9–29.

[129] S. K. Hahn, S. Jelacic, R. V. Maier, P. S. Stayton, A. S. Hoffman, *J. Biomater. Sci., Polym. Ed.* **2004**, *15*, 1111–1119.

[130] D. P. Huynh, M. K. Nguyen, B. S. Pi, M. S. Kim, S. Y. Chae, K. C. Lee, B. S. Kim, S. W. Kim, D. S. Lee, *Biomaterials* **2008**, *29*, 2527–2534.

[131] N. S. Hwang, S. Varghese, P. Theprungsirikul, A. Canver, J. Elisseeff, *Biomaterials* **2006**, *27*, 6015–6023.

[132] Y. Qiu, K. Park, *Adv. Drug Delivery Rev.* **2001**, *53*, 321–339.

[133] S. Chaterji, I. K. Kwon, K. Park, *Prog. Polym. Sci.* **2007**, *32*, 1083–1122.

[134] L. H. Gan, Y. Y. Gan, G. R. Deen, *Macromol.* **2000**, *33*, 7893–7897.

[135] L.H. Gan, G. Roshan Deen, X.J. Loh, Y.Y. Gan, *Polymer* **2001**, *42*, 65–69.

[136] S. Chakravarthi, C. E. Jessop, N. J. Bulleid, *EMBO Rep.* **2006**, *7*, 271–275.

[137] A. Pompella, A. Visvikis, A. Paolicchi, V. D. Tata, A. F. Casini, *Biochem. Pharmacol.* **2003**, *66*, 1499–1503.

[138] R. Cheng, F. Feng, F. Meng, C. Deng, J. Feijen, Z. Zhong, *J. Controlled Release* **2011**, *152*, 2–12.

[139] P. Kuppusamy, H. Li, G. Ilangovan, A. J. Cardounel, J. L. Zweier, K. Yamada, M. C. Krishna, J. B. Mitchell, *Cancer Res.* **2002**, *62*, 307–312.

[140] M. P. Gamcsik, M. S. Kasibhatla, S. D. Teeter, O. M. Colvin, *Biomarkers* **2012**, *17*, 671–691.

[141] J. M. Estrela, A. Ortega, E. Obrador, *Crit. Rev. Clin. Lab. Sci.* **2006**, *43*, 143–181.

[142] F. Meng, W. E. Hennink, Z. Zhong, *Biomaterials* **2009**, *30*, 2180–2198.

[143] F. Meng, R. Cheng, C. Deng, Z. Zhong, *Mater. Today* **2012**, *15*, 436–442.

[144] X. Guo, Y. Cheng, X. Zhao, Y. Luo, J. Chen, W.-E. Yuan, *J. Nanobiotechnol.* **2018**, *16*, 74.

[145] E. Heidarli, S. Dadashzadeh, A. Haeri, *Iran. J. Pharm. Res.* **2017**, *16*, 1273–1304.

[146] H. A. Aliyar, P. D. Hamilton, E. E. Remsen, N. Ravi, *J. Bioact. Compat. Polym.* **2005**, *20*, 169–181.

[147] D. S. Wilson, G. Dalmasso, L. Wang, S. V. Sitaraman, D. Merlin, N. Murthy, *Nat. Mater.* **2010**, *9*, 923–928.

[148] J. Beld, K. J. Woycechowsky, D. Hilvert, *Biochem.* **2007**, *46*, 5382–5390.

[149] Y. Zhou, K. Jie, F. Huang, *Chem. Commun. (Cambridge, U. K.)* **2017**, *53*, 8364–8367.

[150] S. Zhai, X. Hu, Y. Hu, B. Wu, D. Xing, *Biomaterials* **2017**, *121*, 41–54.

[151] M. Shahriari, M. Zahiri, K. Abnous, S. M. Taghdisi, M. Ramezani, M. Alibolandi, *J. Controlled Release* **2019**, *308*, 172–189.

[152] P. Bawa, V. Pillay, Y. E. Choonara, L. C. Du Toit, *Biomed. Mater. (Bristol, England)* **2009**, *4*, 22001.

[153] C. Wang, Q. Chen, Z. Wang, X. Zhang, *Angew. Chem., Int. Ed.* **2010**, *49*, 8612–8615.

[154] M. E. Hahn, N. C. Gianneschi, *Chem. Commun. (Cambridge, U. K.)* **2011**, *47*, 11814–11821.

[155] W. Ke, J. Li, K. Zhao, Z. Zha, Y. Han, Y. Wang, W. Yin, P. Zhang, Z. Ge, *Biomacromolecules* **2016**, *17*, 3268–3276.

[156] H. B. Kern, S. Srinivasan, A. J. Convertine, D. Hockenbery, O. W. Press, P. S. Stayton, *Mol. Pharmaceutics* **2017**, *14*, 1450–1459.

[157] D. Schiffer, G. Tegl, A. Heinzle, E. Sigl, D. Metcalf, P. Bowler, M. Burnet, G. M. Guebitz, *Expert Rev. Mol. Diagn.* **2015**, *15*, 1125–1131.

[158] S. Haas, N. Hain, M. Raoufi, S. Handschuh-Wang, T. Wang, X. Jiang, H. Schönherr, *Biomacromolecules* **2015**, *16*, 832–841.

[159] G. K. Thirunavukkarasu, K. Cherukula, H. Lee, Y. Y. Jeong, I.-K. Park, J. Y. Lee, *Biomaterials* **2018**, *180*, 240–252.

[160] N. Schleich, F. Danhier, V. Préat, *J. Control. Release* **2015**, *198*, 35–54.

[161] J. L. Corchero, A. Villaverde, *Trends Biotechnol.* **2009**, *27*, 468–476.

[162] Ch. Alexiou, W Arnold, R.J. Klein, F.G. Parak, A.S. Lübbe, *Cancer Res.* **2000**, *60*, 6641–6648.

[163] S. Dürr, C. Janko, S. Lyer, P. Tripal, M. Schwarz, J. Zaloga, R. Tietze, C. Alexiou, *Nanotechnol. Rev.* **2013**, *2*, 395–409.

[164] P. T. Ha, T. T. H. Le, T. Q. Bui, H. N. Pham, A. S. Ho, L. T. Nguyen, *New J. Chem.* **2019**, *43*, 5404–5413.

[165] J. Ge, E. Neofytou, T. J. Cahill, R. E. Beygui, R. N. Zare, *ACS nano.* **2012**, *6*, 227–233.

[166] Y.-M. Huh, Y.-w. Jun, H.-T. Song, S. Kim, J.-s. Choi, J.-H. Lee, S. Yoon, K.-s. Kim, J.-S. Shin, J.-S. Suh et al., *J. Am. Chem. Soc.* **2005**, *127*, 12387–12391.

[167] S. Lee, L. Al-Kaabi, A. Mawart, A. Khandoker, H. Alsafar, H. F. Jelinek, K. Khalaf, J.-H. Park, Y.-C. Kim, *J. Drug Targeting* **2018**, *26*, 172–181.

[168] V. Sagar, M. Nair, *Expert Opin. Drug Deliv.* **2018**, *15*, 137–152.

[169] D. A. Christian, S. Cai, D. M. Bowen, Y. Kim, J. D. Pajerowski, D. E. Discher, *Eur. J. Pharm. Biopharm.* **2009**, *71*, 463.

[170] D. Elieh-Ali-Komi, M. R. Hamblin, *Int. J. Curr. Adv. Res.* **2016**, *4*, 411–427.

[171] M. Rinaudo, *Prog. Polym. Sci.* **2006**, *31*, 603–632.

[172] D. de Cassan, S. Sydow, N. Schmidt, P. Behrens, Y. Roger, A. Hoffmann, A. L. Hoheisel, B. Glasmacher, R. Hänsch, H. Menzel, *Colloids Surf. B Biointerfaces* **2018**, *163*, 309–320.

[173] R. Esquivel, J. Juárez, M. Almada, J. Ibarra, M. A. Valdez, *Int. J. Polym. Sci.* **2015**, *2015*, 1–18.

[174] J. Zhao, J. Wu, *Chinese J. Anal. Chem.* **2006**, *34*, 1555–1559.

[175] Q. Meng, C. He, W. Su, X. Zhang, C. Duan, *Sens. Actuators, B* **2012**, *174*, 312–317.

[176] D. Sharma, J. Singh, *Bioconjugate Chem.* **2017**, *28*, 2772–2783.

[177] F. Andrade, F. Goycoolea, D. A. Chiappetta, J. das Neves, A. Sosnik, B. Sarmento, *Int. J. Carbohydr. Chem.* **2011**, *2011*, 1–14.

[178] G. Crini, P.-M. Badot, *Prog. Polym. Sci.* **2008**, *33*, 399–447.

[179] N. M. Alves, J. F. Mano, *Int. J. Biol. Macromol.* **2008**, *43*, 401–414.

[180] T. Caon, L. C. Porto, A. Granada, M. P. Tagliari, M. A. S. Silva, C. M. O. Simões, R. Borsali, V. Soldi, *Eur. J. Pharm. Sci.* **2014**, *52*, 165–172.

[181] M. R. Leedy, H. J. Martin, P. A. Norowski, J. A. Jennings, W. O. Haggard, J. D. Bumgardner in *Advances in Polymer Science*, *Vol. 244* (Hrsg.: R. Jayakumar, J. D. Bumgardner), Springer-Verlag Berlin Heidelberg, Berlin, Heidelberg, **2011**, 129–165.

[182] T. Kean, M. Thanou, *Adv. Drug Delivery Rev.* **2010**, *62*, 3–11.

[183] K. Tomihata, Y. Ikada, *Biomaterials* **1997**, *18*, 567–575.

[184] S.-C. Hsu, T.-M. Don, W.-Y. Chiu, *Polym. Degrad. Stab.* **2002**, *75*, 73–83.

[185] J. Fangkangwanwong, M. Akashi, T. Kida, S. Chirachanchai, *Biopolymers* **2006**, *82*, 580–586.

[186] J. Fangkangwanwong, M. Akashi, T. Kida, S. Chirachanchai, *Macromol. Rapid Commun.* **2006**, *27*, 1039–1046.

[187] L. C. Chan, B. G. Cox, *J. Org. Chem* **2007**, *72*, 8863–8869.

[188] A. Williams, I. T. Ibrahim, *J. Am. Chem. Soc.* **1981**, *103*, 7090–7095.

[189] M. A. Woodruff, D. W. Hutmacher, *Prog. Polym. Sci.* **2010**, *35*, 1217–1256.

[190] S. J. Hollister, *Nat. Mater.* **2005**, *4*, 518–524.

[191] Q. L. Loh, C. Choong, *Tissue Eng. Part B Rev.* **2013**, *19*, 485–502.

[192] M. Iqbal, J.-P. Valour, H. Fessi, A. Elaissari, *Colloid. Polym. Sci.* **2015**, *293*, 861–873.

[193] T.-S. Jang, E.-J. Lee, H.-E. Kim, Y.-H. Koh, *Mater. Lett.* **2012**, *72*, 157–159.

[194] M. S. S. de B. Monteiro, C. L. Rodrigues, E. Miguez, M. I. B. Tavares, *Mater. Sci. Appl.* **2016**, *07*, 575–592.

[195] S. R. Jameela, N. Suma, A. Jayakrishnan, *J. Biomater. Sci., Polym. Ed.* **1997**, *8*, 457–466.

[196] M. Alami-Milani, P. Zakeri-Milani, H. Valizadeh, R. Salehi, M. Jelvehgari, *Iran. J. Basic Med. Sci.* **2018**, *21*, 153–164.

[197] V. Guarino, G. Gentile, L. Sorrentino, L. Ambrosio in *Encyclopedia of polymer science and technology*, Wiley Interscience, Hoboken, NJ, **2004**, 1–36.

[198] Y. Bourgat, B. Tiersch, J. Koetz, H. Menzel, *Macromol. Biosci.* **2020**, e2000259.

[199] M. Labet, W. Thielemans, *Chem. Soc. Rev.* **2009**, *38*, 3484–3504.

[200] M. Ryner, K. Stridsberg, A.-C. Albertsson, H. von Schenck, M. Svensson, *Macromolecules* **2001**, *34*, 3877–3881.

[201] L. G. Bach, M. R. Islam, X. T. Cao, J. M. Park, K. T. Lim, *J. Alloys Compd.* **2014**, *582*, 22–28.

[202] R. Shi, J. Xue, M. He, D. Chen, L. Zhang, W. Tian, *Polym. Degrad. Stab.* **2014**, *109*, 293–306.

[203] C. L. Salgado, E. M. S. Sanchez, C. A. C. Zavaglia, P. L. Granja, *J. Biomed. Mater. Res., Part A* **2012**, *100*, 243–251.

[204] K.-C. Chou, Y.-D. Cai, *Proteins* **2003**, *53*, 282–289.

[205] M. M. Flocco, S. L. Mowbray, *J. Mol. Biol.* **1994**, *235*, 709–717.

[206] R.E.W. Hancock, T. Falla, M. Brown in *Adv. Microb. Physiol.*, 135–175.

[207] R. E. W. Hancock, D. S. Chapple, *Antimicrob. Agents Chemother.* **1999**, *43*, 1317–1323.

[208] R. E. Hancock, R. Lehrer, *Trends Biotechnol.* **1998**, *16*, 82–88.

[209] S. G. Waley, J. Watson, *Biochem. J.* **1953**, *55*, 328–337.

[210] D. Quong, J. N. Yeo, R. J. Neufeld, *J. Microencapsulation* **1999**, *16*, 73–82.

[211] J. Rodríguez-Hernández, M. Gatti, H.-A. Klok, *Antimicrob. Agents Chemother.* **2003**, *4*, 249–258.

[212] K. Barlos, O. Chatzi, D. Gatos, G. Stavropoulos, *Int. J. Pept. Protein Res.* **1991**, *37*.

[213] P.-N. Cheng, J. S. Nowick, *J. Org. Chem.* **2011**, *76*, 3166–3173.

[214] K. J. Jensen, P. Tofteng Shelton, S. L. Pedersen, *Peptide Synthesis and Applications*, Humana Press, Totowa, NJ, **2013**.

[215] D. P. Nair, M. Podgórski, S. Chatani, T. Gong, W. Xi, C. R. Fenoli, C. N. Bowman, *Chem. Mater.* **2014**, *26*, 724–744.

[216] M. Sangermano, R. Bongiovanni, G. Malucelli, A. Priola, A. Harden, N. Rehnberg, *J. Polym. Sci. A Polym. Chem.* **2002**, *40*, 2583–2590.

[217] M. Uygun, M. A. Tasdelen, Y. Yagci, *Macromol. Chem. Phys.* **2010**, *211*, 103–110.

[218] A. Dondoni, A. Marra, *Chem. Soc. Rev.* **2012**, *41*, 573–586.

[219] H. Kakwere, S. Perrier, *J. Am. Chem. Soc.* **2009**, *131*, 1889–1895.

[220] B. H. Northrop, S. H. Frayne, U. Choudhary, *Polym. Chem.* **2015**, *6*, 3415–3430.

[221] J. P. Tam, C. R. Wu, W. Liu, J. W. Zhang, *J. Am. Chem. Soc.* **1991**, *113*, 6657–6662.

[222] A. B. Lowe, *Polym. Chem.* **2010**, *1*, 17–36.

[223] J. E. Hein, V. V. Fokin, *Chem. Soc. Rev.* **2010**, *39*, 1302–1315.

[224] J.-F. Lutz, *Angew. Chem. Int. Ed.* **2007**, *46*, 1018–1025.

[225] A. Deiters, T. A. Cropp, D. Summerer, M. Mukherji, P. G. Schultz, *Bioorg. Med. Chem. Lett.* **2004**, *14*, 5743–5745.

[226] J.-F. Lutz, H. Schlaad, *Polymer* **2008**, *49*, 817–824.

[227] Bapi Sarker, *Advanced Hydrogels Concepts Based on Combinations of Alginate, Gelatin and Bioactive Glasses for Tissue Engineering*. *Doctoral Thesis*. University in St. Louis, Washington, **2015**.

[228] Wee, Gombotz, *Adv. Drug Delivery Rev.* **1998**, *31*, 267–285.

[229] A. H. E. Machado, D. Lundberg, A. J. Ribeiro, F. J. Veiga, M. G. Miguel, B. Lindman, U. Olsson, *J. Colloid Interface Sci* **2013**, *29*, 15926–15935.

[230] S. Mazzitelli, M. Borgatti, G. Breveglieri, R. Gambari, C. Nastruzzi, *J. Cell Commun. Signal.* **2011**, *5*, 157–165.

[231] O. Smidsrod, G. Skjakbrk, *Trends Biotechnol.* **1990**, *8*, 71–78.

[232] R. Bhattarai, A. Shrestha, N. Dhandapani, *Chron. Young Sci.* **2011**, *2*, 192.

[233] H. H. Tønnesen, J. Karlsen, *Drug Dev. Ind. Pharm.* **2002**, *28*, 621–630.

[234] R. E. Webber, K. R. Shull, *Macromolecules* **2004**, *37*, 6153–6160.

[235] K. I. Draget, G. Skjåk Bræk, O. Smidsrød, *Carbohydr. Polym.* **1994**, *25*, 31–38.

[236] X. Wang, H. Garth Spencer, *Polymer* **1998**, *39*, 2759–2764.

[237] B. A. Aderibigbe, B. Buyana, *Pharmaceutics* **2018**, *10*, 42.

[238] D. Das, S. Bang, S. Zhang, I. Noh, *Nanomaterials* **2017**, *7*, 389.

[239] M. Otterlei, K. Ostgaard, G. Skjåk-Braek, O. Smidsrød, P. Soon-Shiong, T. Espevik, *J. Immunother.* **1991**, *10*, 286–291.

[240] U. Zimmermann, G. Klöck, K. Federlin, K. Hannig, M. Kowalski, R. G. Bretzel, A. Horcher, H. Entenmann, U. Sieber, T. Zekorn, *Electrophoresis* **1992**, *13*, 269–274.

[241] J. Lee, K. Y. Lee, *Pharm. Res.* **2009**, *26*, 1739–1744.

[242] L. Wang, J. Shansky, C. Borselli, D. Mooney, H. Vandenburgh, *Tissue Eng. Part A* **2012**, *18*, 2000–2007.

[243] T. Y. Wong, L. A. Preston, N. L. Schiller, *Annu. Rev. Microbiol.* **2000**, *54*, 289–340.

[244] K. H. Bouhadir, K. Y. Lee, E. Alsberg, K. L. Damm, K. W. Anderson, D. J. Mooney, *Biotechnol. Prog.* **2001**, *17*, 945–950.

[245] K. Huang, L. D. Wu, *J. Int. Med. Res.* **2008**, *36*, 1149–1160.

[246] H. Stanton, F. M. Rogerson, C. J. East, S. B. Golub, K. E. Lawlor, C. T. Meeker, C. B. Little, K. Last, P. J. Farmer, I. K. Campbell et al., *Nature* **2005**, *434*, 648–652.

[247] E. Arner, *Curr. Opin. Pharmacol.* **2002**, *2*, 322–329.

[248] H. Nagase, M. Kashiwagi, *Arthritis Res. Ther.* **2003**, *5*, 94–103.

[249] L. S. Lohmander, P. J. Neame, J. D. Sandy, *Arthritis Rheum.* **1993**, *36*, 1214–1222.

[250] A. D. Verderosa, C. de La Fuente-Núñez, S. C. Mansour, J. Cao, T. K. Lu, R. E. W. Hancock, K. E. Fairfull-Smith, *Eur. J. Med. Chem.* **2017**, *138*, 590–601.

[251] G.-F. Zhang, X. Liu, S. Zhang, B. Pan, M.-L. Liu, *Eur. J. Med. Chem.* **2018**, *146*, 599–612.

[252] K. Drlica, X. Zhao, *Microbiol. Mol. Biol. Rev.* **1997**, *61*, 377–392.

[253] N. B. Patel, S. D. Patel, J. N. Patel, J. C. Patel, Y. S. Gorgamwala, *Int. J. Biol. Chem* **2010**, *5*, 37–45.

[254] R. Cormier, W. N. Burda, L. Harrington, J. Edlinger, K. M. Kodigepalli, J. Thomas, R. Kapolka, G. Roma, B. E. Anderson, E. Turos et al., *Bioorg. Med. Chem. Lett.* **2012**, *22*, 6513–6520.

[255] J.L. Vázquez, S. Merino, Ò. Doměnech, M. Berlanga, M. Viñas, M.T. Montero, J. Hernández-Borrell, *Int. J. Pharm.* **2001**, *220*, 53–62.

[256] Y.-Q. Hu, Z. Xu, S. Zhang, X. Wu, J.-W. Ding, Z.-S. Lv, L.-S. Feng, *Eur. J. Med. Chem.* **2017**, *136*, 122–130.

[257] Z. Xu, C. Gao, Q.-C. Ren, X.-F. Song, L.-S. Feng, Z.-S. Lv, *Eur. J. Med. Chem.* **2017**, *139*, 429–440.

[258] Y.-Q. Hu, C. Gao, S. Zhang, L. Xu, Z. Xu, L.-S. Feng, X. Wu, F. Zhao, *Eur. J. Med. Chem.* **2017**, *139*, 22–47.

[259] D. Sriram, P. Yogeeswari, G. Senchani, D. Banerjee, *Bioorg. Med. Chem. Lett.* **2007**, *17*, 2372–2375.

[260] A. V. Bogdanov, E. F. Akhmetova, S. V. Bukharov, V. F. Mironov, *Russ. J. Gen. Chem.* **2014**, *84*, 1860–1862.

[261] A. A.-M. Abdel-Aziz, A. S. El-Azab, A. M. Alanazi, Y. A. Asiri, I. A. Al-Suwaidan, A. R. Maarouf, R. R. Ayyad, T. Z. Shawer, *J. Enzyme Inhib. Med. Chem.* **2016**, *31*, 796–809.

[262] R. Pignatello, A. Leonardi, V. Fuochi, G. Petronio Petronio, A. S. Greco, P. M. Furneri, *Nanomaterials (Basel, Switzerland)* **2018**, *8*, 304.

[263] D. Passi, M. Singh, S. R. Dutta, S. Sharma, M. Atri, J. Ahlawat, A. Jain, *J. Oral Biol. Craniofac. Res.* **2017**, *7*, 58–61.

[264] R. Poveda Roda, J. V. Bagan, J. M. Sanchis Bielsa, E. Carbonell Pastor, *Med. Oral Patol. Oral Cir. Bucal* **2007**, *12*, E186-92.

[265] C. R. Chen, M. Malik, M. Snyder, K. Drlica, *J. Mol. Biol.* **1996**, *258*, 627–637.

[266] G. del Solar, R. Giraldo, M. J. Ruiz-Echevarría, M. Espinosa, R. Díaz-Orejas, *Microbiol. Mol. Biol. Rev.* **1998**, *62*, 434–464.

[267] M. O'Donnell, L. Langston, B. Stillman, *Cold Spring Harbor Perspect. Biol.* **2013**, *5*, a010108.

[268] S. W. Matson, *Prog. Nucleic Acid Res. Mol. Biol.* **1991**, *40*, 289–326.

[269] D. G. Waller, A. P. Sampson in *Medical Pharmacology and Therapeutics (Fifth Edition)* (Hrsg.: D. G. Waller, A. P. Sampson), Elsevier, **2018**, 581–629.

[270] A. B. Khodursky, B. J. Peter, M. B. Schmid, J. DeRisi, D. Botstein, P. O. Brown, N. R. Cozzarelli, *Proc. Natl. Acad. Sci. U. S. A.* **2000**, *97*, 9419–9424.

[271] R. G. Finch, D. Greenwood, S. R. Norrby, R. J. Whitley (Hrsg.) *Antibiotic and Chemotherapy (Ninth Edition)*, W.B. Saunders, London, **2010**.

[272] F. M. Barnard, A. Maxwell, *Antimicrob. Agents Chemother.* **2001**, *45*, 1994–2000.

[273] G. A. Jacoby, *Clin. Infect. Dis.* **2005**, *41*, S120-S126.

[274] R. Nitzsche, *Intensivkurs* **2011**, Malvern Instruments.

[275] Malvern Instruments Ltd, "Zetasizer Nano user manual", zu finden unter https://www.malvernpanalytical.com/en/learn/knowledge-center/user-manuals/MAN0485EN.

[276] S.-J. Park, M.-K. Seo (Hrsg.) *Interface Science and Technology*, *volume 18*, Academic Press is an imprint of Elsevier, Amsterdam, **2011**.

[277] Malvern Instruments Ltd, "Dynamic Light Scattering: An Introduction in 30 Minutes", zu finden unter https://www.malvernpanalytical.com/en/learn/knowledge-center/technical-notes/TN101104DynamicLightScatteringIntroduction.

[278] D. Möbius, R. Miller, *Novel methods to study interfacial layers*, Elsevier, Amsterdam, **2001**.

[279] H. G. Tompkins, *A user's guide to ellipsometry*, Academic Press, Boston, **1993**.

[280] H. Motschmann, R. Teppner, *Studies in Interface Science* **2001**, *11*, 1–42.

[281] M. Matsumoto, W. Udomsinprasert, P. Laengee, S. Honsawek, K. Patarakul, S. Chirachanchai, *Macromol. Rapid Commun.* **2016**, *37*, 1618–1622.

[282] G. C. Tron, T. Pirali, R. A. Billington, P. L. Canonico, G. Sorba, A. A. Genazzani, *Med. Res. Rev.* **2008**, *28*, 278–308.

[283] G. T. Hermanson, *Bioconjugate Techniques,* 3. Aufl., Elsevier/AP, Amsterdam, **2013**.

[284] J. S. Nanda, J. R. Lorsch, *Methods Enzymol.* **2014**, *536*, 79–86.

[285] W. A. R. van Heeswijk, M. J. D. Eenink, J. Feijen, *Synthesis* **1982**, *1982*, 744–747.

[286] D. E. Discher, A. Eisenberg, *Science* **2002**, *297*, 967.

[287] M. Danaei, M. Dehghankhold, S. Ataei, F. Hasanzadeh Davarani, R. Javanmard, A. Dokhani, S. Khorasani, M. R. Mozafari, *Pharmaceutics* **2018**, *10*, 57.

[288] J. Saito, A. Kita, Y. Higuchi, Y. Nagata, A. Ando, K. Miki, *J. Biol. Chem.* **1999**, *274*, 30818–30825.

[289] S. Sydow, A. Aniol, C. Hadler, H. Menzel, *Biomolecules* **2019**, *9*, 573.

[290] F. F. Buck, A. J. Vithayathil, M. Bier, F. F. Nord, *Arch. Biochem. Biophys.* **1962**, *97*, 417–424.

[291] J. K. Park, K. Shimono, N. Ochiai, K. Shigeru, M. Kurita, Y. Ohta, K. Tanaka, H. Matsuda, M. Kawamukai, *J. Bacteriol.* **1999**, *181*, 6642.

[292] T. Jiang, R. James, S. G. Kumbar, C. T. Laurencin in *Natural and Synthetic Biomedical Polymers* (Hrsg.: S. G. Kumbar, C. T. Laurencin, M. Deng), Elsevier, Amsterdam, **2014**, S. 91–113.

[293] M. Shimosaka, M. Nogawa, Y. Ohno, M. Okazaki, *Biosci. Biotechnol. Biochem.* **1993**, *57*, 231–235.

[294] S. de Luca, F. Chen, P. Seal, M. H. Stenzel, S. C. Smith, *Biomacromolecules* **2017**, *18*, 3665–3677.

[295] C. R. Arciola, D. Campoccia, L. Montanaro, *Nat. Rev. Microbiol.* **2018**, *16*, 397–409.

[296] J. C. McPherson, R. Runner, T. B. Buxton, J. F. Hartmann, D. Farcasiu, I. Bereczki, E. Rőth, S. Tollas, E. Ostorházi, F. Rozgonyi et al., *Eur. J. Med. Chem.* **2012**, *47*, 615–618.

[297] W. Chen, D. Wang, C. Dai, D. Hamelberg, B. Wang, *Chem. Commun.* **2012**, *48*, 1736–1738.

[298] J.-C. Rossi, B. Maret, K. Vidot, J.-P. Francoia, M. Cangiotti, S. Lucchi, C. Coppola, M. F. Ottaviani, *Macromol. Biosci.* **2015**, *15*, 275–290.

[299] D. C. Kennedy, C. S. McKay, M. C. B. Legault, D. C. Danielson, J. A. Blake, A. F. Pegoraro, A. Stolow, Z. Mester, J. P. Pezacki, *J. Am. Chem. Soc.* **2011**, *133*, 17993–18001.

[300] E. Lallana, R. Riguera, E. Fernandez-Megia, *Angew. Chem. Int. Ed.* **2011**, *50*, 8794–8804.

[301] N. Akeroyd, *Thesis (PhD (Chemistry and Polymer Science))*, University of Stellenbosch, Stellenbosch, **2010**.

[302] P. Klahn, V. Fetz, A. Ritter, W. Collisi, B. Hinkelmann, T. Arnold, W. Tegge, K. Rox, S. Hüttel, K. I. Mohr et al., *Chem. Sci.* **2019**, *10*, 5197–5210.

[303] K. Schug, H. M. McNair, *J. Sep. Science* **2002**, *25*, 759–766.

[304] M. Thakur, S. Pandey, A. Mewada, V. Patil, M. Khade, E. Goshi, M. Sharon, *J. Drug Deliv.* **2014**, *2014*, 282193.

[305] T. K. Giri, A. Thakur, A. Alexander, Ajazuddin, H. Badwaik, D. K. Tripathi, *Acta Pharmaceutica Sinica B* **2012**, *2*, 439–449.

[306] S. Pistone, D. Qoragllu, G. Smistad, M. Hiorth, *Soft Matter* **2015**, *11*, 5765–5774.

[307] N. Poth, V. Seiffart, G. Gross, H. Menzel, W. Dempwolf, *Biomolecules* **2015**, *5*, 3–19.

[308] S. Sydow, D. de Cassan, R. Hänsch, T. R. Gengenbach, C. D. Easton, H. Thissen, H. Menzel, *Biomater. Sci.* **2018**, *7*, 233–246.

[309] D. Pinto, C. Santos, A. Silva, *Research Signpost* **2007**, *37661*, 397–475.

[310] C. Ji, P. A. Miller, M. J. Miller, *ACS Med. Chem. Lett.* **2015**, *6*, 707–710.

[311] Nikola Ojkic, Elin Lilja, Susana Direito, Angela Dawson, Rosalind J. Allen, Bartlomiej Waclaw, *Antimicrob. Agents Chemother.* **2020**, *64*, 02487-02419.

[312] A. Cederlund, G. H. Gudmundsson, B. Agerberth, *FEBS J.* **2011**, *278*, 3942–3951.

[313] H. D. M. Coutinho, K. M. Lôbo, D. A. C. Bezerra, I. Lôbo, *Indian J. Pharmacol.* **2008**, *40*, 3–9.

[314] W. van 't Hof, E. C. Veerman, E. J. Helmerhorst, A. V. Amerongen, *Biol. Chem.* **2001**, *382*, 597–619.

[315] U. Grether, H. Waldmann, *Chemistry* **2001**, *7*, 959–971.